

TESIS DOCTORAL

# RENDIMIENTO DE COMBUSTIBLES BAJOS EN CARBONO EN MOTORES DE COMBUSTIÓN INTERNA

PhD THESIS

## PERFORMANCE OF LOW CARBON FUELS IN INTERNAL COMBUSTION ENGINES

AUTOR

RAFAEL ORTIZ IMEDIO

DIRECTORES

PROF. DRA. INMACULADA ORTIZ URIBE

DR. ALFREDO ORTIZ SAINZ DE AJA

UNIVERSIDAD DE CANTABRIA

Escuela de **Doctorado** de la Universidad de Cantabria

Santander **2021**



**UNIVERSIDAD DE CANTABRIA**



ESCUELA DE DOCTORADO DE LA UNIVERSIDAD DE CANTABRIA

PROGRAMA DE DOCTORADO EN INGENIERÍA QUÍMICA, DE LA  
ENERGÍA Y DE PROCESOS

**Performance of low carbon fuels in internal  
combustion engines**

*Rendimiento de combustibles bajos en carbono en  
motores de combustión interna*

Tesis Doctoral presentada para optar al título de Doctor por  
la Universidad de Cantabria

**Rafael Ortiz Imedio**

Dirigida por:

Prof. Dra. Inmaculada Ortiz Uribe

Dr. Alfredo Ortiz Sainz de Aja

Santander, 2021





## **Programa de Doctorado en Ingeniería Química, de la Energía y de Procesos**

**(BOE núm 16, de 19 de enero de 2015, RUCT: 5601000)**

The research described in this thesis has been conducted at the Advanced Separation Processes research group of the Chemical and Biomolecular Engineering Department at the University of Cantabria.

This thesis has been financially supported by the European Regional Development Fund within the framework of the Interreg Atlantic Program through the project “HYLANTIC” – EAPA\_204/2016 and within the framework of the Interreg SUDOE Program through the project PEMFC-SUDOE (SOE1/P1/E0293 – INTERREG SUDOE/FEDER, UE), “Energy Sustainability at the SUDOE Region: Red PEMFC-SUDOE”. The three months research stay at the Institute of Energy and Climate Research – Techno-Economic Systems analysis (IEK-3) in Forschungszentrum Jülich, Germany, under the supervision of Martin Robinius has been also financed through the “HYLANTIC” project.

Likewise, Rafael Ortiz acknowledges the University of Cantabria for the Concepción Arenal postgraduate research grant. Furthermore, the author is grateful to the Santander Supercomputación support group at the University of Cantabria who provided access to the supercomputer Altamira Supercomputer at the Institute of Physics of Cantabria (IFCA-CSIC), member of the Spanish Supercomputing Network, to perform the simulations shown in Chapter 4 of this thesis.



## AGRADECIMIENTOS

En primer lugar, me gustaría agradecer toda la ayuda proporcionada por la catedrática Inmaculada Ortiz, supervisora de esta tesis y directora del grupo de investigación Procesos Avanzados de Separación del departamento de Ingenierías Química y Biomolecular. Gracias a su amplia experiencia y su capacidad de proporcionar ideas innovadoras, ha sido posible el desarrollo de esta tesis. Además, su continuo seguimiento del trabajo ha permitido enfocarlos de la forma más óptima.

Quiero agradecer de forma especial al Dr. Alfredo Ortiz, que confió en mí para hacer el TFM, trabajar en el proyecto HYLANTIC y realizar esta tesis bajo su supervisión. Siempre me ha apoyado y me ha animado a continuar, y a pesar de su apretada agenda, siempre sacaba un rato para escucharme, ayudarme y orientarme cuál era la mejor manera de afrontar la siguiente tarea y reto que se presentaban. Además, ha sido un compañero estupendo durante los viajes, permitiéndome conocer más rincones de este mundo maravilloso.

I would also like to express my gratitude to Dr. Martin Robinius for accepting me for a three-months research stay in his research group to learn many things. I also want to thank to Dr. Heidi Heinrichs, Dr. Dilara Caglayan and Dr. Severin Ryberg for their help during the research stay. And thanks to Michael, Natascha, Nikhil, Devesh, Anxhela, Simonas, Timo and all of you that share that time with me, making me feel as home.

Quiero dar las gracias también al catedrático Luis M. Gandía, al catedrático Pedro M. Diéguez y al Dr. José Carlos Urroz por su ayuda y colaboración para la realización de los experimentos del capítulo 3 de esta tesis en su banco de ensayo de motores.

Quiero agradecer a mis compañeros de departamento y de despacho con los que he compartido tantos momentos durante estos años, haciéndome más divertido el día a día y aprendiendo mucho de ellos. En especial Daniel Gorri, Marcos, Domingo, Víctor, Estela, Marta, Dana, Carla, Tamara, Dani, Laura, Arantza, old Víctor, Carolina, Gema, Pedro, Guillermo y Lucía, sois geniales y me habéis ayudado muchísimo todo este tiempo, alegrándome y animándome a seguir.

## Agradecimientos

---

Mil gracias a mis compañeros de carrera y a mis amigos, que me han acompañado y me han regalado muchos buenos momentos. En especial a Ana, Berta, Luisda, Cris, María, Sandra, Pablo y Nuria por las buenas risas que nos hemos echado juntos.

Muchas gracias a toda mi comunidad, porque siempre habéis rezado por mí, y me habéis apoyado y escuchado pacientemente cuando tenía mis momentos de mayor desánimo, haciéndome seguir y volviendo a enfocarme en lo más importante.

Mi más cariñoso agradecimiento va a mi familia entera, rezando por mí, animándome, entendiéndome y queriéndome siempre, independientemente de mi estado de humor o de los problemas que surgieran. Sin vosotros no habría llegado hasta aquí. En especial, muchas gracias a mis padres, Fernando y Ana, transmitiéndome amor, la Fe y enseñándome dónde está verdaderamente la vida.

Finalmente, mi agradecimiento más importante es para Dios, porque me ha dado la vida, me Ama sin límites, me otorga día a día la Fe, la Esperanza y la fuerza para hacer su voluntad cada día. Además, me ha puesto en la Iglesia, en el mejor sitio que podría estar para conocer a Jesucristo y vivir una vida plena llena de Amor.

¡Muchas gracias a todos!

# TABLE OF CONTENTS

<b>TABLE OF CONTENTS .....</b>	<b>1</b>
<b>SUMMARY THESIS SCOPE AND LAYOUT .....</b>	<b>5</b>
<b>i. Motivation .....</b>	<b>7</b>
<b>ii. Thesis objectives.....</b>	<b>8</b>
<b>iii. Thesis structure .....</b>	<b>10</b>
<b>RESUMEN ALCANCE Y ESTRUCTURA DE LA TESIS .....</b>	<b>13</b>
<b>i. Motivación.....</b>	<b>15</b>
<b>ii. Objetivos de la tesis.....</b>	<b>17</b>
<b>iii. Estructura de la tesis .....</b>	<b>18</b>
<b>CHAPTER 1 INTRODUCTION.....</b>	<b>21</b>
<b>1.1. Global energy system situation .....</b>	<b>23</b>
<b>1.2. Hydrogen energy vector .....</b>	<b>29</b>
<b>1.3. Internal combustion engines technology.....</b>	<b>34</b>
<b>1.3.1. Engine configuration.....</b>	<b>34</b>
<b>1.3.2. Engine operating parameters .....</b>	<b>40</b>
<b>1.4. Low carbon fuels .....</b>	<b>45</b>
<b>1.5. CFD simulation .....</b>	<b>52</b>
<b>References.....</b>	<b>56</b>
<b>CHAPTER 2 RENEWABLE ENERGY SYSTEMS COUPLING WITH HYDROGEN INFRASTRUCTURE INCLUDING MARITIME TRANSPORT .....</b>	<b>71</b>
<b>2.1. Introduction .....</b>	<b>73</b>
<b>2.2. Methodology.....</b>	<b>75</b>
<b>2.2.1. Energy system modeling software .....</b>	<b>75</b>
<b>2.2.2. System definition .....</b>	<b>76</b>
<b>2.2.3. Ship electricity and hydrogen demands.....</b>	<b>79</b>
<b>2.2.4. Scenarios.....</b>	<b>85</b>
<b>2.3. Results and discussion.....</b>	<b>86</b>

## Table of Contents

---

2.3.1. Impact of ship H <sub>2</sub> demand.....	86
2.3.2. Analysis of scenario S100 .....	92
2.4. Conclusions .....	98
Nomenclature .....	99
References .....	100
Appendix .....	105
CHAPTER 3 EXPERIMENTAL PERFORMANCE OF LOW CARBON FUELS IN INTERNAL COMBUSTION ENGINES .....	111
3.1. Introduction.....	113
3.2. Methodology .....	115
3.2.1. Test bench .....	115
3.2.2. Fuel gases.....	118
3.2.3. Experimental methods.....	119
3.3. Results and discussion.....	120
3.3.1. Engine performance .....	120
3.3.2. Emissions.....	127
3.4. Conclusions .....	133
Nomenclature .....	134
References .....	136
CHAPTER 4 COMBUSTION ANALYSIS OF LOW CARBON FUELS IN INTERNAL COMBUSTION ENGINES WITH CFD .....	143
4.1. Introduction.....	145
4.2. Simulation methodology .....	147
4.2.1. CFD software .....	147
4.2.2. Planning of simulation runs .....	153
4.3. Results and discussion.....	157
4.3.1. Engine performance .....	157
4.3.2. Dynamic evolution variables .....	161
4.3.3. Volumetric efficiency .....	167

4.3.4.    Sensitivity analysis of COG fuel low-content components .....	173
4.3.5.    Spark advance sensitivity analysis.....	174
4.4. Conclusions.....	178
Nomenclature.....	180
References.....	182
Appendix.....	187
CHAPTER 5 CONCLUSIONS AND FUTURE WORK.....	201
4.5. Conclusions.....	203
4.6. Future work.....	205
CAPÍTULO 5 CONCLUSIONES Y TRABAJO FUTURO .....	207
5.1. Conclusiones .....	209
5.2. Trabajo futuro .....	212
APPENDIX I SCIENTIFIC CONTRIBUTIONS .....	215





# SUMMARY

---

THESIS SCOPE AND LAYOUT



## **i. Motivation**

Low carbon fuels are key to the transition to a sustainable energy system with lower polluting emissions and less dependence on fossil fuels. Renewable energy sources (RES) enable a more distributed generation of clean energy across the different regions of the world. However, most renewable energies suffer fluctuations leading to intermittency in the energy supply. In this sense, hydrogen as an energy vector can play a pivotal role in the wide deployment of RES. The coupling of renewable energies with hydrogen allows the balance of the grid, dampening the fluctuations in natural resources through long-term storage. In addition, hydrogen can be employed in a wide range of sectors, from transport and stationary applications to industry, substituting conventional fossil fuels and mitigating the adverse effects on climate change due to greenhouse gas emissions.

Among the challenging sectors with great opportunities for hydrogen penetration, it is worth mentioning the maritime sector. In the Atlantic area of Europe, this sector presents a high contribution to freight and passenger transport and nowadays is responsible for high impact on the pollution of the region. Thus, this situation could be considerably improved by changing to a system where the energy required by the maritime transport in the region is provided by electricity and hydrogen.

Currently, some industrial processes produce hydrogen-rich industrial waste streams, that despite proceeding from non-renewable energies, are usually characterized by high energy content. Therefore, purification or recovery of valuable constituents from waste streams allowing the final conversion of  $H_2$  to energy becomes a key challenge that approaches the benefits of wastes circularity to energy decarbonization. Coke oven gas, a by-product of coke manufacture with high volumetric percentage of hydrogen and methane, can be used in a wide range of applications, especially in the steel and coke industry. Nevertheless, in periods with low demand, coke oven gas is directly flared off, throwing away its energy content. Thus, the recovery alternative for further conversion to electricity by using the gas in internal combustion engines (ICEs) coupled to generator systems presents high interest.

Internal combustion engines are a very mature and worldwide deployed technology. Gasoline and diesel, obtained from fossil fuels, have been commonly employed as conventional fuels depending on the engine configuration. However, increasingly restrictive regulations require the increment of engine efficiency while reducing pollutant emissions. These policies limit their applicability and make a great pressure on engine manufacturers to develop alternative and still expensive technologies, such as fuel cells. Therefore, the substitution of conventional fuels by low carbon fuels emerges as a feasible solution to extend the use of ICEs in a relatively cheap manner. This thesis analyzes and proves the feasibility of fueling ICEs with low carbon fuels, such as hydrogen, methane and coke oven gas, with high performance and low emissions, paving the way to a more sustainable energy system.

This thesis has been carried out within the framework of the project HYLANTIC - EAPA\_204/2016, co-financed by the European Regional Development Fund in the context of the Interreg Atlantic program. The HYLANTIC project focused on the deployment of a transnational network to advance the research and development, implementation and commercialization of hydrogen as energy vector in the Atlantic area of Europe. The project scope covered i) hydrogen generation through renewable energy and local waste streams, ii) the safe storage in pressurized tanks and iii) H<sub>2</sub> application in fuel cells or ICEs, with a special focus on the maritime sector. The work developed in this thesis interlinks with the project activities that addressed the coupling of the hydrogen vector and renewable energy sources and the recovery of fuels from industrial waste streams to be used in internal combustion engines.

### **ii. Thesis objectives**

Based on the motivation previously exposed, the overall objective of this thesis is twofold: 1) The first main goal is the assessment of a futuristic European energy system based on the coupling between renewable energies and the hydrogen energy vector for the maritime sector in the Atlantic area of Europe, and 2) The second main objective is the evaluation of the technical and energy performance of an internal combustion engine fueled with low carbon fuels recovered from industrial waste gases. This second target has focused on the study of coke oven gas

as fuel source in a spark ignition engine. Furthermore, the engine performance has been compared with the use of pure hydrogen and pure methane as combustion fuels; the comparison has been made because hydrogen and methane are the main constituents of coke oven gas, thus, the contribution of each fuel to the combustion phenomena has been analyzed.

In order to achieve the global objective, the research has been divided into the following specific objectives:

- State-of-the-art review of energy system models developed at different scales and their boundary conditions, including the penetration of renewable energies and the hydrogen employment as energy vector.
- Forecast of the electric and hydrogen energy demand in the Atlantic region, including the maritime transport in the Atlantic area of Europe, in the horizon 2050. Additionally, different penetration scenarios of hydrogen demand in ships will be assessed to observe its impact on the hydrogen infrastructure.
- State-of-the-art review of internal combustion engines fueled with low carbon fuels, especially hydrogen, methane and coke oven gas.
- Experimental evaluation of the technical performance of a spark ignition engine fueled with coke oven gas, and the comparison with hydrogen and methane, together with evaluation of emissions of exhaust gases.
- Development of a computational fluid dynamics simulation model able to predict the performance of the engine under a wide range of operating conditions and to understand the combustion behavior of the target low carbon fuels.

### iii. Thesis structure

This thesis has been structured in five chapters following the main objectives previously exposed.

In order to understand the context and the motivation that has led to the realization of this thesis, **Chapter 1** begins with a general introduction of the global energy system, exposing the current dependence on fossil fuels. In this sense, the increasing deployment of renewable energies in many countries requires its coupling with hydrogen as energy vector to balance the grid and to feed different sectors in a sustainable way. Afterward, a summary of the mode of operation and the main parameters of the internal combustion engine technology is provided to understand its behavior. A review of hydrogen, methane and coke oven gas characteristics as low carbon fuels is also given. Finally, a brief explanation of the computational fluid dynamics simulation tool focused on internal combustion engines is detailed.

**Chapter 2** focuses on European energy system scenarios in the horizon 2050 based on 100% renewable energies coupled to hydrogen as energy vector. The model used optimizes the distribution of the RES and the hydrogen infrastructure, minimizing the total annual costs and the capacity of the technologies involved to satisfy the electric and hydrogen demands across Europe. As the maritime sector has a significant contribution in the transport of freight and passengers in the European Atlantic area, different penetration scenarios of ship hydrogen demand in that region are included to analyze its impact on the European energy system. The work of this chapter has been done in collaboration with the Institute of Energy and Climate Research – Techno-Economic System Analysis (IEK-3) in Forschungszentrum, Jülich, Germany, during a research stay of three months between November 2019 and January 2020.

In **Chapter 3**, the results of the tests of a port-fuel spark ignition engine fueled with synthetic coke oven gas mixture, pure hydrogen and pure methane are reported. The engine speed has been varied between 2000 and 5000 rpm, the air to fuel ratio ranged from 1 to 2 and the optimum spark advance was selected to obtain maximum brake torque. Performance results in terms of power, brake mean effective pressure, thermal efficiency and specific energy consumption are analyzed and

compared between the three fuels. Finally, the specific emissions of NO<sub>x</sub>, unburnt hydrocarbons, carbon monoxide and carbon dioxide are assessed. The experiments were conducted in collaboration with the Engineering Department from the Public University of Navarra in Pamplona, Spain.

In **Chapter 4**, the methodology for the development of computational fluid dynamics simulations with the geometry of a symmetric cylinder of the same engine than in **Chapter 3** and at the same operating conditions is detailed. Performance results in terms of power, heat released, volumetric efficiency and evolution of the pressure and temperature variables inside the cylinder are analyzed for the three fuels. Afterward, the combustion flame evolution within the cylinder is studied for the three fuels at a specific engine speed showing the NO mass fraction generation. Finally, a spark advance sensitivity analysis was conducted to observe the influence of this variable on the engine performance. Simulations were validated through a wide range of performance variables and emissions, showing good agreement between simulations and experiments.

At the end of each chapter, the nomenclature and references employed and useful appendices to further understand the chapter are included. **Chapter 5**, which is also translated to Spanish, summarizes the main conclusions of the work carried out during this thesis and the recommended future work to continue this research line. Finally, a list of the scientific contributions by the author of this thesis is listed in **Appendix I**.





# RESUMEN

---

ALCANCE Y ESTRUCTURA DE  
LA TESIS



## **i. Motivación**

Los combustibles bajos en carbono son clave para la transición hacia un sistema energético sostenible con menos emisiones contaminantes y menos dependiente de los combustibles fósiles. Las fuentes de energía renovables (RES, por sus siglas en inglés) permiten una generación de energía limpia más distribuida en las diferentes regiones del mundo. Sin embargo, la mayoría de las energías renovables sufren fluctuaciones que provocan intermitencia en el suministro energético. En este sentido, el hidrógeno como vector energético puede desempeñar un papel fundamental en la amplia implementación de las RES. El acoplamiento de las energías renovables con el hidrógeno permite equilibrar la red, amortiguando las fluctuaciones de los recursos naturales mediante el almacenamiento a largo plazo. Además, el hidrógeno puede emplearse en un amplio rango de sectores, desde el transporte y las aplicaciones estacionarias hasta la industria, sustituyendo a los combustibles fósiles convencionales y mitigando los efectos adversos sobre el cambio climático debidos a las emisiones de gases de efecto invernadero.

Entre los sectores con grandes oportunidades de penetración del hidrógeno, cabe mencionar el sector marítimo. En el área atlántica de Europa, este sector presenta un alto porcentaje del transporte de mercancías y pasajeros y, actualmente, es responsable de una alta contribución en la contaminación de la región. Por lo tanto, esta situación podría mejorar considerablemente si se cambiara a un sistema en el que la energía requerida por el transporte marítimo de la región fuera suministrada con electricidad e hidrógeno.

Actualmente, algunos procesos industriales producen corrientes residuales industriales ricas en hidrógeno, que, a pesar de proceder de energías no renovables, suelen caracterizarse por un alto contenido energético. Por lo tanto, la purificación o recuperación de componentes valiosos de las corrientes residuales, permitiendo la conversión final de  $H_2$  en energía, se convierte en un reto clave que traduce los beneficios de la circularidad de los residuos en descarbonización energética. El gas de coque, un subproducto de la fabricación de coque con alto porcentaje volumétrico de hidrógeno y metano, puede utilizarse en una amplia gama de aplicaciones, especialmente en la industria del acero y el coque. Sin embargo, en periodos de baja demanda, el gas de coque se quema

directamente, desechando su contenido energético. Por ello, la alternativa de recuperación para su posterior conversión en electricidad mediante el uso del gas en motores de combustión interna (ICEs, por sus siglas en inglés) acoplados a sistemas generadores presenta gran interés.

Los motores de combustión interna son una tecnología muy madura e implementada en todo el mundo. La gasolina y el gasóleo, obtenidos a partir de combustibles fósiles, se han empleado habitualmente como combustibles convencionales en función de la configuración del motor. Sin embargo, las normativas, cada vez más restrictivas, exigen aumentar la eficiencia de los motores y reducir las emisiones contaminantes. Estas políticas limitan su aplicabilidad y ejercen una gran presión sobre los fabricantes de motores para que desarrollen tecnologías alternativas y todavía costosas, como las pilas de combustible. Por lo tanto, la sustitución de los combustibles convencionales por los de bajo contenido en carbono surge como una solución viable para prolongar el uso de los ICEs de una manera relativamente barata. Esta tesis analiza y demuestra la viabilidad de alimentar los motores de combustión interna con combustibles bajos en carbono, como el hidrógeno, el metano y el gas de coque, con alto rendimiento y bajas emisiones, allanando el camino hacia un sistema energético más sostenible.

Esta tesis se ha realizado en el marco del proyecto HYLANTIC - EAPA\_204/2016, cofinanciado por el Fondo Europeo de Desarrollo Regional en el contexto del programa Interreg Atlantic. El proyecto HYLANTIC se centró en el despliegue de una red transnacional para avanzar en la investigación y desarrollo, implementación y comercialización del hidrógeno como vector energético en el espacio atlántico de Europa. El alcance del proyecto abarcaba i) la generación de hidrógeno a través de energías renovables y corrientes residuales locales, ii) el almacenamiento seguro en tanques presurizados e, iii) la aplicación del H<sub>2</sub> en pilas de combustible o ICEs, con especial énfasis en el sector marítimo. El trabajo desarrollado en esta tesis interrelaciona las actividades del proyecto que abordaron el acoplamiento del vector hidrógeno y las fuentes de energía renovables y la recuperación de combustibles procedentes de corrientes residuales industriales para su uso en motores de combustión interna.

## **ii. Objetivos de la tesis**

En base a la motivación anteriormente expuesta, el objetivo general de esta tesis es doble: 1) El primer objetivo global es la evaluación de un sistema energético europeo futurista basado en el acoplamiento de las energías renovables y el hidrógeno como vector energético para el sector marítimo en la zona atlántica de Europa, y 2) El segundo objetivo principal es la evaluación del rendimiento técnico y energético de un motor de combustión interna alimentado con combustibles bajos en carbono recuperados de gases residuales industriales. Este segundo objetivo se ha enfocado en el estudio del gas de coque como fuente de combustible en un motor de encendido por chispa. Además, el rendimiento del motor se ha comparado con el uso de hidrógeno puro y metano puro como combustibles; la comparación se ha realizado porque el hidrógeno y el metano son los principales constituyentes del gas de coque, analizándose la contribución de cada combustible a los fenómenos de combustión.

Para lograr el objetivo global, la investigación se ha dividido en los siguientes objetivos específicos:

- Revisión del estado del arte de los modelos de sistemas energéticos desarrollados a diferentes escalas y sus condiciones de contorno, incluyendo la penetración de las energías renovables y el empleo del hidrógeno como vector energético.
- Previsión de la demanda de energía eléctrica y de hidrógeno en la región atlántica, incluyendo el transporte marítimo en el espacio atlántico de Europa, en el horizonte 2050. Además, se evaluarán diferentes escenarios de penetración de la demanda de hidrógeno en barcos para observar su impacto en la infraestructura del hidrógeno.
- Revisión del estado del arte de motores de combustión interna alimentados con combustibles bajos en carbono, especialmente hidrógeno, metano y gas de coque.
- Evaluación experimental del rendimiento técnico de un motor de encendido por chispa alimentado con gas de coque, y su comparación con hidrógeno y metano, junto con la evaluación de las emisiones de los gases de escape.

- Desarrollo de un modelo de simulación de dinámica de fluidos computacional capaz de predecir el rendimiento del motor en un amplio rango de condiciones de funcionamiento y de comprender el comportamiento de la combustión de los combustibles de bajo contenido en carbono.

### iii. Estructura de la tesis

Esta tesis se ha estructurado en cinco capítulos siguiendo los objetivos principales expuestos anteriormente.

Para entender el contexto y la motivación que ha llevado a la realización de esta tesis, el **Capítulo 1** comienza con una introducción general del sistema energético mundial, exponiendo la actual dependencia de los combustibles fósiles. En este sentido, el creciente despliegue de las RES en muchos países requiere su acoplamiento con el hidrógeno como vector energético para equilibrar la red y alimentar diferentes sectores de forma sostenible. A continuación, se presenta un resumen del modo de funcionamiento y los principales parámetros de la tecnología de los motores de combustión interna para entender su comportamiento. También se hace una revisión de las características del hidrógeno, el metano y el gas de coque como combustibles bajos en carbono. Por último, se detalla una breve explicación de la herramienta de simulación de dinámica de fluidos computacional enfocada a los ICEs.

El **Capítulo 2** se centra en los escenarios del sistema energético europeo en el horizonte 2050 basados en energías 100% renovables acopladas a hidrógeno como vector energético. El modelo utilizado optimiza la distribución de las RES y la infraestructura de  $H_2$ , minimizando los costes totales anuales y la capacidad de las tecnologías implicadas para satisfacer la demanda eléctrica y de hidrógeno en toda Europa. Dado que el sector marítimo tiene una importante contribución en el transporte de mercancías y pasajeros en el espacio atlántico europeo, se incluyen diferentes escenarios de penetración de la demanda de  $H_2$  en barcos en esa región para analizar su impacto en el sistema energético europeo. El trabajo de este capítulo se ha realizado en colaboración con el Instituto de Investigación Energética y Climática - Análisis de Sistemas Tecnológico-Económicos (IEK-3) en Forschungszentrum, Jülich, Alemania, durante una

estancia de investigación de tres meses entre noviembre de 2019 y enero de 2020.

En el **Capítulo 3** se presentan los resultados de las pruebas de un motor de encendido por chispa alimentado con una mezcla de gas de coque sintético, hidrógeno puro y metano puro. La velocidad del motor se ha variado entre 2000 y 5000 rpm, la relación aire/combustible osciló entre 1 y 2 y se seleccionó el avance óptimo de chispa para obtener el máximo par efectivo. Se analizan los resultados de rendimiento en términos de potencia, presión media efectiva, eficiencia térmica y consumo específico de energía y se comparan entre los tres combustibles. Por último, se evalúan las emisiones específicas de NO<sub>x</sub>, hidrocarburos no quemados, monóxido de carbono y dióxido de carbono. Los experimentos se realizaron en colaboración con el Departamento de Ingeniería de la Universidad Pública de Navarra en Pamplona, España.

En el **Capítulo 4** se detalla la metodología para el desarrollo de simulaciones de dinámica de fluidos computacional con la geometría de un cilindro simétrico del mismo motor que en el **Capítulo 3** y en las mismas condiciones de funcionamiento. Se analizan los resultados de rendimiento en términos de potencia, calor liberado, eficiencia volumétrica y evolución de las variables de presión y temperatura en el interior del cilindro para los tres combustibles. Posteriormente, se estudia la evolución de la llama de combustión en el interior del cilindro para los tres combustibles a una determinada velocidad del motor, mostrando la generación de la fracción másica de NO. Por último, se realiza un análisis de sensibilidad del avance de chispa para observar la influencia de esta variable en el rendimiento del motor. Las simulaciones fueron validadas a través de un amplio rango de variables de rendimiento y emisiones, obteniendo buena concordancia entre las simulaciones y los resultados experimentales.

Al final de cada capítulo se incluye la nomenclatura y las referencias empleadas, así como apéndices útiles para la comprensión del capítulo. El **Capítulo 5**, que también está traducido al español, resume las principales conclusiones del trabajo realizado durante esta tesis y los trabajos futuros recomendados para continuar esta línea de investigación. Por último, en el Apéndice I se incluye una relación de las contribuciones científicas del autor de esta tesis.





# CHAPTER 1

---

## INTRODUCTION



## 1.1. Global energy system situation

Climate change is a global concern that requires the cooperation of many countries, sectors and organizations to reduce its negative impact on natural resources and on the health of living beings. In order to achieve effective results in its abatement, the Conference of the Parties (COP) 21 from Paris in 2015 concluded a Climate Agreement that established goals to limit the global temperature increase to 1.5 °C above pre-industrial levels [1]. To achieve this goal, a reduction of global CO<sub>2</sub> emissions by 45% by 2030 relative to the 2010 level and to net zero around mid-century is required, as recognized in the COP26 in Glasgow in 2021 [2]. This has fostered governments and societies to change their environmentally-harmful policies and behaviors in favor of more sustainable pathways of energy consumption and generation.

One of the key factors contributing to climate change has been the dependence on fossil fuels in the main sectors of today's society, which has led to an unsustainable situation of greenhouse gas (GHG) emissions and pollution. The estimated global primary energy consumption in 2019 was 584 exajoules (EJ), with 33% coming from oil, 27% from coal (mainly consumed in China), 24.2% from natural gas (NG), 4.3% from nuclear, 6.5% from hydroelectricity and 5% from the rest of renewable energy sources (RES) [3].

The distribution of the energy consumed by fuel and world region in the year 2019 is graphed in Figure 1.1 [3]. Energy data from the year 2019 has been retrieved, as the year 2020 was an exceptional case due to the pandemic COVID-19 situation, reducing the energy consumption by 4.5% with respect to the previous year. In addition, CO<sub>2</sub> emissions in each region in the year 2019 are also depicted in Figure 1.1.

As can be observed, oil and natural gas were the main pillars of energy consumption in all the world regions. The major consumers of oil were the US, China, India and the Russian Federation. Globally, oil slowed down its growth rate in 2019 with a global value of growth of 0.8% compared to the average annual growth rate of 1.1% in the 2008 – 2018 period. In the case of NG, it was mainly consumed in the US, China and the Russian Federation. The global growth rate slowed down from 2.5%, which was the annual average growth rate in previous ten years, to a 2% growth rate in 2019.

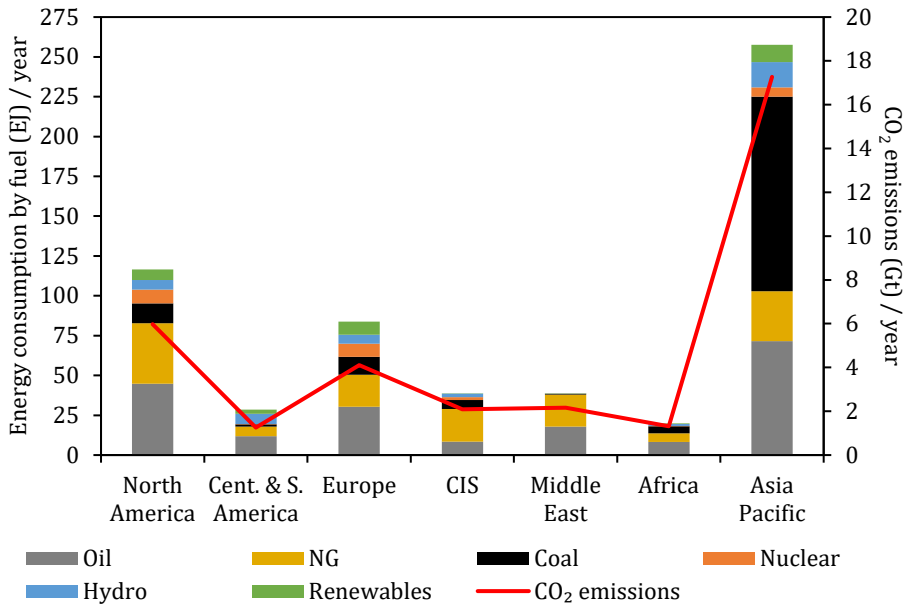


Figure 1.1. Distribution of energy consumption by fuel and by world region and CO<sub>2</sub> emissions in 2019 [3].

Efforts directed to the abatement of climate change by many countries and regions achieved a reduction of 0.6% in the global consumption of coal in 2019, compared to an average annual growth rate of 0.8% in the 2008 – 2018 period. The highest coal consumers in 2019 were China and India, consuming around 100 EJ in that year and with a growth rate per annum of the previous ten years of 1.7% and 5.5%, respectively. On the other hand, hydroelectricity and RES global consumption increased by 0.8% and 12.2% with respect to 2018. Nevertheless, their consumptions were only significant in Europe and North America or countries like China and Brazil [3].

On the other hand, it is interesting to observe the contribution of each fuel to the total regional energy consumption in 2019, as detailed in Table 1.1. The main fuel shares came from oil, NG and coal in all the regions, with the exception of Central & South America, with a contribution of hydro electricity higher than NG and coal. In the case of the Middle East, coal was barely employed, while in the Asia Pacific almost half of the energy proceeded from this high polluting fossil fuel. In contrast, Europe, has a more uniform fuel share consumption, reducing the dependence on a specific fuel source.

Table 1.1. Share of each fuel to the regional consumption in 2019 (%).

<b>Fuel</b>	<b>North America</b>	<b>Cent. &amp; S. America</b>	<b>Europe</b>	<b>CIS</b>	<b>Middle East</b>	<b>Africa</b>	<b>Asia Pacific</b>
<b>Oil</b>	38.4	41.5	36.3	21.6	45.9	41.7	27.8
<b>NG</b>	32.7	20.8	23.8	53.4	51.8	27.2	12.2
<b>Coal</b>	10.6	5.2	13.5	14.3	1.0	22.5	47.5
<b>Nuclear</b>	7.4	0.8	9.9	4.9	0.2	0.7	2.2
<b>Hydro</b>	5.2	22.3	6.8	5.7	0.8	5.9	6.2
<b>Renewables</b>	5.7	9.5	9.8	0.1	0.3	2.1	4.2

Regarding CO<sub>2</sub> emissions, a total amount of around 34.17 Gt were emitted in 2019 (Figure 1.1). A clear relationship between energy consumption and CO<sub>2</sub> emissions can be noticed, with the highest relative values in fossil fuel-based regions. This trend must be modified to maintain a high energy consumption while low CO<sub>2</sub> emissions are generated, as observed in the regions with the highest percentages of nuclear, hydroelectricity and RES, which generate lower CO<sub>2</sub> emissions with respect to their energy consumption. In this sense, the global growth rate of CO<sub>2</sub> emissions in 2019 was 0.5%, less than half of the average annual growth rate of the 2008 – 2018 period (1.1%), slowing down their generation as the global energy consumption increased at an average annual growth of 1.6% in that 10 years period.

The main contributors to CO<sub>2</sub> emissions in 2020 were the electricity and heating sectors, with a share of 39.6% of the total energy-related CO<sub>2</sub> emissions [4]. Next, transport and industry followed in the ranking of CO<sub>2</sub> emissions, with contributions of 25.5% and 20.8%, respectively. Finally, buildings and other sectors accounted for 8.6% and 5.5% of the total CO<sub>2</sub> emissions in 2020.

Within the transport sector, the maritime mode is one of the main CO<sub>2</sub> emissions sources, with a contribution of 2.89% to global CO<sub>2</sub> emissions in 2018 [5], increasing from a value of 2.76% in 2012 [6]. In 2018, the International Maritime Organization (IMO) established the target of reducing the total annual GHG emissions in the sector by 50% or more by 2050 as compared to 2008 in order to be aligned with the Paris Climate Agreement goals [1,7]. Moreover, and beyond GHG emissions, a link between particulate matter (PM) emissions from global shipping and health effects was evaluated, with around 60,000 premature deaths

estimated annually [8]. For these reasons, many scientific studies and projects are being developed to achieve the target established by the IMO by 2050 using more bio-friendly systems and fuels to decarbonize the sector [9–13].

Besides the GHG emissions, there are additional issues with fossil fuels, as their reserves are unevenly distributed across the world. The locations of the proved reserves of the three main fossil fuels in 2019 are graphed in Figure 1.2. The main oil resources are placed in the Middle East (especially in Saudi Arabia and Iran, constituting 17.2% and 9% share of the total reserves), in South America (mainly in Venezuela, being the 17.5% of the total oil reserves), and in North America (especially in Canada, with a share of 9.8% of the total).

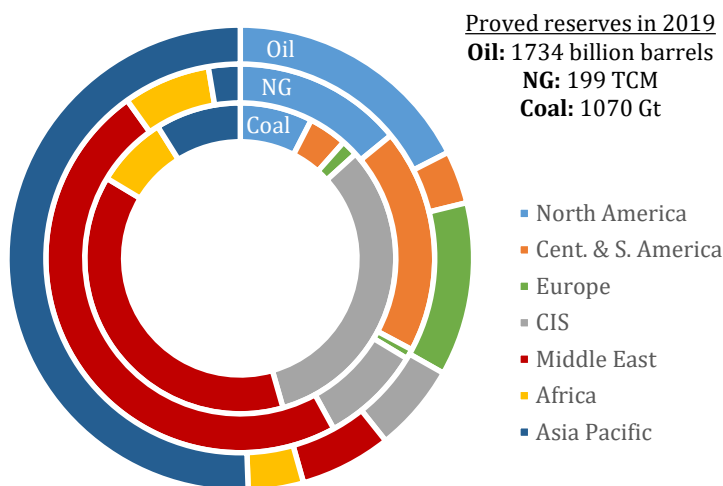


Figure 1.2. Proved reserves of fossil fuels (outer ring: oil, middle ring: natural gas, inner ring: coal) in 2019 in the world [3].

In the case of natural gas, the two main reserves are placed in the Middle East (mainly in Iran and Qatar, with shares of 16.1% and 12.4% of the total) and in the Commonwealth of Independent States (CIS) region (especially in Russian Federation and Turkmenistan, comprising the 19.1% and 9.8% of the total NG reserves). Regarding coal, the main reserves are located in the Asia Pacific region (mainly in Australia and China, with 13.9% and 13.2% of the total reserves), in the US in North America (23.3% of the total) and in the Russian Federation within the CIS region (15.2% of the global reserves).

These disparities cause many important trade issues between countries due to geopolitical and economic reasons becoming a stumbling block for a constant energy supply for other countries. In addition, as these fossil fuels reserves are limited, their extraction and trade prices vary with time, increasing as the offer diminishes due to reserves depletion.

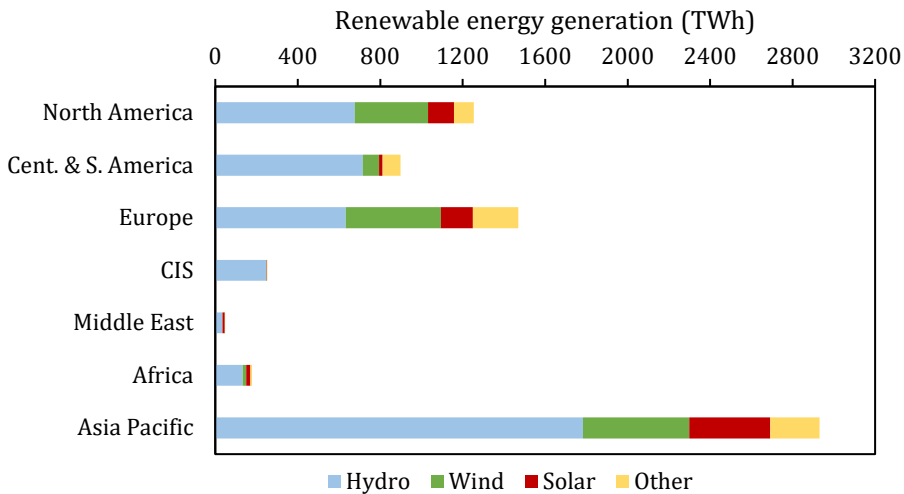


Figure 1.3. Renewable energy generation in the world by hydro, wind, solar and other sources (geothermal, biomass and others) [3].

Therefore, the energy system of a country based on the import of fossil fuels causes instability in its electricity price. Efforts should be focused on the achievement of more stable energy systems independent from fossil fuels. In this sense, RES (including hydroelectricity) can play a key role as energy is generated in a more distributed way. The installed capacity of RES in the world increased globally by 50% in the five years between 2013 (1563 GW) and 2018 (2351 GW) [14]. The energy generation of renewable energies in TWh in 2019 across the world regions is graphed in Figure 1.3, including hydro, wind, solar and other energy sources (geothermal, biomass, and other sources). The main regions where renewable energy was generated in 2019 were the Asia Pacific with 41.7% of the global energy produced with RES, which meant 2930 TWh from the total 7028 TWh; Europe with a contribution of 20.9%; North America (17.8%); and Brazil in South America (7.4%). It is interesting to realize that despite the high fossil fuel dependence of Asia Pacific (and

more specifically China), this region is also the highest producer of renewable energy.

Hydro is the main RES as it has been employed for decades in most of the regions of the world, accounting for 60% of the global energy generated with RES. China is the main promoter of hydro, generating around 1270 TWh in 2019, followed by Brazil with 400 TWh and Canada with 382 TWh. On the other hand, regarding the other RES, a predominance of wind energy generation over solar can be noticed, especially in Europe and North America, generating 462 TWh and 355 TWh from wind, respectively, while the production from solar was 155 TWh and 125 TWh, respectively. In the case of Asia Pacific there is a more homogeneous distribution, with 514 TWh from wind and 394 TWh from solar energy.

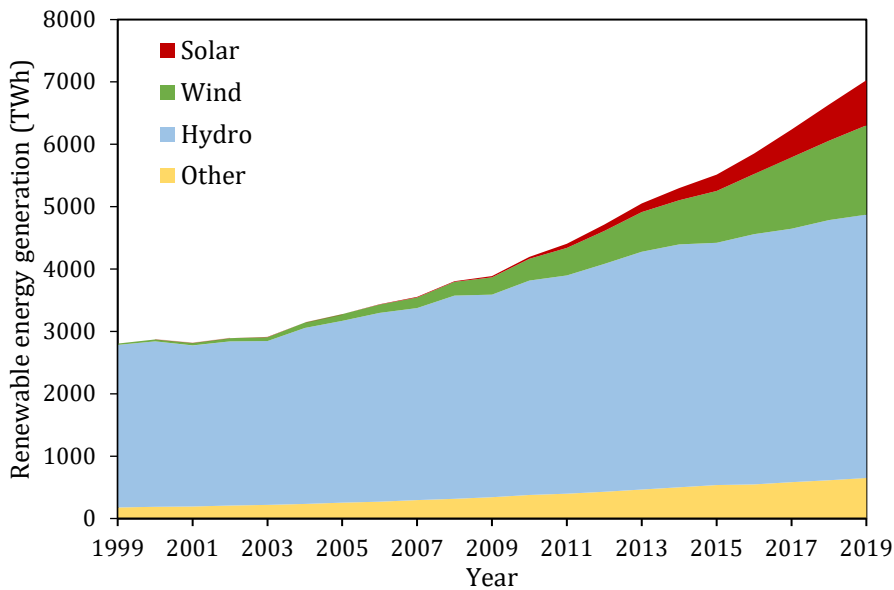


Figure 1.4. Renewable energy generation (TWh) trend from 1999 to 2019 of solar, wind, hydro and other sources (geothermal, biomass and others) [3].

However, the energy generation with RES is increasing quickly, as can be noticed in Figure 1.4, with annual growth rates in 2019 of 12.6% for wind, 24.3% for solar and 6% for the other sources. These figures mean an increase in the energy generation of 160 TWh with wind, 141 TWh with solar and 36.8 TWh of other sources, respectively. Hydro source had a



lower annual growth rate in 2019 of 1.2%; however, this meant an increase of 50.8 TWh with respect to the year 2018.

China was the largest contributor to renewables growth in 2019 (70.8 TWh of hydro, 39.9 TWh of wind and 46.9 TWh of solar). Additionally, the US promoted a growth of 27.7 TWh of wind and 14.1 TWh of solar in 2019 and Germany 16 TWh of wind. In terms of annual growth rate, the regions with higher increase in solar energy in that year were Africa (96.7%), the Middle East (95.4%) and the CIS region (55.8%), meaning increases of 9.5 TWh, 5.8 TWh and 0.6 TWh, respectively.

Therefore, despite the current high energy generation from fossil fuels in most of the world regions, renewable energies are becoming increasingly attractive as they enable the reduction of dependency on energy imports from other countries or regions. Furthermore, the increase of energy generation from RES reduces GHG emissions from fossil fuels, limiting the negative impact of climate change and preserving the welfare of our world's nature.

Nevertheless, energy systems based on high penetration of wind and solar renewable sources tend to suffer a higher variability in the energy generation due to fluctuations and intermittencies of their natural sources [15]. On the other hand, hydroelectricity, geothermal and biomass are more stable sources, which can be used on demand. Therefore, an energy vector with long-term storage capability and able to balance the energy system during periods of high demand and low RES supply is required [15,16]. In this sense, hydrogen, which is the most abundant element in the universe, has been found as one of the most interesting alternatives in the last decades [17] as a potentially suitable energy carrier included in many country roadmaps and studies [18].

## **1.2. Hydrogen energy vector**

Hydrogen provides high versatility to the energy system as energy vector, as represented in Figure 1.5. This gas enables the grid balance with long-term storage compared to batteries, compressed air, flywheels or capacitors, which are suited for short-term storage [15]. Furthermore, H<sub>2</sub> can be transported in liquid form in trucks, large containers and ships and in gaseous form via pipelines or trucks [19–21]. In addition, H<sub>2</sub> fuel can be

used in a high number of applications, such as electricity generation, transportation [22–25], as raw material in industry (chemical, metallurgical [26,27] and refineries), injected in the natural gas network [28,29] for heat and gas distribution systems or to balance the electric grid [30,31]. In this way, the coupling of different sectors can be facilitated [32].

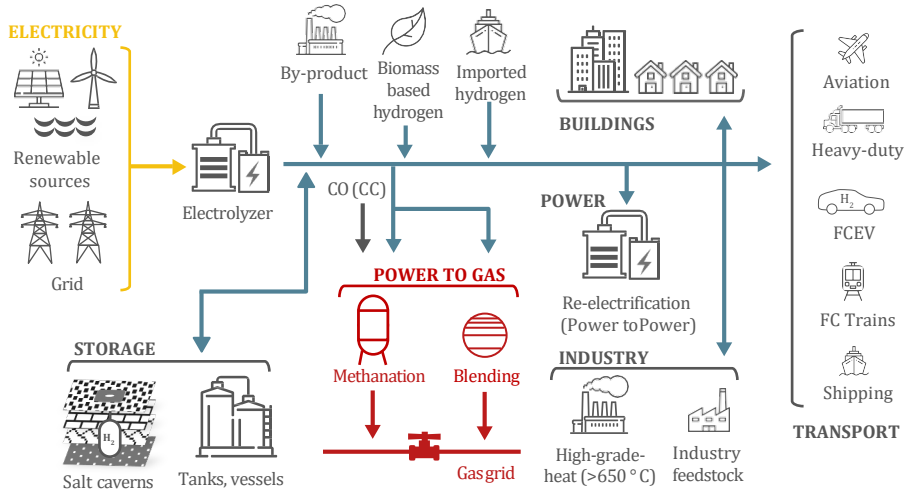
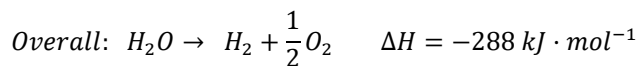


Figure 1.5. Hydrogen as energy vector (modified from [33]).

Currently, 50 million metric tons of hydrogen are generated annually worldwide [18]. Almost 96% of the  $H_2$  is produced with fossil fuels, being 48% obtained from steam reforming of natural gas, 30% from partial oxidation of oil and 18% from coal gasification [34]. Only 4% is generated by water electrolysis, which is an environmentally clean process when coupled to RES and whose production cost is decreasing as new research reduces the expensive materials required [15,35]. On the other hand,  $H_2$  can be recovered from industrial hydrogen-rich waste streams using separation techniques [36].

Three main electrolyzers types have been developed so far: alkaline, solid oxide (SOEC) and proton exchange membrane (PEM) electrolyzers [37–40]. PEM technology offers high  $H_2$  purity, high efficiency and faster dynamic response than alkaline type; besides, they can work at higher current densities and with smaller sizes. On the other hand, SOEC is the less developed type with challenges regarding the durability of the ceramic materials, long-term operation and costly materials to withstand

the high temperatures [37]. All of these electrolyzers promote the next overall reaction:



Regarding the conversion from hydrogen to electricity, different technologies are available or under research. Fuel cells generate electricity and heat through electrochemical reactions, which are the reversed electrolysis reactions. Different fuel cells types can be distinguished depending on the fuel and the electrolyte, highlighting the alkaline (AFC), phosphoric acid (PAFC), polymer electrolyte (PEMFC) and solid oxide (SOFC) fuel cells. PEMFC are commonly used in portable and stationary applications [22,41,42], operating at low temperatures and providing continuous electricity supply at high efficiency levels and power densities [43]. On the other hand, SOFCs, promising systems with high efficiency, are still under research for large applications with some challenges to be overcome: reduce the cost and the working temperature and increase the reliability of the cell and the balance of the plant [44].

However, there are alternative technologies for the conversion of  $H_2$  to electricity, such as gas turbines and internal combustion engines (ICEs). The advantage of gas turbines is the production of big amounts of energy in the MW or GW range in a cost effective and flexible way in the shorter term, whilst fuel cells require more research and time to be scaled at those ranges of power capacities [45]. Between hydrogen open cycle gas turbines (OCGTs) and hydrogen combined cycle gas turbines (CCGTs), the latter can avoid  $NO_x$  emissions through stoichiometric combustion of  $H_2$  and  $O_2$ , products of electrolysis, and with the presence of helium as inert gas, it would generate only water vapor that could be separated by condensation [45]. Hydrogen internal combustion engines are based on a very mature technology, with lower costs and easier scalable than gas turbines, which can be adapted to be fed with hydrogen, mixtures of  $H_2$  and methane, or industrial waste streams [23,46,47].

As electricity generated from RES is very intermittent and fluctuating depending on the resources available, energy can be stored when energy generation is higher than the demand and it can be employed later as a backup for the periods of low energy generation and high demand. In the case of energy systems at a large scale, long-term or even seasonal storage

is required. Hydrogen can be stored in liquid form, in metal or chemical hydrides [48–50] and in gaseous form (vessels, salt caverns or the gas grid).

Salt caverns, in both thin-bedded structures and salt domes, become an advantageous alternative as a big amount of energy can be stored with relatively low costs [51,52]. The surrounding rock salt of the caverns is inert with hydrogen and is very gastight, while possible reactions between  $H_2$  and microorganisms or mineral constituents in depleted fields and aquifers can take place [52]. Typical salt caverns for  $H_2$  storage would have a geometrical storage volume of 700000  $m^3$  with a net working gas storage capacity of around 6 million kg of  $H_2$  and energy storage of 100 GWh [53]. The underground storage potential at the European level was investigated in the work of Caglayan et al. [54]. On the other hand, vessels enable a more distributed storage of  $H_2$  in smaller volumes and with a quicker and cheaper emptying and filling protocols. Vessels are more versatile than salt caverns and  $H_2$  can be stored as compressed or liquefied gas.

An alternative to hydrogen energy carrier is the power to gas route, as depicted in Figure 1.5. This consists of the production of  $H_2$  from electricity and its injection directly into the gas grid in limited concentrations [55,56]. The project HyDeploy in the UK has tested blends up to 20% of  $H_2$  in a private natural gas network to feed 100 homes and 30 university buildings at Keele University for 18 months, requiring no changes in their existing appliances and without any disruption, and abating over 27 t of  $CO_2$  [57]. On the other hand, with the addition of  $CO_2$ , synthetic methane can be produced to feed the natural gas pipelines without any limitations for the current grid [39,58].

Finally, one of the main advantages of  $H_2$  as energy vector is its utilization in a wide range of applications, from stationary to mobility purposes. Hydrogen has been mainly employed in stationary systems through fuel cells for residential, uninterruptible power supply (UPS), backup systems, combined heat and power (CHP) and micro CHP applications [59,60]. However, the use of hydrogen in gas turbines and ICEs for stationary purposes at different scales is currently under research [61–64].

Regarding mobility, fuel cells have been tested in different transport modes (automobiles, buses, trucks, trains, forklifts, bicycles, airplanes, etc.) and they are already commercially available in some of these applications [41,65,66]. In the maritime sector, fuel cells have gained much attention in ships and submarines as they can be used as power auxiliary units or for propulsion depending on the ship power requirements [11,67–70]. In addition, fuel cells can be also used as an alternative to cold ironing, reducing the emissions at ports [71]. Other projects are focused on hybrid power systems to enhance the transition to cleaner fuels reducing emissions in comparison to original engines [10,72–74]. Furthermore, some companies are developing liquefied H<sub>2</sub> carriers to promote the transport and use of hydrogen in different countries [20,21,75].

On the other hand, the Atlantic coast of Europe is characterized by many important ports, with intensive cargo ship traffic for trading with other countries and it is a remarkable tourist area with many passenger ships. This high volume of ships implies a significant amount of GHGs and other harmful emissions being released in the region [76,77]. In this sense, several projects have been launched in this area to promote the generation and use of H<sub>2</sub> [78–82] and some companies are developing fuel cell powered ships [83–85] or use H<sub>2</sub> as fuel for ICEs [86–90] or as auxiliary support, combined with renewable energy technologies [91]. These investigations and developments prove that electricity and hydrogen could be used as cleaner power sources for ships.

However, high investment and a number of challenges must be addressed in order to achieve the established targets. For this reason, energy system models, as well as the simulation and analysis of optimal possible future scenarios, help policy-makers and companies to make decisions in order to adjust their actions and investments in an optimal way.

Therefore, hydrogen as energy vector will play a key role in the future for the decarbonization of the energy system. A suitable infrastructure for H<sub>2</sub> must be progressively deployed in order to have all the hydrogen chain elements connected and easily available. As this requires a huge investment for both gas suppliers and application manufacturers, usually known as the “chicken and egg” problem, mature technologies easily

adapted to  $H_2$  should be employed first. In this way, more environmentally-friendly technologies can be used while the  $H_2$  infrastructure demand increases and starts to be deployed. Thus, ICEs could become a key technology for the transition to a cleaner and more sustainable society.

### **1.3. Internal combustion engines technology**

Internal combustion engines (ICEs) are characterized by a very mature and well-established technology worldwide. The ICEs have played significant roles since their invention, powering vehicles, generating electricity and providing mechanical power in a wide range of applications [92]. The size of ICEs range from some watts in model airplanes engines to thousands of kilowatts per cylinder in ships and stationary engines [93].

#### **1.3.1. Engine configuration**

The two main parameters of an ICE are the bore (B), which is the cylinder diameter, and the stroke (S), which is the distance traveled by the piston from the upper point, or top dead center (TDC), to the bottom point, or bottom dead center (BDC) (see Figure 1.6). The connecting rod (length L in Figure 1.6) transforms the linear movement of the piston to a rotational movement of the crankshaft (diameter l).

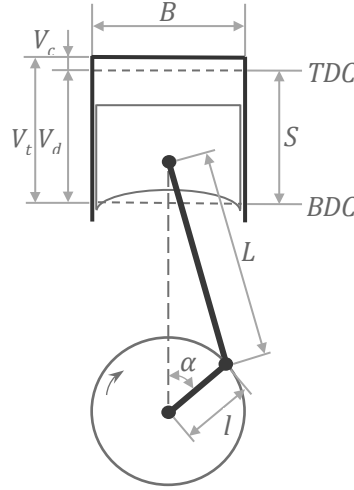


Figure 1.6. Basic geometry of a reciprocating ICE. B: cylinder bore, S: stroke, L: connecting rod length, l: crankshaft diameter,  $\alpha$ : rotation angle, TDC: top dead center, BDC: bottom dead center,  $V_t$ : total volume,  $V_d$ : displaced volume,  $V_c$ : clearance volume.

The total volume ( $V_t$ ) of the cylinder is defined as the sum of the displaced volume ( $V_d$ ) by the piston in its movement and the clearance volume ( $V_c$ ), which is the remaining volume where the combustion takes place when the piston is in TDC. The compression ratio ( $r_c$ ) is defined as the ratio of the total volume and the clearance volume:

$$r_c = \frac{V_d + V_c}{V_c} \quad (1.1)$$

Two main types of reciprocating ICEs can be distinguished: spark-ignition (SI) engines, invented by Nikolaus Otto in 1876 and usually fueled with gasoline; and compression-ignition (CI) engines, invented by Rudolf Diesel in 1892 and usually fueled with gasoil (or diesel as commonly named) [92]. In the first type of engine, the combustion of the air-fuel mixture is carried out through the ignition of a spark inside each cylinder, usually before the TDC. In the case of CI engines, combustion is produced due to the compression at high pressure of the charge of air and fuel. In addition to these two types of engines, homogeneous charge compression ignition (HCCI) engines have been developed as a combination of SI and CI configurations to integrate their individual advantages.

In current SI engines, two injection configurations are commonly used. In the port-fuel injection (PFI) configuration, depicted in Figure 1.7a, fuel is usually injected in the intake manifold next to the intake valve of

each cylinder, starting the creation of the mixture with air before entering into the cylinder and promoting a homogeneous mixture. In this case, engine load is usually quantitatively controlled restricting the air flow from the intake manifold with a throttle.

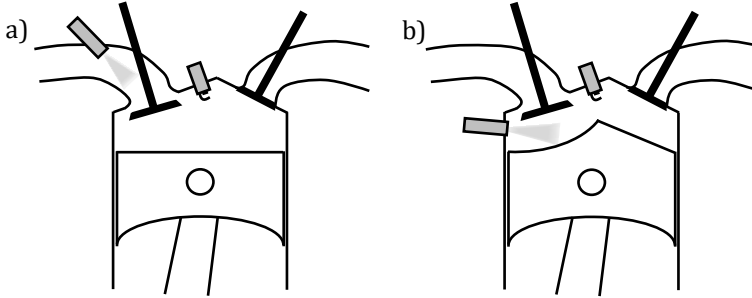


Figure 1.7. a) Port-fuel injection and b) direct injection systems.

On the other hand, in the direct injection (DI) configuration, graphed in Figure 1.7b, the air is introduced through the intake manifold but the fuel is injected at high pressure directly into the cylinder during the intake or the compression stroke. In this case, the engine load is qualitatively controlled varying the quantity of fuel injected into the cylinder, modifying the mixture richness. DI configuration avoids the presence of fuel in the intake manifold, increases the air introduced during the intake stroke, reduces the air temperature within the cylinder and allows the variation of the mixture homogeneity according to the operating condition [92]. Therefore, DI enhances the output performance and increases the fuel consumption efficiency, in addition to greater operating versatility.

Regarding CI engines, a DI configuration is used, introducing the air through the intake manifold and the diesel fuel is injected at high pressure into the cylinder at the end of the compression stroke. This kind of engine has a higher compression ratio than SI engines, heating the air at greater values at the end of the compression stroke, and vaporizing the atomized fuel droplets. Thus, the high pressure ignites the vaporized fuel, creating a flame front that burns the remaining diesel fuel [94].



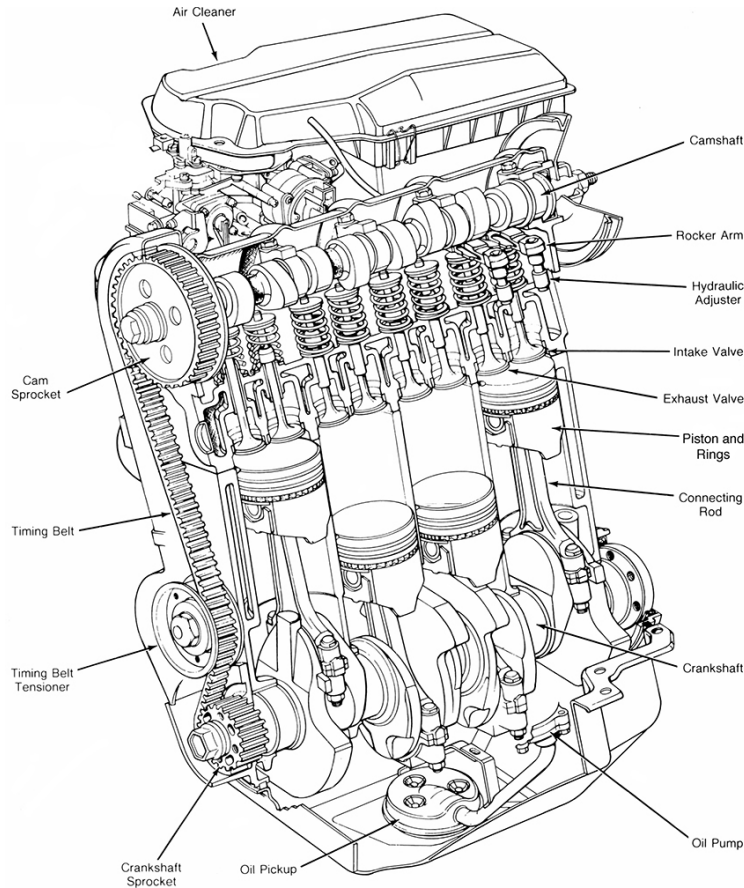


Figure 1.8. Main parts of a four cylinder spark ignition internal combustion engine [92].

The main parts of a four cylinder SI engine are indicated in Figure 1.8 [92]. In each cylinder, the work generated during the combustion through the linear movement of the piston is transformed to a rotational movement of the crankshaft with the aid of the connecting rods. In addition, this crankshaft is connected through a timing belt to the camshaft, which opens and closes the intake and exhaust valve at the right timings. The intake valve enables the input of air or air-fuel mixture from the intake manifold, and the exhaust valve allows the exhaust of gases from combustion to the exhaust manifold.

The majority of ICEs, in both SI and CI configurations, operate with a four-stroke cycle. The crankshaft requires turning two revolutions through four strokes of a piston to complete a cycle. The sequence of the four strokes is graphed in Figure 1.9 [92].

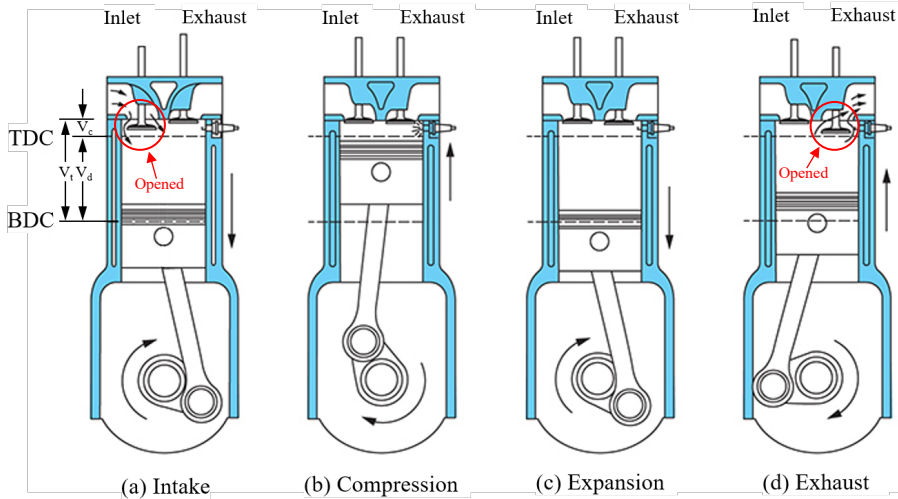


Figure 1.9. Phases of a four-stroke cycle: a) intake, b) compression, c) expansion and d) exhaust. TDC: top dead center, BDC: bottom dead center,  $V_c$ : clearance volume,  $V_d$ : volume displaced,  $V_t$ : total volume (adapted from [92]).

The phases of a four-stroke cycle are as follows:

- 1) Intake stroke: the piston moves downwards from the top dead center (TDC) to the bottom dead center (BDC), drawing fresh air or an air-fuel mixture into the cylinder through the opened intake valve. Usually, the intake valve opens before TDC to favor gas exhaust from the cylinder and closes after BDC.
- 2) Compression stroke: the piston moves upwards from BDC to TDC compressing the fresh air or the air-fuel mixture. Before TDC, the spark is ignited for combustion in a SI engine, or the fuel is injected into the cylinder in a CI engine.
- 3) Expansion stroke: the power stroke in which the high-temperature and high-pressure gases from combustion push the piston down to BDC, forcing the rotation of the crankshaft. The exhaust valve is opened before BDC to start expelling the gases out of the cylinder, reducing the pressure to almost the exhaust system pressure.
- 4) Exhaust stroke: the piston moves upwards from BDC to TDC expelling the remaining gases from the combustion out of the cylinder with the exhaust valve opened. Opening the exhaust valve before BDC in the previous stroke reduces the force required by the piston in this stroke. Finally, the exhaust valve is closed after

TDC to favor gas exhaust with the fresh air or air-fuel mixture coming from the intake manifold. The cycle starts again.

As explained, a power stroke is obtained from each cylinder in a complete cycle, requiring two revolutions of the crankshaft, which means 720 crank angle degrees (CAD). The four-stroke phases and the valves opening and closing timings can also be drawn with the valve timing diagram (see Figure 1.10).

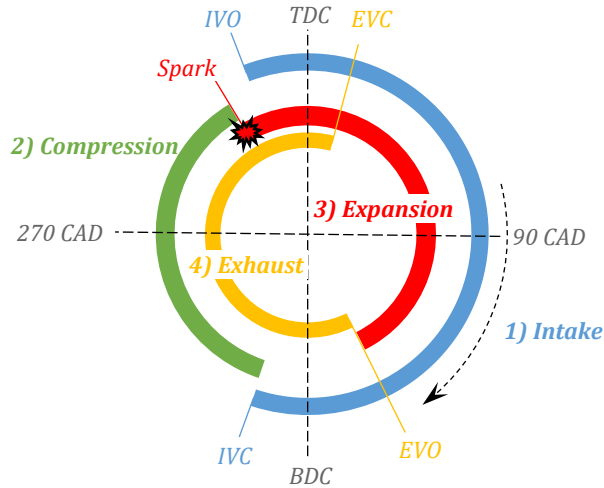


Figure 1.10. Valve timing diagram with the four-stroke phases. IVO: intake valve opening, IVC: intake valve closure, EVO: exhaust valve opening, EVC: exhaust valve closure.

A valve overlap period is created between intake valve opening (IVO) and exhaust valve closure (EVC), in which flow exchanges between intake and exhaust manifolds are generated depending on the engine operating condition. When the pressure in the intake manifold is lower than the pressure in the exhaust manifold, a backflow of exhaust gases into the intake manifold through the cylinder is produced. However, when the intake manifold pressure is higher than the exhaust manifold pressure, scavenging is favored, reducing the residual mass fraction inside the cylinder.

The delay in intake valve closure (IVC) after BDC at the start of the compression stroke induces a higher amount of air or air-fuel mixture into the cylinder at high engine speed due to the ram effect [92]. On the other hand, early IVC reduces the backflow of air and residual mass from the cylinder to the intake manifold at low engine speed.

Finally, early exhaust valve opening (EVO) before BDC favor the expelling of the exhaust gases at high engine speed with the blowdown process, decreasing the cylinder pressure to nearly the exhaust manifold pressure. In this way, the work carried out by the piston during the exhaust stroke is reduced.

### 1.3.2. Engine operating parameters

The indicated work generated inside the cylinder during a four-stroke cycle can be obtained integrating around the curve of the pressure – volume diagram, also known as indicator diagram, with Equation (1.2).

$$W_i = \oint p \cdot dV \quad (1.2)$$

The indicator diagram describes the evolution of the pressure inside the cylinder as the piston moves through the four strokes. The typical diagram of a four-stroke naturally-aspirated SI engine operating at wide open throttle (WOT) is graphed in Figure 1.11, in which two main loops can be distinguished. In the upper loop, A, positive work is generated during the compression and expansion strokes due to the thermal energy released during the air-fuel mixture combustion. The spark is ignited some CAD before the TDC because the combustion requires a finite time, finishing after TDC. The high pressure and enthalpy of the gases after combustion forces the piston downwards during the expansion stroke, generating the work and power output of the engine [93].

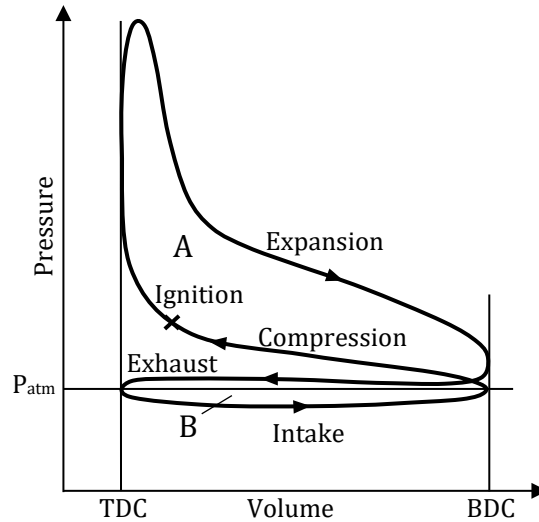


Figure 1.11. Indicator (pressure – volume) diagram in a naturally-aspirated four-stroke SI engine. A: output work delivered during compression and expansion strokes, B: pump work produced by the engine in the exhaust and intake processes.

The lower loop, B, usually named pump work, is produced during the exhaust and intake strokes. In the case of Figure 1.11, as it is the diagram of a typical naturally-aspirated engine, the pressure of the incoming air during the intake stroke is lower than the pressure of the exhaust gases, generating a vacuum inside the cylinder, even below atmospheric pressure. Thus, the piston has to exert work on the gases, generating negative work and reducing the net work generated by the engine. In addition, as the engine is operating at WOT, the fresh air flow has low restrictions and pressure drops during the intake, remaining at nearly atmospheric pressure.

In the case of operating at part-load, the air flow would be restricted through the throttle (butterfly valve) of the intake manifold, generating a pressure drop inside the cylinder during the intake stroke and the beginning of the compression stroke [93]. In addition, the fuel injected would be reduced to match the air decrease. Therefore, the pump work (area B) would be greater than in WOT operation and less thermal energy would be released during the combustion due to the lower fuel input, reducing the net indicated work of the cycle.

On the other hand, if a supercharger or turbocharger is installed, the pressure of the intake air would be higher than the atmospheric pressure and the exhaust gas pressure. Thus, positive work would be carried out by the gases to the piston during the exhaust and intake loop. Additionally, as a higher amount of air would be introduced in the cylinder, a greater fuel quantity would be injected, increasing the thermal energy released during the combustion and the net indicated work [93].

Although the work generated by each cylinder is calculated with the integration of the pressure – volume curve, the useful work available at the crankshaft is reduced. This output work, usually named brake work, is obtained by subtracting the friction work from mechanical and rubbing frictions, such as bearings, pistons, and other mechanical components, and the work required to drive ancillary systems such as water pump, oil pump, camshaft, etc. The ratio of the brake power obtained at the crankshaft and the power generated inside the cylinder is called mechanical efficiency ( $\eta_m$ ), as expressed in Equation (1.3).

$$\eta_m = \frac{W_b}{W_i} \quad (1.3)$$

Where  $W_b$  is the brake work obtained at the crankshaft and  $W_i$  is the work generated inside the cylinder. Typical values of mechanical efficiency for modern automotive engines at WOT are nearly 90% at low speeds and decrease to 75% at the maximum rated engine speed [92].

The generated power by cylinder ( $P_i$ ) is calculated with the indicated work by cycle with Equation (1.4), in which  $N$  is the engine speed and  $n_R$  is the number of crank revolutions per cycle (2 for a four-stroke engine).

$$P_i = \frac{W_i \cdot N}{n_R} \quad (1.4)$$

The brake power can be obtained by subtracting the power frictions or applying the  $\eta_m$  calculated.

In order to compare the performance independently of the engine size, the mean effective pressure (MEP) parameter can be calculated as the work generated in each cycle divided by the cylinder volume displaced by the piston ( $V_d$ ), as expressed in Equation (1.5). Brake or indicated MEP values can be obtained depending on the power value used.

$$MEP = \frac{P \cdot n_R}{N \cdot V_d} \quad (1.5)$$

Another interesting parameter independent of the engine size is the specific fuel consumption (SFC), defined as the fuel mass flow rate ( $\dot{m}_f$ ) employed in a cycle divided by the power obtained on that same cycle, as calculated in Equation (1.6). This parameter describes the engine efficiency of the fuel supplied to generate work at a specific operating condition [92].

$$SFC = \frac{\dot{m}_f}{P} \quad (1.6)$$

On the other hand, in order to obtain a dimensionless parameter that relates the work generated and the fuel chemical energy supplied, the thermal efficiency ( $\eta_t$ ) can be employed. The  $\eta_t$  is calculated with the Equation (1.7), in which  $m_f$  is the fuel mass and LHV is the lower heating value of the fuel.

$$\eta_t = \frac{W}{m_f \cdot LHV} = \frac{P}{\dot{m}_f \cdot LHV} \quad (1.7)$$

Combining the Equations (1.6) and (1.7),  $\eta_t$  and SFC parameters are related with Equation (1.8).

$$\eta_t = \frac{1}{SFC \cdot LHV} \quad (1.8)$$

In order to generate suitable combustion according to the operating conditions of the engine, the air-fuel mixture must be adjusted properly. The air-fuel ratio ( $\lambda$ ) is usually modified by varying the quantity of fuel injected in both PFI and DI engines. The  $\lambda$  is calculated with the mass flow rates of air ( $\dot{m}_{air}$ ) and fuel, as expressed in Equation (1.9).

$$\lambda = \frac{\lambda_{real}}{\lambda_{st}} = \frac{\frac{\dot{m}_{air}}{\dot{m}_f}}{\lambda_{st}} \quad (1.9)$$

The air-fuel ratio is 1 when the air supplied is the required quantity for the complete consumption of the fuel in the combustion process, also named stoichiometric mixture. In the case of operating at leaner air-fuel mixtures ( $\lambda > 1$ ), there is an excess of air introduced in the cylinder with respect to the quantity of fuel injected, remaining  $O_2$  unburnt after

combustion. The inverse of  $\lambda$  is the fuel-air ratio ( $\Phi$ ), sometimes used in literature.

As the air flow rate is restricted through the intake system with diverse obstacles (air filter, intake duct, throttle valve in SI engines, intake manifold and intake valve), the air introduced in the cylinder is lower than the quantity than the volume displacement could induct [92]. In this sense, the volumetric efficiency ( $\eta_v$ ), calculated with Equation (1.10), is the ratio of the actual mass of air introduced in the cylinder and the theoretical mass that would enter.

$$\eta_v = \frac{m_{air}}{\rho_{air} \cdot V_d} = \frac{\dot{m}_{air} \cdot n_R}{\rho_{air} \cdot N \cdot V_d} \quad (1.10)$$

In naturally-aspirated engines, depending on the air density ( $\rho_{air}$ ) taken as reference, either at atmospheric conditions or at the intake manifold, different values of  $\eta_v$  will be obtained due to the consideration of more or less intake system losses. In the case of turbocharged engines, as the air is introduced at a higher pressure than atmospheric conditions, the  $\eta_v$  is higher than the unity.

The quantity of air introduced in the cylinder highly governs the power and the performance obtained in an engine. As higher mass of air is inducted in the cylinder, higher fuel mass can be also introduced, increasing the quantity of chemical energy that can be released and converted to mechanical energy [93]. However, if the operation at part-load is desired in SI engines, the throttle valve is partially closed, reducing the volumetric efficiency as the restriction of the air flow is increased.

Conventionally, ICEs have been fueled with fossil fuels derivatives, e.g. gasoline and diesel, enabling a high penetration of this technology in a wide range of applications and scale sizes at a relatively low cost. Nevertheless, the climate change threat exposed in section 1.1 promotes the study of alternative fuels to reduce the environmental impact of conventional fuels that have a high contribution to greenhouse gas emissions (GHG) and atmospheric pollution.



## 1.4. Low carbon fuels

Internal combustion engines can be easily fed with unconventional liquid or gaseous fuels after making small preliminary modifications to withstand different combustion conditions [46,64,95–98]. Alcohols (e.g. ethanol, methanol and butanol) and biogas are common alternative fuels studied in spark ignition (SI) and compression ignition (CI) engines, reporting lower emissions and particulate matters [99,100]. However, they are usually blended with conventional fuels, gasoline and diesel, respectively, maintaining the dependence on fossil fuels [101–103]. On the other hand, hydrogen and methane are receiving great attention as potential gaseous fuels that can be used to avoid blends with high pollutant fossil fuels [46,104].

During  $H_2$  combustion, no emissions of  $CO_2$ ,  $CO$  and hydrocarbons (HCs) are formed as there is no carbon component in the fuel. However, this gas has a higher tendency to produce abnormal combustion phenomena and generate higher thermal  $NO_x$  emissions at air-fuel ratios close to the stoichiometric one [105–109]. Therefore, the use of leaner air-fuel mixtures to reduce combustion temperature limits the power generation in ICEs. In addition, the lower gas density of  $H_2$  compared to gasoline reduces the intake air, and thus, lower volumetric efficiency is achieved [110].

On the other hand, natural gas or its main constituent,  $CH_4$ , is the cleanest fossil fuel with the highest hydrogen to carbon ratio as only one carbon atom is found in its composition [47]. Natural gas reserves in the total world were around 199 trillion cubic meters (TCM) at the end of 2019, with a consumption of 3.9 TCM for that year [3]. Methane has a higher resistance to auto-ignition than gasoline, and thus, the former gas is less prone to knocking. In this way, richer air-fuel mixtures and higher compression ratios can be employed, providing higher power performance and thermal efficiency [47,111]. However, the higher flame temperature of  $CH_4$  compared to gasoline at stoichiometric mixtures increases  $NO_x$  emissions, requiring the use of a three-way catalyst (TWC) or leaning the air-fuel mixture [47]. As methane has a low laminar flame speed, the latter strategy increases the combustion duration and reduces the thermal efficiency, implying the use of fuel mixtures with higher laminar flame speed.

Mixtures of  $H_2$  and  $CH_4$  have been widely studied at different hydrogen fractions, combining the advantages of both fuels and increasing the flammability limits. Generally, a higher contribution of  $H_2$  reduces the combustion duration due to the higher laminar flame speed, increasing the thermal efficiency [112]. On the other hand, higher  $H_2$  percentages in the fuel rises the combustion temperature, increasing the  $NO_x$  emissions and the heat losses [47]. The contribution of  $CH_4$  is the reduction of the tendency to knock, enabling the engine operation at richer air-fuel mixtures, which increases the engine performance [113,114]. Therefore, optimization of the engine operating conditions must be carried out to compensate the disadvantages without compromising the engine performance.

In addition to the use of mixtures of  $H_2$  and  $CH_4$  as gaseous fuels in ICEs, there are industrial waste streams with high content of both of them, increasing their suitability as fuels at the same time they are valorized. An interesting example of these industrial waste streams is coke oven gas (COG), a by-product generated during coke manufacture.

Coke has been employed for centuries as a reducing agent for the production of hot metal, removing the oxygen indirectly by forming carbon dioxide or directly using its carbon content, in addition to supplying the heat required for the reduction process [26]. Coke is manufactured through the coal pyrolysis (carbonization) in coke oven batteries heating the coal in an oxygen-free atmosphere, with the main products being coke (solid), coke oven gas and liquids. Coal is heated up to 1000 – 1100 °C for 14 – 28 hours by heat exchange with fuel gases and preheated air that flow through flue channels in the walls surrounding the coke ovens, heating the wall bricks to 1150 – 1350 °C [26]. In addition, regeneration chambers below the coke ovens impart the residual heat from flue-gases to coke ovens. An example of the design of the coke oven battery in a coke plant in Birmingham, Alabama (USA) is shown in Figure 1.12 [115].

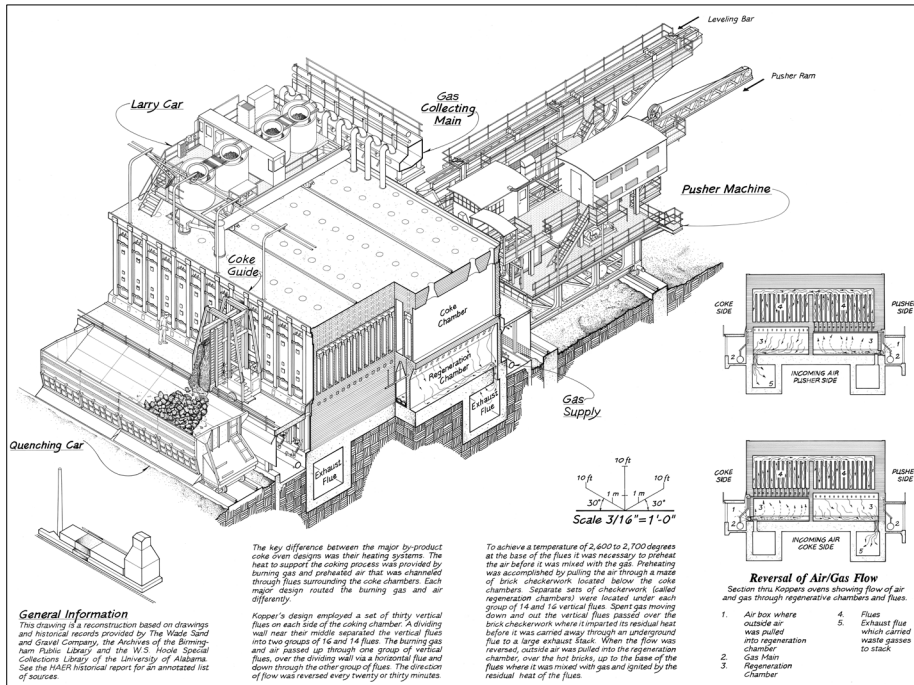


Figure 1.12. Drawing of a coke oven battery in a coke plant in Birmingham (Alabama, USA) [115].

Raw coke oven gas is the main by-product of coke manufacture generated in integrated steel mills or coke making enterprises [36,116]. The output product from a typical coke-making plant in energy terms is around 42.7 GJ/t of coke, with an energy distribution of 69.6% in the coke itself, 17.9% in the COG, 2.8% in tar, some minor components and 8.6% in energy loss [117]. In terms of mass, the coke and COG obtained per ton of dry coal are around 700 – 800 kg and 140 – 200 kg, respectively [26]. To get an idea of the high volume production of COG, approximately 681000 million tons of metallurgical coke were produced globally in 2019 [118], and with a production around 360 – 518 Nm<sup>3</sup> COG/ton coke [26], a total amount between 245 and 353 trillion Nm<sup>3</sup> of COG were generated in 2019.

Raw COG collected from coke ovens must be purified before it can be further used. The cleaning strategy includes the removal of dust, tar, naphthalene, light oil (mainly BTX, which is benzene, toluene and xylene), sulfurous compounds and cracking of ammonia to hydrogen [26,117,121]. Around 25 – 45 kg of tar, 3 kg of ammonia, 2.5 kg of H<sub>2</sub>S and up to 15 kg of light oil can be recovered per ton of coke produced [26]. An example of

the main cleaning COG stages in a coke plant in Birmingham, Alabama (USA) is shown in Figure 1.13 [122].

The typical volumetric composition of cleaned COG is 36-62% of  $H_2$ , 16-32% of  $CH_4$ , 2-10% of  $N_2$ , 3-8% of  $CO$ , 1-5% of  $CO_2$  and small traces of other compounds [26,117,123].

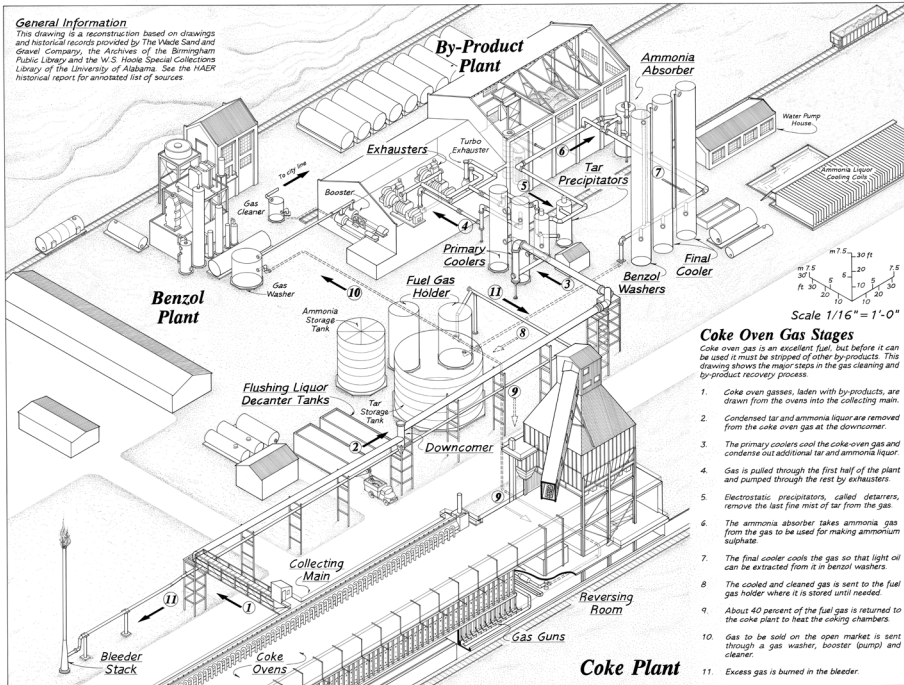


Figure 1.13. Drawing of the coke oven gas cleaning stages in a coke plant in Birmingham (Alabama, USA) [122].

COG can be used in a wide range of applications [117,124]:

- combustion fuel in blast furnaces stoves, furnaces in steel mills, under firing of coke ovens or in power plants to generate electricity and/or heat [26]
- reducing agent in direct reduction iron production instead of natural gas in countries with high content of coal and low NG available
- feedstock for  $H_2$  purification through the separation with pressure swing adsorption, cryogenic distillation or membrane separation. The remaining gas after  $H_2$  separation

could be used as process fuel in steel mills with the additional support of NG [116]

- syngas ( $H_2+CO$ ) production through partial oxidation (with  $O_2$ ), dry reforming (with  $CO_2$ , generating low  $H_2/CO$  ratio) or steam reforming (with  $H_2O$ , generating high  $H_2/CO$  ratio)
- methanol synthesis with syngas generated in a previous step
- methanation of COG to obtain  $CH_4$  [125]

Despite the high number of alternative applications for cleaned COG, this gas is sometimes flared off during periods of low demand for safety reasons [26,36]. Therefore, in these situations to maximize its yield, the high energy content in cleaned COG can be harnessed through devices placed at the coke plants where it is produced, generating electricity at the same time that pollutant emissions are controlled. Internal combustion engines, described in section 1.3, are a mature technology that provides a low cost, quick and flexible energy conversion, supporting the coke plant electricity demand with the addition of generator systems.

Many generator systems used in industry produce electricity with a determined frequency according to the number of magnetic poles and the speed of the coupled engine. Therefore, the thermal efficiency, the power and the emissions generated with the ICE are dictated by that specific engine speed, which can be far from the optimal operating condition. In this regard, there are variable speed generator systems that allow working at optimal engine speed with higher efficiency and power and lower pollutant emissions maintaining the electricity frequency desired. This can be accomplished with power electronics or with devices, such as the Continuous Variable Transmission (CVT) system [126,127].

The composition of the synthetic COG employed as fuel in **Chapters 3** and **4** of this thesis is shown in Table 1.2.

Table 1.2. Composition of COG in percentage by volume and by weight.

Composition	$H_2$	$CH_4$	CO	$N_2$	$CO_2$
vol%	57	30	6	5	2
wt%	11.6	48.5	16.9	14.1	8.9

In order to compare the performance of H<sub>2</sub>, CH<sub>4</sub> and COG when used as fuels in ICEs, their physicochemical properties are listed in Table 1.3. As can be seen, the lower heating value (LHV) per unit mass of H<sub>2</sub> is much higher than the value of CH<sub>4</sub>; however, LHV of COG is the lowest due to the 16.9 wt% of CO in the composition (Table 1.2), a component that barely contributes with a value of 10.1 MJ/kg [92]. On the other hand, LHV per unit volume or per mol decreases as the H<sub>2</sub> content increases because of the lower density. Low densities and volumetric LHVs of gases explain a decrease in power output compared to gasoline or diesel fuels due to the bigger space filled, resulting in less intake of fresh air and lower engine volumetric efficiency. This disadvantage can be compensated by employing a higher compression ratio, turbocharging and direct injection (DI) to increase the pressure of the fuel gases [47].

As mentioned for Equation (1.9), the stoichiometric ratio ( $\lambda_{st}$ ) is the ratio of mass flow rates of air and fuel that completely burns all the fuel with the air available. If there is an excess of air, the air-fuel mixture is lean, while if there is less air than the quantity required, the mixture is rich. The calculation of  $\lambda_{st}$  is carried out with the stoichiometric reaction of the fuel with oxygen. In the case of COG, as it is constituted by diverse fuels with different proportions, a general reaction has been deduced in **Chapter 3**.

Table 1.3. Typical physicochemical properties of H<sub>2</sub>, CH<sub>4</sub> and COG calculated at STP conditions.

Gas	H <sub>2</sub>	CH <sub>4</sub>	COG
LHV (MJ/kg)	120.00 [92]	50.00 [92]	39.86
LHV (kJ/mol)	241.91	802.12	395.50
LHV (MJ/m <sup>3</sup> )	10.65	35.32	17.41
Density (kg/m <sup>3</sup> ) at STP	0.09	0.71	0.44
Molecular weight (g/mol)	2.02 [92]	16.04 [92]	9.92
Stoichiometric ratio ( $\lambda_{st}$ )	34.21	17.20	12.72
Flammability range (vol%)	4.0 - 75.0 [128]	5.3 - 15.0 [128]	4.4 - 34.0 [129]
Laminar flame speed (m/s)	2.65 - 3.25 [130]	0.38 [130]	0.68 - 0.88 [131,132]

STP means standard temperature (273.15 K) and pressure conditions (10<sup>5</sup> Pa) according to IUPAC [133].

The flammability limits are the range of fuel-air mixtures compositions, in percentage by volume, in which they are able to ignite and propagate in a self-sustained way. The range of  $H_2$  is far wider compared to  $CH_4$ . The COG upper flammability limit is almost half of the  $H_2$  due to the high volume content of hydrogen in the mixture.

Laminar flame speed ( $S_L$ ) is a characteristic of the air-fuel chemical reactivity, combustion enthalpy and physical diffusivity, influencing the rate of heat release in SI engines.  $S_L$  strongly rises with the increase of  $H_2$  percentage in the fuel composition enhancing the mixture chemical reactivity by increasing the concentration of H, O and OH radical species [47]. This trend is linear up to 50% of  $H_2$  with a slight increase due to the less-reactive component,  $CH_4$ . From 50% to 90% of  $H_2$ , there is an exponential increase in  $S_L$ , ascending finally very rapidly in the range 90 – 100%. This non-linear behavior caused by the contribution of the slowly reacting methane affects strongly the chemical kinetics and the flame propagation process [47,134,135]. High  $S_L$  values reduce the combustion duration, increasing the extent of the isochoric heat addition, which increases the thermal efficiency. On the other hand, higher  $H_2$  percentages decrease the quenching distance, increase the combustion temperature and enhance the convective heat transfer, implying higher wall heat transfer and less thermal efficiency [47]. Therefore, many phenomena are involved in the combustion of these gaseous fuels in ICEs.

In summary,  $H_2$  benefits of a higher laminar flame speed, reducing the combustion duration and increasing the thermal efficiency; wider flammability limits that enable the operation with lean air-fuel mixtures; and zero hydrocarbon emissions. Besides, the high combustion temperature with rich air-fuel mixtures increases NOx emissions, heat losses (reducing the thermal efficiency) and the abnormal combustion tendency, requiring the use of lean mixtures. If a mixture of  $H_2 - CH_4$  is employed, higher combustion duration but a lower temperature is achieved, reducing the heat losses and NOx emissions and increasing the thermal efficiency. In addition, richer air-fuel mixtures with higher volumetric efficiency can be used without abnormal combustion, increasing the engine performance. A deeper review of  $H_2-CH_4$  mixtures is carried out in the introduction of **Chapter 3**.

Optimization of the ICE design and the operating conditions according to the different fuels employed are key issues to further develop this technology and increase its efficiency and environmental sustainability. Computational fluid dynamics (CFD) simulations offer a versatile tool to achieve a comprehensive understanding of the fluid dynamics and the combustion behavior inside ICEs. In this way, the need to carry out test bench engine experiments is reduced, thus saving money, and focusing only on the most interesting conditions observed and predicted by the computer simulations.

### **1.5. CFD simulation**

Computational fluid dynamics, which are computer-based simulations, are increasingly deployed in research and industry to analyze systems involving fluid flow, heat transfer and chemical reactions [136]. In this way, optimization of the design and the operating condition of the system can be achieved through a comprehensive understanding of the phenomena involved in its operation. The governing equations of fluid flow are the conservation laws of physics, which are partial differential equations and can be described as follows:

- The fluid mass is conserved (continuity)
- The rate of variation of momentum of a fluid particle equals the sum of forces on the particle (second law of Newton)
- The rate of change of energy of a fluid particle is equal to the sum of heat addition to the particle and the rate of work done on the particle (first law of thermodynamics)

The Navier-Stokes equations are combined with the previous equations in the case of Newtonian fluids, in which the viscous stresses are proportional to the rates of deformation. In addition, two equations of state are included with the assumption of thermodynamic equilibrium [136]. Thus, the flow is governed by five nonlinear partial differential equations and two algebraic equations. Supplying the suitable auxiliary conditions (initial and boundary conditions), the system is mathematically closed and can be solved numerically [137].



CFD codes resolve fluid flow problems with numerical algorithms, based on three main steps [136]:

- In the pre-processor stage, the inputs of the flow problem are applied to the CFD program, defining the geometry of the region studied (computational domain), generating the grid or mesh which divides the domain into a number of smaller cells, and defining the fluid properties and the initial and boundary conditions.
- In the solver stage, the numerical solution technique is applied. In the case of the finite volume method, first, an integration of the governing equations of fluid flow over all the control volumes of the domain is applied, then the integral equations are converted into a system of algebraic equations and lastly, the solution of the equations is achieved by an iterative method.
- In the post-processor stage, the CFD results can be visualized in terms of graphs, plots or 3D snapshots across the domain.

For this thesis, the steps to carry out the CFD simulations of the ICE can be visualized in the block diagram represented in Figure 1.14. As the first step, the software Autodesk® Inventor® has been employed to design the cylinder geometry, including the intake and exhaust manifolds and the valves. After that, the geometry is imported to the commercially available Ansys® software, focused on performing computational fluid dynamics simulations. The geometry is imported to the package Ansys Mesh®, where the mesh is generated. One of the main important steps to obtain an accurate solution is the mesh generation with a high number of cells, especially, in the regions with a higher gradient of flow properties. Nevertheless, the employment of a very refined mesh with a higher number of cells increases the computational cost. Therefore, a trade-off between a high enough number of cells to achieve a grid independent solution and reasonable simulation times must be reached.

In the case of Ansys software, the Forte® package is specially designed for ICE applications. This software automatically generates the volume mesh on-the-fly during the simulation, adapting the grid to the movement of the geometry elements, such as the valves and the piston [138]. Moreover, the mesh can be refined according to the geometry and

to the evolution of the variables inside the domain. Thus, a great versatility can be achieved with this tool, refining the mesh in the regions and during the more important periods for a high calculation accuracy with less computational effort.

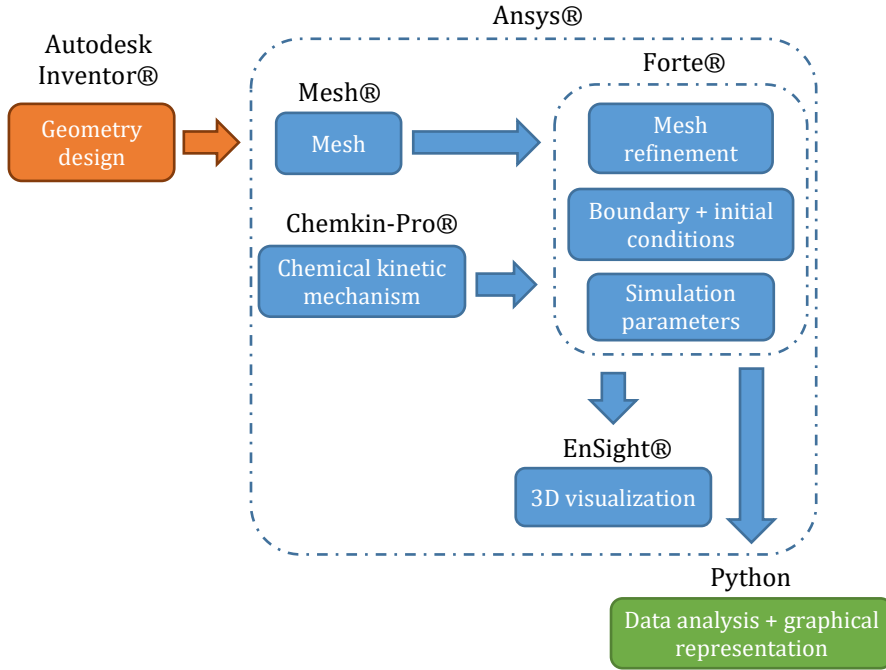


Figure 1.14. Block diagram of CFD engine simulations steps.

In terms of combustion, the software is linked with Ansys Chemkin-Pro® solver, which is the gold standard for chemical kinetic simulation. This package reduces the computational efforts grouping cells with similar kinetic conditions at each time step, which eliminates duplicate calculations. Moreover, Chemkin-Pro reduces the kinetics on the fly at every time step with a dynamic adaptive chemistry, using only the necessary chemistry at each time [138]. This package requires the input of the chemical kinetic mechanism, in which the chemical reactions with their Arrhenius rate coefficients and the thermodynamic properties of the species involved are described.

As the working fluids in ICEs are turbulent due to the flow motion inside the cylinder and during the flow exchanges with the manifolds, the basic fluid dynamics are governed by the Navier-Stokes equations. As there is a wide range of flow length scales, the Reynolds-Averaged-Navier-Stokes (RANS) approach is employed, avoiding the calculation of small-scale structures and fluctuations and retaining the main effects of the averaged flow and combustion characteristics [139].

Once the mesh refinements and the chemical kinetic mechanism are introduced in Forte, the spark ignition timing and the boundary conditions for all the walls, as well as for the input and output surfaces and their corresponding fluids, are defined. In addition, the initial conditions for the gas flow in all the domain regions are defined. Afterward, simulation parameters such as the engine speed, the simulation duration and the time step are introduced as inputs. Nevertheless, in the case of the last parameter, the time step is adaptively determined at each time according to the convergence and constraints of the fluids. Finally, to run the simulation, the number of parallel computational cores are selected, according to the computer availability, that determines the duration of the simulation.

Afterward, the results of the simulation are collected in very large spreadsheets of thousands of rows, which are treated to obtain graphs of the evolution of the variables. Python language offers a fast and automatic method of selection and graphical representation of the most relevant variables and simulation time, facilitating the comparison between simulation cases. On the other hand, snapshots of the 3D distribution of many variables across the domain in the desired crank angle degrees can be visualized with Ansys EnSight® package.

CFD software has been employed in ICEs by several studies to assess different fuels performance [140–145], operating conditions [146–151] and to prevent abnormal combustion, such as knocking or backfire [107,152–154]. In this way, a comprehensive understanding of the combustion phenomena and the fluid dynamics inside the ICE can be achieved, selecting and optimizing the operating conditions accordingly to the fuel type and application desired. A further review of CFD studies in ICEs is detailed in **Chapter 4**.

## References

- [1] Nations U. The Paris Agreement. 2015.
- [2] Conference of the Parties. Decision 1/CP.26. Draft COP decision proposed by the President. 2021.
- [3] Looney B. BP Statistical Review of World Energy, 2020 | 69th Edition. Bp 2020;69:66.
- [4] IEA. World Energy Outlook 2021. 2021.
- [5] Faber J, Hanayama S, Zhang S, Pereda P, Comer B, Hauerhof E, et al. Fourth IMO Greenhouse Gas Study 2020. 2021.
- [6] Smith TWP, Jalkanen JP, Anderson BA, Corbett JJ, Faber J, Hanayama S, et al. Third IMO Greenhouse Gas Study 2014. London: 2014. doi:10.1007/s10584-013-0912-3.
- [7] UNCTAD. Review of Maritime Transport 2019. New York: 2019.
- [8] Corbett JJ, Winebrake JJ, Green EH, Kasibhatla P, Eyring V, Lauer A. Mortality from ship emissions: A global assessment. *Environ Sci Technol* 2007;41:8512–8. doi:10.1021/es071686z.
- [9] Liu J, Duru O, Law AWK. Assessment of atmospheric pollutant emissions with maritime energy strategies using bayesian simulations and time series forecasting. *Environ Pollut* 2021;270:116068. doi:10.1016/j.envpol.2020.116068.
- [10] Trillos JCG, Wilken D, Brand U, Vogt T. Life cycle assessment of a hydrogen and fuel cell ropax ferry prototype. *Sustain Prod Life Cycle Eng Manag* 2021:5–23. doi:10.1007/978-3-030-50519-6\_2.
- [11] Perčić M, Vladimir N, Fan A. Life-cycle cost assessment of alternative marine fuels to reduce the carbon footprint in short-sea shipping: A case study of Croatia. *Appl Energy* 2020;279. doi:10.1016/j.apenergy.2020.115848.
- [12] Pratt JW, Klebanoff LE. Feasibility of the SF-BREEZE: a Zero-Emission, Hydrogen Fuel Cell, High-Speed Passenger Ferry. 2016.
- [13] Fuel cell technology in ships (FCSHIP) 2004. <https://cordis.europa.eu/project/id/G3RD-CT-2002-00823> (accessed February 24, 2021).
- [14] IRENA International Renewable Energy Agency. Renewable capacity statistics 2019. Abu Dhabi: 2019.

- 
- [15] Gahleitner G. Hydrogen from renewable electricity: An international review of power-to-gas pilot plants for stationary applications. *Int J Hydrogen Energy* 2013;38:2039–61. doi:10.1016/j.ijhydene.2012.12.010.
- [16] Ban M, Yu J, Shahidehpour M, Yao Y. Integration of power-to-hydrogen in day-ahead security-constrained unit commitment with high wind penetration. *J Mod Power Syst Clean Energy* 2017;5:337–49. doi:10.1007/s40565-017-0277-0.
- [17] Stolten D, Emonts B. Hydrogen Science and Engineering. Materials, Processes, Systems and Technology. Volume 1. Weinheim: Wiley-VCH Verlag GmbH & Co. KGaA; 2016.
- [18] Hanley ES, Deane JP, Gallachóir BPÓ. The role of hydrogen in low carbon energy futures—A review of existing perspectives. *Renew Sustain Energy Rev* 2018;82:3027–45. doi:10.1016/j.rser.2017.10.034.
- [19] Sherif SA, Barbir F, Veziroglu TN. Towards a hydrogen economy. *Electr J* 2005;18:62–76. doi:10.1016/j.tej.2005.06.003.
- [20] First liquid hydrogen carrier. *Mot* 2014. <https://www.motorship.com/news101/ships-and-shipyards/first-liquid-hydrogen-carrier> (accessed December 3, 2019).
- [21] Liquefied Hydrogen Bunker Vessel Designed. *Marit Exec* 2019. <https://www.maritime-executive.com/article/liquefied-hydrogen-bunker-vessel-designed> (accessed December 3, 2019).
- [22] Sharaf OZ, Orhan MF. An overview of fuel cell technology: Fundamentals and applications. *Renew Sustain Energy Rev* 2014;32:810–53. doi:10.1016/j.rser.2014.01.012.
- [23] Verhelst S. Recent progress in the use of hydrogen as a fuel for internal combustion engines. *Int J Hydrogen Energy* 2014;39:1071–85. doi:10.1016/j.ijhydene.2013.10.102.
- [24] Ruhnau O, Bannik S, Otten S, Praktiknjo A, Robinius M. Direct or indirect electrification? A review of heat generation and road transport decarbonisation scenarios for Germany 2050. *Energy* 2019;166:989–99. doi:10.1016/j.energy.2018.10.114.
- [25] Rose PK, Neumann F. Hydrogen refueling station networks for heavy-duty vehicles in future power systems. *Transp Res Part D Transp Environ* 2020;83:102358. doi:10.1016/j.trd.2020.102358.

- [26] Remus R, Aguado Monsonet MA, Roudier S, Sancho LD. Best Available Techniques (BAT) Reference Document for Iron and Steel Production. vol. BREF-IS. 2013. doi:10.2791/97469.
- [27] Otto A, Robinius M, Grube T, Schiebahn S, Praktiknjo A, Stolten D. Power-to-steel: Reducing CO<sub>2</sub> through the integration of renewable energy and hydrogen into the German steel industry. *Energies* 2017;10. doi:10.3390/en10040451.
- [28] Dodds PE, Demoullin S. Conversion of the UK gas system to transport hydrogen. *Int J Hydrogen Energy* 2013;38:7189–200. doi:10.1016/j.ijhydene.2013.03.070.
- [29] Nastasi B, Lo Basso G. Hydrogen to link heat and electricity in the transition towards future Smart Energy Systems. *Energy* 2016;110:5–22. doi:10.1016/j.energy.2016.03.097.
- [30] Sherif SA, Barbir F, Veziroglu TN. Wind energy and the hydrogen economy-review of the technology. *Sol Energy* 2005;78:647–60. doi:10.1016/j.solener.2005.01.002.
- [31] Grüger F, Hoch O, Hartmann J, Robinius M, Stolten D. Optimized electrolyzer operation: Employing forecasts of wind energy availability, hydrogen demand, and electricity prices. *Int J Hydrogen Energy* 2019;4:4387–97. doi:10.1016/j.ijhydene.2018.07.165.
- [32] Robinius M, Otto A, Heuser P, Welder L, Syranidis K, Ryberg DS, et al. Linking the power and transport sectors - Part 1: The principle of sector coupling. *Energies* 2017;10. doi:10.3390/en10070956.
- [33] IRENA. Hydrogen From Renewable Power. Technology outlook for the energy transition. Abu Dhabi: 2018.
- [34] Corbo P, Migliardini F, Veneri O. Hydrogen Fuel Cells for Road Vehicles. vol. 11. 2011. doi:10.1007/978-0-85729-136-3.
- [35] Holladay JD, Hu J, King DL, Wang Y. An overview of hydrogen production technologies. *Catal Today* 2009;139:244–60. doi:10.1016/j.cattod.2008.08.039.
- [36] Yáñez M, Ortiz A, Brunaud B, Grossmann IE, Ortiz I. Contribution of upcycling surplus hydrogen to design a sustainable supply chain: The case study of Northern Spain. *Appl Energy* 2018;231:777–87. doi:10.1016/j.apenergy.2018.09.047.
- [37] Carmo M, Fritz DL, Mergel J, Stolten D. A comprehensive review on PEM water electrolysis. *Int J Hydrogen Energy* 2013;38:4901–34.

- doi:10.1016/j.ijhydene.2013.01.151.
- [38] National Academy of Sciences. The Hydrogen Economy: Opportunities, Costs, Barriers, and R&D Needs. Washington, DC: National Academies Press; 2004.
  - [39] Tichler R, Bauer S. Power-to-Gas. Elsevier Inc.; 2016. doi:10.1016/B978-0-12-803440-8/00018-X.
  - [40] Ursúa A, Gandía LM, Sanchis P. Hydrogen production from water electrolysis: Current status and future trends. *Proc IEEE* 2012;100:410–26. doi:10.1109/JPROC.2011.2156750.
  - [41] Nonobe Y. Development of the fuel cell vehicle mirai. *IEEJ Trans Electr Electron Eng* 2017;12:5–9. doi:10.1002/tee.22328.
  - [42] van Biert L, Godjevac M, Visser K, Aravind P V. A review of fuel cell systems for maritime applications. *J Power Sources* 2016;327:345–64. doi:10.1016/j.jpowsour.2016.07.007.
  - [43] Mekhilef S, Saidur R, Safari A. Comparative study of different fuel cell technologies. *Renew Sustain Energy Rev* 2012;16:981–9. doi:10.1016/j.rser.2011.09.020.
  - [44] Choudhury A, Chandra H, Arora A. Application of solid oxide fuel cell technology for power generation - A review. *Renew Sustain Energy Rev* 2013;20:430–42. doi:10.1016/j.rser.2012.11.031.
  - [45] Schatz M, Wachter M. Thermodynamic modeling of a closed gas turbine process working with helium and stoichiometric combustion of hydrogen and oxygen. 13th Eur. Turbomach. Conf. Turbomach. Fluid Dyn. Thermodyn. ETC13, 2019, p. 13.
  - [46] Escalante Soberanis MA, Fernandez AM. A review on the technical adaptations for internal combustion engines to operate with gas/hydrogen mixtures. *Int J Hydrogen Energy* 2010;35:12134–40. doi:10.1016/j.ijhydene.2009.09.070.
  - [47] Yan F, Xu L, Wang Y. Application of hydrogen enriched natural gas in spark ignition IC engines: from fundamental fuel properties to engine performances and emissions. *Renew Sustain Energy Rev* 2018;82:1457–88. doi:10.1016/j.rser.2017.05.227.
  - [48] Simón J. HyUnder - Assessment of the potential, the actors and relevant business cases for large scale and seasonal storage of renewable electricity by hydrogen underground storage in Europe 2015. <http://hyunder.eu/> (accessed March 6, 2020).

- [49] Steward D, Saur G, Penev M, Ramsden T. Lifecycle Cost Analysis of Hydrogen Versus Other Technologies for Electrical Energy Storage. 2009.
- [50] Clegg S, Mancarella P. Storing renewables in the gas network: Modelling of power-to-gas seasonal storage flexibility in low-carbon power systems. *IET Gener Transm Distrib* 2016;10:566–75. doi:10.1049/iet-gtd.2015.0439.
- [51] Steinke F, Wolfrum P, Hoffmann C. Grid vs. storage in a 100% renewable Europe. *Renew Energy* 2013;50:826–32. doi:10.1016/j.renene.2012.07.044.
- [52] Crotogino F, Donadei S, Bünger U, Landinger H. Large-Scale Hydrogen Underground Storage for Securing Future Energy Supplies. 18th World Hydrog. Energy Conf. 2010 - WHEC 2010, vol. 78, Essen: 2010, p. 37–45. doi:10.1109/INTMAG.2015.7157557.
- [53] Ozarslan A. Large-scale hydrogen energy storage in salt caverns. *Int J Hydrogen Energy* 2012;37:14265–77. doi:10.1016/j.ijhydene.2012.07.111.
- [54] Caglayan DG, Weber N, Heinrichs HU, Linßen J, Robinius M, Kukla PA, et al. Technical potential of salt caverns for hydrogen storage in Europe. *Int J Hydrogen Energy* 2020;45:6793–805. doi:10.1016/j.ijhydene.2019.12.161.
- [55] Melaina MW, Antonia O, Penev M. Blending Hydrogen into Natural Gas Pipeline Networks: A Review of Key Issues. 2013. doi:10.2172/1068610.
- [56] Winkler-Goldstein R, Rastetter A. Power to gas: The Final Breakthrough for the Hydrogen Economy? *Green* 2013;3:69–78. doi:10.1515/green-2013-0001.
- [57] HyDeploy 2021. <https://hydeploy.co.uk/> (accessed October 28, 2021).
- [58] Robinius M, Raje T, Nykamp S, Rott T, Müller M, Grube T, et al. Power-to-Gas: Electrolyzers as an alternative to network expansion – An example from a distribution system operator. *Appl Energy* 2018;210:182–97. doi:10.1016/j.apenergy.2017.10.117.
- [59] Adamson K-A. Stationary fuel cells. An overview. Elsevier; 2020.
- [60] Maestre VM, Ortiz A, Ortiz I. Challenges and prospects of renewable hydrogen-based strategies for full decarbonization of stationary power applications. *Renew Sustain Energy Rev* 2021;152:111628.



- doi:10.1016/j.rser.2021.111628.
- [61] Durusut E, Erbay Y, Joos M, Tahir F. Study 3: Hydrogen for Power Generation -Opportunities for hydrogen and CCS in the UK power mix. 2019.
  - [62] Tsujimura T, Suzuki Y. Development of a large-sized direct injection hydrogen engine for a stationary power generator. *Int J Hydrogen Energy* 2019;44:11355–69. doi:10.1016/j.ijhydene.2018.09.178.
  - [63] Avadhanula VK, Lin C Sen, Witmer D, Schmid J, Kandulapati P. Experimental study of the performance of a stationary diesel engine generator with hydrogen supplementation. *Energy and Fuels* 2009;23:5062–72. doi:10.1021/ef900311w.
  - [64] Sáinz D, Diéguez PM, Urroz JC, Sopena C, Guelbenzu E, Pérez-Ezcurdia A, et al. Conversion of a gasoline engine-generator set to a bi-fuel (hydrogen/gasoline) electronic fuel-injected power unit. *Int J Hydrogen Energy* 2011;36:13781–92. doi:10.1016/j.ijhydene.2011.07.114.
  - [65] Hong BK, Kim SH, Kim CM. Powering the Future through Hydrogen and Polymer Electrolyte Membrane Fuel Cells. Current commercialisation and key challenges with focus on work at Hyundai. *Johnson Matthey Technol Rev* 2020;64:236–51. doi:10.1595/205651319x15744200036826.
  - [66] Matsunaga M, Fukushima T, Ojima K. Advances in the Power train System of Honda FCX Clarity Fuel Cell Vehicle. *SAE Tech. Pap.*, 2009. doi:10.4271/2009-01-1012.
  - [67] Tronstad T, Hogmoen Astrand H, Petra Haugom G, Lagnfeldt L. Study on the Use of Fuel Cells in Shipping. 2017.
  - [68] De-Troya JJ, Álvarez C, Fernández-Garrido C, Carral L. Analysing the possibilities of using fuel cells in ships. *Int J Hydrogen Energy* 2016;41:2853–66. doi:10.1016/j.ijhydene.2015.11.145.
  - [69] Rivarolo M, Rattazzi D, Lamberti T, Magistri L. Clean energy production by PEM fuel cells on tourist ships: A time-dependent analysis. *Int J Hydrogen Energy* 2020;45:25747–57. doi:10.1016/j.ijhydene.2019.12.086.
  - [70] GEV, Ballard Developing Hydrogen Fuel Cell-Powered n.d. <https://www.marinelink.com/news/gev-ballard-developing-hydrogen-fuel-485145> (accessed February 24, 2021).

- [71] Sembler WJ, Kumar S, Palmer D. Fuel cells as an alternative to cold ironing. *J Fuel Cell Sci Technol* 2009;6:0310091–03100911. doi:10.1115/1.3006305.
- [72] Yuan Y, Wang J, Yan X, Shen B, Long T. A review of multi-energy hybrid power system for ships. *Renew Sustain Energy Rev* 2020;132:15. doi:10.1016/j.rser.2020.110081.
- [73] Roh G, Kim H, Jeon H, Yoon K. Fuel Consumption and CO2 Emission Reductions of Ships Powered by a Fuel-Cell-Based Hybrid Power Source. *J Mar Sci Eng* 2019;7:230. doi:10.3390/jmse7070230.
- [74] Hornblower Hybrid: The World's First Hydrogen Hybrid Ferry n.d. <https://www.marineinsight.com/future-shipping/hornblower-hybrid-the-worlds-first-hydrogen-hybrid-ferry/> (accessed February 24, 2021).
- [75] NYK Steps into the Future with Super Eco Ship 2050. *World Marit News* 2018. <https://worldmaritimenews.com/archives/264771/nyk-steps-into-the-future-with-super-eco-ship-2050/> (accessed December 13, 2019).
- [76] Eyring V, Isaksen ISA, Berntsen T, Collins WJ, Corbett JJ, Endresen O, et al. Transport impacts on atmosphere and climate: Shipping. *Atmos Environ* 2010;44:4735–71. doi:10.1016/j.atmosenv.2009.04.059.
- [77] Buhaug Ø, Corbett JJ, Endresen O, Eyring V, Faber J, Hanayama S, et al. Second IMO GHG Study 2009. 2009.
- [78] Ortiz A. HYLANTIC - Atlantic Network for Renewable Generation and Supply of Hydrogen to promote High Energy Efficiency 2018. <http://hylantic.com/> (accessed February 24, 2020).
- [79] Pang E. HySeas III - Realising the world's first sea-going hydrogen-powered RoPax ferry and a business model for European islands 2019. <https://www.hyseas3.eu/the-project/> (accessed February 24, 2020).
- [80] Arguedas Ortiz D. How hydrogen is transforming these tiny Scottish islands. *BBC Future* 2019. <https://www.bbc.com/future/article/20190327-the-tiny-islands-leading-the-way-in-hydrogen-power> (accessed February 24, 2020).
- [81] Mikkola J. FLAGSHIPS - Clean waterborne transport in Europe

2019. <https://flagships.eu/> (accessed March 6, 2020).
- [82] e-SHyIPS Project 2021. <https://e-shyips.com/project/> (accessed November 16, 2021).
- [83] Singh J. Auriga Energy - Developing efficient hydrogen fuel cell products and solutions. Auriga Energy 2019. <http://www.auriga-energy.com/> (accessed February 24, 2020).
- [84] Nemo H2: The First Ecofriendly Electrical Boat | Join the EcoLuxury Revolution! n.d. <https://ecoluxuryrevolution.wordpress.com/2009/12/19/nemo-h2-the-first-ecofriendly-electrical-boat/> (accessed February 24, 2021).
- [85] Global Energy Ventures. Compressed Hydrogen Ship C-H2 2021. <https://gev.com/hydrogen/> (accessed November 16, 2021).
- [86] BeHydro n.d. <https://www.behydro.be/en/home.html> (accessed November 16, 2021).
- [87] CMB.Tech. Hydrotug n.d. <https://cmb.tech/solutions/marine/hydrotug> (accessed November 16, 2021).
- [88] CMB.Tech. HydroBingo 2021. <https://cmb.tech/solutions/marine/hydrobingo> (accessed November 16, 2021).
- [89] CMB.Tech. Hydrocat n.d. <https://cmb.tech/solutions/marine/hydrocat> (accessed November 16, 2021).
- [90] CMB.Tech. Hydroville 2021. <http://hydroville.be/en/> (accessed November 16, 2021).
- [91] Erussard V, Delafosse J. Energy Observer. Energy Obs 2019. <http://www.energy-observer.org/en/#hydrogene> (accessed December 13, 2019).
- [92] Heywood JB. Internal combustion engine fundamentals. New York: McGraw-Hill Education; 2018.
- [93] Pulkrabek WW. Engineering Fundamentals of the Internal Combustion Engine. Pearson Education Limited; 1997.
- [94] Brady RN. Internal Combustion (Gasoline and Diesel) Engines. Encycl. Energy, vol. 3, 2004, p. 515–28. doi:10.1016/b0-12-

176480-x/00089-9.

- [95] Sopena C, Diéguez PM, Sáinz D, Urroz JC, Guelbenzu E, Gandía LM. Conversion of a commercial spark ignition engine to run on hydrogen: Performance comparison using hydrogen and gasoline. *Int J Hydrogen Energy* 2010;35:1420–9. doi:10.1016/j.ijhydene.2009.11.090.
- [96] Gonca G, Cakir M, Sahin B. Performance Characteristics and Emission Formations of a Spark Ignition (SI) Engine Fueled with Different Gaseous Fuels. *Arab J Sci Eng* 2017. doi:10.1007/s13369-017-2906-3.
- [97] Yilmaz IT, Gumus M. Effects of hydrogen addition to the intake air on performance and emissions of common rail diesel engine. *Energy* 2018;142:1104–13. doi:10.1016/j.energy.2017.10.018.
- [98] Sáinz D, Diéguez PM, Sopena C, Urroz JC, Gandía LM. Conversion of a commercial gasoline vehicle to run bi-fuel (hydrogen-gasoline). *Int J Hydrogen Energy* 2012;37:1781–9. doi:10.1016/j.ijhydene.2011.10.046.
- [99] Zhen X, Wang Y, Liu D. Bio-butanol as a new generation of clean alternative fuel for SI (spark ignition) and CI (compression ignition) engines. *Renew Energy* 2020;147:2494–521. doi:10.1016/j.renene.2019.10.119.
- [100] Ghadikolaie MA, Wong PK, Cheung CS, Ning Z, Yung KF, Zhao J, et al. Impact of lower and higher alcohols on the physicochemical properties of particulate matter from diesel engines: A review. *Renew Sustain Energy Rev* 2021;143:110970. doi:10.1016/j.rser.2021.110970.
- [101] Pan S, Li X, Han W, Huang Y. An experimental investigation on multi-cylinder RCCI engine fueled with 2-butanol/diesel. *Energy Convers Manag* 2017;154:92–101. doi:10.1016/J.ENCONMAN.2017.10.047.
- [102] Pan S, Cai K, Cai M, Du C, Li X, Han W, et al. Experimental study on the cyclic variations of ethanol/diesel reactivity controlled compression ignition (RCCI) combustion in a heavy-duty diesel engine. *Energy* 2021;237:121614. doi:10.1016/J.ENERGY.2021.121614.
- [103] Shrivastava K, Thipse SS, Patil ID. Optimization of diesel engine performance and emission parameters of Karanja biodiesel-ethanol-diesel blends at optimized operating conditions. *Fuel*

- 2021;293:120451. doi:10.1016/J.FUEL.2021.120451.
- [104] Masuk NI, Mostakim K, Kanka SD. Performance and Emission Characteristic Analysis of a Gasoline Engine Utilizing Different Types of Alternative Fuels: A Comprehensive Review. *Energy & Fuels* 2021;35:4644–69. doi:10.1021/ACS.ENERGYFUELS.0C04112.
  - [105] Verhelst S, Wallner T. Hydrogen-fueled internal combustion engines. *Prog Energy Combust Sci* 2009;35:490–527. doi:10.1016/j.pecs.2009.08.001.
  - [106] Moreno F, Muñoz M, Arroyo J, Magén O, Monné C, Suelves I. Efficiency and emissions in a vehicle spark ignition engine fueled with hydrogen and methane blends. *Int J Hydrogen Energy* 2012;37:11495–503. doi:10.1016/j.ijhydene.2012.04.012.
  - [107] Diéguez PM, Urroz JC, Sáinz D, Machin J, Arana M, Gandía LM. Characterization of combustion anomalies in a hydrogen-fueled 1.4 L commercial spark-ignition engine by means of in-cylinder pressure, block-engine vibration, and acoustic measurements. *Energy Convers Manag* 2018;172:67–80. doi:10.1016/j.enconman.2018.06.115.
  - [108] Heffel JW. NO<sub>x</sub> emission reduction in a hydrogen fueled internal combustion engine at 3000 rpm using exhaust gas recirculation. *Int J Hydrogen Energy* 2003;28:1285–92. doi:10.1016/S0360-3199(02)00289-6.
  - [109] Verhelst S, Verstraeten S, Sierens R. A comprehensive overview of hydrogen engine design features. *Proc Inst Mech Eng Part D J Automob Eng* 2007;221:911–20. doi:10.1243/09544070JAUTO141.
  - [110] White CM, Steeper RR, Lutz AE. The hydrogen-fueled internal combustion engine: a technical review. *Int J Hydrogen Energy* 2006;31:1292–305. doi:10.1016/j.ijhydene.2005.12.001.
  - [111] Akansu SO, Dulger Z, Kahraman N, Veziroğlu TN. Internal combustion engines fueled by natural gas - Hydrogen mixtures. *Int J Hydrogen Energy* 2004;29:1527–39. doi:10.1016/j.ijhydene.2004.01.018.
  - [112] Wang J, Huang Z, Fang Y, Liu B, Zeng K, Miao H, et al. Combustion behaviors of a direct-injection engine operating on various fractions of natural gas-hydrogen blends. *Int J Hydrogen Energy* 2007;32:3555–64. doi:10.1016/j.ijhydene.2007.03.011.

- [113] Rao A, Wu Z, Kumar Mehra R, Duan H, Ma F. Effect of hydrogen addition on combustion, performance and emission of stoichiometric compressed natural gas fueled internal combustion engine along with exhaust gas recirculation at low, half and high load conditions. *Fuel* 2021;304:121358. doi:10.1016/j.fuel.2021.121358.
- [114] Xu J, Zhang X, Liu J, Fan L. Experimental study of a single-cylinder engine fueled with natural gas-hydrogen mixtures. *Int J Hydrogen Energy* 2010;35:2909–14. doi:10.1016/j.ijhydene.2009.05.039.
- [115] Heintz E. Thomas Coke Ovens 1952 - Thomas By-Product Coke Works, 1200 Tenth Street West, Thomas, Jefferson County, AL 1992.
- [116] Joseck F, Wang M, Wu Y. Potential energy and greenhouse gas emission effects of hydrogen production from coke oven gas in U.S. steel mills. *Int J Hydrogen Energy* 2008;33:1445–54. doi:10.1016/j.ijhydene.2007.10.022.
- [117] Razzaq R, Li C, Zhang S. Coke oven gas: Availability, properties, purification, and utilization in China. *Fuel* 2013;113:287–99. doi:10.1016/j.fuel.2013.05.070.
- [118] EIA. Coal and coke. International Energy Statistics 2020. <https://www.eia.gov/international/data/world> (accessed November 18, 2021).
- [119] Ramírez-Santos ÁA, Castel C, Favre E. A review of gas separation technologies within emission reduction programs in the iron and steel sector: Current application and development perspectives. *Sep Purif Technol* 2018;194:425–42. doi:10.1016/j.seppur.2017.11.063.
- [120] IISI. World steel in figures. 2021.
- [121] Caillat S. Burners in the steel industry: Utilization of by-product combustion gases in reheating furnaces and annealing lines. *Energy Procedia* 2017;120:20–7. doi:10.1016/j.egypro.2017.07.152.
- [122] Carlini E. Coke Oven Gas Flow - 1952 - Thomas By-Product Coke Works, 1200 Tenth Street West, Thomas, Jefferson County, AL 1992.
- [123] Chen WH, Lin MR, Leu TS, Du SW. An evaluation of hydrogen production from the perspective of using blast furnace gas and

- coke oven gas as feedstocks. *Int J Hydrogen Energy* 2011;36:11727–37. doi:10.1016/j.ijhydene.2011.06.049.
- [124] Bermúdez JM, Arenillas A, Luque R, Menéndez JA. An overview of novel technologies to valorise coke oven gas surplus. *Fuel Process Technol* 2013;110:150–9. doi:10.1016/j.fuproc.2012.12.007.
- [125] Qin Z, Zhao Y, Yi Q, Shi L, Li C, Yan X, et al. Methanation of coke oven gas over Ni-Ce/ $\gamma$ -Al<sub>2</sub>O<sub>3</sub> catalyst using a tubular heat exchange reactor: Pilot-scale test and process optimization. *Energy Convers Manag* 2020;204:112302. doi:10.1016/j.enconman.2019.112302.
- [126] Jian L, Chau KT. Design and analysis of a magnetic-gearred electronic-continuously variable transmission system using finite element method. *Prog Electromagn Res* 2010;107:47–61.
- [127] CVT Corp. Ind Most Powerful Mech CVTs 2016. <https://www.cvtcorp.com/main.php?i=15> (accessed December 7, 2019).
- [128] Karim GA. Hydrogen as a spark ignition engine fuel. *Int J Hydrogen Energy* 2003;28:569–77. doi:10.1016/S0360-3199(02)00150-7.
- [129] Corporation USS. Clean Coke Oven Gas. Safety Data Sheet (SDS). Exposure 2010;82493:1–8.
- [130] Wang J, Wei Z, Zhang M, Huang Z. A review of engine application and fundamental study on turbulent premixed combustion of hydrogen enriched natural gas. *Sci China Technol Sci* 2014;57:445–51. doi:10.1007/s11431-014-5471-y.
- [131] Feng H, Zhang W, Zhang J, Wang X, Zhang X. Availability analysis of a coke oven gas fueled spark ignition engine. *Int J Hydrogen Energy* 2018;43:1835–45. doi:10.1016/j.ijhydene.2017.11.125.
- [132] Liu G, Zhou J, Wang Z, Liu J. Study of Laminar Flame Speeds of Premixed Coke Oven Gas Flame Using Kinetic Simulation. 11th China-Japan-Korea Student Symp., Hangzhou: 2017.
- [133] D. McNaught A, Wilkinson A. IUPAC Compendium of Chemical Terminology. Gold Book. 2nd ed. 1997.
- [134] Di Sarli V, Di Benedetto A. Laminar burning velocity of hydrogen-methane/air premixed flames. *Int J Hydrogen Energy* 2007;32:637–46. doi:10.1016/j.ijhydene.2006.05.016.
- [135] Donohoe N, Heufer A, Metcalfe WK, Curran HJ, Davis ML, Mathieu O, et al. Ignition delay times, laminar flame speeds, and mechanism

- validation for natural gas/hydrogen blends at elevated pressures. *Combust Flame* 2014;161:1432–43. doi:10.1016/j.combustflame.2013.12.005.
- [136] Versteeg HK, Malalasekera W. *An Introduction to Computational Fluid Dynamics. The Finite Volume Method. Second Ed.*: Pearson Education Limited; 2007.
- [137] Anderson JDJ. *Computational Fluid Dynamics. The basics with applications*. New York, NY: McGraw-Hill, Inc.; 1995.
- [138] Ansys®. *Accelerate your engine combustion CFD with Ansys Forte* 2016.
- [139] Ansys®. *Academic Research Forte, Release 2021 R1, Help System, Forte Theory Manual*, Ansys Inc. 2021.
- [140] Fu J, Zhong L, Zhao D, Liu Q, Shu J, Zhou F, et al. Effects of hydrogen addition on combustion, thermodynamics and emission performance of high compression ratio liquid methane gas engine. *Fuel* 2021;283:119348. doi:10.1016/j.fuel.2020.119348.
- [141] Kan X, Zhou D, Yang W, Zhai X, Wang CH. An investigation on utilization of biogas and syngas produced from biomass waste in premixed spark ignition engine. *Appl Energy* 2018;212:210–22. doi:10.1016/j.apenergy.2017.12.037.
- [142] Stylianidis N, Azimov U, Kawahara N, Tomita E. Chemical Kinetics and Computational Fluid-Dynamics Analysis of H<sub>2</sub>/CO/CO<sub>2</sub>/CH<sub>4</sub> Syngas Combustion and NO<sub>x</sub> Formation in a Micro-Pilot-Ignited Supercharged Dual Fuel Engine. *SAE Tech Pap* 2017;2017-Sept. doi:10.4271/2017-24-0027.
- [143] Zaker K, Askari MH, Jazayeri A, Ebrahimi R, Zaker B, Ashjaee M. Open cycle CFD investigation of SI engine fueled with hydrogen/methane blends using detailed kinetic mechanism. *Int J Hydrogen Energy* 2015;40:14006–19. doi:10.1016/j.ijhydene.2015.08.040.
- [144] Gharehghani A, Hosseini R, Mirsalim M, Yusaf TF. A computational study of operating range extension in a natural gas SI engine with the use of hydrogen. *Int J Hydrogen Energy* 2015;40:5966–75. doi:10.1016/j.ijhydene.2015.03.015.
- [145] Wang T, Zhang X, Xu J, Zheng S, Hou X. Large-eddy simulation of flame-turbulence interaction in a spark ignition engine fueled with methane/hydrogen/carbon dioxide. *Energy Convers Manag*



- 2015;104:147–59. doi:10.1016/j.enconman.2015.05.030.
- [146] Yang Z, Zhang F, Wang L, Wang K, Zhang D. Effects of injection mode on the mixture formation and combustion performance of the hydrogen internal combustion engine. *Energy* 2018;147:715–28. doi:10.1016/j.energy.2018.01.068.
- [147] Kosmadakis GM, Rakopoulos DC, Rakopoulos CD. Investigation of nitric oxide emission mechanisms in a SI engine fueled with methane/hydrogen blends using a research CFD code. *Int J Hydrogen Energy* 2015;40:15088–104. doi:10.1016/j.ijhydene.2015.09.025.
- [148] Fanelli E, Viggiano A, Braccio G, Magi V. On laminar flame speed correlations for H<sub>2</sub>/CO combustion in premixed spark ignition engines. *Appl Energy* 2014;130:166–80. doi:10.1016/j.apenergy.2014.05.012.
- [149] Rakopoulos CD, Kosmadakis GM, Pariotis EG. Evaluation of a combustion model for the simulation of hydrogen spark-ignition engines using a CFD code. *Int J Hydrogen Energy* 2010;35:12545–60. doi:10.1016/j.ijhydene.2010.09.002.
- [150] Dennis PA, Dingli RJ, Abbasi Atibeh P, Watson HC, Brear MJ, Voice G. Performance of a port fuel injected, spark ignition engine optimised for hydrogen fuel. *SAE Tech Pap* 2012. doi:10.4271/2012-01-0654.
- [151] Knop V, Benkenida A, Jay S, Colin O. Modelling of combustion and nitrogen oxide formation in hydrogen-fuelled internal combustion engines within a 3D CFD code. *Int J Hydrogen Energy* 2008;33:5083–97. doi:10.1016/j.ijhydene.2008.06.027.
- [152] Subramanian KA, Salvi BL. A Numerical Simulation of Analysis of Backfiring Phenomena in a Hydrogen-Fueled Spark Ignition Engine. *J Eng Gas Turbines Power* 2016;138:1–10. doi:10.1115/1.4033182.
- [153] Duan J, Liu F, Sun B. Backfire control and power enhancement of a hydrogen internal combustion engine. *Int J Hydrogen Energy* 2014;39:4581–9. doi:10.1016/j.ijhydene.2013.12.175.
- [154] Liu X, Liu F, Zhou L, Sun B, Schock HJ. Backfire prediction in a manifold injection hydrogen internal combustion engine. *Int J Hydrogen Energy* 2008;33:3847–55. doi:10.1016/j.ijhydene.2008.04.051.



# **CHAPTER 2**

---

**RENEWABLE ENERGY SYSTEMS  
COUPLING WITH HYDROGEN  
INFRASTRUCTURE INCLUDING  
MARITIME TRANSPORT**



## 2.1. Introduction

The simulation and analysis of optimal possible future scenarios with energy system models are playing an important role in recent years, helping policy-makers and companies in decision-making in order to tailor their actions and investments in an optimal way.

Several system models have addressed the deployment of a high-penetration renewable energy scenario at the European level, investigating the influence of isolated and interconnected countries cases on renewable shares and energy system costs [1–4]. Child et al. [1] highlighted the importance of an interconnected European scenario with a 100% renewable energy sources (RES) power system to reduce the storage capacity and the total annual costs (TAC). In turn, other models have considered the coupling of renewable energy with the transport and heating sectors [5–8]. Cebulla et al. [7] realized that coupling between sectors reduced the requirement for electrical energy storage. Moreover, short-term storage was more suitable for regions with frequent periods with excess of RES.

In contrast, other studies have focused on decarbonizing the energy system by utilizing  $H_2$  as an energy vector at different regional levels and accounting for diverse generation technologies and demands. An energy study for Europe with different shares of RES and assuming a power demand by 2050 was assessed by Gils et al. [9]; however,  $H_2$  was considered only as a storage resource and solely becoming important at high solar contribution. On the other hand, a  $H_2$  deployment scenario was cost-optimally designed by Samsatli et al. [10], satisfying a 100% penetration assumption for fuel cell electric vehicles (FCEVs) as domestic transport demand across Great Britain, with onshore wind turbines for energy generation. Pressurized vessels, underground salt caverns, and depleted oil and gas fields, were considered as storage solutions and  $H_2$  pipelines and electricity lines for commodities transmission. In the cases of Robinius et al. and Welder et al. [11,12], a hypothetical energy system for Germany in 2050 was developed. In the former study, a  $H_2$  transmission and distribution pipeline grid was created to cover the future demand of FCEVs with surplus energy from diverse RES. In the latter work, only eligible onshore wind was used, but with consideration of both mobile and industrial  $H_2$  demand. Additionally, a new hydrogen

transmission pipeline infrastructure was designed on the basis of compressed natural gas pipelines, highways and railways and utilizing salt caverns and gas pipes as storage systems. In the study by Guandalini et al. [13], a power-to-gas system was applied to Italy in 2050, producing an amount of H<sub>2</sub> equivalent to 5-6% of all natural gas consumption, or 6-8% of the total transportation fuel supply. Tlili et al. [14] assessed the potential of generating H<sub>2</sub> in France with RES and nuclear energy by the 2035 horizon.

Finally, Caglayan et al. 2021 [15] designed a European hydrogen infrastructure to supply electricity and H<sub>2</sub> in a 100% renewable energy scenario by 2050. The electricity was based on the e-Highway “100% RES” project [16] but substituting electric vehicles with FCEVs. Underground salt caverns were considered for storage [17], as well as different conversion technologies, with electrical grids and hydrogen pipelines for energy transport.

However, none of the previous models of energy systems has considered the implications of maritime transport despite its high anthropogenic CO<sub>2</sub> emissions [18]. Furthermore, as explained in **Chapter 1**, the high volume of ships along the Atlantic coast of Europe implies that a significant amount of greenhouse gases (GHGs) and other harmful emissions are released in the region [19,20]. Therefore, many projects and technologies based on H<sub>2</sub> and electricity are being applied to this sector to promote more sustainable power sources for ships [21–26]. Hence, the impact of the new hydrogen and electric demand for shipping on the future European energy system has to be addressed.

The main novelty of this chapter is the study of the impact of a futuristic electric and hydrogen maritime sector on the European energy system in 2050 for a scenario with 100% renewable energy sources. This impact has been considered including the estimated electrical and hydrogen demand of ships from the ports of the Atlantic coast of Europe in that year. The transport activities of freight and passenger ships in the main ports of this coast that were registered in the Eurostat database [27] have been included. The optimized energy model minimizes the total annual costs of an interconnected European system based on an electrical and H<sub>2</sub> infrastructure that selects the most adequate technologies and capacities in each region. The model provides an optimal design of the

infrastructure of the energy system across Europe to satisfy the electric and H<sub>2</sub> demands in all of the regions. Furthermore, the hourly operation time series of all the technologies through the year 2050 are calculated for every region. In this way, a snapshot corresponding to a 100% renewable energy system configuration required in 2050 with a high penetration of ships based on electricity and H<sub>2</sub> is shown to promote the transition by the corresponding policy agents.

In this chapter, the technologies and the electricity and hydrogen demands included as input for the energy system model are first described. Then, a discussion of the results is conducted in terms of TAC, technology capacities, the state of charge, the operation of some technologies and the electrical and hydrogen balance in two regions. Finally, the main conclusions are drawn.

The work carried out in this chapter was conducted within the framework of the HYLANTIC project [21] in the Techno-Economic Systems Analysis department from the Institute of Energy and Climate Research (IEK-3), in Forschungszentrum Jülich, Germany, where the research stay was conducted. This work was developed under the supervision of Dr. Martin Robinius and Dr. Heidi Heinrichs, and in collaboration with the PhD candidate Dilara Gülcin Caglayan.

## **2.2. Methodology**

This section briefly describes the energy system model and the boundaries employed. Then, the main technologies considered in each region for optimization are provided. Ultimately, a detailed explanation of the methodology employed to calculate ship electricity and hydrogen demands is presented, as well as the scenarios considered in this study.

### **2.2.1. Energy system modeling software**

The optimized design of the energy system discussed herein is based on a program developed in the Python language named Framework for Integrated Energy System Assessment (FINE) [28], which is explained in detail in Welder et al. [12]. The code of the program was developed by the

Techno-Economic Systems Analysis department from the Institute of Energy and Climate Research (IEK-3), in Forschungszentrum, Jülich. This program minimizes the TAC of the energy system, selecting and adjusting the capacity of the optimal RES as well as the conversion, transmission and storage technologies in each region. An interconnected electric and hydrogen infrastructure between regions across Europe is designed, with each region represented as a node of a network and transmission between them by edges. The system enables the exchange of electricity and hydrogen commodities and the deployment of specific technologies and capacities in each region in accordance with their specific characteristics. The techno-economic parameters of each technology are defined as input for the optimization problem. In this way, the system is able to satisfy the expected hourly electricity and hydrogen demand across all regions and at all times by 2050. In terms of temporal resolution, the model employs an hourly time series for that year.

### **2.2.2. System definition**

The energy system employed in this work is briefly described here. A more detailed explanation of the system components can be found in the work of Caglayan et al. 2021 [15].

For the regional boundaries of Europe, 96 regions were considered (see Figure A.2.1 in the Appendix) in accordance with the distribution proposed in the e-Highway project [16]. In each region, energy carriers, electricity and hydrogen, could be generated, consumed, converted or stored using the proposed technologies shown in Figure 2.1. The specific investments of every technology were considered constant for all the regions except in the case of onshore and offshore wind, with variable costs according to the size and location of the turbines, as discussed in Ryberg et al. and Caglayan et al. [29,30]. In these studies, the maximum capacity was calculated through diverse land eligibility constraints.



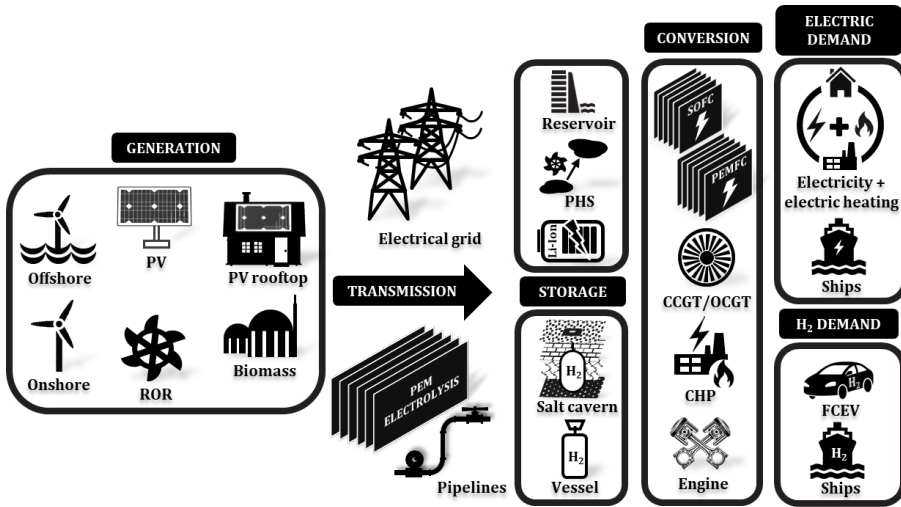


Figure 2.1. Generation, transmission, conversion and storage technologies considered in the model.

Regarding RES generation technologies, onshore, offshore, photovoltaic (PV) fixed or with sun tracking in open fields, as well as PV on rooftops, biomass and run-of-river (ROR) hydropower were considered in the system. The renewable feed-in time series for onshore, offshore and PV were created with the weather dataset, Modern-Era Retrospective Analysis for Research and Application, Version 2 (MERRA-2) [31] and the simulation tool, “RESKit – Renewable Energy Simulation toolkit for Python” [29,32]. The capacities of ROR and hydropower were assumed to be fixed with respect to 2015. In addition, biomass was treated as a commodity that could be acquired when needed to generate electricity with combined heat and power (CHP) technology.

To convert electricity to H<sub>2</sub> by means of a clean process, polymer electrolyte membrane (PEM) electrolyzers were considered to be the best option, with a fast dynamic response to RES fluctuations, high efficiency and smaller size [33]. Regarding the conversion from H<sub>2</sub> to electricity, five technologies were taken into account: PEM fuel cells, solid oxide fuel cells (SOFCs), hydrogen open cycle gas turbines (OCGTs), hydrogen combined cycle gas turbines (CCGTs) and hydrogen gas engines, which have been detailed in **Chapter 1**.

For energy storage, electricity was expected to be stored by using lithium-ion (Li-Ion) batteries, which have a fast and steady response time

and small self-discharge rate (less than 0.3%) [34], and by using pumped hydro storage (PHS) and hydro reservoirs systems with fixed capacities. In the case of hydrogen storage, thin-bedded structures and salt domes were considered with the technical capacity in each region defined from the study of Caglayan et al. 2020 [17]. Salt caverns in domed and bedded salt deposits have the benefit of being very gastight and inert with H<sub>2</sub>, avoiding reactions with microorganisms or minerals, as in depleted fields and aquifers [35]. However, as not all regions feature salt caverns, vessels were also included in the model that could be used as alternative hydrogen storage media in a more distributed way across the regions.

With respect to energy transmission, the electricity was transmitted through high-voltage direct current (HVDC) and high-voltage alternating current (HVAC) lines. As there is no available data for grids at 2050, the grid designed in the “Ten Year Network Development Plan (TYNDP)” for 2030 was considered, as explained in more detail in Syranidis et al. [36], being exogenously fixed and carrying zero investment costs. For H<sub>2</sub>, pipelines were considered to be the best and most economical method for transporting H<sub>2</sub> on a large scale and across significant distances (greater than 200 km) due to their lower operational costs in demand-intensive scenarios [37,38]. The H<sub>2</sub> pipeline grid was developed on a new infrastructure rather than old natural gas (NG) pipelines. However, the shortest path for pipelines between regions was extracted combining the existing infrastructure of roads, railways and NG pipelines.

Finally, for the electricity demand, the estimated value for the year 2050 of the scenario “X-7: 100% RES electricity” of the e-Highway project [16] was used. As in that project, this work includes the demand of a large share of electrified heat demand for space and water heating in residential and non-residential places. However, instead of considering electric vehicles as electricity consumers, a 50% penetration of FCEVs fueled with H<sub>2</sub> has been considered as the expected market penetration for 2050 in this work. This value is in accordance with forecasts found in the literature [39]. The annual hydrogen demand was calculated based on the existing driving behavior, annual driving distance and the total number of passenger vehicles, projecting the result onto the hourly profile of a fueling station. In addition to these demands, electrical and hydrogen demands for ships in the Atlantic area of Europe have been estimated for the year 2050 in the next section.

### 2.2.3. Ship electricity and hydrogen demands

In this chapter, a special emphasis is placed on the Atlantic coastal regions of France, Spain, Ireland, the United Kingdom and Portugal, estimating the electricity and hydrogen demands for ships in 2050 based on the current ship operations in the ports of these regions.

These estimated marine transport demands provide an insight into the shipping decarbonization by 2050 to reduce GHGs and other harmful emissions along the coast and ports of the Atlantic area of Europe. This area is characterized by intensive ship traffic for both trade and leisure. Moreover, this chapter provides a study of the potential of the  $H_2$  vector in the area in a bid to encourage policy-makers and companies to use environmentally-friendly fuels and transport. For this purpose, the methodology shown in Figure 2.2 is employed to estimate the electricity and hydrogen demands for ships in 2050, with values in 2015 obtained from the detailed database Eurostat [27] and growth estimations derived from Khalili et al. [40].

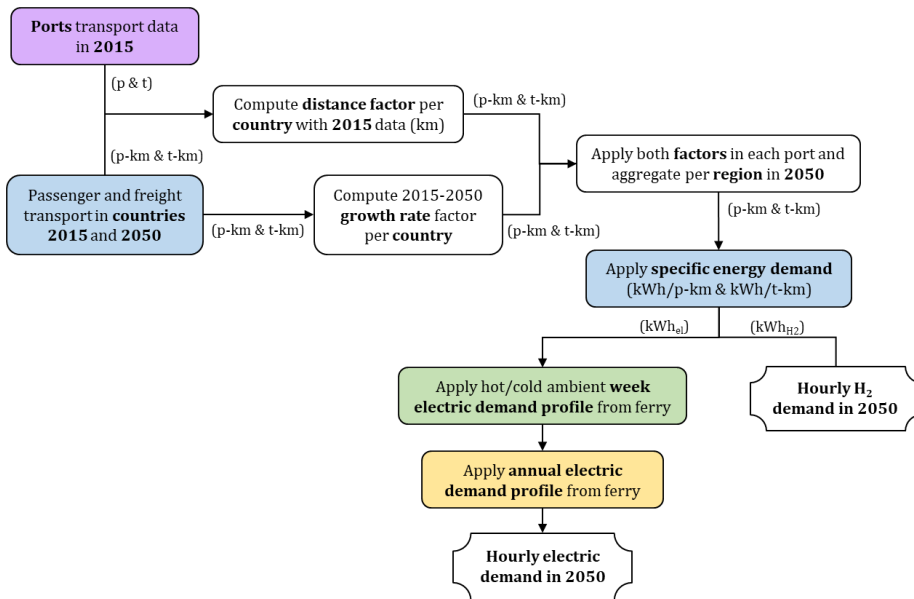


Figure 2.2. Flow chart of the methodology to calculate ship demand. Data: Khalili et al. [40] (blue); Eurostat [27] (pink); Rivarolo et al. [41] (green); and Baldi et al. [42] (yellow).

The marine operations of freight and passenger transport from the ports in the United Kingdom, Ireland, France, Spain and Portugal in the region under study, shown in green in Figure 2.3, and registered in the Eurostat database [27] for the year 2015, were identified. The list of ports of the Atlantic area of Europe included is detailed in Table A.2.1 in the Appendix. These activities are expressed in the Eurostat database in terms of the annual gross weight of goods transported (in tonnes, t) and passengers transported (in passengers, p) for each port.

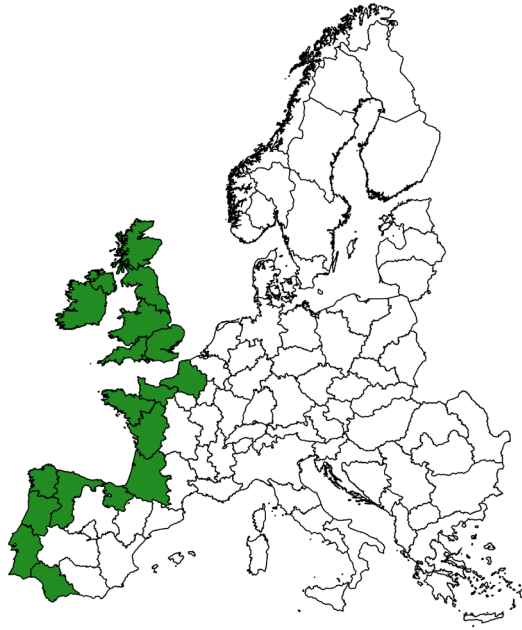


Figure 2.3. Regions of the Atlantic area of Europe considered for the ship demands calculation in green color.

However, to attain a projection of marine activities by 2050 for each port, the values from 2015 for each country from Khalili et al. [40] for both marine freight (in million t-km) and passengers (in million p-km) modes were collected. As is apparent, both data sources have different units for each of the transport modes (freight and passenger) because, in Khalili et al. [40], the weight of the goods or passengers is multiplied by the distance traveled. To find an equivalence in units between both data sources, an average “distance coefficient” (t-km/t and p-km/p) is calculated for each country in 2015. In this way, the data from the Eurostat database [27] can be multiplied by the “distance coefficient” to obtain the same values as in

Khalili et al. [40] for the year 2015 and in the same units. The “distance coefficient” is employed for all the ports of each country, assuming that the average distance traveled is the same for all of them.

Once the marine transport values of all ports have been calculated for the year 2015 using the units of Khalili et al. [40], the “growth ratio” for each country between 2015 and 2050 for the same reference is attained. This is accomplished by dividing the transport estimated value in each country in 2050 by the value in 2015. Furthermore, it is assumed that all the ports in each country grow at the same pace as the country itself in the period from 2015 to 2050, computing the “growth ratio” in each transportation mode for all ports in their respective countries. The calculation of both coefficients for the regions of interest can be found in Table A.2.2 in the Appendix. The results of the average “distance” and “growth ratio” coefficients are collected in Table 2.1.

Table 2.1. Average “distance coefficient” and “growth ratio” between 2050 and 2015 for each country.

Country	Average distance coefficient		Growth ratio 2015-2050 (-)	
	Freight (t-km/t)	Passengers (p-km/p)	Freight	Passengers
<b>UK</b>	4230	251	2.1	5.2
<b>Ireland</b>	4140	190	1.4	1.1
<b>France</b>	6744	238	1.6	2.9
<b>Spain</b>	2942	170	1.3	1.6
<b>Portugal</b>	2552	1089	1.2	1.1

Once the freight and passenger transportation activity values for the year 2050 in each port are quantified, the annual electric and H<sub>2</sub> demands for shipping are calculated with the corresponding specific energy demand estimations for the year 2050. These values are detailed in Table 2.2 and taken from Khalili et al. [40]. As an example, the calculation of the electric and H<sub>2</sub> ship demands from the Spanish ports in 2050 is detailed in Table A.2.3. The resulting ship demands calculated by each port are added up to compute the regional demands for each commodity. In Table A.2.4 and Table A.2.5 in the Appendix the total electric and H<sub>2</sub> ship demands for each region are collected.

Table 2.2. Specific energy demand for marine transport in 2050 [40].

Marine specific energy demand		2050
Electricity	Freight (kWh <sub>el</sub> /t-km)	0.02
	Passenger (kWh <sub>el</sub> /p-km)	0.325
Hydrogen	Freight (kWh <sub>H2</sub> /t-km)	0.029
	Passenger (kWh <sub>H2</sub> /p-km)	0.461

The temporal resolution of the model used in this study is hourly, and for that reason, these annual values must be disaggregated by the hour. As there is a lack of data on hourly electric energy demand in ports, the electric consumption profiles for hotel services and related services from a cruise ship during a typical week of operation, from Rivarolo et al. [41], are employed. These ships can offer an insight into the electrical variability required in ships with high energy demand for non-propulsion processes. The normalized week electrical demand profile from Rivarolo et al. [41] in cold ambient is repeated cyclically in the months between October and April and the warm ambient week in the months between May and September. Moreover, to better represent the energy demand evolution along the year because of differences in ambient temperature, the normalized daily electric power demand profile of a cruise ship, from Baldi et al. [42], is also applied.

The resulting ship electricity demand for ships in the region of the northeast of France is represented in Figure 2.4. Electrical power demand is higher in ships during the summer months than in the winter months due to the needs of the compressors of the heating, ventilation and air conditioning (HVAC) systems, while ferry operations see an increase due to tourism [42]. However, the total electricity demand during summer is lower due to a reduced electricity demand for the rest of the applications (heating, lighting, etc.), as can be seen in Figure 2.4.

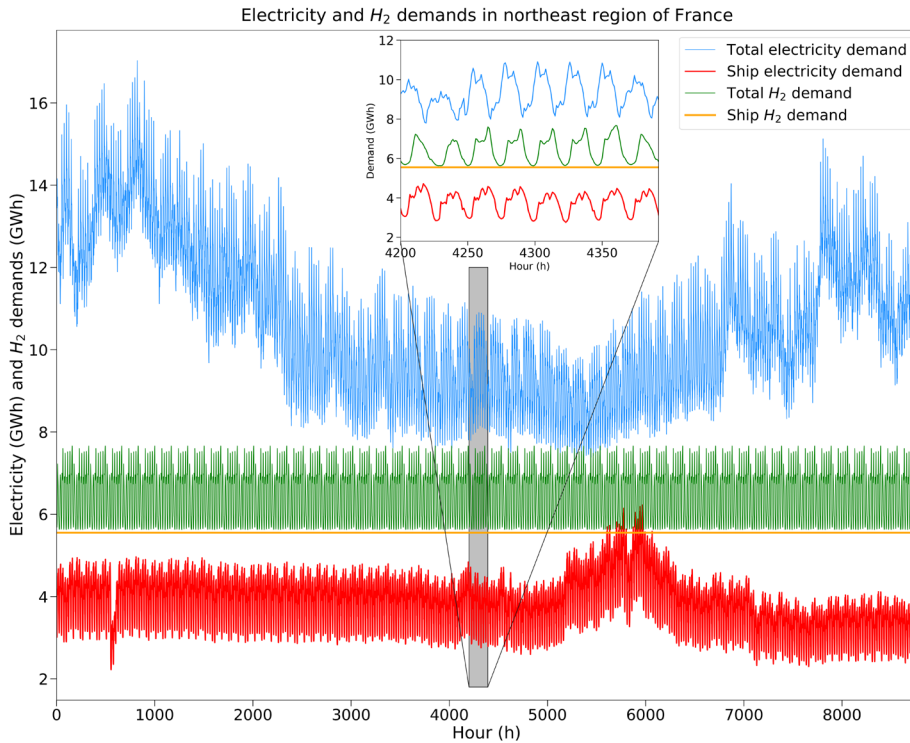


Figure 2.4. Total and ship hourly electricity and H<sub>2</sub> demands (GWh) in the northeast region of France.

H<sub>2</sub> fuel is expected to play a dominant role in 2050 for marine passenger and freight transport. H<sub>2</sub> could be used to reduce emissions [40,43,44], as an auxiliary power supply system [44,45], as a hybrid fuel with biofuels and synfuels [46–48], or to support the high energy demand of auxiliary engines and boilers for the on-board operations of large ships in berth [49–51]. However, the ship H<sub>2</sub> demand profile is considered constant throughout the year because there is no data from hydrogen refueling stations dedicated to marine vessels or the use of this fuel in the maritime setting in the first place, as it is still in the research stage. Nevertheless, due to the dense marine traffic between ports and regions, the fact that maritime trade is usually regular throughout the year and the energy demanded by ships during operation at berth [50,52,53], an average value of H<sub>2</sub> demand can be considered a good approximation. Therefore, the average annual hydrogen demand is divided by the number of hours of a year to obtain an average hourly H<sub>2</sub> demand per region.

In Figure 2.4 the total and ship H<sub>2</sub> demands for the northeast region of France are represented. The ship H<sub>2</sub> demand is constant throughout the year considering the previous assumption and the variable profile of the total H<sub>2</sub> demand corresponds to the hourly profile of a fueling station for the FCEV [15].

Figure 2.5a shows the total annual ship electricity demand (TWh/y) in each of the regions studied on the European Atlantic coast. Its contribution to total electricity demand in each region and along the Atlantic coast is represented in percentage values in black and red, respectively. As can be observed, a high contribution of ship electricity demand is expected by 2050 in each region, especially in the United Kingdom and northeast of France, reaching a third of the total electricity demand in some of those regions. In total, the electricity demand from all the ships along the Atlantic coast would be around 4.26% of the total electricity demand in Europe. This contrasts with the nearly zero electricity demand currently and the important development that must be carried out in the electric marine sector to achieve these values by 2050.

In Figure 2.5b, the total annual ship H<sub>2</sub> demand (TWh/y) in each of the studied regions along the Atlantic coast is plotted and its contribution to the total H<sub>2</sub> demand of each region is represented as percentage values in black. The share of regional ship H<sub>2</sub> demand to the total Atlantic coast H<sub>2</sub> demand is depicted in red. As can be seen, the ship H<sub>2</sub> demand generally predominates over FCEV demand in all the regions (black percentages higher than 50%), highlighting the role of the maritime transport on the Atlantic coast of Europe and the efforts that must be addressed in this sector to achieve this high H<sub>2</sub> demand compared to the null current hydrogen demand.



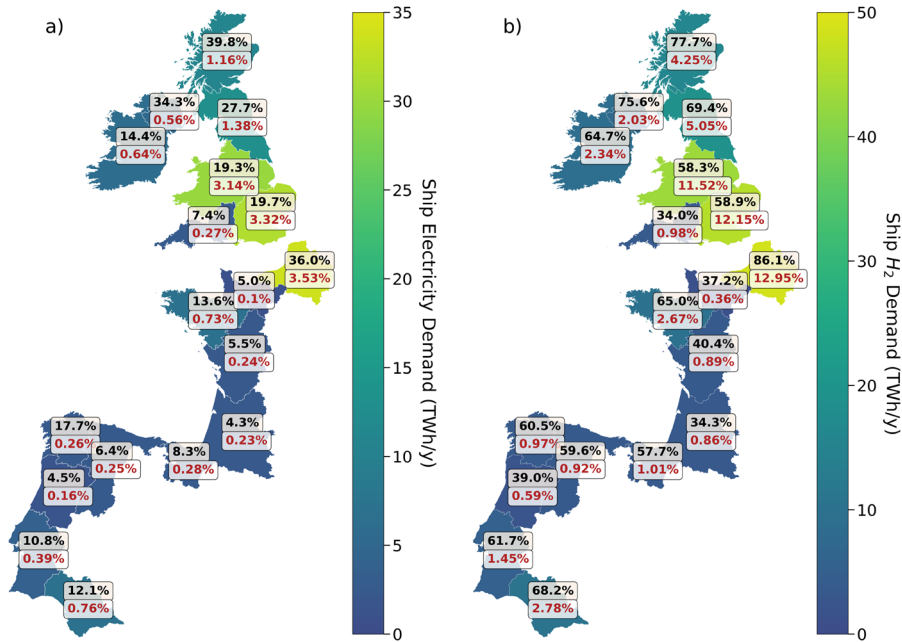


Figure 2.5. Annual ship demand (TWh/y) and its contribution (%) to regional demand (in black) and to total Atlantic coast demand (in red) in terms of electricity (a) and H<sub>2</sub> (b) in each of the regions of the Atlantic coast of Europe considered.

#### 2.2.4. Scenarios

As this study is an estimation of the future consumption of electricity and H<sub>2</sub> for freight and passenger transport ships by 2050, the real values could differ from the predicted ones. Therefore, different penetration scenarios of ship H<sub>2</sub> demand are simulated to analyze its effect on the model. The electricity demand of ships is maintained constant with the value calculated previously in order to be able to emphasize the influence of H<sub>2</sub> as an energy vector for maritime transport. Therefore, all the electrical demands (heat and space derived from the e-Highway project [16] and electricity for ships previously calculated) and hydrogen demand for FCEV (50% market penetration) remain constant and only the H<sub>2</sub> demand for ships is varied with the scenarios.

The range of variation of ship H<sub>2</sub> demand spans from 0% of the values calculated previously, considered the reference case (S0), in which zero H<sub>2</sub> demand is assumed for ships. Scenario S100 is the case in which the ships use 100% of the values of H<sub>2</sub> calculated previously (Figure 2.5). However, in the case that the calculated values in S100 were underestimated in 2050, scenarios of ship H<sub>2</sub> demand up to 160% (S160) have been also included, implying an increase of 60% with respect to the calculated values (scenario S100). Intermediate steps of 20% are included to track the evolution of costs and capacities in the energy system in each of them.

These penetration scenarios enable the analysis of the impact of less polluting vessels for freight and passenger transport concerning the Atlantic area and their requirements in a transition to a more sustainable European energy system.

## **2.3. Results and discussion**

The results obtained in this chapter using the methodology previously discussed are described in this section in order to analyze the economic and technical impact of the additional ship H<sub>2</sub> demand on the European energy system. Then, a study of the energy system behavior in scenario S100 is conducted in order to better understand the relationship between the different technologies considered.

### **2.3.1. Impact of ship H<sub>2</sub> demand**

The model optimizes a 100% RES energy system infrastructure across Europe that should be installed by 2050 to satisfy the expected electric and hydrogen demands with the estimated energy that could be generated with RES that year. Figure 2.6a shows the TAC (10<sup>9</sup> €/y) of the main technologies and storage systems across Europe with respect to the scaled ship hydrogen demand scenarios. The optimized generation technologies that will have the highest TAC values in 2050 will be onshore wind, PV fixed and offshore wind. As the ship H<sub>2</sub> demand increases, the TAC of the technologies rises linearly. However, in the case of electrolyzer and onshore technologies, a steep slope is produced between scenarios 0% (S0) and 160% (S160), increasing their TAC 49.4% and 16.7%, respectively. For the remaining technologies, the slope is very smooth.

These results can be explained with the capacities of generation, conversion and transmission technologies and storage systems that will be installed in 2050, which are shown in Figure 2.6b. Electrolyzer and onshore technologies have variations in capacity values of 49.4% and 17.3% between S0 and S160, respectively, similar to the TAC case, because capacity and TAC are directly related. Therefore, onshore technology will be the main renewable source of electricity to generate hydrogen as the demand from ships increases.

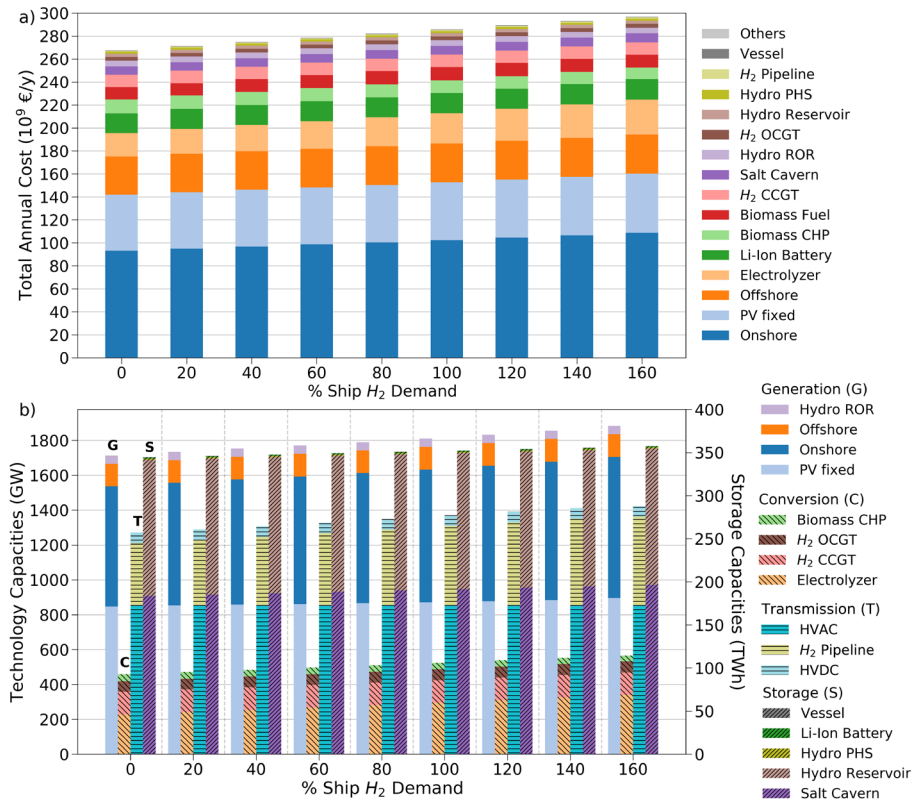


Figure 2.6. a) Variation of total annual costs (TAC, in 10<sup>9</sup> €/y) and b) main generation, conversion and transmission technology capacities (GW) and storage capacities (TWh) versus percentage of ship H<sub>2</sub> demand across all regions of Europe.

It can be noted that fixed PV will have a high installed capacity with a lower variation than onshore wind (5.7%) between the extreme scenarios. Thus, PV is a very important technology for electricity generation, compensating for wind fluctuations, but with little dependence on ship H<sub>2</sub> demand. On the other hand, the offshore

technology will have a smaller installed capacity but make a relatively high contribution to the TAC.

The capacity of H<sub>2</sub> pipelines is defined as the product of the mass flow rate (g/s) and lower heating value (LHV, in MJ/kg) of H<sub>2</sub>. HVAC and HVDC have zero TAC values, as they are defined exogenously, without investment costs or expansion. A remarkable fact is the high contribution of the H<sub>2</sub> pipeline to the total technology transmission capacity but with very little impact on the TAC, with values lower than 0.4% of the TAC for each scenario, demonstrating the importance and feasibility of the use of pipelines for H<sub>2</sub> transport in 2050 with low investment.

In terms of storage capacities, the largest installed systems will be salt caverns and hydro reservoirs, with the former accounting for around 54% of the total installed storage capacity. These systems will be used for long periods and with an increase of 7% for salt cavern capacity between the S0 to S160 scenarios, remaining constant for hydro reservoirs due to the capacity being considered fixed [15]. This 7% variation in salt cavern capacity means 13 TWh, while ship H<sub>2</sub> demand has increased from 0 TWh in scenario S0 to 383 TWh in S160. This result highlights the slight increase in storage requirement when a high amount of H<sub>2</sub> demand is added and the reduced impact on the TAC for the salt caverns installation (Figure 2.6a).

Therefore, the deployment of hydrogen ships in the Atlantic area to promote cleaner transport of freight and passengers requires the reinforcement of the European energy system and its technologies with a relatively low additional TAC (11%) between scenarios S0 and S160.

To determine the impact of ship H<sub>2</sub> demand across the regions of Europe, Figure 2.7a shows the difference in the capacity of the main RES technologies, H<sub>2</sub> pipelines and salt caverns between scenarios S160 and S0. On the other hand, Figure 2.7b displays the layout of the capacities that would be required in 2050 in scenario S160. The total storage capacity is increased from 184 TWh to 197 TWh from the S0 scenario to the S160 case, mainly increasing in Northern Ireland (7 TWh), the southern region of Scotland (3 TWh) and the southwestern United Kingdom (2.7 TWh), but decreases by around 2 TWh in the Wales-Midlands area of the United Kingdom and in the west of Germany. Minor variations are also produced in other regions of Europe.

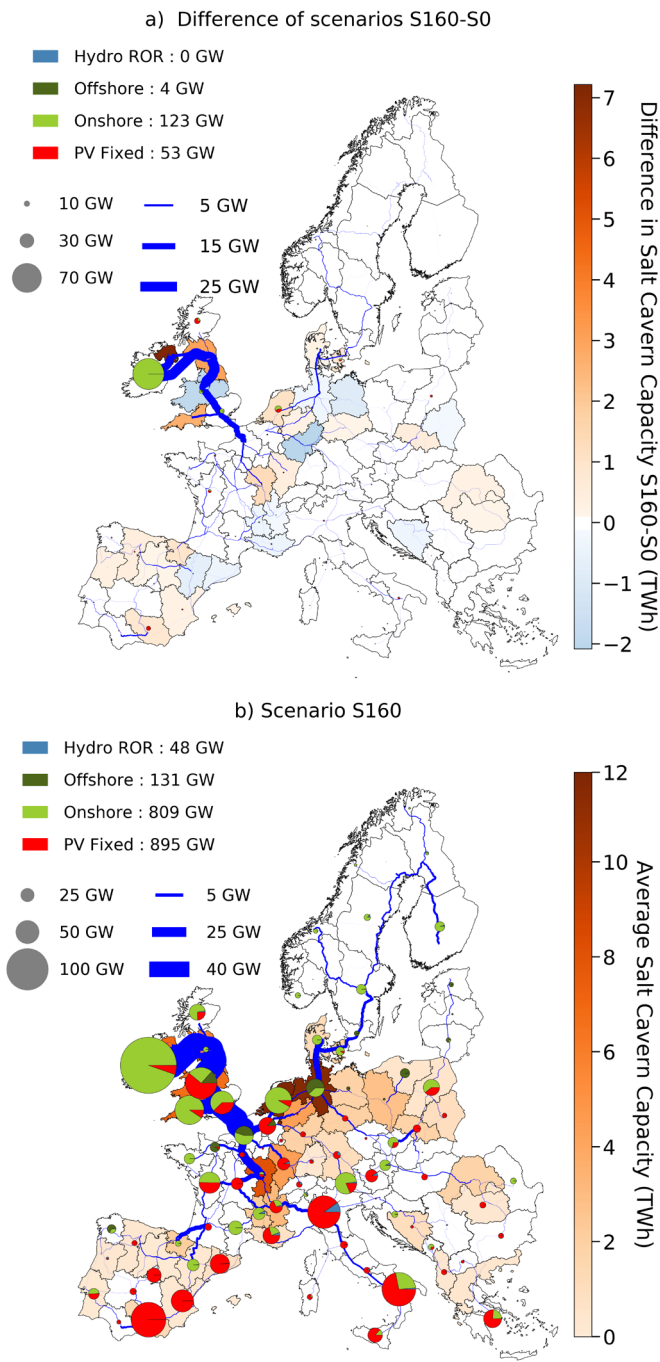


Figure 2.7. a) Difference in salt cavern capacity, RES technologies and H<sub>2</sub> pipelines across regions of Europe between scenarios S160 and S0; b) Capacity distribution in scenario S160.

Analyzing the optimal RES capacities in the two scenarios, a combination of different generation technologies is observed in the center and north of Europe, with the dominance of onshore, while in the southwest PV without tracking predominates, as explained in Caglayan et al. [15]. The main increase is produced for onshore (123 GW) and PV fixed technologies (53 GW). Onshore capacity is mainly increased in Ireland (72 GW) and lower variations are produced in the London area and the Netherlands. On the other hand, the capacity of fixed PV in the field is increased in Scotland, southeast of Spain and the Netherlands. Offshore technology only increases by 4 GW between extreme scenarios, varying only in Wales-Midlands and the north of Germany.

With respect to H<sub>2</sub> pipelines, an important growth in the capacities of Ireland, the United Kingdom and the interconnection with France can be observed in Figure 2.7a. The low cost of electricity generation in Ireland and the United Kingdom and the high full load hours (FLH) of onshore technology favor the conversion from electricity to hydrogen via electrolyzers and transportation with high-capacity pipelines to continental Europe [15]. As the H<sub>2</sub> pipeline between southern Ireland and the south of Scotland achieves the maximum established capacity (48 GW), a reinforcement of the pipeline route southern Ireland – Northern Ireland – southern Scotland is proposed.

Furthermore, the pipelines primarily reinforce their capacities in regions where hydrogen demand has increased, in this case, in the areas along the Atlantic coast where ship H<sub>2</sub> demand has been varied in the studied scenarios. However, the pipelines of other European regions also increase their capacities, as in the case of southeastern Norway or the north of Germany, to support the additional ship H<sub>2</sub> demand with cheaper commodity production.

The increase in the installed capacities (GW) between scenarios S0 and S160 of onshore and fixed PV RES technologies previously discussed can be better observed in Figure 2.8a and Figure 2.8b. Ireland, with an increase of 72.3 GW for onshore, is plotted in green and out of scale so as to be able to appreciate the variation in the remaining regions, as in the case of London, Wales-Midlands and the Netherlands. However, small variations would be required in many other regions in central and

northern Europe to support the production of electricity for  $H_2$  production in the S160 scenario.

A decrease in onshore capacity is observed in the southwest of the Iberian Peninsula and is replaced by fixed PV. This latter technology, along with the main increase in Scotland, southeastern Spain and the Netherlands, also requires minor variations in other regions in the center and south of Europe (Figure 2.8b). Furthermore, a small reduction in the fixed PV installed capacity is produced in Ireland or other regions because the model assumes that electricity can be produced more economically with onshore technology or in adjacent regions.

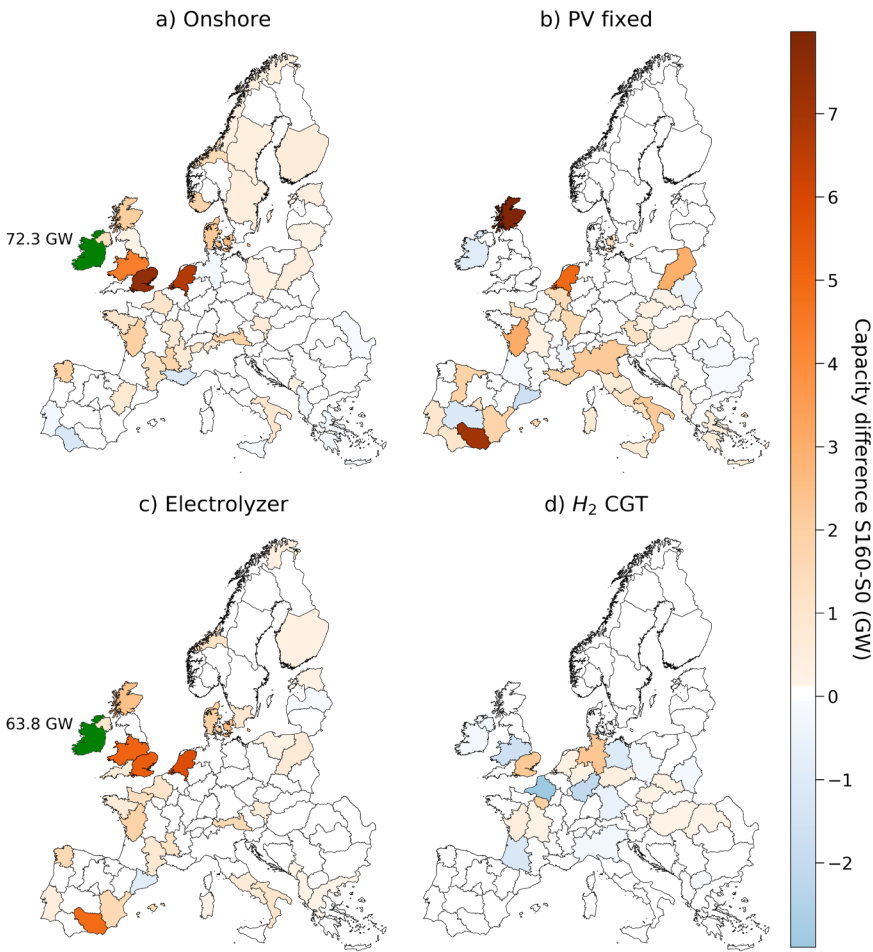


Figure 2.8. Difference in installed capacity (GW) of: a) onshore, b) fixed PV, c) electrolyzers and d)  $H_2$  CGT (CCGT+OCGT) technologies across the regions of Europe between scenarios S160-S0.

Regarding conversion technologies, scenario S160 would require installing an additional 63.8 GW of electrolyzers in Ireland (Figure 2.8c). This value is close to the onshore increase in the same region, confirming Ireland to be the main supplier of H<sub>2</sub> for ship H<sub>2</sub> demand in the Atlantic area. Moreover, electrolyzers capacity would also need to grow in the other regions, where onshore and fixed PV are further deployed to produce H<sub>2</sub> from renewable electricity, as in the case of Scotland, London, Wales-Midlands, the Netherlands and southeastern Spain. Finally, as ship H<sub>2</sub> demand increases, a small variation in the capacity of hydrogen gas turbines (CGT) is required (Figure 2.8d). The capacity increases in the south of Scotland, the Netherlands and in the London area because a higher amount of H<sub>2</sub> is generated with electrolyzers and stored in salt caverns and converted again into electricity with H<sub>2</sub> turbines. On the other hand, the installed capacity decreases in the S160 scenario in Scotland, Wales-Midlands and central Europe. This can be explained because more electricity is produced directly with the reinforcement of RES technologies.

### **2.3.2. Analysis of scenario S100**

In order to better understand the energy system, the analysis of scenario S100 in terms of the operation of different technologies in one region (Figure 2.9), the state of charge of salt caverns in another region (Figure 2.10) and electric and H<sub>2</sub> balances in two other regions (Figure 2.11 and Figure 2.12) is carried out.

In Figure 2.9, operation in the region of London in scenario S100 for the year 2050 for the onshore, fixed PV, electrolyzer and Li-Ion batteries technologies is graphed. With regard to RES, higher electricity generation with onshore technology compared to PV can be observed during fall and winter, despite daily fluctuations. A soft “eye shape” shadow (slightly wider than the PV fixed generation) of lower operation can also be perceived because wind is driven by sun energy, originating boundary layers and turbulences due to the thermal effect on land and the creation of transitions between day and night [54].



On the other hand, electrolyzers harness electricity from both onshore and fixed PV following their characteristic generation patterns throughout each day and during the year. Electrolyzers work at maximum capacity most of the time because the model has optimized their capacities to increase their FLH; however, only a small part of the energy generated is used by them, as electricity is also used to supply the demand in the London area, as well as being exported to neighboring regions.

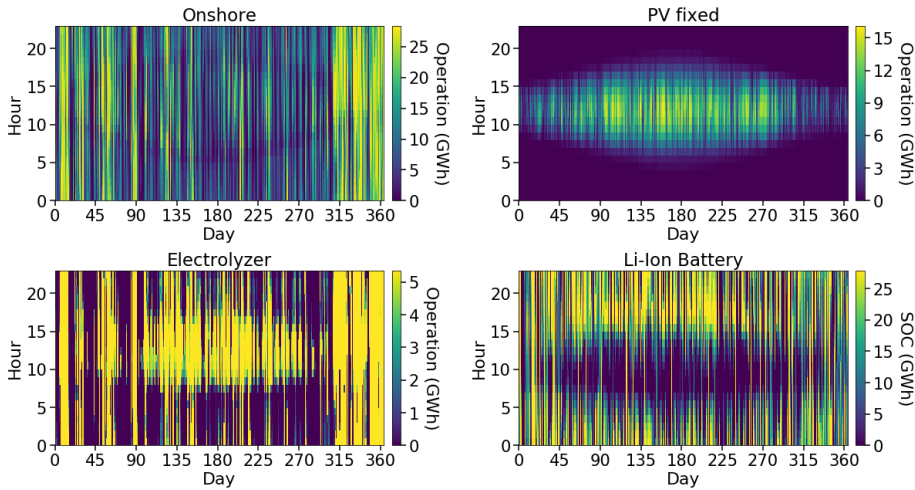


Figure 2.9. Operation of onshore, PV fixed, electrolyzer and SOC of Li-Ion batteries in GWh in the S100 scenario from the region covering London for the year 2050.

In the case of the state of charge (SOC) of Li-Ion batteries, intra-day changes are displayed with large transitions throughout the day, evidencing their use for short-term storage in order to balance electrical and hydrogen demand. In the early hours of the morning, batteries start to be discharged to supply the electricity demand and are charged again after midday with the energy coming from the sun, which is collected with PV. This cycle is repeated almost every day; however, during the first and last days of the year, the pattern is more irregular, in line with the months that have lower sun irradiance, as indicated in the fixed PV graph with the “eye shape” operation. There are some days on which batteries remain charged, as energy can be directly supplied from other sources.

In order to analyze the energy use of salt caverns, Figure 2.10 shows the evolution of the SOC throughout the year 2050 in the S100 scenario in the regions i) Basque Country – Navarre (Spain), ii) Northern Ireland and

iii) The Netherlands. In Figure 2.10a, the SOC, in terms of energy values (TWh), indicates the energy stored every day of the year, while Figure 2.10b shows the percentage of the salt cavern capacity that is filled. As can be observed, the energy stored diminishes during the spring season and the beginning of fall, due to a reduction in the energy generated with onshore and PV fixed technologies. On the contrary, at the end of the spring and during summer, the electric demand is lower (Figure 2.4) and energy generation with PV is increased (Figure 2.9), charging the salt caverns for the rest of the year. Additionally, at the end of the year, onshore generation is increased and the electric demand is still not at maximum values, enabling the storage of more H<sub>2</sub> for winter and spring.

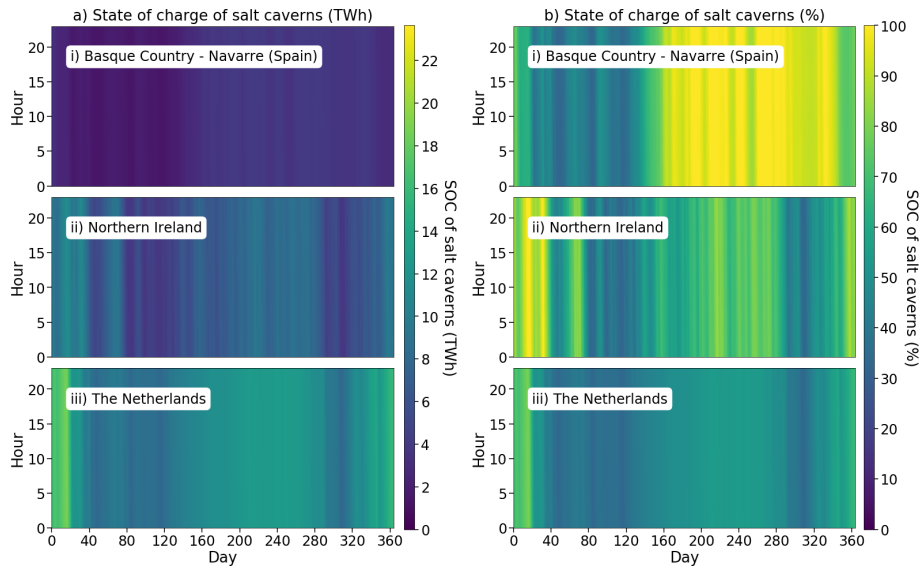


Figure 2.10. SOC of salt caverns in the regions of i) Basque Country - Navarre (Spain), ii) Northern Ireland and iii) The Netherlands in terms of TWh (a) and percentage (b) in the S100 scenario for the year 2050.

In the case of (i), the energy stored is lower than in other regions, because the maximum capacity is nearly 4 TWh (see Figure 2.7); however, during the months of summer and fall, it is nearly at full capacity with values around 100%, confirming the reasons exposed. The system designs the capacities of salt caverns in small regions in accordance with their own demands and from neighboring regions to prevent overcapacities and over costs. For that reason, the Spanish region (i) gets filled up during long periods, to cover mainly their necessities and for a few nearby regions. In

the case of Northern Ireland (ii), there is a higher installed capacity of salt caverns (11.3 TWh), but the periods with full storage are shorter than in the Spanish region, exporting  $H_2$  to other regions with lower capacities and which are not self-sufficient, as can be seen from the pipelines distribution in Figure 2.7. Finally, the Netherlands (iii) salt caverns have the highest storage capacity (23.6 TWh) in Europe, reaching around 80% of the total capacity at the beginning of winter, as can be seen in Figure 2.10b. This region mainly exports  $H_2$  to the rest of regions and provides an extra storage capacity in the center of Europe for the years with higher energy generation and lower demand, avoiding excessive curtailments.

Therefore, good optimization and distribution of the salt caverns across Europe enable the exchange of  $H_2$  between regions to fulfill the high number of sustainable ships estimated in 2050. This fact reinforces the importance of an interconnected Europe to harness the higher energy generation from regions with favorable conditions and support the regions with higher demands and lower generation capabilities.

To analyze the balance of energy production and demand, the model can calculate the hourly operation time series of all technologies in every region in terms of electric and  $H_2$  balances throughout the year 2050. In Figure 2.11 and Figure 2.12, the balances of the regions of Wales-Midlands (United Kingdom) and Ireland during the last days of May and the first ones of June are shown, respectively, as examples of the operation of individual technologies. Positive values mean the generation, production or import of electricity or  $H_2$ , while negative values indicate their consumption or export to other regions.

In Wales-Midlands (Figure 2.11), in the case of electricity, the demand is usually covered with onshore, offshore and fixed PV in the field. Nevertheless, there are some periods that utilize backup electricity production from hydropower,  $H_2$  CCGT or OCGT, or from Li-Ion batteries. In addition, importing from neighboring regions is necessary and more economically beneficial to balance the demand. There are periods in which energy generation with RES is higher than the demand, taking advantage of the energy surplus to export electricity to the neighboring regions, charge Li-Ion batteries or PHS systems or its conversion to  $H_2$  through electrolyzers. However, excess electricity is sometimes curtailed.

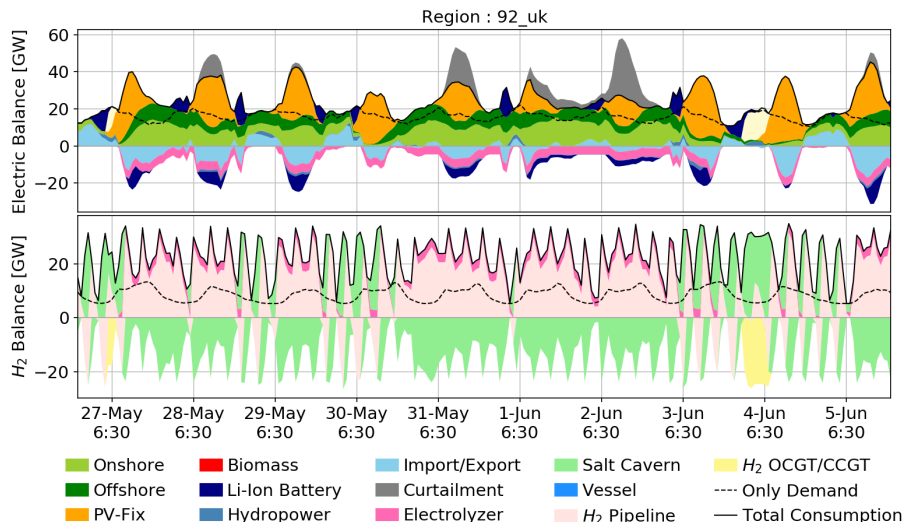


Figure 2.11. Electric (upper) and hydrogen (lower) balance with the operation of individual technologies in the Wales-Midlands (United Kingdom) region with the S100 scenario.

Analyzing the H<sub>2</sub> balance, the commodity is imported through pipelines, possibly from Ireland (Figure 2.12), and used to fulfill H<sub>2</sub> demand and store the surplus in salt caverns. As the import of gas is highly variable, salt caverns must be discharged to satisfy the demand when imports are scarce and to export it to other regions (Figure 2.10). H<sub>2</sub> produced with electrolyzers is stored in salt caverns or used to supply the demand. At certain times, imported H<sub>2</sub> or that from salt caverns is employed to generate electricity with CCGT and OCGT technologies, assisting the electricity demand. At a glance, during this period in this region, H<sub>2</sub> is primarily imported in order to increase the state of charge of the salt caverns to be used as a backup for other periods of the year.

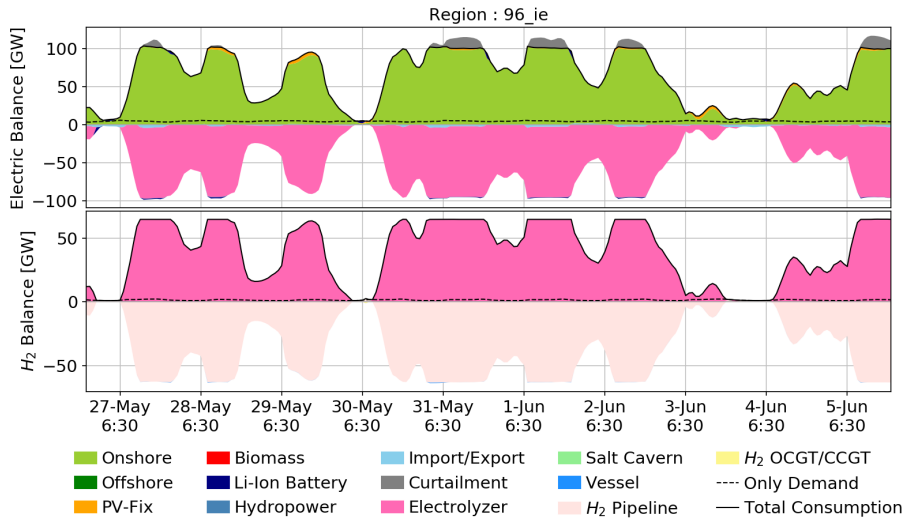


Figure 2.12. Electric (upper) and hydrogen (lower) balance with the operation of individual technologies in the Ireland region with the S100 scenario.

In Ireland (Figure 2.12), the predominant generation of electricity with onshore wind energy is apparent, with the limited addition of PV technology some days. This energy generation is mainly used to supply own demand and is converted to  $H_2$  with electrolyzers. As this region lacks salt caverns, the  $H_2$  is exported to many European regions, making it one of the main suppliers of this commodity.

Curtailments can be observed when the  $H_2$  produced with electrolyzers reaches the maximum capacity of the pipeline and vessels, which is demonstrated as flat caps in the  $H_2$  export profile. However, these capacities and the overall system were optimized by the model to achieve the minimum value of TAC, therefore providing the most feasible energy system based on RES and  $H_2$  by the year 2050. In this way, electricity and  $H_2$  demanded by ships in the Atlantic coast of Europe can be fulfilled, facilitating the transition to a more sustainable energy system.

## 2.4. Conclusions

In this chapter, an optimized 100% RES energy system infrastructure across Europe by 2050 is proposed by the model, minimizing the total annual costs and fulfilling the estimated demand for that year. The layout of the infrastructure is new, with the exception of the electrical grid, based on an estimation corresponding to the year 2030, and some RES technologies localization, e.g. hydropower plants. The electricity demand for space and heating and the hydrogen demand for FCEVs across Europe are included. In addition, the electricity and H<sub>2</sub> demands for shipping along the European Atlantic coast are considered. In order to assess the impact of ship H<sub>2</sub> demand on the European energy system, different penetration scenarios of H<sub>2</sub> demand for freight and passenger marine transport have been considered. The energy model formulated was based on the work of Caglayan et al. [15].

A predominance of H<sub>2</sub> demand from maritime transport compared to FCEV can be observed in the Atlantic coast by 2050 in most of the regions, highlighting the importance of developing the marine sector to reduce pollutant emissions. On the other hand, the higher ship electricity demand during summer has low impact over the total electricity demand in each region. Increasing hydrogen demand for shipping results in higher total annual costs and installed capacities. The main technology expansion occurs in Ireland, increasing the onshore and electrolyzer capacities by 72 GW and 64 GW, respectively. Fixed PV technology also increases its capacity in some regions to support the high H<sub>2</sub> demand from ships, especially during summer, when there is an increase in passenger transport with ferries. In contrast, the capacity of offshore technology is slightly influenced by the penetration of ship demand, varying only 4 GW between scenario S0 with zero ship H<sub>2</sub> demand and scenario S160 with 160% of the estimated ship H<sub>2</sub> demand.

As the ship H<sub>2</sub> demand increases between S0 and S160 scenarios, a reinforcement of the salt cavern storage is required, mainly in the United Kingdom, to extend the capability of balancing the energy system with higher H<sub>2</sub> demand. Salt caverns are discharged during winter and spring when the demand is high and the generation is low and charged again in summer to support the rest of the year.

Pipelines mostly increase their capacities in Ireland, the United Kingdom and the interconnection with France, which strengthens their position as the leading suppliers of energy to Europe, with low costs and high FLH for electricity generation. However, additional minor expansion in the pipeline capacities in the regions of northern Europe is required with the higher demanding scenarios for additional H<sub>2</sub> supply for ships at a lower cost.

Therefore, an appropriate infrastructure for H<sub>2</sub> generation and supply across Europe should be deployed to enable the transition to more sustainable ship transport by 2050, with a relatively low cost but with a high positive impact on the environment.

### **Nomenclature**

CCGT	Combined cycle gas turbine
CHP	Combined heat and power
FCEV	Fuel cell electric vehicle
FLH	Full load hours
GHG	Greenhouse gas
HVAC	High-voltage alternating current
HVDC	High-voltage direct current
Li-Ion	Lithium-ion
NG	Natural gas
OCGT	Open cycle gas turbine
PEM	Polymer electrolyte membrane
PHS	Pumped hydro storage
PV	Photovoltaic
RES	Renewable energy sources
ROR	Run-of-river
SOC	State of charge
SOFC	Solid oxide fuel cell
TAC	Total annual cost

## References

- [1] Child M, Kemfert C, Bogdanov D, Breyer C. Flexible electricity generation, grid exchange and storage for the transition to a 100% renewable energy system in Europe. *Renew Energy* 2019;139:80–101. doi:10.1016/j.renene.2019.02.077.
- [2] Schlachtberger DP, Brown T, Schramm S, Greiner M. The benefits of cooperation in a highly renewable European electricity network. *Energy* 2017;134:469–81. doi:10.1016/j.energy.2017.06.004.
- [3] Schlachtberger DP, Brown T, Schäfer M, Schramm S, Greiner M. Cost optimal scenarios of a future highly renewable European electricity system: Exploring the influence of weather data, cost parameters and policy constraints. *Energy* 2018;163:100–14. doi:10.1016/j.energy.2018.08.070.
- [4] Rodriguez RA, Becker S, Greiner M. Cost-optimal design of a simplified, highly renewable pan-European electricity system. *Energy* 2015;83:658–68. doi:10.1016/j.energy.2015.02.066.
- [5] Victoria M, Zhu K, Brown T, Andresen GB, Greiner M. The role of storage technologies throughout the decarbonisation of the sector-coupled European energy system. *Energy Convers Manag* 2019;201:111977. doi:10.1016/j.enconman.2019.111977.
- [6] Brown T, Schlachtberger D, Kies A, Schramm S, Greiner M. Synergies of sector coupling and transmission reinforcement in a cost-optimised, highly renewable European energy system. *Energy* 2018;160:720–39. doi:10.1016/j.energy.2018.06.222.
- [7] Cebulla F, Naegler T, Pohl M. Electrical energy storage in highly renewable European energy systems: Capacity requirements, spatial distribution, and storage dispatch. *J Energy Storage* 2017;14:211–23. doi:10.1016/j.est.2017.10.004.
- [8] Ruhnau O, Bannik S, Otten S, Praktiknjo A, Robinius M. Direct or indirect electrification? A review of heat generation and road transport decarbonisation scenarios for Germany 2050. *Energy* 2019;166:989–99. doi:10.1016/j.energy.2018.10.114.
- [9] Gils HC, Scholz Y, Pregger T, Luca de Tena D, Heide D. Integrated modelling of variable renewable energy-based power supply in Europe. *Energy* 2017;123:173–88. doi:10.1016/j.energy.2017.01.115.
- [10] Samsatli S, Staffell I, Samsatli NJ. Optimal design and operation of



- integrated wind-hydrogen-electricity networks for decarbonising the domestic transport sector in Great Britain. *Int J Hydrogen Energy* 2016;41:447–75. doi:10.1016/j.ijhydene.2015.10.032.
- [11] Robinius M, Otto A, Heuser P, Welder L, Syranidis K, Ryberg DS, et al. Linking the power and transport sectors - Part 1: The principle of sector coupling. *Energies* 2017;10. doi:10.3390/en10070956.
  - [12] Welder L, Ryberg DS, Kotzur L, Grube T, Robinius M, Stolten D. Spatio-temporal optimization of a future energy system for power-to-hydrogen applications in Germany. *Energy* 2018;158:1130–49. doi:10.1016/j.energy.2018.05.059.
  - [13] Guandalini G, Robinius M, Grube T, Campanari S, Stolten D. Long-term power-to-gas potential from wind and solar power: A country analysis for Italy. *Int J Hydrogen Energy* 2017;42:13389–406. doi:10.1016/j.ijhydene.2017.03.081.
  - [14] Tlili O, Mansilla C, Robinius M, Syranidis K, Reuss M, Linssen J, et al. Role of electricity interconnections and impact of the geographical scale on the French potential of producing hydrogen via electricity surplus by 2035. *Energy* 2019;172:977–90. doi:10.1016/j.energy.2019.01.138.
  - [15] Caglayan DG, Heinrichs HU, Robinius M, Stolten D. Robust design of a future 100% renewable european energy supply system with hydrogen infrastructure. *Int J Hydrogen Energy* 2021;46:29376–90. doi:10.1016/j.ijhydene.2020.12.197.
  - [16] Bruninx K, Orlic D, Couckuyt D, Grisey N, Betraoui B, Anderski T, et al. e-Highway 2050. D 2.1 Data sets of scenarios for 2050. 2015.
  - [17] Caglayan DG, Weber N, Heinrichs HU, Linßen J, Robinius M, Kukla PA, et al. Technical potential of salt caverns for hydrogen storage in Europe. *Int J Hydrogen Energy* 2020;45:6793–805. doi:10.1016/j.ijhydene.2019.12.161.
  - [18] Faber J, Hanayama S, Zhang S, Pereda P, Comer B, Hauerhof E, et al. Fourth IMO Greenhouse Gas Study 2020. 2021.
  - [19] Eyring V, Isaksen ISA, Berntsen T, Collins WJ, Corbett JJ, Endresen O, et al. Transport impacts on atmosphere and climate: Shipping. *Atmos Environ* 2010;44:4735–71. doi:10.1016/j.atmosenv.2009.04.059.
  - [20] Buhaug Ø, Corbett JJ, Endresen O, Eyring V, Faber J, Hanayama S, et al. Second IMO GHG Study 2009. 2009.

- [21] Ortiz A. HYLANTIC - Atlantic Network for Renewable Generation and Supply of Hydrogen to promote High Energy Efficiency 2018. <http://hylantic.com/> (accessed February 24, 2020).
- [22] e-SHyIPS Project 2021. <https://e-shyips.com/project/> (accessed November 16, 2021).
- [23] CMB.Tech. Hydroville 2021. <http://hydroville.be/en/> (accessed November 16, 2021).
- [24] Pang E. HySeas III - Realising the world's first sea-going hydrogen-powered RoPax ferry and a business model for European islands 2019. <https://www.hyseas3.eu/the-project/> (accessed February 24, 2020).
- [25] Mikkola J. FLAGSHIPS - Clean waterborne transport in Europe 2019. <https://flagships.eu/> (accessed March 6, 2020).
- [26] Global Energy Ventures. Compressed Hydrogen Ship C-H2 2021. <https://gev.com/hydrogen/> (accessed November 16, 2021).
- [27] Eurostat Database. Your key to European statistics. Eur Comm n.d. <https://ec.europa.eu/eurostat/data/database> (accessed November 25, 2019).
- [28] Welder L, Heinrichs H, Linßen J, Robinius M, Stolten D. FINE - Framework for Integrated Energy System Assessment. GitHub 2018. <https://github.com/FZJ-IEK3-VSA/FINE> (accessed February 24, 2020).
- [29] Ryberg DS, Caglayan DG, Schmitt S, Linßen J, Stolten D, Robinius M. The future of European onshore wind energy potential: Detailed distribution and simulation of advanced turbine designs. *Energy* 2019;182:1222–38. doi:10.1016/j.energy.2019.06.052.
- [30] Caglayan DG, Ryberg DS, Heinrichs H, Linßen J, Stolten D, Robinius M. The techno-economic potential of offshore wind energy with optimized future turbine designs in Europe. *Appl Energy* 2019;255:113794. doi:10.1016/j.apenergy.2019.113794.
- [31] Gelaro R, McCarty W, Suárez MJ, Todling R, Molod A, Takacs L, et al. The Modern-Era Retrospective Analysis for Research and Applications, Version 2 (MERRA-2). *J Clim* 2017;30:5419–54. doi:10.1175/JCLI-D-16-0758.1.
- [32] Ryberg DS, Caglayan DG, Schmitt S, Linssen J, Stolten D, Robinius M. RESKit - Renewable Energy Simulation toolkit for Python. GitHub Repos 2019. <https://github.com/FZJ-IEK3-VSA/RESKit> (accessed

August 21, 2020).

- [33] Vincent I, Bessarabov D. Low cost hydrogen production by anion exchange membrane electrolysis: A review. *Renew Sustain Energy Rev* 2018;81:1690–704. doi:10.1016/j.rser.2017.05.258.
- [34] Javed MS, Zhong D, Ma T, Song A, Ahmed S. Hybrid pumped hydro and battery storage for renewable energy based power supply system. *Appl Energy* 2020;257:114026. doi:10.1016/j.apenergy.2019.114026.
- [35] Crotochino F, Donadei S, Bünger U, Landinger H. Large-Scale Hydrogen Underground Storage for Securing Future Energy Supplies. 18th World Hydrog. Energy Conf. 2010 - WHEC 2010, vol. 78, Essen: 2010, p. 37–45. doi:10.1109/INTMAG.2015.7157557.
- [36] Syranidis K, Markowitz P, Linssen J, Robinius M, Stolten D. Flexible demand for higher integration of renewables into the european power system. *Int Conf Eur Energy Mark EEM* 2018;2018-June. doi:10.1109/EEM.2018.8469962.
- [37] Reuß M, Grube T, Robinius M, Preuster P, Wasserscheid P, Stolten D. Seasonal storage and alternative carriers: A flexible hydrogen supply chain model. *Appl Energy* 2017;200:290–302. doi:10.1016/j.apenergy.2017.05.050.
- [38] Reuß M, Welder L, Thürauf J, Linßen J, Grube T, Schewe L, et al. Modeling hydrogen networks for future energy systems: A comparison of linear and nonlinear approaches. *Int J Hydrogen Energy* 2019;44:32136–50. doi:10.1016/j.ijhydene.2019.10.080.
- [39] Fuel Cells and Hydrogen Joint Undertaking. A portfolio of power-trains for Europe: a fact-based analysis. The role of Battery Electric Vehicles, Plug-in Hybrids and Fuel Cell Electric Vehicles. 2010.
- [40] Khalili S, Rantanen E, Bogdanov D, Breyer C. Global Transportation Demand Development with Impacts on the Energy Demand and Greenhouse Gas Emissions in a Climate-Constrained World. *Energies* 2019;12:3870. doi:10.3390/en12203870.
- [41] Rivarolo M, Rattazzi D, Magistri L. Best operative strategy for energy management of a cruise ship employing different distributed generation technologies. *Int J Hydrogen Energy* 2018;43:23500–10. doi:10.1016/j.ijhydene.2018.10.217.
- [42] Baldi F, Ahlgren F, Nguyen T-V, Thern M, Andersson K. Energy and exergy analysis of a cruise ship. *Energies* 2018;11:1–41.

doi:10.3390/en11102508.

- [43] MariGreen - Perspectives for the Use of Hydrogen as Fuel in Inland Shipping. A Feasibility Study. 2018.
- [44] Hydrogen Council. Hydrogen Scaling Up. A sustainable pathway for the global energy transition. 2017.
- [45] ITF. Decarbonising Maritime Transport. Pathways to zero-carbon shipping by 2035. 2018.
- [46] Lloyd's Register, UMAS. Zero-Emission Vessels 2030. How do we get there? 2017.
- [47] Samadi S, Lechtenböhmer S, Schneider C, Arnold K, Fishedick M, Schüwer D, et al. Decarbonization Pathways for the Industrial Cluster of the Port of Rotterdam. 2016.
- [48] Smith T, Raucci C, Hosseinloo SH, Rojon I, Calleya J, Fuente SD La, et al. CO<sub>2</sub> Emissions from International Shipping: Possible reduction targets and their associated pathways. vol. October. 2016. doi:10.1002/yd.20075.
- [49] Abbasov F, Earl T, Calvo Ambel C, Hemmings B, Gilliam L. Roadmap to decarbonising European shipping. *Transp Environ Rep* 2018;22.
- [50] Smith TWP, Jalkanen JP, Anderson BA, Corbett JJ, Faber J, Hanayama S, et al. Third IMO Greenhouse Gas Study 2014. London: 2014. doi:10.1007/s10584-013-0912-3.
- [51] Sembler WJ, Kumar S, Palmer D. Fuel cells as an alternative to cold ironing. *J Fuel Cell Sci Technol* 2009;6:0310091–03100911. doi:10.1115/1.3006305.
- [52] Marine Traffic 2020. [www.marinetraffic.com](http://www.marinetraffic.com) (accessed May 11, 2020).
- [53] Eyring V, Isaksen ISA, Berntsen T, Collins WJ, Corbett JJ, Endresen O, et al. Transport impacts on atmosphere and climate: Shipping. *Atmos Environ* 2010;44:4735–71. doi:10.1016/j.atmosenv.2009.04.059.
- [54] Stull RB. An Introduction to Boundary Layer Meteorology. vol. 13. Dordrecht: Springer Netherlands; 1988. doi:10.1007/978-94-009-3027-8.

## Appendix

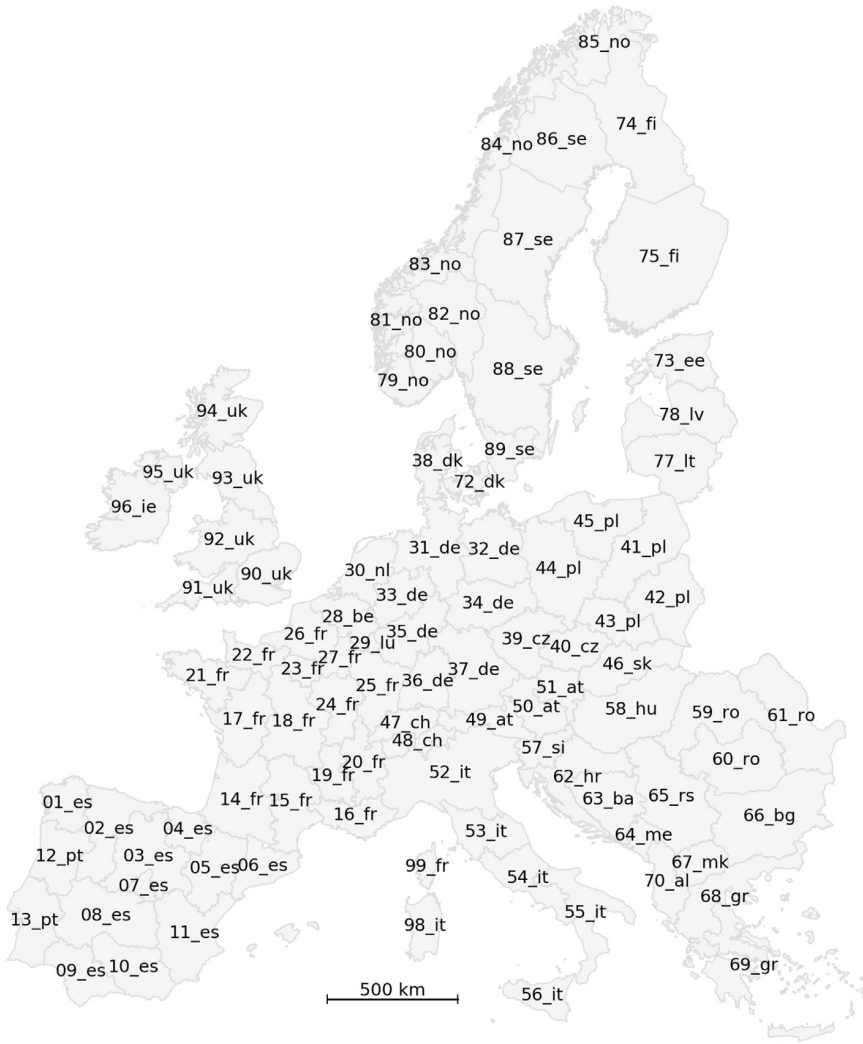


Figure A.2.1. Regional boundaries of Europe and names defined in the model [15].

Table A.2.1. Ports by region collected from Eurostat database [27] (1/3)

Spain				Portugal	
01_es	02_es	04_es	09_es	12_pt	13_pt
Ferrol	Avilés	Bermeo	Algeciras	Aveiro	Faro
La Coruña	Gijón	Bilbao	Barbate	Figueira da Foz	Lisboa
Marín-Pontevedra	Santander	Pasajes	Cádiz	Leixões	Portimão
Vigo			Huelva	Viana do Castelo	Setubal
Villagarcía (de Arosa)			Málaga		Sines
			Sevilla		

Table A.2.1. Ports by region collected from Eurostat database [27] (2/3)

France					The United Kingdom
14_fr	17_fr	21_fr	22_fr	26_fr	90_uk
Bayonne	La Rochelle	Brest	Caen	Boulogne-sur-Mer	Dover
Bordeaux	Les Sables d'Olonne	Douarnenez	Cherbourg	Dieppe	Felixstowe
		Lorient		Dunkerque	Great Yarmouth
		Nantes Saint-Nazaire		Calais	Harwich
		Roscoff		Le Havre	Ipswich
		St Malo		Rouen	London
					Medway
					Newhaven
					Portsmouth
					Ramsgate
					Shoreham
					Southampton

Table A.2.1. Ports by region collected from Eurostat database [27] (3/3)

The United Kingdom					Ireland
91_uk	92_uk	93_uk	94_uk	95_uk	96_ie
Bristol	Boston	Cairnryan	Aberdeen	Ballylumford	Bantry Bay
Fowey	Cardiff	Goole	Clydeport	Belfast	Cork
Plymouth	Fishguard	Hull	Cromarty Firth	Kilroot Power Station Jetty	Drogheda
Poole	Fleetwood	Loch Ryan Pt	Dundee	Larne	Dublin
Weymouth	Heysham	River Hull & Humber	Forth	Londonderry	Dun Laoghaire
	Holyhead	Stranraer	Glensanda	Warrenpoint	Dundalk
	Immingham	Sunderland	Kirkwall		Galway
	Liverpool	Tees & Hartlepool	Peterhead		Limerick
	Manchester	Troon	Sullom Voe		New Ross
	Milford Haven	Tyne			Rosslare Harbour
	Newport, Gwent				Waterford
	Port Talbot				
	Swansea				
	Trent River				

Table A.2.2. Freight and passenger maritime transport for each country at 2015 (Eurostat and Khalili) and 2050 (Khalili) and calculation of distance and growth coefficients.

Country	Freight				Passengers			
	2015		2050		2015		2050	
	Eurostat (M ton)	Khalili (M ton-km)	Khalili (M ton-km)	Distance (km)	Growth ratio (2050/2015)	Eurostat (M p)	Khalili (M p-km)	Growth ratio (2050/2015)
<b>UK</b>	485.50	2053793	4319620	4230	2.1	27.81	6975	5.2
<b>Ireland</b>	49.34	204276	294013	4140	1.4	2.75	521	1.1
<b>Portugal</b>	85.23	217535	269995	2552	1.2	0.58	635	1.1
<b>France</b>	293.43	1978923	3135804	6744	1.6	26.13	6224	2.9
<b>Spain</b>	447.05	1315637	1682127	2942	1.3	24.52	4156	1.6

In which 'Distance (km)' coefficient is calculated as the ratio of 'Khalili (M ton-km)' at 2015 and 'Eurostat (M ton)' for each country and transport mode. This coefficient indicates the average distance that should be multiplied to Eurostat values in '(M ton)' to obtain '(M ton-km)'.

'Growth ratio (2050/2015)' for each country and transport mode is obtained as the ratio of 'Khalili (M ton-km)' at 2050 and at 2015. This factor indicates the projected growth between both years according to Khalili et al.



Table A.2.3. Calculation of ship electricity and H<sub>2</sub> demands from Spanish ports in 2050.

	Freight						Passengers				
	2015			2050			2015		2050		
	M ton	M ton	M ton	M ton-km	GWh <sub>el</sub>	GWh <sub>H<sub>2</sub></sub>	M p	M p	M p-km	GWh <sub>el</sub>	GWh <sub>H<sub>2</sub></sub>
<b>Country</b>											
<b>Spain</b>	447.05	571.58	1681587.72	33631.7	48766.0	3131.92	24.52	39.96	6793.76	2207.97	3131.92
<b>Algeciras</b>	79.38	101.49	298572.02	5971.44	8658.59	699.01	5.47	8.92	1516.28	492.79	699.01
<b>Avilés</b>	5.11	6.53	19202.65	384.05	556.88	0.00	0.00	0.00	0.00	0.00	0.00
<b>Barbate</b>	0.00	0.00	0.00	0.00	0.00	0.00	0.00	0.00	0.00	0.00	0.00
<b>Bermeo</b>	0.25	0.31	921.58	18.43	26.73	0.00	0.00	0.00	0.00	0.00	0.00
<b>Bilbao</b>	30.98	39.60	116513.62	2330.27	3378.89	12.64	0.10	0.16	27.43	8.91	12.64
<b>Cádiz</b>	2.93	3.75	11025.07	220.50	319.73	2.94	0.02	0.04	6.37	2.07	2.94
<b>Ferrol</b>	12.76	16.31	47997.22	959.94	1391.92	0.00	0.00	0.00	0.00	0.00	0.00
<b>Gijón</b>	21.06	26.93	79214.21	1584.28	2297.21	0.00	0.00	0.00	0.00	0.00	0.00
<b>Huelva</b>	27.22	34.80	102377.76	2047.56	2968.96	4.21	0.03	0.05	9.14	2.97	4.21
<b>La Coruña</b>	13.93	17.81	52394.45	1047.89	1519.44	0.13	0.00	0.00	0.28	0.09	0.13
<b>Málaga</b>	2.25	2.87	8448.41	168.97	245.00	33.85	0.27	0.43	73.42	23.86	33.85
<b>Marín-Pontevedra</b>	2.11	2.70	7948.13	158.96	230.50	0.00	0.00	0.00	0.00	0.00	0.00
<b>Pasajes</b>	3.57	4.57	13439.97	268.80	389.76	0.00	0.00	0.00	0.00	0.00	0.00
<b>Santander</b>	5.30	6.78	19932.39	398.65	578.04	26.31	0.21	0.34	57.07	18.55	26.31
<b>Sevilla</b>	4.19	5.36	15772.13	315.44	457.39	1.79	0.01	0.02	3.88	1.26	1.79
<b>Vigo</b>	3.52	4.51	13255.66	265.11	384.41	0.00	0.00	0.00	0.00	0.00	0.00
<b>Vilagarcía (de Arosa)</b>	1.03	1.31	3855.58	77.11	111.81	0.00	0.00	0.00	0.00	0.00	0.00

Table A.2.4. Ship electricity and H<sub>2</sub> demands for each region (1/2)

	Spain				Portugal		France		
	01_es	02_es	04_es	09_es	12_pt	13_pt	14_fr	17_fr	21_fr
Annual Demand									
Electric (GWh <sub>el</sub> /y)	2509.11	2385.53	2626.42	9246.86	1525.31	3751.77	2220.24	2305.30	6919.31
H <sub>2</sub> (GWh <sub>H2</sub> /y)	3638.21	3458.44	3808.02	13391.46	2211.69	5439.55	3219.34	3342.69	10022.78

Table A.2.5. Ship electricity and H<sub>2</sub> demands for each region (2/2)

	France		The United Kingdom							Ireland
	22_fr	26_fr	90_uk	91_uk	92_uk	93_uk	94_uk	95_uk	96_ie	
Annual Demand										
Electric (GWh <sub>el</sub> /y)	948.59	33601.33	36471.89	2552.87	29848.98	13102.39	11010.44	5282.64	6062.82	
H <sub>2</sub> (GWh <sub>H2</sub> /y)	1364.51	48626.96	52642.88	3689.55	43231.80	18955.18	15964.92	7632.58	8785.17	

# **CHAPTER 3**

---

**EXPERIMENTAL PERFORMANCE OF  
LOW CARBON FUELS IN INTERNAL  
COMBUSTION ENGINES**



### 3.1. Introduction

The global deployment of internal combustion engines (ICEs) fueled with conventional fossil fuels has led to an unsustainable situation due to high emission of pollutants and high dependency on the reservoirs located in specific world regions. Therefore, the use of more environmentally-friendly alternative fuels can help to extend the life of this mature and easily accessible technology.

Hydrogen and natural gas (NG), or methane as its main constituent, have received much attention over the last few decades due to their suitable characteristics as gaseous fuels in ICEs. These gases provide several advantages compared to conventional fuels. The use of mixtures of  $H_2$  and  $CH_4$  combine their individual benefits, widening the operation range of ICEs with suitable fuel properties; this has promoted the publication of interesting reviews [1–4]. In addition, many investigations have been conducted to study the influence of the composition of  $H_2$  and  $CH_4$  mixtures on various types of ICE: spark ignition (SI) [5–12], compression ignition (CI) [13–17] and homogeneous charge compression ignition (HCCI) [18–20], as well as of different configurations of fuel injection systems and experimental conditions.

In the study of Rao et al. [21], mixtures of  $H_2$  and NG containing between 0 and 50 vol%  $H_2$  were fueled to a six-cylinder heavy-duty engine at partial load and stoichiometric conditions. Lower combustion duration and lower emissions of CO and hydrocarbons (HC) were reported when higher  $H_2$  percentages were used; but NO<sub>x</sub> emissions were increased. Earlier spark timings contributed to raise NO<sub>x</sub> emissions, reducing the available oxygen for complete combustion, increasing also CO and hydrocarbon emissions. In contrast, higher exhaust gas recirculation (EGR) ratios increased the combustion duration and reduced the NO<sub>x</sub>, CO and hydrocarbon emissions [21].

Hora et al. [22] tested mixtures of hydrogen-enriched compressed natural gas (HCNG) containing between 0 and 30 vol%  $H_2$  in a port fuel single-cylinder spark ignition (SI) engine at 1500 rpm. With higher  $H_2$  fractions and loads, the brake thermal efficiency ( $\eta_t$ ) increased and the specific fuel consumption and HC, CO and CO<sub>2</sub> emissions were reduced. Mixtures up to 30 vol%  $H_2$  were also used by Kahraman et al. [23] in a four-cylinder SI engine. The higher  $H_2$  content of the fuel also raised the  $\eta_t$

and reduced HC, CO and CO<sub>2</sub> emissions. HC values showed a minimum at  $\lambda = 1.2$ , then they were increased for higher air-fuel ratios due to the reduction of the mixture flammability. On the contrary, mixtures up to 20% of CH<sub>4</sub> were analyzed in a four-cylinder port-fuel SI engine in the study of Diéguez et al. [24]. A reduction in  $\eta_t$  and an increase in specific emissions of HC, CO and NO<sub>x</sub> were observed as the percentage of CH<sub>4</sub> in the mixture was raised.

In addition to H<sub>2</sub> – CH<sub>4</sub> mixtures, industrial residual waste streams with high H<sub>2</sub> and CH<sub>4</sub> percentages can be also employed as fuels in ICEs, harnessing their energy content. Cleaned coke oven gas (COG), as explained in **Chapter 1**, is generated in the coke industry after extracting valuable components such as tar, light oil, sulfur and ammonia. This waste stream can be used as fuel in stationary ICEs coupled to the plants where it is produced due to its interesting composition and its high volumetric flow generated per ton of coke (360 – 518 Nm<sup>3</sup>/ton coke) [25]. The typical composition of COG consists of around 90 vol% of combustible gases (H<sub>2</sub>, CH<sub>4</sub> and CO), and the rest are inert gases: (N<sub>2</sub>, CO<sub>2</sub>) and small traces of other compounds [26,27].

Regarding compression ignition engines, COG was compared with pure H<sub>2</sub> and producer gases (constituted of CO, H<sub>2</sub>, CH<sub>4</sub>, CO<sub>2</sub> and N<sub>2</sub> and generated from gasification of organic material at relatively low temperatures) with different H<sub>2</sub> percentages adding a pilot amount of diesel for all the gases in a supercharged dual-fuel engine [28,29]. As the H<sub>2</sub> content was increased, higher efficiency but lower output power and emissions were recorded because leaner air-fuel mixtures were required to avoid knocking, observing an important influence of the air-fuel ratio and the timing of the pilot diesel injection.

In the case of SI engines, gas mixtures similar to COG were compared with other synthesis gases with different compositions in a port-fuel single-cylinder SI engine [30,31]. Results showed the good combustion stability of the gas mixture similar to COG and the good anti-knock properties of CH<sub>4</sub>, CO and CO<sub>2</sub> constituents [30]. Knocking was also reduced in a similar way by diluting the fuel mixture with EGR or by leaning the air-fuel mixture with excess of air [31].

On the other hand, a synthetic mixture composed of 55% of H<sub>2</sub> and 45% NG was used as a methanized COG and compared with NG and a

mixture with 30%  $H_2$  and 70% of NG in a turbocharged six-cylinder SI engine [32]. The methanized COG mixture presented higher efficiency and  $NO_x$  emissions than the other fuels but produced lower torque and emissions of CO and HC; in addition, the optimum  $\lambda$  increased at higher loads.

The main purpose of this chapter is to investigate the feasibility of using hydrogen-rich waste streams such as COG in SI engines at the industries where they are produced, harnessing their energy content in a sustainable way. Despite the interesting research works previously mentioned that focused on the study of COG as alternative fuel, there is no study on the assessment of the performance of ICEs when a mixture with the real composition of clean COG is used at different engine speeds and air-fuel ratios. Therefore, the main novelty of this work is the use of a gas mixture with a typical composition of COG waste stream that can be produced in a coke manufacture plant as engine fuel. The SI engine was operated at wide open throttle (WOT) and optimum spark advance to obtain maximum brake torque (MBT), varying  $\lambda$  and the engine speed to reach the optimum operating conditions.

This study is aimed to help the interested industries to take advantage of this opportunity according to the ICE and generator system available to achieve efficient electricity generation with low pollutant emissions. To further understand the behavior of the COG waste stream composition and the benefits that this fuel can provide, a comparison with pure  $H_2$  and pure  $CH_4$  gaseous fuels is carried out because they are the key components of COG.

## **3.2. Methodology**

### **3.2.1. Test bench**

The experiments collected in this chapter have been carried out in the facilities of the Laboratory of Internal Combustion Engines of the Public University of Navarre (UPNA) within the framework of a collaboration. The test bench and the engine used were previously adapted to work with gaseous fuels, as described in detail in Sopena et al. [33].

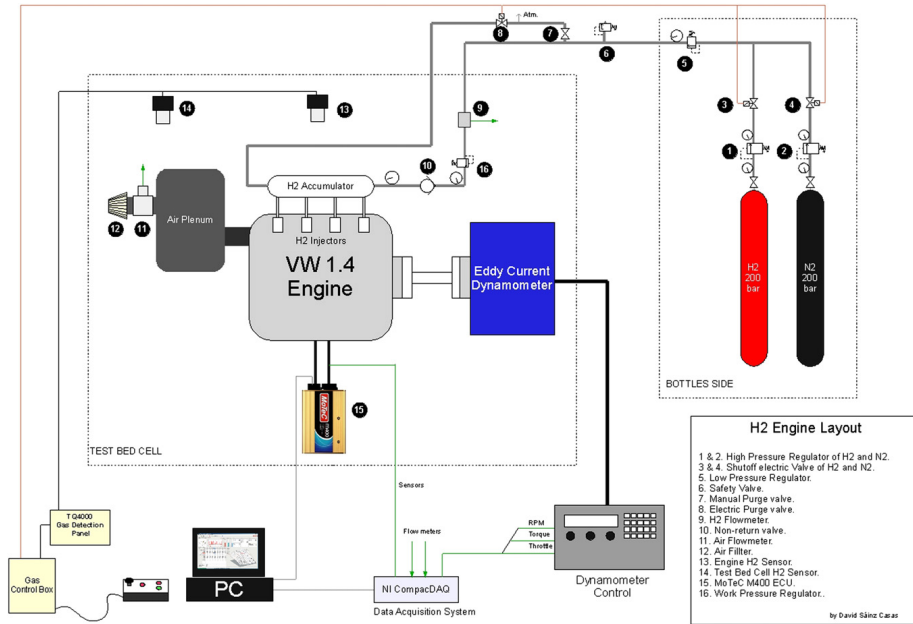


Figure 3.1. Scheme of experimental test bench [33].

In summary, as can be observed in Figure 3.1, the test bench was composed of an eddy current dynamometer AVL 80 with a BME 300 control unit to control the torque, the accelerator position and the engine speed. A Bosch ETT 008.31 analyzer was used for CO<sub>2</sub> ( $\pm 0.1\%$ ), CO ( $\pm 0.001\%$ ) and HC ( $\pm 2$  ppm) emission measurement and a Horiba MEXA-720NOx for NOx ( $\pm 30$  ppm) quantification in the exhaust gases. The gas and air mass flow rates were measured with a precision of  $\pm 0.5\%$  with Bronkhorst flow meters. In addition, the data acquisition system was based on three modules of a National Instruments Ni-CompacDAQ and was connected to a LabView program in a computer, which collected and showed real-time information of the equipment [33].

Regarding the ICE, a Volkswagen Polo 1.4L naturally aspirated port-fuel spark ignition engine with four cylinders in line was employed, with the specifications shown in Table 3.1. The four-stroke engine is characterized by a compression ratio of 10.5:1 with a pent-roof chamber and a double overhead camshaft (DOHC) configuration, employing two inlet valves and two exhaust valves per cylinder. Running on gasoline, the maximum brake power (MBP) and maximum brake torque (MBT) reached were 59 kW at 5000 rpm and 132 Nm at 3800 rpm, respectively.



Table 3.1. Specifications of the original engine from UPNA (adapted from [33]).

Base vehicle	Volkswagen Polo 1.4
Type	Spark Ignition
Original fuel	Gasoline 95 NO
Cylinder line/head material	Aluminum
Number of cylinders	4 in line
Bore/Stroke (mm)	76.5/75.6
Swept volume (cm <sup>3</sup> )	1390
Compression ratio	10.5:1
Valve train configuration	DOHC
Number of valves per cylinder	4
Fuel injection system	Port-injection
Ignition system	Single spark ignition coil
Maximum brake power	59 kW at 5000 rpm
Maximum brake torque	132 Nm at 3800 rpm

The main ICE modifications to be fueled with gaseous fuels were the integration of a metallic gas accumulator to maintain constant pressure for gas injection, a cast manifold to prevent the breakdown in case of backfire and Quantum PQ2-3200 gas injectors. The accumulator had a second input connected to a venting line to purge the complete circuit with nitrogen gas in case of emergency or long-term shutdown. Besides, the original electronic control unit was replaced by a programmable MoteC M 400 to calibrate the sensors and actuators and to introduce the injection and ignition timing maps desired for each fuel. Moreover, a wideband lambda sensor Bosch LSU 4.6 was employed instead of the original sensor to operate at lean mixtures. In addition, the three-way catalyst (TWC) was removed from the exhaust because the operation at lean fuel mixtures with low reducing chemical species in the exhaust gases reduces the efficiency of the TWC system [33].

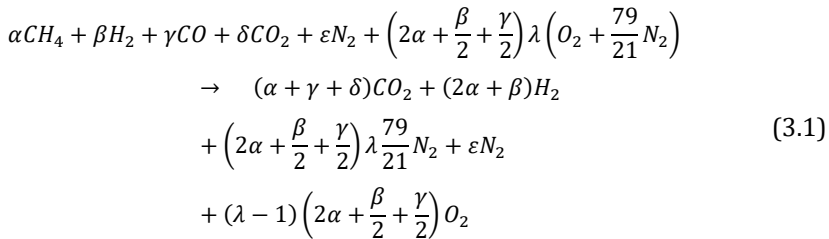
### 3.2.2. Fuel gases

The experiments have been carried out with pure hydrogen ( $\geq 99.8\%$ ), pure methane ( $\geq 99.5\%$ ) and a synthetic gas mixture of coke oven gas with the composition indicated in Table 1.2; gas cylinders were purchased to Nippon Gases Spain. Gaseous fuels were stored in gas cylinders of 50 L at 200 bar, feeding the test bench with two pressure reduction stages. In the first stage, a high-pressure regulator connected to the gas cylinders reduces the pressure to 9 bar. In the second stage, a low-pressure regulator connected to the gas accumulator added to the engine reduces the pressure to 3 bar, suitable for the fuel injectors [24].

The relative  $\lambda$ , calculated in Equation (1.9), is defined as the actual air-fuel ratio ( $\lambda_{real}$ ) in the mixture divided by the stoichiometric air-fuel ratio ( $\lambda_{st}$ ) for that fuel. The latter one is calculated with the stoichiometric reaction of the fuel with oxygen.

$$\lambda = \frac{\lambda_{real}}{\lambda_{st}} = \frac{\frac{\dot{m}_{air}}{\dot{m}_f}}{\lambda_{st}} \quad (1.9)$$

To calculate the  $\lambda_{st}$  of COG, the general chemical reaction for the complete combustion of 1 mol of COG for a given air-fuel ratio ( $\lambda$ ) value is expressed in Equation (3.1).



The parameters  $\alpha$ ,  $\beta$ ,  $\gamma$ ,  $\delta$  and  $\varepsilon$  are factors multiplying the stoichiometric coefficients that correspond to the volumetric percentages of the composition of COG shown in Table 1.2 ( $\alpha = 0.3$ ,  $\beta = 0.57$ ,  $\gamma = 0.06$ ,  $\delta = 0.02$ ,  $\varepsilon = 0.05$ ) and  $\lambda$  is the specific operating condition value. For the cases of pure gases ( $H_2$  and  $CH_4$ ), a null value for the parameters of the components not found in the fuels is given. In the case of  $H_2$ ,  $\beta = 1$  and the rest of parameters ( $\alpha$ ,  $\gamma$ ,  $\delta$  and  $\varepsilon$ ) are zero; in contrast, for  $CH_4$ , all the parameters are zero ( $\beta$ ,  $\gamma$ ,  $\delta$  and  $\varepsilon$ ) and  $\alpha = 1$ .

### 3.2.3. Experimental methods

The study of pure  $H_2$ , pure  $CH_4$  and synthetic COG has been conducted through experiments at a wide speed range from 2000 to 5000 rpm and WOT for full load with maximum air inlet flow (Table 3.2). The spark advance was selected to obtain the MBT in each working condition. The  $\lambda$  range was varied between 1 and 2. However,  $\lambda$  values for  $H_2$  were set at 1.5 and 2 to avoid the risk of combustion anomalies such as pre-ignition, backfire and knocking with fuel-rich mixtures [34]. In the case of  $CH_4$ ,  $\lambda$  is limited to 1 and 1.5 due to poor combustion at leaner compositions increasing emissions of unburnt methane. On the other hand, COG combines the advantages of both pure fuel gases extending the range of operation from 1 to 2. The good knocking resistance of  $CH_4$  allowed the reduction of air-fuel ratio for COG without abnormal combustion phenomena except at 5000 rpm for  $\lambda = 1$ . Additionally, the higher volumetric lower heating value (LHV) of  $CH_4$  constituent increased the power performance of COG. In contrast, the wider flammability range of  $H_2$  component with a higher laminar flame speed enabled burning the fuel gas at lean  $\lambda$  ratios.

Table 3.2. Experimental test conditions for  $H_2$ ,  $CH_4$  and COG.

Fuel	$\lambda$	Speed (rpm)	Spark advance	Load
$H_2$	1.5 , 2	2000 – 5000	Optimum	WOT
$CH_4$	1 , 1.5	2000 – 5000	Optimum	WOT
COG	1 , 1.5 , 2	2000 – 5000	Optimum	WOT

For the experiments with COG ( $\lambda = 1.5$ ) at 5000 rpm and COG ( $\lambda = 1$ ) at the whole range of engine speeds, the fuel gas injection pressure was increased to 4 bar instead of 3 bar, pressure used in the rest of the experiments, because the gas injectors were not able to inject the required COG volume at those operating conditions. Even though, the engine was able to reach stoichiometric  $\lambda$  conditions up to 4000 rpm.

### 3.3. Results and discussion

The performance of the ICE was tested in terms of brake mean effective pressure, power, thermal efficiency and specific energy consumption for each gas. On the other hand, emissions of NO<sub>x</sub>, HC, CO and CO<sub>2</sub> were collected at the engine exhaust, analyzed, and calculated per energy unit (g/kWh) to normalize the results.

#### 3.3.1. Engine performance

The performance comparison of the three gases has been carried out at optimum spark advance and WOT to achieve the MBT, and hence, the highest power values at each test condition. Figure 3.2 shows the spark advance in crank angle degrees (CAD) BTDC for pure H<sub>2</sub>, pure CH<sub>4</sub> and COG varying the engine speed between 2000 and 5000 rpm and  $\lambda$  values between 1 and 2. In the case of COG at  $\lambda = 1$ , only 4000 rpm were reached due to abnormal combustion at higher speeds.

As the H<sub>2</sub> concentration in the fuel increases, the spark advance angle decreases because of the higher laminar flame speed ( $S_L$ ) and therefore, improved chemical reactivity of the mixture and lower combustion duration [2,35]. This effect can be observed through the lower advance of pure H<sub>2</sub> and COG compared to pure CH<sub>4</sub>. Also, COG requires a higher spark advance than pure H<sub>2</sub> for the same  $\lambda$  due to the presence of inert gases, as well as CO and CH<sub>4</sub> (Table 1.2). In addition, lean air-fuel mixtures (high  $\lambda$ ) entail increased spark advance to burn the high air percentage in the combustion chamber [33].

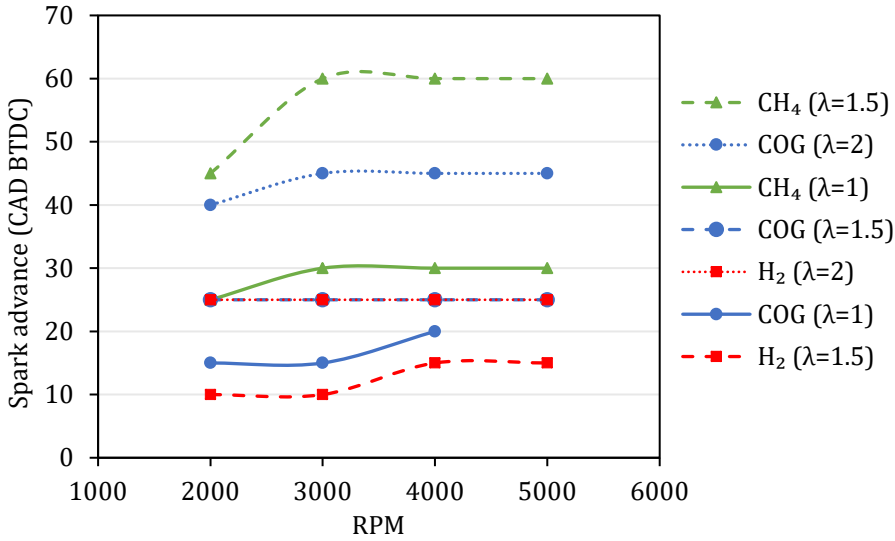


Figure 3.2. Spark advance angle (CAD BTDC) versus engine speed (rpm) of H<sub>2</sub> (red squares), CH<sub>4</sub> (green triangles) and COG (blue dots) at WOT and different  $\lambda$  values.

In general, at low speeds, the required spark advance angle becomes lower because there is a longer period of time available to burn the air-fuel mixture, meanwhile at higher speeds, the period of time available for the same angle is lower, requiring a higher spark advance to compensate this fact.

In order to assess the engine performance, the brake mean effective pressure (BMEP) parameter (in kPa) is typically used, employing the brake power in the Equation (1.5). This parameter removes the dependency on the engine size by dividing the work obtained per cycle by the cylinder volume displaced ( $V_d$ , in m<sup>3</sup>), and is calculated with Equation (3.2) [36].

$$BMEP = \frac{P_b \cdot n_R}{N \cdot V_d} \quad (3.2)$$

Figure 3.3 shows the engine BMEP using the three fuels considered versus the engine speed at the different  $\lambda$  conditions and WOT. For  $\lambda$  values higher than 1, COG provides greater BMEP than pure H<sub>2</sub> and pure CH<sub>4</sub>, thanks to the higher volumetric LHV (17.41 MJ/m<sup>3</sup>) than that of H<sub>2</sub> (10.65 MJ/m<sup>3</sup>), and higher  $S_L$  (0.68 – 0.88 m/s) than for CH<sub>4</sub> (0.38 m/s). Operating at  $\lambda = 2$ , the difference between COG and H<sub>2</sub> is very small, possibly due to the diluent effect of air. However, in the case of  $\lambda = 1$ , the

performance of pure  $\text{CH}_4$  prevails over COG because the latter has a high composition in weight percentage of inert gases,  $\text{N}_2$  and  $\text{CO}_2$ , decreasing the LHV and the effective power, and therefore, reducing the  $\eta_t$  of the engine. Comparing  $\text{H}_2$  and  $\text{CH}_4$ , at  $\lambda = 1.5$ , the former gas supplies higher BMEP taking advantage of the higher  $S_L$  and the wider flammability range.

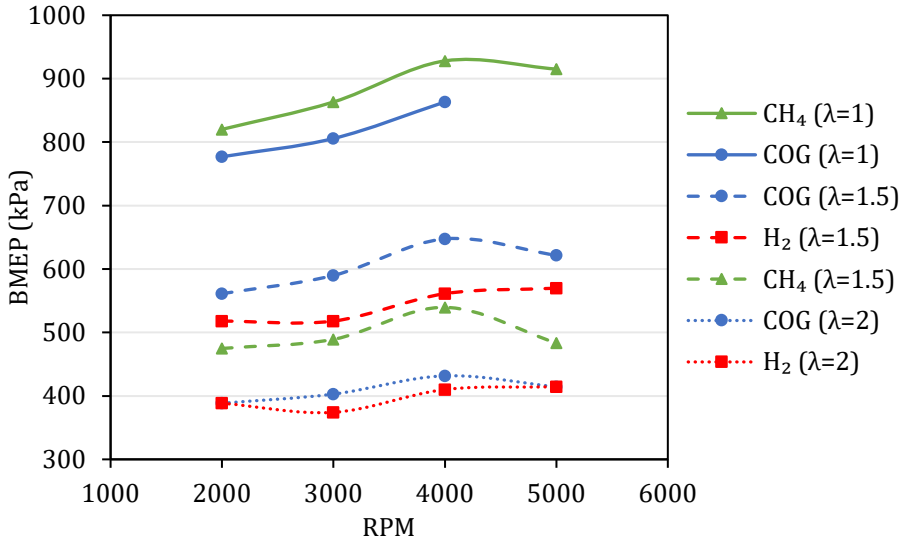


Figure 3.3. BMEP (kPa) versus engine speed (rpm) of  $\text{H}_2$  (red squares),  $\text{CH}_4$  (green triangles) and COG (blue dots) at WOT and different  $\lambda$  values.

A higher percentage of  $\text{H}_2$  in the fuel provides a more stable combustion, decreasing the variation of the BMEP values throughout the range of speeds [37]. For COG and  $\text{CH}_4$  at every  $\lambda$  condition, the maximum BMEP value is reached at 4000 rpm, meanwhile, for pure  $\text{H}_2$  the greatest BMEP value is obtained at 5000 rpm.

Regarding the engine power with the three gaseous fuels at different engine speeds and varying  $\lambda$ , the most important factor is the  $\lambda$  ratio, as can be highlighted in Figure 3.4. As the mixture becomes leaner, the power decreases due to the excess of air which reduces the combustion temperature and the heat released.

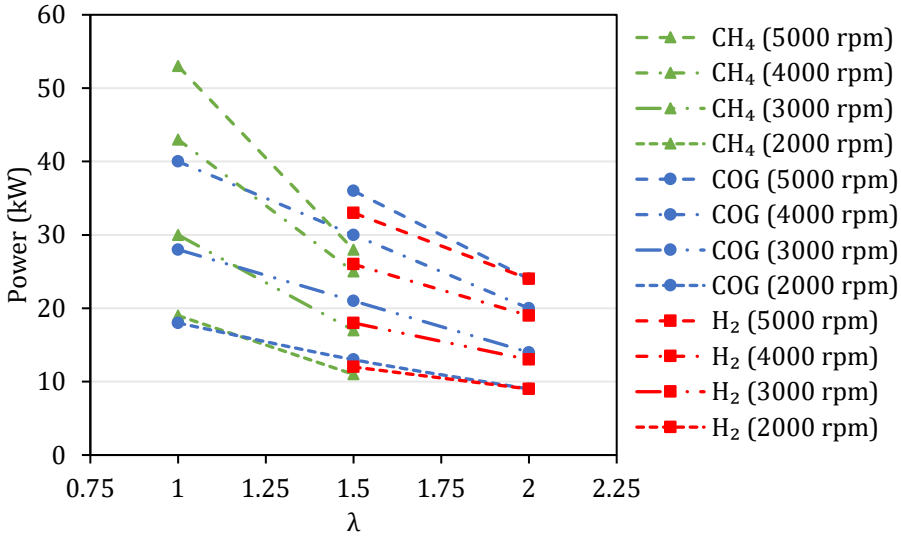


Figure 3.4. Power (kW) versus air-fuel ratio ( $\lambda$ ) of H<sub>2</sub> (red squares), CH<sub>4</sub> (green triangles) and COG (blue dots) at different engine speed values and WOT.

At  $\lambda = 1$ , CH<sub>4</sub> prevails over COG on the whole range of speeds, increasing the difference as the engine speed rises. In the case of  $\lambda = 1.5$ , COG dominates over pure H<sub>2</sub> and pure CH<sub>4</sub> at each engine speed, especially in the high part of the range. However, H<sub>2</sub> performs similar to CH<sub>4</sub> at that air-fuel ratio, except in the case of 5000 rpm, where the power difference increases due to the steeper slope of CH<sub>4</sub> at that speed. On the other hand, at  $\lambda = 2$ , COG power results are very similar to pure H<sub>2</sub>, widening the difference at medium speeds.

In order to study the engine efficiency, the thermal efficiency ( $\eta_t$ ) parameter relates the ratio of the power obtained and the energy of the fuel required, as calculated with Equation (1.8).

$$\eta_t = \frac{1}{SFC \cdot LHV} = \frac{P}{\dot{m}_f \cdot LHV} \quad (1.8)$$

Figure 3.5 shows the  $\eta_t$  of the three gases under consideration at different engine speeds and  $\lambda$  values. As observed in Equation (1.8), with a specific fuel energy quantity introduced in the cylinder, higher brake power values rise the thermal efficiency. In addition, for constant power generation, a lower volumetric LHV increases  $\eta_t$  because the same amount of power can be provided with a lower energy content fuel.

In this case, comparing the three gases at  $\lambda = 1.5$  and 4000 rpm, increase in the efficiency by 7.0% and 10.3% is obtained with COG compared to pure  $H_2$  and pure  $CH_4$ , respectively. Although the volumetric LHV of COG is an intermediate value between those of  $CH_4$  and  $H_2$ , the power (and hence, BMEP) achieved is higher at that  $\lambda$  (Figure 3.4), predominating in the ratio of  $\eta_t$ . Comparing  $H_2$  and  $CH_4$  at  $\lambda = 1.5$ , the former has lower volumetric LHV and higher power is achieved than with the latter, following the trend previously explained. Despite the fact that a lower power value is achieved at  $\lambda = 1$  with COG than with  $CH_4$ , the first one has half the value of LHV by volume (Table 1.3), predominating in a significant way in  $\eta_t$ . In the case of  $\lambda = 2$  with  $H_2$  and COG,  $H_2$  has lower brake power and lower volumetric LHV than COG, reducing  $\eta_t$ .

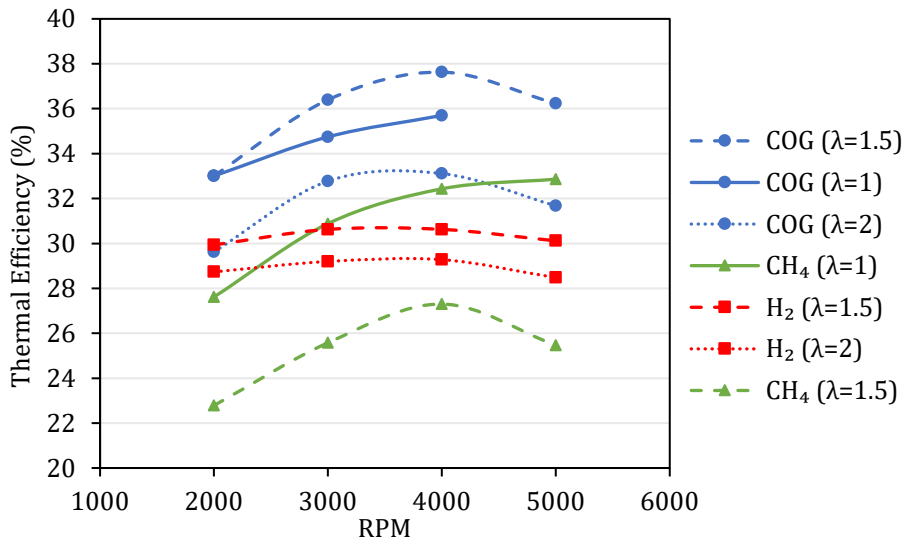


Figure 3.5. Thermal efficiency ( $\eta_t$ ) versus engine speed (rpm) of  $H_2$  (red squares),  $CH_4$  (green triangles) and COG (blue dots) at different  $\lambda$  values.

Considering each fuel individually, lower  $\lambda$  leads to greater  $\eta_t$  because the power delivered increases significantly while the fuel energy required rises in a minor proportion. However, there is an exception for COG, providing the maximum  $\eta_t$  at  $\lambda = 1.5$  and decreasing for richer mixtures ( $\lambda = 1$ ) due to incomplete combustion because there is less oxygen available in the combustion chamber [38–41]. With fuel lean mixtures (high  $\lambda$  values) the efficiency also decreases due to the less stable combustion [2,39,40].



Regarding the effect of the engine speed, the maximum efficiency is achieved at 4000 rpm for all the gases except in the case of  $\text{CH}_4$  ( $\lambda = 1$ ), that is reached at 5000 rpm. This dependence of  $\eta_t$  on the engine speed can be harnessed by the industries interested on using the clean COG waste stream in ICEs to generate electricity coupling the engine to the generator with systems like power electronics or continuous variable transmission (CVT) systems [42,43]. These devices allow maintaining constant the current frequency produced and at the same time operate the engine at optimal conditions with higher power output and lower fuel consumption.

In the case of  $\text{H}_2$ , a small variation of the  $\eta_t$  curves is observed throughout the whole range of engine speeds, revealing higher combustion stability due to complete combustion, in good accordance with the literature [37,44].

On the other hand, Figure 3.6 graphs the specific energy consumption (SEC, in MJ/kWh) at WOT and different  $\lambda$  values varying the engine speed. The SEC, calculated with Equation (3.3), represents the amount of total fuel energy that is needed to produce 1 kW of power during 1 h of operation in the engine [13]. A reverse relationship can be observed between  $\eta_t$  and SEC curves, following the same trends.

$$SEC = \frac{LHV \cdot Q_f \cdot 60}{P \cdot V_m \cdot 1000} \quad (3.3)$$

In which  $P$  is the brake power (kW),  $V_m$  is the standard molar volume (22.71 L/mol at 273.15 K and 1 bar),  $Q_f$  is the volumetric fuel flow rate (L/min) and LHV is in kJ/mol. Although  $\text{H}_2$  has a higher  $Q_f$  than  $\text{CH}_4$  due to its low density, its lower LHV (241.91 kJ/mol) and higher power output at  $\lambda = 1.5$  reduce the SEC result compared to  $\text{CH}_4$ . On the other hand, COG, with intermediate  $Q_f$  and LHV (395.50 kJ/mol) but with the highest power output (Figure 3.4), provides the lowest values of SEC at that  $\lambda$ .

If  $\text{CH}_4$  and COG are compared at  $\lambda = 1$ , methane gets closer to COG curve as the power delivered by the former is greater than the latter; however, the lower LHV of COG (the half than  $\text{CH}_4$ ) prevails, reducing its SEC value. In contrast, in the case of  $\lambda = 2$ , although COG has higher LHV than  $\text{H}_2$ , COG delivers more power and needs less  $Q_f$ , predominating in this case.

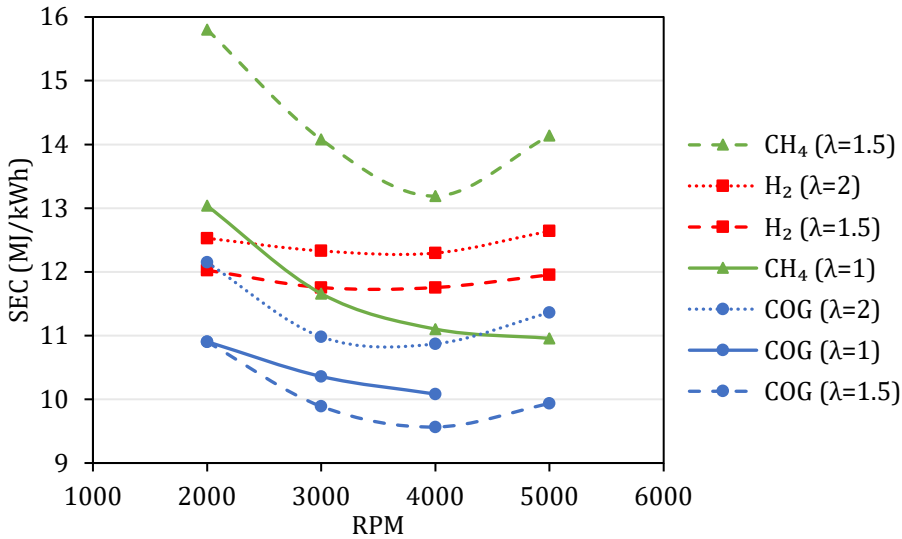


Figure 3.6. Specific energy consumption (SEC, in MJ/kWh) versus engine speed (rpm) of H<sub>2</sub> (red squares), CH<sub>4</sub> (green triangles) and COG (blue dots) at different  $\lambda$  values.

As the  $\lambda$  ratio increases, the SEC value increases as well because even though lower fuel volume is injected at higher  $\lambda$ , the power is significantly reduced, and therefore, more energy contained in the fuel is required per unit of mechanical energy delivered. However, in the case of COG, the minimum SEC values are obtained at  $\lambda = 1.5$  and they increase for richer mixtures because there is less excess of oxygen available with  $\lambda = 1$ , causing a less efficient combustion and more fuel is consumed to give the same amount of mechanical energy [45,46].

Regarding the effect of the engine speed, the minimum SEC value is reached at 4000 rpm for all the gases except in the case of CH<sub>4</sub> ( $\lambda = 1$ ), achieved at 5000 rpm. This effect is the opposite of the one commented for  $\eta_t$ . Furthermore, as mentioned before (Figure 3.5), the higher combustion stability of H<sub>2</sub> in the whole range of speeds is also proven in the almost constant values of SEC, with a variation around 3% between the lowest and highest values.

With the analysis of the performance results carried out, the importance of  $\lambda$  and the engine speed working at MBT and WOT is highlighted, obtaining for this engine the greatest BMEP value at  $\lambda = 1$  and 4000 rpm for COG. However, higher  $\eta_t$  and lower SEC are achieved at  $\lambda = 1.5$  and 4000 rpm. Therefore, industry stakeholders interested in using

this waste stream in ICEs have the option of working at higher power values or with higher efficiency performance reducing the fuel consumption. In these cases, to operate at a speed different than the one used with conventional generators, a power electronics system or a CVT device is necessary to adapt the engine speed to the desired electricity frequency given as output by the generator.

### 3.3.2. Emissions

Once the performance and efficiency of the combustion of the gaseous fuels have been described, the specific NO<sub>x</sub>, HC, CO and CO<sub>2</sub> emissions are discussed in what follows. Specific emissions were calculated according to Equation (3.4) (written for the case of NO<sub>x</sub>) [24].

$$sNO_x = \frac{60 \cdot 10^{-6}}{V_m} \cdot \frac{Q_f \cdot N_e \cdot M_{NO_x} \cdot C_{NO_x}}{P} \quad (3.4)$$

Where the specific emissions of NO<sub>x</sub> ( $sNO_x$ ) are in g/kWh,  $N_e$  are the exhaust moles formed assuming complete combustion of 1 mol of fuel with Equation (3.1),  $M_{NO_x}$  (g/mol) is the molecular weight of the gas (assumed as 30 g/mol considering the main product is NO) and  $C_{NO_x}$  (ppm) is the concentration of NO<sub>x</sub> in the exhaust. For HC, CO and CO<sub>2</sub> pollutants, the exhaust measurements have been done on dry gases and the exponent “-6” in Equation (3.4) is changed to “-2” because they are measured in “%” instead of “ppm”.

The  $sNO_x$  measured in the exhaust is shown in Figure 3.7. These emissions depend mainly on the temperature reached during combustion and the concentration of the reactants (N<sub>2</sub> and O<sub>2</sub>) in the air-fuel mixture, as it is well known with the extended Zeldovitch model [24]. The experiments carried out in the literature show that in the case of working at constant spark timing, the  $sNO_x$  emissions are increased with higher H<sub>2</sub> content in the mixture at the same  $\lambda$  value [22,24,47–49]. However, if the spark timing is optimized to obtain the MBT, the specific NO<sub>x</sub> emissions are similar or even lower with higher H<sub>2</sub> contents at the same  $\lambda$  value and speed than leaner mixtures [24,48]. With high H<sub>2</sub> contents, the optimum spark timing is retarded (Figure 3.2), reducing the work in the compression stroke and decreasing the combustion temperature, and hence, reducing NO<sub>x</sub> emissions. Hoekstra et al. [47] and Shudo et al. [50]

also prove that as the spark timing is delayed, the NO<sub>x</sub> emissions are reduced. Therefore, a trade-off between higher NO<sub>x</sub> emissions with higher H<sub>2</sub> contents and reduced emissions due to the delayed spark timing is produced in the experiments carried out in this study.

As the spark timing of pure H<sub>2</sub> with  $\lambda = 1.5$  is significantly delayed for MBT (10 CAD at 2000 and 3000 rpm and 15 CAD at 4000 and 5000 rpm), the NO<sub>x</sub> emissions have similar values than with CH<sub>4</sub>, which is ignited at a very advanced spark timing (45 CAD at 2000 rpm and 60 CAD at higher speeds). On the other hand, COG presents lower NO<sub>x</sub> values at all  $\lambda$  values because this gas incorporates both benefits commented: lower H<sub>2</sub> content than pure H<sub>2</sub>, and lower spark advance than pure CH<sub>4</sub>.

As can be observed from each gas independently, fuel-rich mixtures (low  $\lambda$  values) favor NO<sub>x</sub> generation due to the dominant effect of temperature, however, at  $\lambda$  values close to 1, the O<sub>2</sub> concentration is small, limiting the NO<sub>x</sub> formation [39]. There is an exception for the case of CH<sub>4</sub> at low engine speeds, probably because the power delivered is not so great and the fuel consumption is still high, increasing the ratio between emissions and power produced.

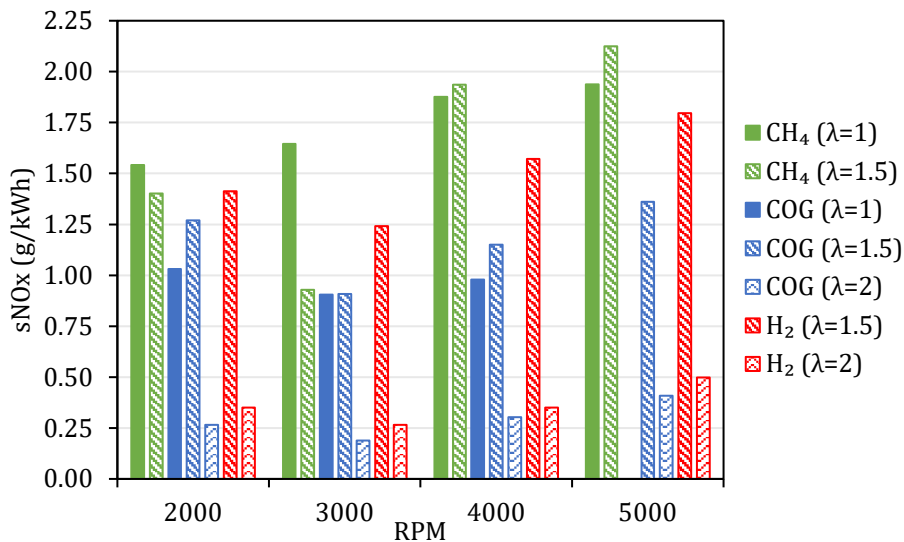


Figure 3.7. Specific NO<sub>x</sub> emissions (sNO<sub>x</sub>, in g/kWh) versus engine speed (rpm) of CH<sub>4</sub>, COG and H<sub>2</sub> at different  $\lambda$  values.

Operating at lean mixtures (high  $\lambda$  values), the NO<sub>x</sub> emissions drop due to the excess air in the cylinder, reducing the combustion temperature [51]. COG at  $\lambda = 2$  delivers the lowest NO<sub>x</sub> emissions due to the important contribution of components different than H<sub>2</sub> and the dilution effect of air, decreasing the temperature during the combustion and hence, the thermal NO<sub>x</sub> formation. The greatest influence of  $\lambda$  in sNO<sub>x</sub> values is observed for pure H<sub>2</sub>; thus, in H<sub>2</sub> engines, limiting the combustion temperature by air dilution would be an interesting strategy to reduce NO<sub>x</sub> emissions.

This trade-off between low O<sub>2</sub> concentration and reduced combustion temperature at low and high  $\lambda$  values, respectively, explains the higher emissions of COG combustion at  $\lambda = 1.5$  than at  $\lambda = 1$ , achieving better combustion.

The minimum emissions are achieved at 3000 rpm for almost all the gases and tested conditions. At higher speeds, better turbulence favors the mixture in the combustion chamber, and therefore, higher NO<sub>x</sub> emissions due to better combustion phenomena are generated [4].

In Figure 3.8, the evolution of the specific hydrocarbons emissions (sHC, in g/kWh) at different  $\lambda$  values across the speed range tested is graphed. HC emissions are mainly produced because of incomplete combustion caused by quenching of the flame near the cylinder walls, in which the heat loss to the cold wall is higher than the net heat energy release from the combustion, stopping the chemical reactions in the flame. Besides, local air-fuel heterogeneities and unburned fuel trapped in crevices not reached by the flame favor the emissions of unburned HC [52].

At  $\lambda$  values above 1 but close to the unit, the flames has minimal quenching distances because reactions are most exothermic at stoichiometric conditions, allowing a high exhaust temperature and, oxidizing the HC formed through crevice and flame quenching [53,54]. As the mixture becomes leaner, the flammability is reduced and sHC rise. This effect can be clearly observed for CH<sub>4</sub> due to its lower flammability range, resulting in higher quenching distances when the air excess increases, raising the emissions very steeply [53]. In the case of COG, as the flammability range is wider, the mixture can still burn properly with  $\lambda = 1.5$ , although at higher  $\lambda$  values, sHC emissions strongly rise as well [55].

The fraction of  $H_2$  in COG also reduces the quenching distance, as the flame is able to propagate closer to the wall, reducing the HC emissions [41,46,53]. The same trend can be observed in Ma et al. [48], increasing the emissions in a steeper way with richer fuel mixtures in the case of pure  $CH_4$ , and delaying the effect to leaner mixtures when the  $H_2$  fraction increases.

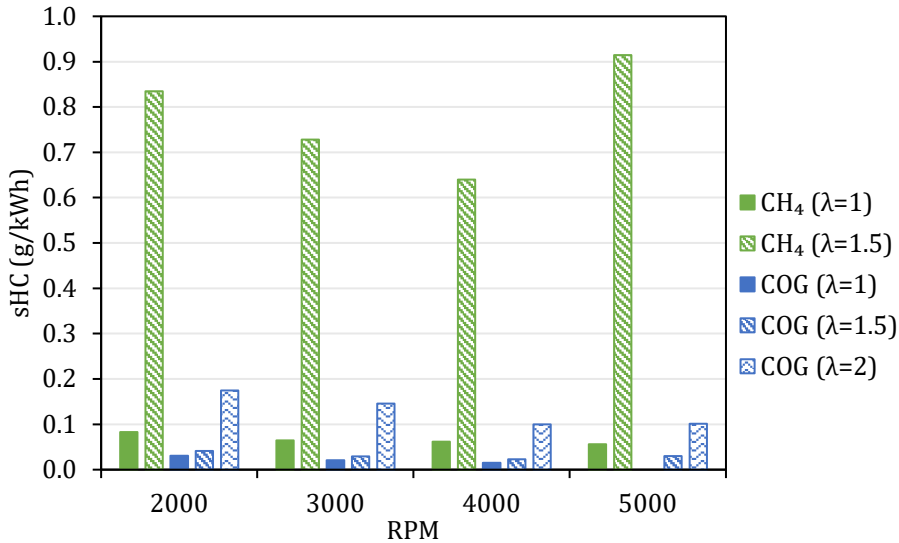


Figure 3.8. Specific hydrocarbons emissions (sHC, in g/kWh) versus engine speed (rpm) of  $CH_4$  and COG at different  $\lambda$  values.

In addition, as COG is enriched with  $H_2$ , the fuel carbon content is lower and the quenching distance is smaller, reducing the sHC emissions, as can be observed in the comparison between  $CH_4$  and COG [45].

The sHC emissions decrease with the rise of engine speed thanks to the improved fuel combustion due to a better mixing associated with more intense turbulence inside the cylinder. However, the emissions of  $CH_4$  ( $\lambda = 1.5$ ) rise again at 5000 rpm because the power and  $\eta_t$  drops rapidly at that engine speed, as can be seen in Figure 3.4 and Figure 3.5.

Figure 3.9 depicts the specific carbon monoxide emissions (sCO, in g/kWh) of the engine exhaust for  $CH_4$  and COG. As COG includes a fraction of CO in its composition, it has a higher tendency to emit carbon monoxide in the case of incomplete combustion. On the other hand, hydrogen enrichment helps to reduce the sCO emissions, as it can be observed in the comparison between  $CH_4$  and COG, by increasing the combustion

temperature and the concentration of OH radicals, which promote the oxidation of CO to CO<sub>2</sub> [56]. The highest CO emissions are produced with CH<sub>4</sub> ( $\lambda = 1$ ) because CO is formed as an intermediate product of CH<sub>4</sub> oxidation when the O<sub>2</sub> available in the air-fuel mixture is low, limiting the complete combustion in the cylinder to form CO<sub>2</sub> [52]. With a leaner mixture in both fuels ( $\lambda = 1.5$ ), the increase of O<sub>2</sub> content is beneficial to reduce the sCO emissions drastically, promoting a more complete combustion [46]. The same trend is observed in Açıkgöz et al. [57] and in Ma et al. [48], increasing the CO emissions as the excess air ratio approaches to stoichiometric conditions.

However, at even leaner mixtures in the case of COG ( $\lambda = 2$ ), although the carbon content in the air-fuel mixture is lower, the sCO values rise again because a more unstable combustion, lower combustion temperature reducing oxidation rates and a higher probability of large-scale flame quenching, limiting the complete oxidation of the fuel and then increasing sCO [39,48,52,58]. In addition, the reduction of the generated power at this condition is more pronounced than the sCO emissions produced [24,45].

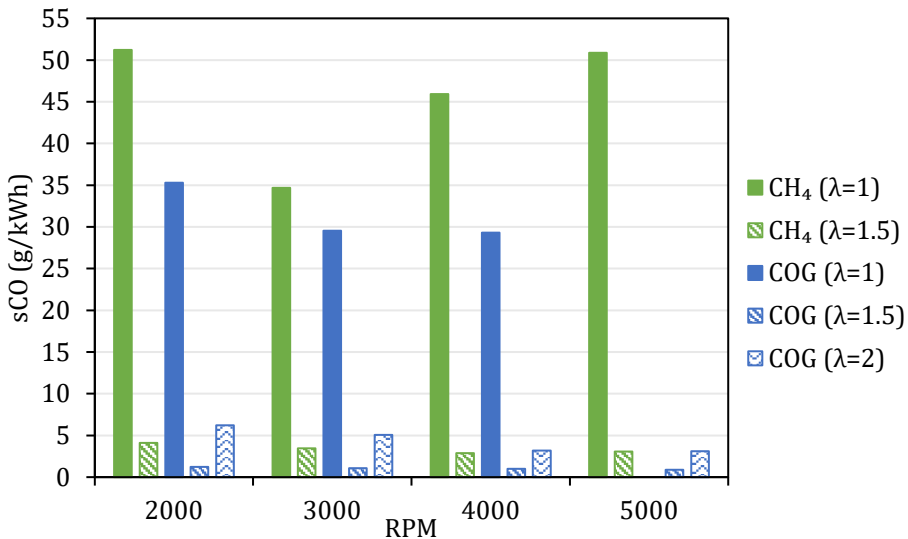


Figure 3.9. Specific carbon monoxide emissions (sCO, in g/kWh) versus engine speed (rpm) of CH<sub>4</sub> and COG at different  $\lambda$  values.

In general, as the engine speed increases, the emissions are reduced because the increased turbulence inside the cylinder favors the

combustion, except in the case of  $\text{CH}_4$  ( $\lambda = 1$ ), with a minimum at 3000 rpm. This can be explained because the air-fuel mixture is so rich that at higher engine speeds, the available time to complete the combustion is lower leading to increased emissions.

Finally, the specific emissions of carbon dioxide ( $s\text{CO}_2$ , in g/kWh) are graphed in Figure 3.10. These emissions arise as products of the complete combustion of a hydrocarbon fuel. In contrast to the other pollutants, the influence of  $\lambda$  and the engine speed on  $s\text{CO}_2$  emissions is very small. Generally, with rich mixtures, the specific  $\text{CO}_2$  emissions decrease because of a limited oxygen availability. Moreover, with very lean mixtures the  $\text{CO}_2$  emissions also decrease because the carbon content is reduced and the combustion is poor [45]. However, at medium  $\lambda$  values (1.5),  $\text{CO}_2$  emissions increase because the efficiency is higher, and the  $\text{O}_2$  concentration is adequate to achieve complete combustion. Considering specific emissions, the same reasoning can be applied, nevertheless, the power reduction with lean mixtures is more pronounced than the emissions generated, raising the  $s\text{CO}_2$  values, especially at higher engine speeds [45,49].

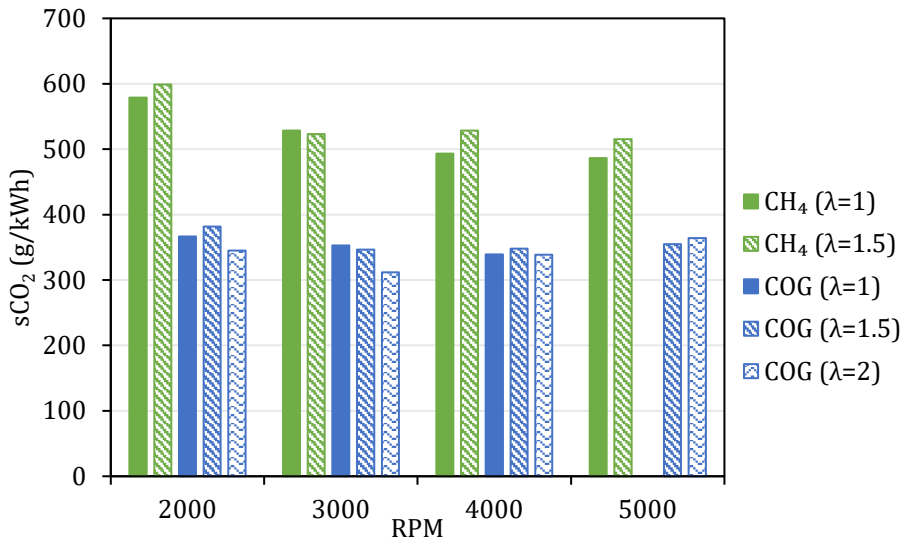


Figure 3.10. Specific carbon dioxide emissions ( $s\text{CO}_2$ , in g/kWh) versus engine speed (rpm) of  $\text{CH}_4$  and  $\text{COG}$  at different  $\lambda$  values.

Besides, the  $\text{H}_2$  fraction on the fuel composition of  $\text{COG}$  has a clear effect on  $s\text{CO}_2$ , which decreases as the H/C ratio of the mixtures increases.



It should be noted that COG has typically a little fraction of  $\text{CO}_2$  in its composition, which is an inert gas as concerns combustion, and therefore, it has a direct contribution to carbon dioxide emissions.

In summary, considering the emissions results of COG, this waste stream can be operated in this engine at  $\lambda = 2$  to obtain lower values of  $\text{sNO}_x$  and  $\text{sCO}_2$  but with a higher amount of  $\text{sHC}$  and  $\text{sCO}$  than working at  $\lambda = 1.5$ . Regarding the engine speed, operating at 3000 rpm reduces the emissions of  $\text{sNO}_x$  and  $\text{sCO}_2$  but increases slightly the  $\text{sHC}$  and  $\text{sCO}$  values compared to 4000 rpm.

### 3.4. Conclusions

A comparative experimental study of pure  $\text{H}_2$ ,  $\text{CH}_4$  and COG gaseous fuels in a Volkswagen Polo 1.4 L port-injection SI engine has been developed in this chapter. Experiments were carried out at full load (WOT) and optimal spark advance to obtain MBT.  $\lambda$  values between 1 and 2 were selected varying the engine speed between 2000 and 5000 rpm. The main conclusions regarding the comparisons of the three gases are summarized as follows.

- For  $\lambda$  values higher than 1, COG provides greater BMEP and power than pure  $\text{H}_2$  and pure  $\text{CH}_4$ , due to the favorable influence of the higher LHV of COG in comparison to  $\text{H}_2$  and higher  $S_L$  value compared to  $\text{CH}_4$ . With leaner mixtures, the BMEP and power decrease, being this reduction more pronounced at high speeds.
- COG delivers the greatest  $\eta_t$  values. At  $\lambda = 1.5$ , a  $\eta_t$  increase of 7.0% and 10.3% were obtained with COG with respect to  $\text{H}_2$  and  $\text{CH}_4$  in the maximum values, respectively. Gaseous fuels with lower volumetric LHV reduce the SEC.
- The optimized spark advance at MBT can reduce  $\text{sNO}_x$  due to lower combustion temperature. COG has lower emissions because of lower  $\text{H}_2$  content and lower spark advance than  $\text{CH}_4$ . Very low and very high  $\lambda$  values reduce the  $\text{O}_2$  concentration and the temperature, respectively, reducing  $\text{sNO}_x$ .

- The flammability of the mixture is reduced with high  $\lambda$  values and the sHC emissions rise. By enriching the fuel with  $H_2$ , the fuel carbon content is lower, the quenching distance is smaller, and the combustion temperature is higher, reducing sHC emissions.
- The highest sCO emissions are produced with  $CH_4$  ( $\lambda = 1$ ) because the  $O_2$  available is low. At lean mixtures ( $\lambda = 2$ ) the sCO values rise again because of a more unstable combustion. On the other hand, sCO<sub>2</sub> emissions rise with intermediate  $\lambda$  values due to better combustion and decrease as the H/C ratio of the mixture increases.
- The major strength of COG is the combination of the advantages of pure  $H_2$  and pure  $CH_4$ , widening the  $\lambda$  range of operation from 1 to 2, with very good performance and emissions results comparable to pure gases.

These results reveal COG as a very good fuel for ICEs. This gas comes from an industrial waste stream and can be applied in stationary engines coupled to generator systems with power electronics or CVT systems to work at optimal conditions while maintaining the electricity frequency desired. The optimum conditions for using COG in the engine employed in this chapter were with  $\lambda = 1.5$  at 4000 rpm achieving high power performance and  $\eta_t$ , the lowest SEC, moderate NO<sub>x</sub> and CO<sub>2</sub> emissions, and small values of sHC and sCO. At 3000 rpm or  $\lambda = 2$ , lower values of sNO<sub>x</sub> can be achieved but the combustion performance and efficiency are reduced. Another way to reduce emissions is by incorporating a three-way catalytic converter (TWC) in the exhaust. Thus, the operating conditions should be optimized for each engine and the purpose of the application.

## Nomenclature

BMEP	Brake mean effective pressure
BTDC	Before top dead center
CAD	Crank angle degree
$C_{NO_x}$	Concentration of NO <sub>x</sub> in the exhaust (ppm)
COG	Coke oven gas
CVT	Continuous variable transmission

---

DI	Direct injection
DOHC	Double overhead camshaft
EGR	Exhaust gas recirculation
HCNG	Hydrogen-enriched compressed natural gas
ICE	Internal combustion engine
LHV	Lower heating value
MBP	Maximum brake power
MBT	Maximum brake torque
$\dot{m}_{air}$	Mass flow rate of air (g/s)
$\dot{m}_f$	Mass flow rate of fuel (g/s)
$M_{NO_x}$	Molecular weight of NO <sub>x</sub> (g/mol)
$N$	Engine speed (rpm)
$N_e$	Exhaust moles with complete combustion
NG	Natural gas
$n_R$	Revolutions per cycle
$P$	Power (kW)
$Q_f$	Fuel flow rate (L/min)
sfc	Specific fuel consumption (g/kWh)
SEC	Specific energy consumption (MJ/kWh)
SI	Spark ignition
$S_L$	Laminar flame speed (m/s)
sNO <sub>x</sub>	Specific NO <sub>x</sub> emissions (g/kWh)
STP	Standard temperature and pressure (273.15 K, 1 bar)
TDC	Top dead center
TWC	Three way catalyst
$V_d$	Displaced volume (m <sup>3</sup> )
$V_m$	Molar volume (L/mol)
WOT	Wide open throttle
$\eta_t$	Thermal efficiency
$\lambda$	Air-fuel ratio
$\lambda_{act}$	Real air-fuel ratio
$\lambda_{st}$	Stoichiometric air-fuel ratio

## References

- [1] Yan F, Xu L, Wang Y. Application of hydrogen enriched natural gas in spark ignition IC engines: from fundamental fuel properties to engine performances and emissions. *Renew Sustain Energy Rev* 2018;82:1457–88. doi:10.1016/j.rser.2017.05.227.
- [2] Mehra RK, Duan H, Juknelevičius R, Ma F, Li J. Progress in hydrogen enriched compressed natural gas (HCNG) internal combustion engines - A comprehensive review. *Renew Sustain Energy Rev* 2017;80:1458–98. doi:10.1016/j.rser.2017.05.061.
- [3] Luo S, Ma F, Mehra RK, Huang Z. Deep insights of HCNG engine research in China. *Fuel* 2020;263:116612. doi:10.1016/j.fuel.2019.116612.
- [4] Alrazen HA, Ahmad KA. HCNG fueled spark-ignition (SI) engine with its effects on performance and emissions. *Renew Sustain Energy Rev* 2018;82:324–42. doi:10.1016/j.rser.2017.09.035.
- [5] Karim GA, Wierzbka I, Al-Alousi Y. Methane-hydrogen mixtures as fuels. *Int J Hydrogen Energy* 1996;21:625–31. doi:10.1016/0360-3199(95)00134-4.
- [6] Ceper BA, Birsan EB, Akansu SO, Kahraman N. Experimental Study Of Hydrogen In Internal Combustion Engines. *Clean Technol* 2009 Bioenergy, Renewables, Storage, Grid, Waste Sustain 2009;3:191–4.
- [7] Huang Z, Liu B, Zeng K, Huang Y, Jiang D, Wang X, et al. Combustion characteristics and heat release analysis of a spark-ignited engine fueled with natural gas-hydrogen blends. *Energy and Fuels* 2007;21:2594–9. doi:10.1021/ef0701586.
- [8] Ma F, Wang M, Jiang L, Chen R, Deng J, Naeve N, et al. Performance and emission characteristics of a turbocharged CNG engine fueled by hydrogen-enriched compressed natural gas with high hydrogen ratio. *Renew Energy* 2010;35:6438–47. doi:10.1016/j.ijhydene.2010.03.111.
- [9] Rakopoulos CD, Scott MA, Kyritsis DC, Giakoumis EG. Availability analysis of hydrogen/natural gas blends combustion in internal combustion engines. *Energy* 2008;33:248–55. doi:10.1016/j.energy.2007.05.009.
- [10] Navarro E, Leo TJ, Corral R. CO<sub>2</sub> emissions from a spark ignition engine operating on natural gas-hydrogen blends (HCNG). *Appl*

- Energy 2013;101:112–20. doi:10.1016/j.apenergy.2012.02.046.
- [11] Hu E, Huang Z, Liu B, Zheng J, Gu X. Experimental study on combustion characteristics of a spark-ignition engine fueled with natural gas-hydrogen blends combining with EGR. *Int J Hydrogen Energy* 2009;34:1035–44. doi:10.1016/j.ijhydene.2008.11.030.
  - [12] Li Y, Bi M, Li B, Zhou Y, Gao W. Effects of hydrogen and initial pressure on flame characteristics and explosion pressure of methane/hydrogen fuels. *Fuel* 2018;233:269–82. doi:10.1016/j.fuel.2018.06.042.
  - [13] Yilmaz IT, Gumus M. Effects of hydrogen addition to the intake air on performance and emissions of common rail diesel engine. *Energy* 2018;142:1104–13. doi:10.1016/j.energy.2017.10.018.
  - [14] Zhou JH, Cheung CS, Leung CW. Combustion and Emission of a Compression Ignition Engine Fueled with Diesel and Hydrogen-Methane Mixture. *Int J Mech Mechatronics Eng* 2013;7:112–7.
  - [15] Mansor MRA, Abbood MM, Mohamad TI. The influence of varying hydrogen-methane-diesel mixture ratio on the combustion characteristics and emissions of a direct injection diesel engine. *Fuel* 2017;190:281–91. doi:10.1016/j.fuel.2016.11.010.
  - [16] Dimitriou P, Tsujimura T. A review of hydrogen as a compression ignition engine fuel. *Int J Hydrogen Energy* 2017;42:24470–86. doi:10.1016/j.ijhydene.2017.07.232.
  - [17] Avadhanula VK, Lin C Sen, Witmer D, Schmid J, Kandulapati P. Experimental study of the performance of a stationary diesel engine generator with hydrogen supplementation. *Energy and Fuels* 2009;23:5062–72. doi:10.1021/ef900311w.
  - [18] Yoon W, Park J. Parametric study on combustion characteristics of virtual HCCI engine fueled with methane-hydrogen blends under low load conditions. *Int J Hydrogen Energy* 2019;44:15511–22. doi:10.1016/j.ijhydene.2019.04.137.
  - [19] Mariani A, Unich A, Minale M. Methane / Hydrogen Blends in Controlled Auto Ignition Engines with EGR: Evaluation of NO<sub>x</sub> Emissions. *Chem Eng Trans* 2019;74:301–6. doi:10.3303/CET1974051.
  - [20] Wong YK, Karim GA. An analytical examination of the effects of hydrogen addition on cyclic variations in homogeneously charged compression – ignition engines. *Int J Hydrogen Energy*

2000;25:1217–24.

- [21] Rao A, Wu Z, Kumar Mehra R, Duan H, Ma F. Effect of hydrogen addition on combustion, performance and emission of stoichiometric compressed natural gas fueled internal combustion engine along with exhaust gas recirculation at low, half and high load conditions. *Fuel* 2021;304:121358. doi:10.1016/j.fuel.2021.121358.
- [22] Hora TS, Agarwal AK. Experimental study of the composition of hydrogen enriched compressed natural gas on engine performance, combustion and emission characteristics. *Fuel* 2015;160:470–8. doi:10.1016/j.fuel.2015.07.078.
- [23] Kahraman N, Çeper B, Akansu SO, Aydın K. Investigation of combustion characteristics and emissions in a spark-ignition engine fuelled with natural gas-hydrogen blends. *Int J Hydrogen Energy* 2009;34:1026–34. doi:10.1016/j.ijhydene.2008.10.075.
- [24] Diéguez PM, Urroz JC, Marcelino-Sádaba S, Pérez-Ezcurdia A, Benito-Amurrio M, Sáinz D, et al. Experimental study of the performance and emission characteristics of an adapted commercial four-cylinder spark ignition engine running on hydrogen-methane mixtures. *Appl Energy* 2014;113:1068–76. doi:10.1016/j.apenergy.2013.08.063.
- [25] Remus R, Aguado Monsonet MA, Roudier S, Sancho LD. Best Available Techniques (BAT) Reference Document for Iron and Steel Production. vol. BREF-IS. 2013. doi:10.2791/97469.
- [26] Yáñez M, Ortiz A, Brunaud B, Grossmann IE, Ortiz I. Contribution of upcycling surplus hydrogen to design a sustainable supply chain: The case study of Northern Spain. *Appl Energy* 2018;231:777–87. doi:10.1016/j.apenergy.2018.09.047.
- [27] Corporation USS. Clean Coke Oven Gas. Safety Data Sheet (SDS). Exposure 2010;82493:1–8.
- [28] Roy MM, Tomita E, Kawahara N, Harada Y, Sakane A. Performance and emissions of a supercharged dual-fuel engine fueled by hydrogen-rich coke oven gas. *Int J Hydrogen Energy* 2009;34:9628–38. doi:10.1016/j.ijhydene.2009.09.016.
- [29] Roy MM, Tomita E, Kawahara N, Harada Y, Sakane A. Comparison of performance and emissions of a supercharged dual-fuel engine fueled by hydrogen and hydrogen-containing gaseous fuels. *Int J Hydrogen Energy* 2011;36:7339–52.

- doi:10.1016/j.ijhydene.2011.03.070.
- [30] Szwaja S. Hydrogen rich gases combustion in the IC engine. *J KONES Powertrain Transp* 2009;16:447–54.
  - [31] Szwaja S. Dilution of fresh charge for reducing combustion knock in the internal combustion engine fueled with hydrogen rich gases. *Int J Hydrogen Energy* 2019;44:19017–25. doi:10.1016/j.ijhydene.2018.10.134.
  - [32] Naeve N, He Y, Deng J, Wang M, Ma F. Waste Coke Oven Gas Used as a Potential Fuel for Engines. *SAE Tech. Pap.*, vol. 2011- 01-09, 2011. doi:10.4271/2011-01-0920.
  - [33] Sopena C, Diéguez PM, Sáinz D, Urroz JC, Guelbenzu E, Gandía LM. Conversion of a commercial spark ignition engine to run on hydrogen: Performance comparison using hydrogen and gasoline. *Int J Hydrogen Energy* 2010;35:1420–9. doi:10.1016/j.ijhydene.2009.11.090.
  - [34] Diéguez PM, Urroz JC, Sáinz D, Machin J, Arana M, Gandía LM. Characterization of combustion anomalies in a hydrogen-fueled 1.4 L commercial spark-ignition engine by means of in-cylinder pressure, block-engine vibration, and acoustic measurements. *Energy Convers Manag* 2018;172:67–80. doi:10.1016/j.enconman.2018.06.115.
  - [35] Karim GA. Hydrogen as a spark ignition engine fuel. *Int J Hydrogen Energy* 2003;28:569–77. doi:10.1016/S0360-3199(02)00150-7.
  - [36] Heywood JB. *Internal combustion engine fundamentals*. New York: McGraw-Hill Education; 2018.
  - [37] Sun Y, Yu X, Dong W, Tang Y. Effects of hydrogen direct injection on engine stability and optimization of control parameters for a combined injection engine. *Int J Hydrogen Energy* 2018;43:6723–33. doi:10.1016/j.ijhydene.2018.02.033.
  - [38] Ceper BA, Akansu SO, Kahraman N. Investigation of cylinder pressure for H<sub>2</sub>/CH<sub>4</sub> mixtures at different loads. *Int J Hydrogen Energy* 2009;34:4855–61. doi:10.1016/j.ijhydene.2009.03.039.
  - [39] Ma F, Wang M, Jiang L, Deng J, Chen R, Naeve N, et al. Performance and emission characteristics of a turbocharged spark-ignition hydrogen-enriched compressed natural gas engine under wide open throttle operating conditions. *Int J Hydrogen Energy* 2010;35:12502–9. doi:10.1016/j.ijhydene.2010.08.053.

- [40] Park C, Kim C, Choi Y, Won S, Moriyoshi Y. The influences of hydrogen on the performance and emission characteristics of a heavy duty natural gas engine. *Int J Hydrogen Energy* 2011;36:3739–45. doi:10.1016/j.ijhydene.2010.12.021.
- [41] Ma F, Wang J, Wang Y, Wang Y, Li Y, Liu H, et al. Influence of different volume percent hydrogen/natural gas mixtures on idle performance of a CNG engine. *Energy and Fuels* 2008;22:1880–7. doi:10.1021/ef7006485.
- [42] Jian L, Chau KT. Design and analysis of a magnetic-g geared electronic-continuously variable transmission system using finite element method. *Prog Electromagn Res* 2010;107:47–61.
- [43] CVT Corp. Ind Most Powerful Mech CVTs 2016. <https://www.cvtcorp.com/main.php?i=15> (accessed December 7, 2019).
- [44] Moreno F, Arroyo J, Muñoz M, Monné C. Combustion analysis of a spark ignition engine fueled with gaseous blends containing hydrogen. *Int J Hydrogen Energy* 2012;37:13564–73. doi:10.1016/j.ijhydene.2012.06.060.
- [45] Bauer CG, Forest TW. Effect of hydrogen addition on the performance of methane-fueled vehicles. Part I: effect on S.I. engine performance. *Int J Hydrogen Energy* 2001;26:55–70. doi:10.1016/S0360-3199(00)00067-7.
- [46] Xu J, Zhang X, Liu J, Fan L. Experimental study of a single-cylinder engine fueled with natural gas-hydrogen mixtures. *Int J Hydrogen Energy* 2010;35:2909–14. doi:10.1016/j.ijhydene.2009.05.039.
- [47] Hoekstra RL, Van Blarigan P, Mulligan N. NO<sub>x</sub> emissions and efficiency of hydrogen, natural gas, and hydrogen/natural gas blended fuels. *SAE Tech Pap* 1996;961103. doi:10.4271/961103.
- [48] Ma F, Wang Y, Liu H, Li Y, Wang J, Zhao S. Experimental study on thermal efficiency and emission characteristics of a lean burn hydrogen enriched natural gas engine. *Int J Hydrogen Energy* 2007;32:5067–75. doi:10.1016/j.ijhydene.2007.07.048.
- [49] Moreno F, Muñoz M, Arroyo J, Magén O, Monné C, Suelves I. Efficiency and emissions in a vehicle spark ignition engine fueled with hydrogen and methane blends. *Int J Hydrogen Energy* 2012;37:11495–503. doi:10.1016/j.ijhydene.2012.04.012.
- [50] Shudo T, Shimamura K, Nakajima Y. Combustion and emissions in



- a methane DI stratified charge engine with hydrogen pre-mixing. JSAE Rev 2000;21:3–7. doi:10.1016/S0389-4304(99)00061-2.
- [51] Mehra RK, Duan H, Luo S, Rao A, Ma F. Experimental and artificial neural network (ANN) study of hydrogen enriched compressed natural gas (HCNG) engine under various ignition timings and excess air ratios. Appl Energy 2018;228:736–54. doi:10.1016/j.apenergy.2018.06.085.
  - [52] Yan F, Xu L, Wang Y. Application of hydrogen enriched natural gas in spark ignition IC engines: from fundamental fuel properties to engine performances and emissions. Renew Sustain Energy Rev 2018;82:1457–88. doi:10.1016/j.rser.2017.05.227.
  - [53] Yan F, Xu L, Wang Y. Application of hydrogen enriched natural gas in spark ignition IC engines: from fundamental fuel properties to engine performances and emissions. Renew Sustain Energy Rev 2018;82:1457–88. doi:10.1016/j.rser.2017.05.227.
  - [54] Zaker K, Askari MH, Jazayeri A, Ebrahimi R, Zaker B, Ashjaee M. Open cycle CFD investigation of SI engine fueled with hydrogen/methane blends using detailed kinetic mechanism. Int J Hydrogen Energy 2015;40:14006–19. doi:10.1016/j.ijhydene.2015.08.040.
  - [55] Akansu SO, Kahraman N, Çeper B. Experimental study on a spark ignition engine fuelled by methane-hydrogen mixtures. Int J Hydrogen Energy 2007;32:4279–84. doi:10.1016/j.ijhydene.2007.05.034.
  - [56] Wu L, Kobayashi N, Li Z, Huang H. Experimental study on the effects of hydrogen addition on the emission and heat transfer characteristics of laminar methane diffusion flames with oxygen-enriched air. Int J Hydrogen Energy 2016;41:2023–36. doi:10.1016/j.ijhydene.2015.10.132.
  - [57] Açikgöz B, Çelik C, Soyhan HS, Gökalp B, Karabağ B. Emission characteristics of an hydrogen-CH<sub>4</sub> fuelled spark ignition engine. Fuel 2015;159:298–307. doi:10.1016/j.fuel.2015.06.043.
  - [58] Akansu SO, Dulger Z, Kahraman N, Veziroğlu TN. Internal combustion engines fueled by natural gas - Hydrogen mixtures. Int J Hydrogen Energy 2004;29:1527–39. doi:10.1016/j.ijhydene.2004.01.018.



# **CHAPTER 4**

---

**COMBUSTION ANALYSIS OF LOW  
CARBON FUELS IN INTERNAL  
COMBUSTION ENGINES WITH CFD**



## 4.1. Introduction

Low carbon fuels report significant advantages over conventional fossil fuels for their use in internal combustion engines (ICEs). As explained in **Chapter 3**, coke oven gas (COG) is an industrial waste stream with high content of hydrogen and methane gases, widening the air-fuel ratio ( $\lambda$ ) operation range with a high performance output, as well as reducing the abnormal combustion tendency and the emissions. However, a more comprehensive analysis of the evolution of the fluid dynamics and the combustion within the cylinders is required to further understand the phenomena involved with these low carbon fuels.

In this sense, computational fluid dynamics (CFD) simulations enable a high accuracy calculation and visualization of the thermodynamic properties of the fluids if the geometry domain, the boundary conditions and the chemical mechanisms are correctly defined. Thereby, optimization of the geometry and the operating conditions of ICEs can be done reducing the number of test bench engine experiments.

Several studies have used CFD software to assess spark ignition (SI) ICEs with different configurations and fuels. Hydrogen has been widely studied as combustion fuel using CFD models in direct injection (DI) [1–3] and port-fuel injection (PFI) locations [4–7]. Besides the analysis of the performance and emissions, the start of injection (SOI) has been studied to reduce the residual  $H_2$  in the intake manifold and to avoid backfire in PFI engines [8–11]. Generally, temperature, OH mass and NO<sub>x</sub> emissions distribution in the cylinder are the main variables plotted in 3D graphs. Regarding the kinetics of combustion reactions, the mechanisms more widely employed in literature are Gri-Mech, which is a detailed mechanism optimized for combustion of natural gas, or reduced mechanisms focused on  $H_2$  combustion reactions [2,12,13].

On the other hand,  $CH_4$  or natural gas (NG) CFD models have been carried out in dual fuel diesel engines [14–16], homogeneous charge compression ignition (HCCI) [17,18] and in SI engines [19–21], analyzing pressure, temperature, emissions and the influence of injection [11]. Mixtures of  $H_2$  and  $CH_4$  gaseous fuels have been also studied through CFD models, analyzing different percentages of  $H_2$  in the composition [22–25]. Different air-fuel ratios at a single engine speed were considered in order to study the main combustion and performance variables, such as

pressure, temperature, rate of heat release, combustion duration, efficiency, flow velocity and emissions. Moreover, two compression ratios (CR) and two engine speeds at different loads were compared in Laget et al. [26].

Few studies with CFD models deal with COG and syngas with high volumetric H<sub>2</sub> percentages. He et al. conducted a study focused on the reduction and optimization of the kinetic mechanism of COG combustion [27]. This mechanism was employed in a CFD model in the KIVA-CHEMKIN® software of a cylinder from a SI engine. The model was validated with experiments in terms of in-cylinder pressure and NO emissions, showing good agreement between simulated and experimental data.

On the other hand, Stylianidis et al. [28] developed a new combustion mechanism for syngas mixtures together with the kinetics of the reactions. However, a modification in the rate constants of the reaction  $\text{H}_2\text{O}_2 + \text{H} = \text{H}_2 + \text{HO}_2$  was needed to improve the match between simulated and experimental data in the case of fuels with high H<sub>2</sub> concentration, as in the case of coke oven feedstock [28]. The authors compared the results obtained with the new chemical kinetic mechanism with previous mechanisms reported for syngas and validated the CFD model in a micro-pilot ignited supercharged dual fuel diesel engine. Results showed good agreement in the evolution of the in-cylinder pressure and the rate of heat release at different syngas compositions, equivalence ratio and SOI angles.

In consequence, a comprehensive analysis aimed to provide a deeper understanding of the performance of the combustion of COG compared with its main components (H<sub>2</sub> and CH<sub>4</sub>) in a SI engine through CFD is still unaccomplished. Therefore, in this work simulations of H<sub>2</sub>, CH<sub>4</sub> and COG in a port-fuel cylinder from a Volkswagen Polo 1.4L engine have been carried out simulating the experimental operating conditions reported in **Chapter 3**. The engine has been run at wide open throttle (WOT) and the spark advance (SA) has been selected to achieve the maximum brake torque (MBT). Variations in engine speed between 2000 rpm – 5000 rpm and air-fuel ratio between 1 and 2 have been considered.

The model validation has been carried out with different variables. Afterward, the performance assessment in terms of power, heat release, pressure, temperature, flame growth speed, OH concentration and NO

emissions are provided in this work. In addition, the volumetric efficiency has been compared in order to observe the effects of the different fuel characteristics. Finally, a spark advance sensitivity analysis has been carried out for COG to analyze the impact of this variable on combustion and support the arguments exposed.

## **4.2. Simulation methodology**

### **4.2.1. CFD software**

A CFD model of a cylinder from a naturally-aspirated four-cylinder port-fuel injection SI engine has been developed. The original engine is a Volkswagen Polo 1.4L adapted to be driven with gaseous fuels [29]. Specifications of the original engine were detailed in Table 3.1.

Due to the symmetrical position of the hydrogen injector in the intake manifold and the unthrottled operation, a symmetrical flow field was assumed without swirl [1]. The vertical plane through the injector's central axis was defined as a symmetry plane, reducing the computational domain and the time effort for each simulation. Thus, a high number of simulations could be carried out without significant loss in results accuracy. The geometry of a symmetrical cylinder with the intake and exhaust valves and manifolds (Figure 4.1a) was designed with Autodesk® Inventor 2020 and exported to Ansys® Academic Research Workbench, Release 2019 R3. This geometry was processed with the packages Ansys® SpaceClaim® and Mesh® to redefine the boundary walls and to create the initial computational mesh, as shown in Figure 4.1b.

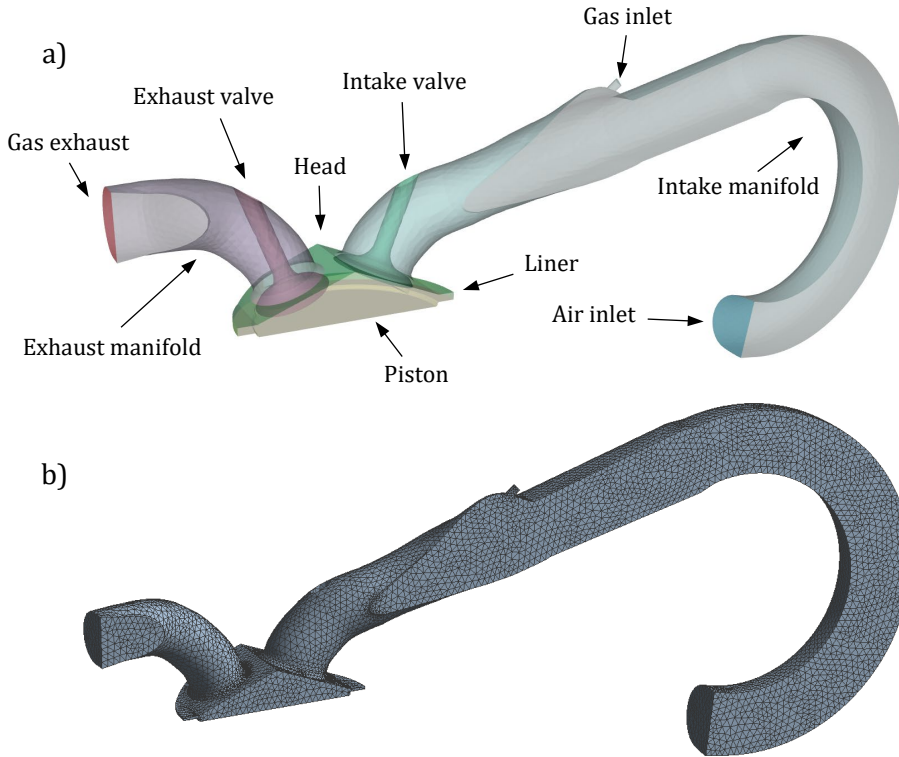


Figure 4.1. 3D symmetrical a) geometry model and b) initial mesh of a cylinder from the engine. (Screenshots used courtesy of ANSYS, Inc.)

Afterward, the model was handled in the package Ansys® Forte®, which is a special module focused on ICEs using proven mathematical techniques and algorithms and automatically generating the moving volume mesh on-the-fly during the simulation [30]. In addition, Forte® is able to modify the initial mesh (Figure 4.1b) to refine the average cell size in the regions of interest to increase the calculation accuracy.

In order to obtain mesh independent results with the simulations, a mesh size sensitivity analysis was carried out varying the global element size of the mesh. The results of the analysis are calculated and shown in Table A.4.1 in the Appendix. Finally, a global element size of 2.5 mm was selected, with very good results and reasonable computational time and fluid cells number, around 315000 cells when the exhaust valve (EVO) is opened. Smaller cells as fractions of the global mesh size were created near the walls, the symmetry plane, the open boundaries, inside the cylinder and near the valves where higher flow velocity gradients, heat



transfer and chemical reactions were produced. The resulting average cell size inside the cylinder was 1.25 mm.

However, a variable mesh during the spark ignition in the spark region and in the squish periods within the cylinder was also applied to improve combustion calculations [31]. Furthermore, a solution adaptive mesh refinement for temperature was added within the cylinder based on the gradient of the temperature field from the spark time to the EVO event. Both refinements enabled a reduction of the average cell size to 0.625 mm in the regions and periods with the most intense computational requirements.

Regarding the engine geometry, the boundary conditions of the model are detailed in Table 4.1. The valves and the piston were configured as moving parts, defining the profile movement and direction for each of the valves, and the stroke (7.56 cm), the connecting rod length and the direction of displacement for the piston. The valves lift profiles are graphed in Figure 4.2a, indicating the exhaust valve opening (EVO) and exhaust valve closure (EVC) events for the exhaust valve and the intake valve opening (IVO) and intake valve closure (IVC) events for the intake valve. These valve events are also detailed in Table 4.1. In Figure 4.2b, the variation of the position of the piston during a cycle is graphed, with a duration of 720 crank angle degrees (CAD) of rotation of the crankshaft, which means two revolutions of this shaft and four strokes of the piston. The bottom dead center (BDC) represents the lowest position of the piston in the cylinder and the top dead center (TDC) is the highest position.

On the other hand, all walls were set up with the Law of the Wall slip condition for the shear stress, implying a flexible mesh size near them, and with constant wall temperatures. The air and the gaseous fuel entered into the domain through Inlet surfaces type and the exhaust gas left the domain through an Outlet surface.

Table 4.1. Boundary geometries and conditions.

Boundary region	Boundary type	Condition	Value
Air inlet	Inlet	2000 rpm	0.092 MPa, 314 K
		3000 rpm	0.091 MPa, 311 K
		4000 rpm	0.089 MPa, 309 K
		5000 rpm	0.088 MPa, 307 K
Gas inlet	Inlet		298 K
Gas exhaust	Outlet		0.101 MPa
Intake manifold	No moving wall		313 K
Exhaust manifold	No moving wall		500 K
Head	No moving wall		400 K
Liner	No moving wall		400 K
Piston	Moving wall		500 K
Intake valve	Moving wall	IVO (18.2 dBTDC)	400 K
		IVC (15.2 dABDC)	
Exhaust valve	Moving wall	EVO (19.4 dBBDC)	550 K
		EVC (16.4 dATDC)	

IVO: intake valve opening, IVC: intake valve closure, EVO: exhaust valve opening, EVC: exhaust valve closure.

In the case of the fuel, the Inlet surface was settled in the place of the original place of the port-fuel gasoline injector as a circular area with a diameter of 3.4 mm. Fuel was introduced at a constant injection speed (m/s) during a variable pulse width (PW), which depended on the gas and the operating condition. The injection profile of CH<sub>4</sub> at  $\lambda = 1$  and 3000 rpm is graphed in Figure 4.2b, with an injection speed of 115 m/s, a PW of 149 CAD and with the end of injection (EOI) at 485 CAD.

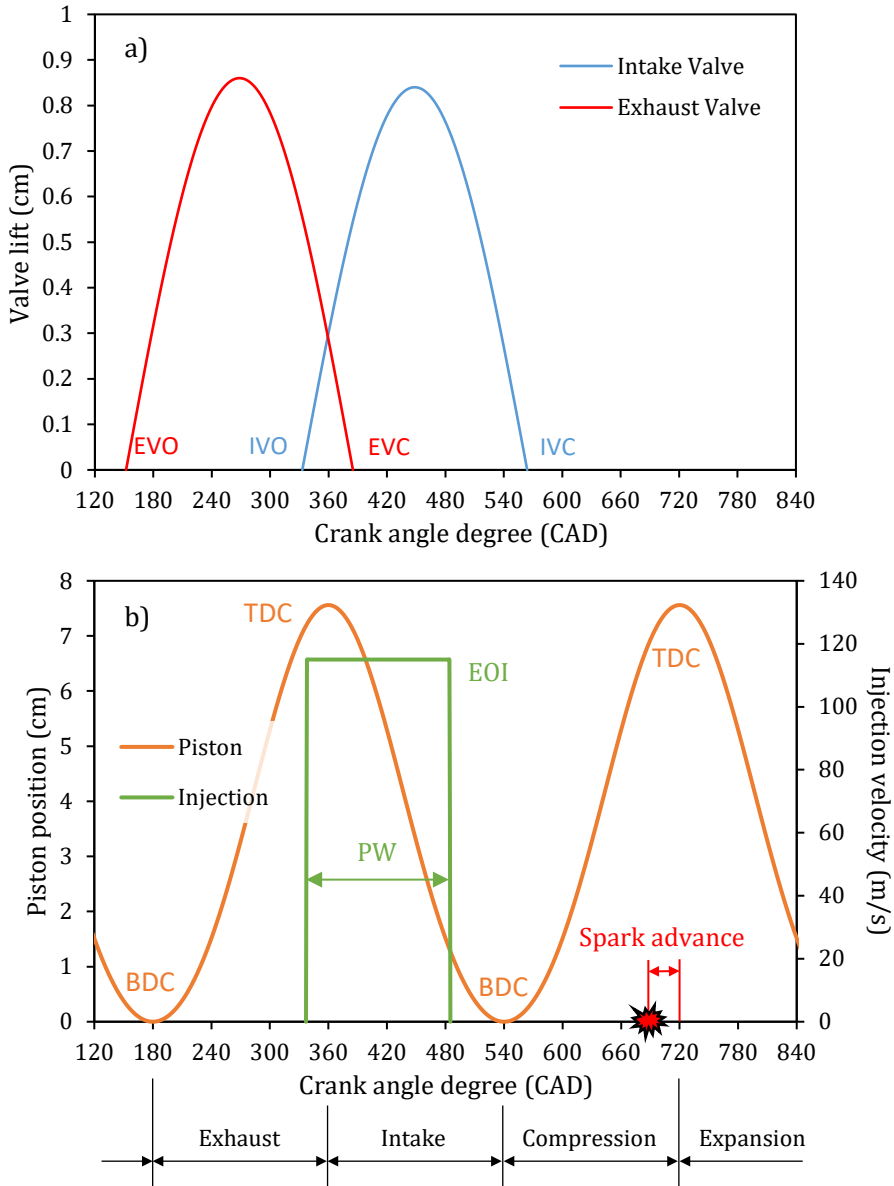


Figure 4.2. a) Intake and exhaust valve lift profiles (cm) and b) Piston position (cm) and injection velocity (m/s) of  $\text{CH}_4$  at  $\lambda=1$  and 3000 rpm. EVO: exhaust valve opening, EVC: exhaust valve closure, IVO: intake valve opening, IVC: intake valve closure, PW: pulse width, TDC: top dead center, BDC: bottom dead center.

The simulation domain can be divided into three regions: intake manifold, cylinder and exhaust manifold. Each of these regions was initialized with a gas composition, pressure and temperature values.

Different chemical kinetic mechanisms have been found in the literature for simulation of the combustion of hydrogen, methane and mixtures of fuels. These mechanisms define the reaction pathways and the evolution of the reaction rates during combustion, leading to changes in the species concentration. In order to compare the three gaseous fuels under the same simulation conditions, the detailed Gri-Mech 3.0 mechanism with 325 reactions and 53 species, was selected to consider all the reactions involving hydrogen and hydrocarbons as well as the NO<sub>x</sub> emissions [32].

The turbulent flow model used in this study was the Reynolds-Averaged-Navier-Stokes (RANS) Re-Normalization Group (RNG)  $k$ - $\epsilon$  model, aiming to capture the average of the entire flow field while preserving the main effects of turbulence on the averaged flow and combustion characteristics [31]. Furthermore, the RNG  $k$ - $\epsilon$  model is the default and recommended turbulence model in Ansys® Forte® with better engine simulation results compared to the standard version of the  $k$ - $\epsilon$  model [33]. On the other hand, the Table Library included in Forte with prebuilt laminar flame speeds has been employed for the gaseous fuels [34]. These built-in flame speed values cover a wide range of operating conditions and are the recommended option by the software support.

The calculations were performed with Message Passing Interface (MPI) solver (for parallel computing calculation) in a workstation with two processors Intel® Xeon® Gold 6148 and 256 GB RAM and in the supercomputer Altamira Supercomputer at the Institute of Physics of Cantabria (IFCA-CSIC). Simulations of at least four consecutive cycles have been done for each case of study to reach a quasi-steady state, requiring between 30 and 45 h for the calculation of four cycles with 16 computational cores.

Afterward, as the simulation results are collected in huge datasheets with thousands of rows, the data were handled and analyzed using Python language. This method allows the selection and graphical representation of the more interesting data in an automatic way and facilitates the comparison between simulated results. On the other hand, the Ansys® Enight® enables the visualization of the 3D evolution of many of the variables inside the domain.

### 4.2.2. Planning of simulation runs

The simulations carried out in this chapter were based on the experiments of  $H_2$ ,  $CH_4$  and COG performed in **Chapter 3**. The engine speed was varied in the range 2000 rpm – 5000 rpm and the air-fuel ratio between 1 and 2. In addition, full load (WOT) and optimum spark advance were selected to obtain maximum brake torque. Spark advance is defined as crank angle degrees (CAD) before the top dead center (TDC) at the end of the compression stroke which is “720” in this work, as represented in Figure 4.2b. The spark timings selected are shown in Table 4.2 with a duration of 1 ms and a rate of energy release of the spark event of 20 J/s.

Gaseous fuels were injected using a time-varying velocity profile according to the density and specification of the mass flow rate of the injectors (Quantum PQ2-3200). The injection velocity,  $v$  in m/s, was calculated with Equation (4.1):

$$v = \frac{\dot{m}}{\rho \cdot A} \quad (4.1)$$

Where  $\dot{m}$  is the mass flow rate (g/s),  $\rho$  is the fuel density (g/m<sup>3</sup>) and  $A$  is the injection area (m<sup>2</sup>). The resulting half of the injection area due to the symmetrical part of the CFD geometry model is 4.478 mm<sup>2</sup>, calculated with the gas nozzle diameter (3.4 mm). The density of each fuel was determined at 3 bar, injection pressure employed in the experiments, and 298K. Injection mass flow rates of  $H_2$ , COG and  $CH_4$  at 3 bar are 0.6 g/s, 1.4 g/s and 2 g/s, respectively. However, in the case of simulations of COG at  $\lambda = 1$  and in the case of  $\lambda = 1.5$  at 5000 rpm, the density was calculated at 4 bar and 298K, as the injection pressure was increased during these experiments, with an injection mass flow rate of 1.62 g/s. As the symmetry plane of the geometry divides the injection area to the half, the mass flow rates were also halved for the calculation of the injection velocity. The resulting values of the injection velocity for each simulation run are collected in Table 4.2.

Table 4.2. Simulation planning and spark and injection specifications at each operating condition.

Fuel	$\lambda$	Engine Speed (rpm)	Spark advance (CAD)	Injection pressure (bar) ; velocity (m/s)	Pulse width (CAD)	EOI (CAD)
<b>H<sub>2</sub></b>	1.5	2000	10	3 ; 275	93	485
		3000	10		150	490
		4000	15		216	495
		5000	15		278	500
	2	2000	25		76	485
		3000	25		120	490
		4000	25		179	495
		5000	25		225	500
<b>CH<sub>4</sub></b>	1	2000	25	3 ; 115	96	480
		3000	30		149	485
		4000	30		230	490
		5000	30		284	495
	1.5	2000	45		69	485
		3000	60		107	490
		4000	60		164	495
		5000	60		201	500
<b>COG</b>	1	2000	15	4 ; 113	145	480
		3000	15		228	485
		4000	20		346	490
	1.5	2000	25	3 ; 150	121	495
		3000	25		191	490
		4000	25		288	495
		5000	25	4 ; 113	310	500
	2	2000	40	3 ; 150	97	485
		3000	45		152	490
		4000	45		226	495
		5000	45		282	500

The end of injection (EOI) CAD for each engine speed and air-fuel ratio are also shown in Table 4.2. These EOI values were selected to be earlier at lower engine speeds and richer air-fuel mixtures to reduce the residual fuel in the intake manifold, according to the recommendations of Liu et al. [8]. For instance, at  $\lambda = 1.5$ , the EOI values would be 500 CAD at 5000 rpm and 485 CAD at 2000 rpm, while at  $\lambda = 1$ , the EOI values recommended are

495 CAD at 5000 rpm and 480 CAD at 2000 rpm. In this way, enough time was provided for the gas to enter into the cylinder due to the travel distance from the injector to the intake valve [35]. Therefore, the accumulation of the fuel in the intake manifold was reduced during the subsequent cycles, diminishing the possibility of backfire. Finally, the pulse width, defined as the number of CAD in which injection is produced, was adjusted to achieve the desired  $\lambda$  value.

An example of fuel injection is visualized with snapshots in Figure 4.3 in terms of  $H_2$  mole fraction for the case of  $H_2$  at  $\lambda = 1.5$  and 4000 rpm. The injection starts in 280 CAD (Table 4.2), 10 CAD before the first snapshot. As observed,  $H_2$  is injected into the intake manifold during the expansion stroke, providing time to reach the intake valve until IVO event (Table 4.1). Once the intake valve has moved a certain lift and the piston starts to reduce pressure within the cylinder due to its downward movement, the fuel is dragged with the air into the cylinder. As the intake stroke progresses, a more homogeneous air-fuel mixture is created with the aid of the swirls inside the cylinder. The injection ends at 495 CAD (Table 4.2), which provides enough time to the accumulated  $H_2$  in the intake manifold to be drawn into the cylinder until the IVC event (Table 4.1).

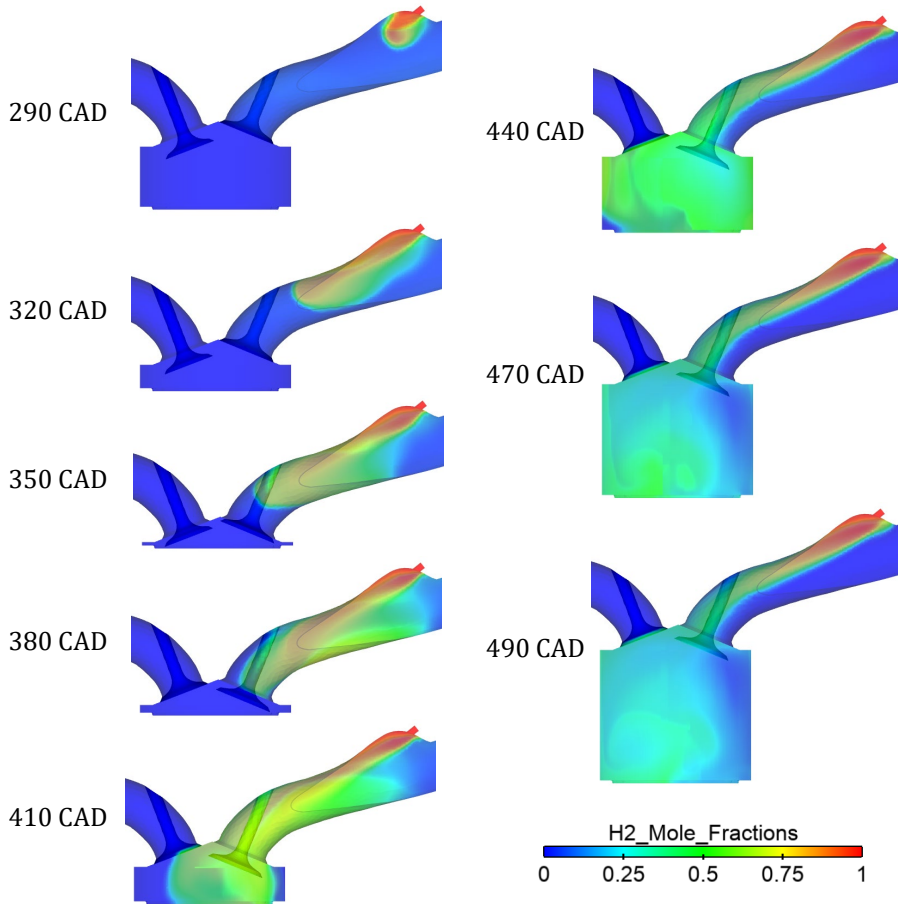


Figure 4.3. Snapshots of H<sub>2</sub> mole fraction during injection at  $\lambda=1.5$  and 4000 rpm. (Screenshots used courtesy of ANSYS, Inc.)

Finally, as the software provides the “indicated” values inside the cylinder, to obtain comparable results with the experiments (“brake” values), a mechanical efficiency ( $\eta_m$ ) correlation was applied, only dependent on engine speed [36]. The maximum  $\eta_m$  was considered as 90% at 2000 rpm, decreasing linearly to 75% at 5000 rpm [37].



### 4.3. Results and discussion

The simulation results exposed in this section correspond to the fourth cycle of the engine, since the variability between cycles is reduced from this cycle onwards. First of all, the engine performance in terms of output power and heat released is described. In addition, the evolution of some variables inside the cylinder is graphed, such as pressure, temperature, apparent heat release rate (AHRR) and mass fraction of OH and NO. Afterward, the fluid dynamics in terms of volumetric efficiency and mass flow rates and mass exchanges between the cylinder and the manifolds are studied. Finally, a sensitivity analysis of the spark advance with COG is carried out to observe the influence of this variable on the engine performance.

#### 4.3.1. Engine performance

In the first place, the simulated in-cylinder pressure has been validated with experimental results, demonstrating the good match between model predictions and experimental performance. The average in-cylinder pressure curves for  $H_2$  at different engine speeds and air-fuel ratios are shown in Figure 4.4. Peak pressure relative errors of 3.37%, 1.08% and 0.88% are obtained for 2000 rpm, 5000 rpm and 3200 rpm cases, respectively. In addition, the pressure evolution inside the cylinder for  $CH_4$  at 1800 rpm is also graphed in Figure 4.4, with a peak pressure relative error of 0.65%. Therefore, this good agreement between simulated and experimental results makes the model very reliable in the in-cylinder pressure variable. Regarding the air-fuel ratio trend, the employment of leaner mixtures ( $\lambda = 2$ ) reduces the pressure within the cylinder. In addition, the role of spark advance is highly apparent, increasing the maximum pressure of the curve at 2000 rpm over the 5000 rpm curve due to the higher spark advance in the case of  $H_2$ , and even higher pressure with  $CH_4$  with an earlier spark ignition timing.

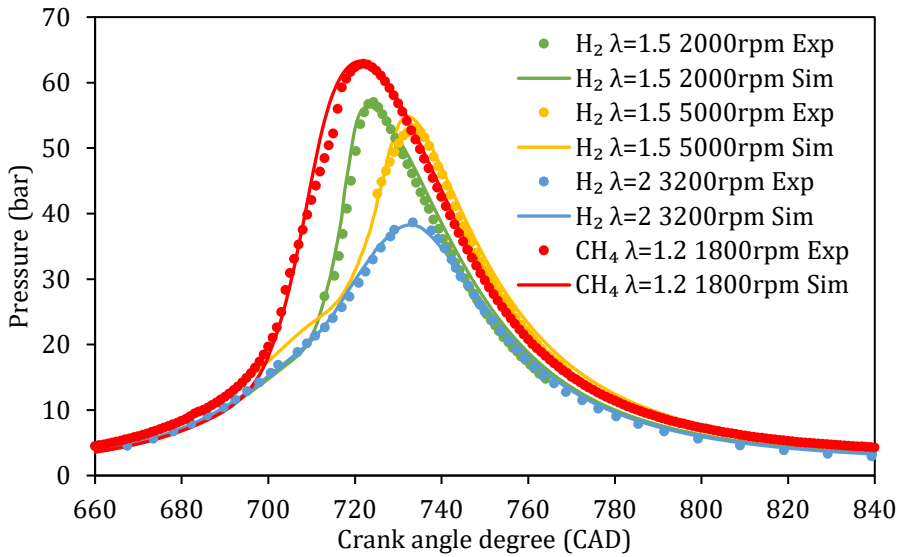


Figure 4.4. Experimental (dots) and simulated (lines) results of in-cylinder pressure (bar) for  $H_2$  at  $\lambda=1.5$  (2000 rpm and 5000 rpm) and at  $\lambda=2$  (3200 rpm) and  $CH_4$  at  $\lambda=1.5$  and 1800 rpm versus the crank angle degree (CAD). [5,38]

In addition, validation results between experiments and simulations are provided in the Appendix with a parity graph of the brake mean effective pressure (BMEP) and brake specific fuel consumption (BSFC) in Figure A.4.1. A bar graph comparing the experimental and simulated  $CO_2$  emissions in %vol has been also plotted in Figure A.4.2. Furthermore, the weighted standard deviation ( $\sigma_w$ ) statistical parameter for the performance variables (Table A.4.2) is provided. A good agreement can be noticed, with a deviation lower than 12% for power and BMEP, 14.2% for BSFC and brake specific energy consumption (BSEC) and up to 16.3% for the thermal efficiency ( $\eta_t$ ).

The experimental and simulated brake power of  $H_2$ ,  $CH_4$  and COG are graphed in Figure 4.5. The good agreement between experiments and simulations is observed. Furthermore, the total chemical heat release (CHR) and total wall heat transfer (WHT), two variables directly related to the generated power, of COG,  $CH_4$  and  $H_2$  are graphed at different  $\lambda$  values in Figure 4.6. Both variables are calculated by the software Ansys Forte® inside the cylinder. The CHR (J) is defined as the accumulation of the heat release from the combustion chemical reactions, remaining constant once the combustion is completed. The stages of the evolution of the combustion are calculated in the simulations as the CAD after spark

ignition in which a certain percentage of the total CHR for that cycle is released. According to Heywood et al. [37], two main stages can be differentiated:

- Flame-development stage ( $\Delta\theta_d$ ): crank angle interval between the spark discharge and the time when 10% of the fuel chemical energy has been released. It is mainly influenced by the mixture state, composition and gas motion near the spark plug.
- Rapid-burning angle ( $\Delta\theta_b$ ): crank angle interval required to burn the bulk of the charge, between the end of  $\Delta\theta_d$  and the end of the flame-propagation process (90% of the fuel chemical energy released). The duration of this stage depends on the conditions across the combustion chamber.

The overall burning angle ( $\Delta\theta_o$ ) is defined as the duration of the global burning process, which is the sum of  $\Delta\theta_d$  and  $\Delta\theta_b$ . The stages of combustion of  $H_2$ , COG and  $CH_4$  in all the operational conditions studied in this chapter have been calculated and collected in Table A.4.3 in the Appendix.  $H_2$  combustion takes place at the highest rate due to the higher laminar flame speed ( $S_L$ ), followed by COG and  $CH_4$ . Besides, as the air-fuel mixture becomes leaner (higher  $\lambda$ ), longer combustion durations are produced due to the lower reactivity of the mixture.

On the other hand, the WHT (J) is obtained as the accumulation of heat transfer loss through the walls of the cylinder, varying along the cycle. Therefore, the CHR and the WHT values in Figure 4.6 have been evaluated at EVO before the exhaust process is carried out, and subtracting the heat releases from the previous cycles.

As can be observed in Figure 4.5, the most important factor is the air-fuel ratio, increasing the delivered power as the mixture becomes richer (lower  $\lambda$ ), obtaining higher CHR, pressure and temperature. Nevertheless, the WHT through the walls also increases as the mixture becomes richer (Figure 4.6). In the case of  $CH_4$  at  $\lambda = 1.5$  and high engine speeds, the WHT is higher than at  $\lambda = 1$  due to the very high spark advances, which produce higher heat losses [39].

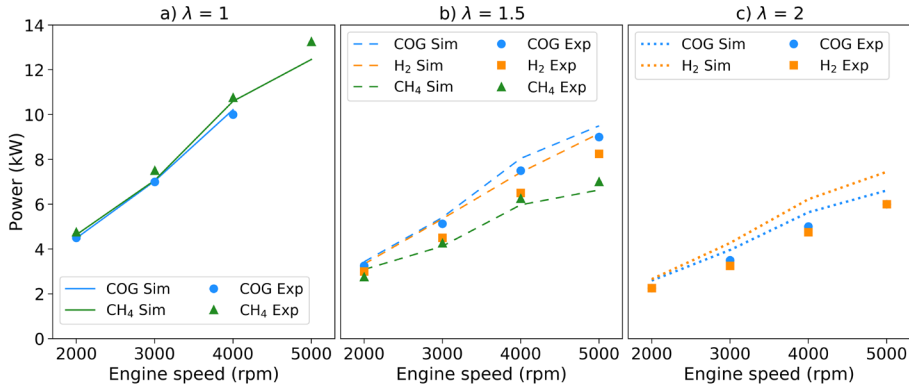


Figure 4.5. Simulated (lines) and experimental (discrete values) brake power (kW) of H<sub>2</sub> (■), CH<sub>4</sub> (▲) and COG (●) versus engine speed at a)  $\lambda=1$  (solid), b)  $\lambda=1.5$  (dashed) and c)  $\lambda=2$  (dotted lines).

In the case of  $\lambda = 1$  (Figure 4.5a), COG and CH<sub>4</sub> provide very similar brake power values because both fuels produce high CHR and WHT, resulting in a low performance difference (Figure 4.6a). At intermediate air-fuel ratio ( $\lambda = 1.5$ ), COG provides the highest power values because the laminar speed ( $S_L$ ) (0.68-0.88 m/s) is higher than for CH<sub>4</sub> (0.38 m/s) and the volumetric lower heating value (LHV) (17.41 MJ/m<sup>3</sup>) is higher than for H<sub>2</sub> (10.65 MJ/m<sup>3</sup>) (see Table 1.3) [40]. As can be observed in Figure 4.6b, COG delivers similar CHR but with the lowest WHT values at  $\lambda = 1.5$  due to a lower value of the maximum temperature, which increases the difference in brake power with respect to H<sub>2</sub> and CH<sub>4</sub>. At 5000 rpm, COG releases 40.1% of WHT less than CH<sub>4</sub> and 14.3% less than H<sub>2</sub>. Thus, the useful energy released with COG is 16.5% and 5.1% higher than CH<sub>4</sub> and H<sub>2</sub> for that case, respectively. On the other hand, CH<sub>4</sub> is the fuel with the highest heat loss through the cylinder walls at  $\lambda = 1.5$  due to the high temperature maintained for a longer time, decreasing the resulting brake power.

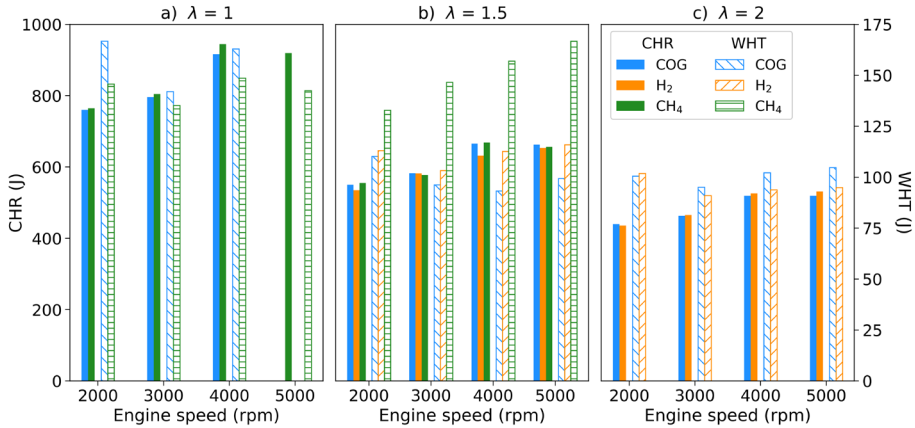


Figure 4.6. Chemical heat release (CHR, in solid bars) and wall heat transfer (WHT, in dashed bars) of COG (blue), CH<sub>4</sub> (green) and H<sub>2</sub> (orange) versus engine speed at a)  $\lambda=1$ , b)  $\lambda=1.5$  and c)  $\lambda=2$ .

With lean mixtures ( $\lambda = 2$ ), COG and H<sub>2</sub> release similar chemical heat. However, as the model predicts higher heat loss through the walls with COG than with H<sub>2</sub> due to a higher peak temperature for a longer period, the useful heat release of COG decreases. In consequence, the simulated brake power of COG is reduced.

Regarding the engine speed, operating at higher values, the power increases for all the gaseous fuels because a higher amount of total mass is dragged into the cylinder. However, in the case of CH<sub>4</sub>, the model predicts that the intake flow is choked at 5000 rpm, resulting in a lower increment in the power performance than the real values obtained through experiments. A deviation between experimental and simulated power values of 16% for CH<sub>4</sub> and  $\lambda = 1$  at 5000 rpm is produced, while the deviation is 15.1% at  $\lambda = 1.5$  and the same engine speed. This explanation is also valid for COG but with a lower effect due to its intermediate density, with a deviation of 5.8% at 5000 rpm and  $\lambda = 1.5$ .

#### 4.3.2. Dynamic evolution variables

In this section, some variables that dynamically vary during the 720 CAD of the cycle are going to be studied. Ansys® Forte® software allows the tracking of many variables during the simulation at different regions and points of the geometry. In Figure 4.7, the average pressure, average

temperature and apparent heat release rate (AHRR) inside the cylinder for the three gaseous fuels are graphed during the fourth simulated cycle in the entire speed range and all air-fuel ratios. The AHRR (J/CAD) is provided by Forte software as a spatially averaged variable inside the cylinder. It is the result of the difference between the rate of chemical heat release from the combustion reactions and the rate of heat transfer loss through the cylinder walls. Comparing the air-fuel ratio at the same engine speed, a clear tendency can be observed, reducing the maximum values as the mixture becomes leaner (higher  $\lambda$ ). This is an expected behavior as lower CHR is delivered when the air excess increases with respect to the fuel mass (Figure 4.6).

If a comparison between gas fuels is carried out at the same  $\lambda$  value, a trade-off between spark advance and  $H_2$  contribution can be highlighted. In the case of  $\lambda = 1$ , graphed in Figure 4.7a, the contribution of  $H_2$  in the composition of COG translates in a higher combustion rate due to its higher laminar flame speed, which increases the slope of pressure and temperature curves and the maximum values of the rate of apparent heat release compared to  $CH_4$ . In addition, as there is little difference in spark advance between the two gases at the four speeds, low effects on the maximum pressures are derived.

When the air-fuel ratio is 1.5 (Figure 4.7b), a smaller difference in the combustion speed is observed between COG and  $CH_4$ . However, pure  $H_2$  provides higher laminar flame speed, shortening the combustion duration (see Table A.4.3) with faster AHRR and delivering the highest temperatures.  $CH_4$  produces the highest pressure values because the spark is advanced up to 45 CAD between  $CH_4$  and  $H_2$ , and up to 35 CAD between  $CH_4$  and COG. However, peak combustion pressure for  $CH_4$  is obtained before the top dead center at engine speeds higher than 3000 rpm, causing waste work from the piston to the gas at high pressures at the end of the compression stroke (Figure 4.5b). On the other hand, COG and  $H_2$  have close spark timing values, and therefore, similar maximum pressures are achieved. The value of the maximum temperatures and the duration in CAD in which these high values are maintained exert influence on the wall heat transfer, increasing the heat loss as longer and higher peak temperatures are achieved (Figure 4.6b).

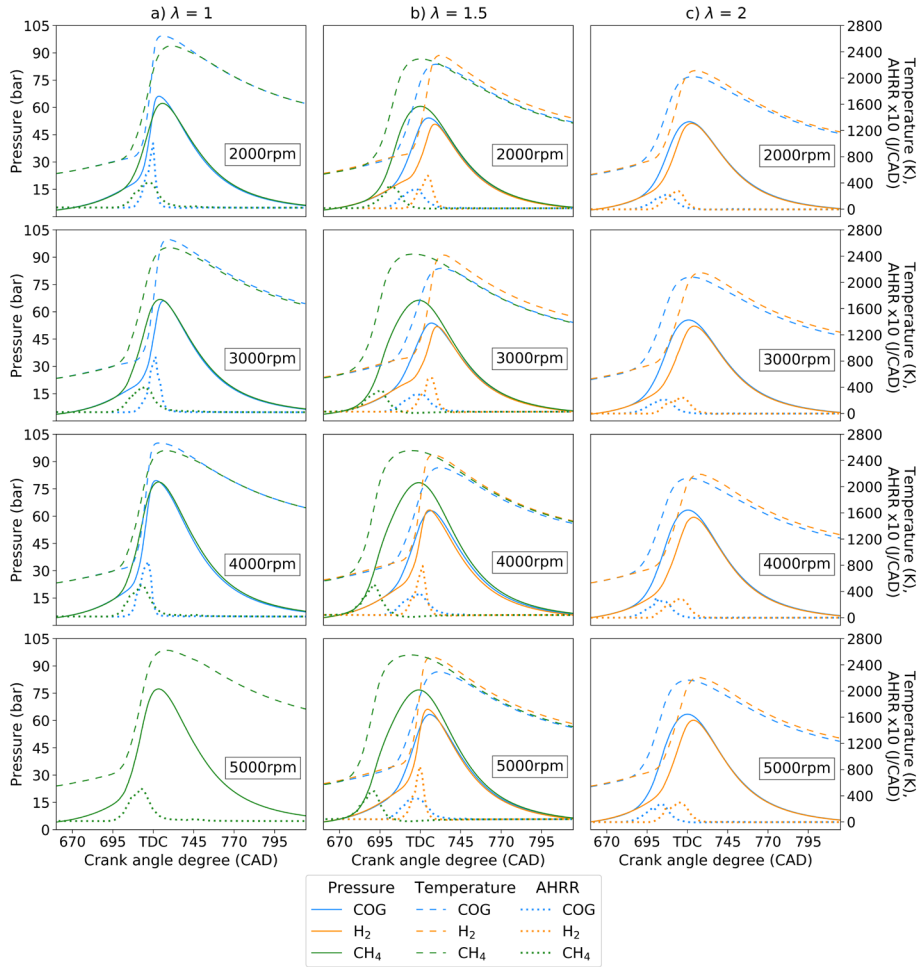


Figure 4.7. Pressure (solid lines), temperature (dashed lines) and AHRR (represented 10 times higher and with dotted lines) inside the cylinder at a)  $\lambda=1$ , b)  $\lambda=1.5$  and c)  $\lambda=2$  for H<sub>2</sub> (orange), CH<sub>4</sub> (green) and COG (blue) gaseous fuels in the entire speed range.

Thus, COG benefits from the advantages of both pure fuels. Suitable peak pressures are achieved while lower peak temperatures than CH<sub>4</sub> and H<sub>2</sub> are obtained, reducing the wall heat transfer. In this way, higher power output is produced with COG, especially at high engine speeds.

Finally, in the case of  $\lambda = 2$  (Figure 4.7c), the laminar flame speed ( $S_L$ ) has a lower influence with very lean mixtures, reducing the difference in the slope of pressure and temperature between H<sub>2</sub> and COG, and reaching similar maximum values in AHRR. The earlier spark timing of COG provides higher pressure values (analyzed in Figure 4.14 in section 4.3.5).

Regarding engine speed, as the rotation speed is increased, the piston displaces at a higher velocity and a greater vacuum is created, inducing a larger mass of air into the cylinder. This phenomenon enables the release of higher chemical energy and power.

The evolution of temperature and mass fraction of OH radical ( $\bullet\text{OH}$ ) and NO inside the cylinder of the three gaseous fuels at 4000 rpm and  $\lambda = 1.5$  is graphed in Figure 4.8 employing the EnSight® module from Ansys®. Four CAD relative to the spark ignition have been selected to compare the three fuels at the same basis, as the spark ignites at different CAD for each gas (Table 4.2). Furthermore, the exhaust valve opening (EVO) CAD has been added to see a comparison of the three fuels when the emissions are exhausted. OH is a very interesting radical for the visualization of flame propagation, as it is the most important intermediate product in combustion with a very high activity due to the presence of unpaired electrons [7,41]. Thus, OH reflects the intensity of combustion [42].

As can be observed, the highest laminar flame speed of  $\text{H}_2$  (2.65 - 3.25 m/s) produces the largest temperature core in the spark region at 10 CAD later than spark ignition (Spark + 10 CAD). This generates a higher mass fraction of OH radical where the highest temperature is achieved [7] and a little production of NO. As the CAD progresses, a high mass fraction core of OH and NO are generated in the spark region due to the high combustion intensity [41], with a fast decrease as moving away from the flame front. After this, a more homogeneous OH concentration is produced and the NO mass fraction is dispersed along the symmetrical plane with higher concentration in the head and piston areas. Finally, at EVO, a quasi-homogeneous temperature and NO concentration within the cylinder are achieved.



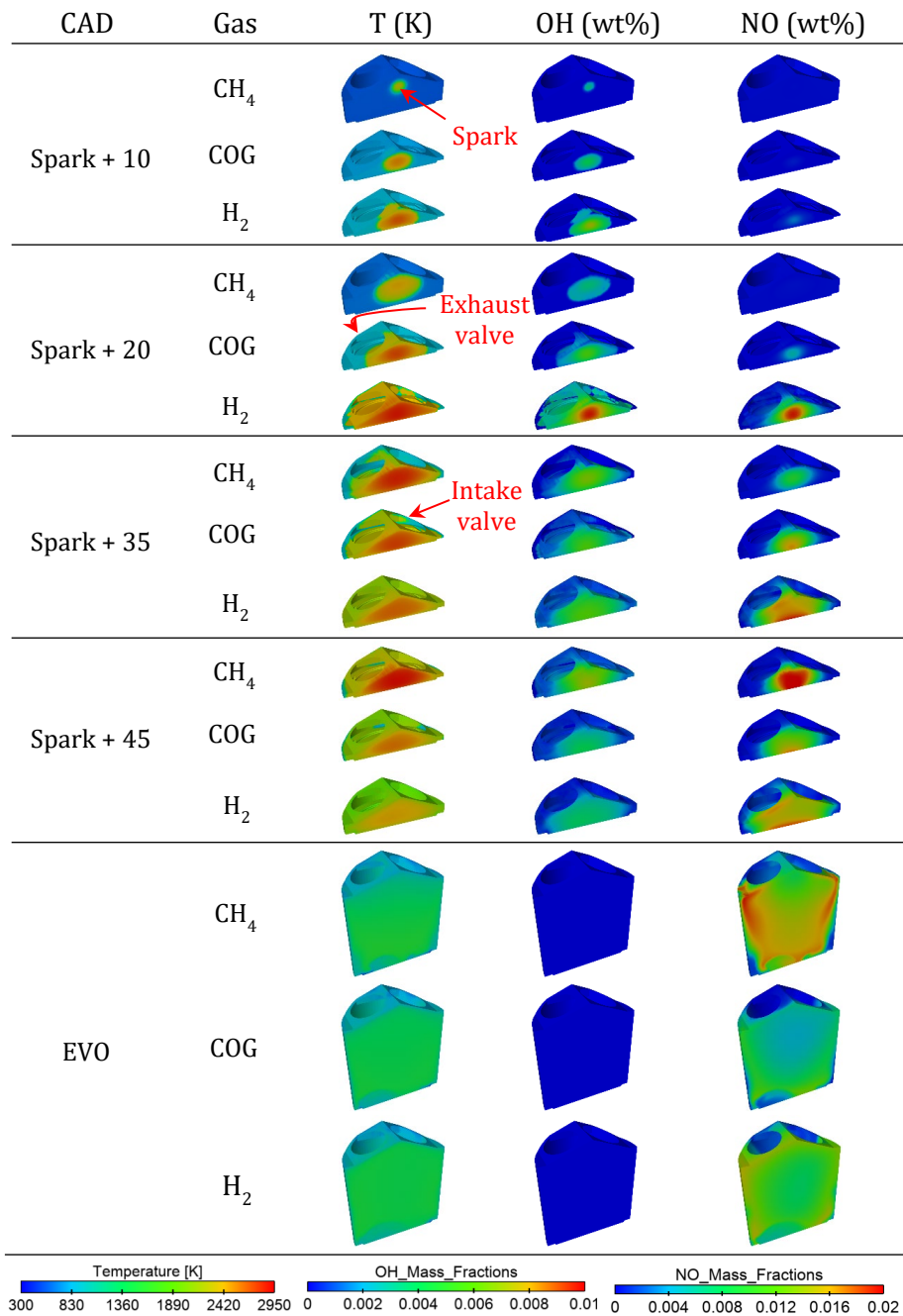


Figure 4.8. Temperature (K) and OH and NO mass fraction (wt%) evolution inside the cylinder of CH<sub>4</sub>, COG and H<sub>2</sub> at four CAD relative to spark timing and at EVO operating at 4000 rpm and  $\lambda=1.5$ . (Screenshots used courtesy of ANSYS, Inc.)

In the case of  $\text{CH}_4$ , the temperature core due to flame propagation grows slower due to a low  $S_L$  (0.38 m/s), reaching the cylinder walls and generating NO at 35 CAD after spark ignition. Nevertheless, due to the high spark advance (60 CAD before TDC in this case), the very high temperature core is maintained for a longer time within the cylinder, increasing NO emissions with a very high concentration mass fraction core of NO in the spark region. At EVO, the NO mass fraction is concentrated heterogeneously, mainly near the cylinder walls and the piston in the central part of the cylinder. Therefore, the high spark advance required for  $\text{CH}_4$  at  $\lambda = 1.5$  increases notably the NO emissions, reducing its feasibility as clean fuel at lean air-fuel mixtures.

On the other hand, COG, with an intermediate  $S_L$  (0.68 – 0.88 m/s), generates a core of temperature and OH with a delay with respect to  $\text{H}_2$ , reaching the cylinder walls in less than 35 CAD after spark ignition. However, the lower maximum values of temperature (Figure 4.7) and OH reached during the combustion produce lower NO emissions. Therefore, this makes COG an interesting alternative gaseous fuel with the highest performance (Figure 4.5b) and lowest NO emissions compared to pure  $\text{H}_2$  and pure  $\text{CH}_4$  at intermediate air-fuel ratios.

In order to provide a further comparison between the fuels, the simulated flame growth speed (m/s), which is the time derivative of the growth of the flame radius, was calculated as the ratio of the increment of the radius (m) and the time elapsed between consecutive simulation steps (s). The resulting flame growth speeds of  $\text{H}_2$ , COG and  $\text{CH}_4$  at 4000 rpm and  $\lambda = 1.5$  are graphed in Figure 4.9. As can be observed, after a first high increment in the spark radius when it is discharged, the speed of the flame growth increases and reaches a maximum value, as expected in a “spherical” shape flame front and then decreases to zero [43]. Initially, the flame has a spherical shape (as seen with the  $\text{CH}_4$  case in Figure 4.8), but as the flame increases and reaches the cylinder boundaries, an ellipsoidal shape is adopted. This can be further observed in the flame brush thickness evolution of COG at 4000 rpm and  $\lambda = 1.5$  graphed in Figure A.4.3 in the Appendix.

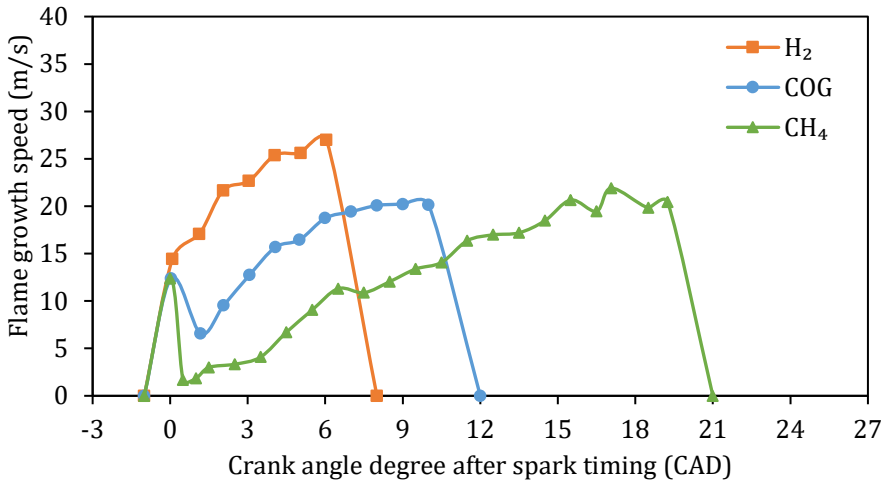


Figure 4.9. Flame growth speed (m/s) versus crank angle degree after spark timing (CAD) of H<sub>2</sub> (orange), COG (blue) and CH<sub>4</sub> (green) at 4000 rpm and  $\lambda=1.5$ .

H<sub>2</sub>, with the highest  $S_L$ , develops the flame faster and in a shorter time period, increasing the temperature and generating the OH mass fraction at a higher rate than the other two gaseous fuels (Figure 4.8). On the other hand, CH<sub>4</sub> has the lowest laminar flame speed and develops the flame at a slower rate, requiring a higher period of crank angle degrees to reach the maximum and then decreases to zero, extinguishing. This can be confirmed with the flame-development angle ( $\Delta\theta_d$ ) from Table A.4.3 (see the Appendix), which describes the CAD between the spark discharges and the release of the 10% of the CHR. COG has an intermediate laminar flame speed but due to the high H<sub>2</sub> percentage, requires less time to reach the maximum spark development before vanishing. Furthermore, a more stable flame development can be observed.

#### 4.3.3. Volumetric efficiency

In order to study the influence of the gas composition, engine speed and air-fuel ratio variables in the cylinder filling process, the volumetric efficiency ( $\eta_v$ ) is graphed in Figure 4.10.  $\eta_v$  is defined as the ratio of the actual mass of air introduced in the cylinder to the theoretical mass that would enter at atmospheric conditions (1 atm and 298 K), as shown in Equation (1.10).

$$\eta_v = \frac{m_{air}}{\rho_{air} \cdot V_d} = \frac{\dot{m}_{air} \cdot n_R}{\rho_{air} \cdot N \cdot V_d} \quad (1.10)$$

Hydrogen has the lowest  $\eta_v$  because this gas displaces a large amount of incoming air due to its lower density, reducing the available air in the cylinder [44]. In consequence, the mixture mass inside the cylinder is reduced, which decreases the power delivered and the CHR (Figure 4.5 and Figure 4.6). CH<sub>4</sub> has the highest  $\eta_v$  due to its higher density. This is confirmed by the experiments carried out with many different fuels by Pourkhesalian et al. [45]. COG, with an intermediate gas density, provides higher  $\eta_v$  values than H<sub>2</sub> but lower than CH<sub>4</sub>.

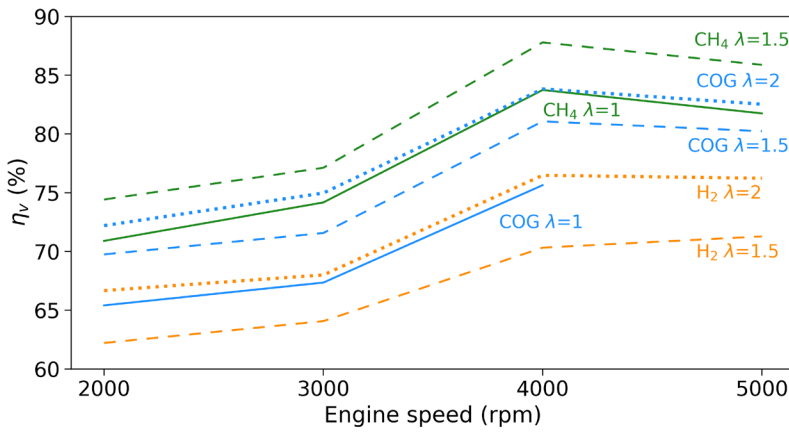


Figure 4.10. Volumetric efficiency of H<sub>2</sub> (orange), CH<sub>4</sub> (green) and COG (blue) at  $\lambda=1$  (solid lines),  $\lambda=1.5$  (dashed lines) and  $\lambda=2$  (dotted lines) versus engine speed.

Regarding  $\lambda$ , as the mixture becomes leaner, lower fuel is required and a higher amount of air is able to enter into the cylinder, getting closer to the theoretical amount [44]. Finally, as the engine speed rises, the piston increases the vacuum created, which drags a higher amount of air into the cylinder, boosting the volumetric efficiency. In the case of CH<sub>4</sub> and COG, as previously mentioned, the maximum values are obtained at 4000 rpm because at higher engine speed, the intake flow becomes choked, limiting the air flow and reducing the volumetric efficiency due to higher pressure loss [45,46]. In the case of H<sub>2</sub>, this effect is delayed to higher engine speeds because the mass of air induced is reduced due to the lower density of H<sub>2</sub>.

A higher leap in the cylinder mass is observed between 3000 rpm and 4000 rpm than for the rest of the engine speeds for all the gases and  $\lambda$ . This effect is a consequence of the wave pressures in the manifolds, which

are induced by the pressure variation inside the cylinder during the intake and exhaust strokes. Wave pressures inside the intake manifold are dependent on the geometry design and the engine speed, but independent of the fuel used or the  $\lambda$  value, as observed in Figure 4.11 for the three fuels in the entire range of air-fuel ratios and engine speeds.

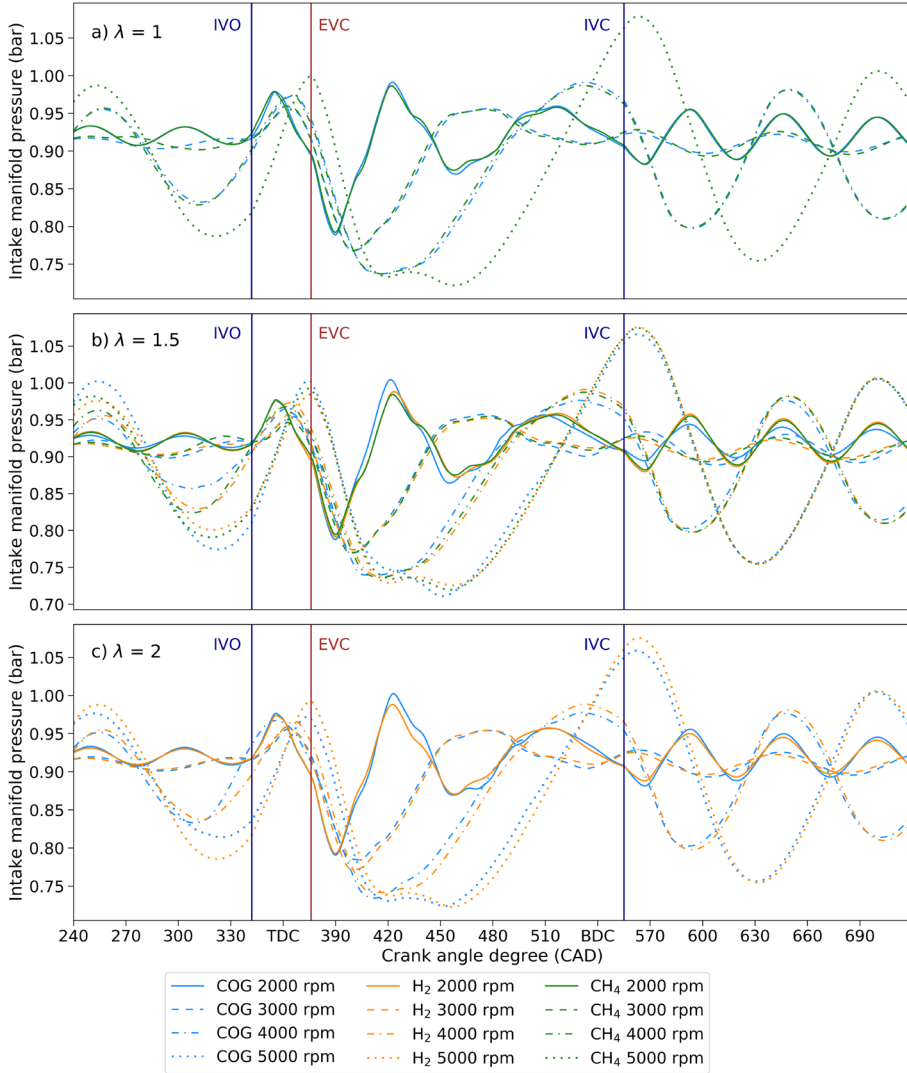


Figure 4.11. Intake manifold pressure (bar) of COG (blue), H<sub>2</sub> (orange) and CH<sub>4</sub> (green) at a)  $\lambda=1$ , b)  $\lambda=1.5$  and c)  $\lambda=2$  in the whole range of engine speeds (IVO: intake valve opening, EVC: exhaust valve closure, IVC: intake valve closure).

As in the intake manifold case, the wave pressures in the exhaust manifold, graphed in Figure 4.12 for the three fuels at all operating conditions, depend on the geometry design and the engine speed. However, as can be observed, there is also a dependence on the  $\lambda$  value and the combustion process, especially at low  $\lambda$  and high engine speeds.

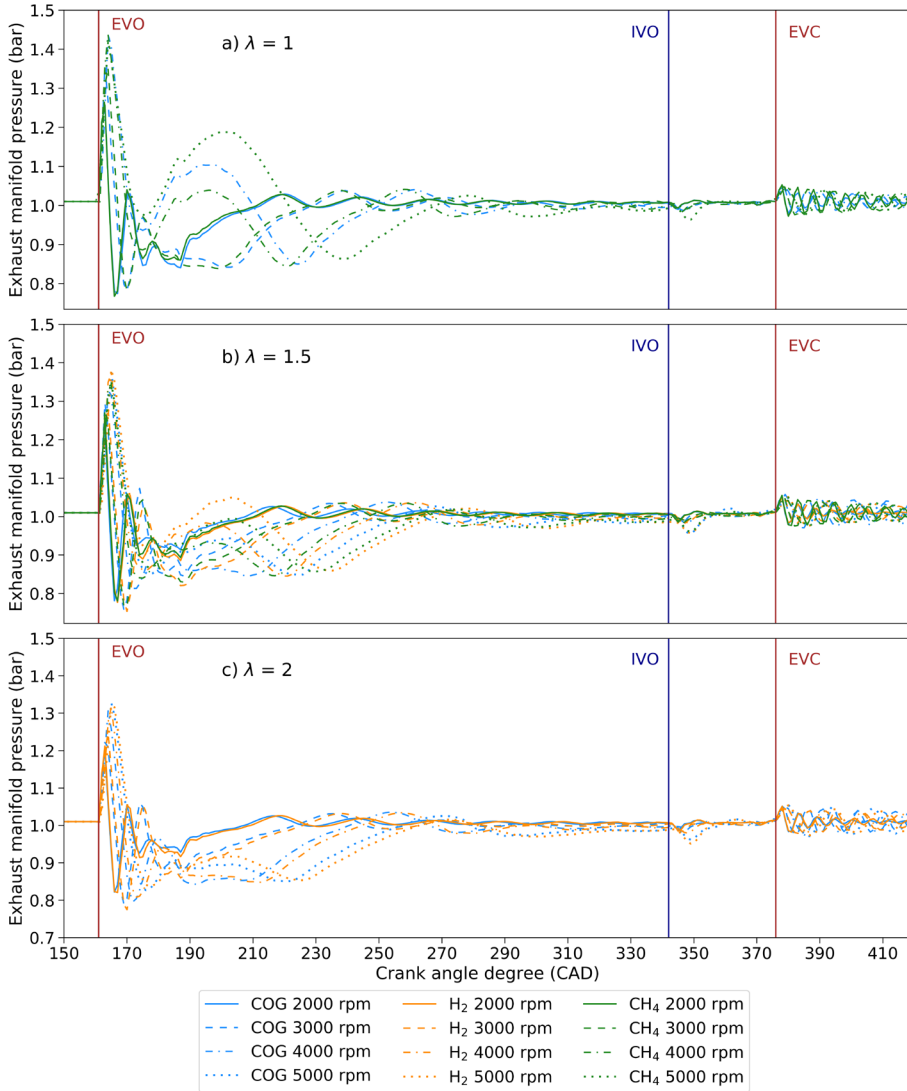


Figure 4.12. Exhaust manifold pressure (bar) of COG (blue), H<sub>2</sub> (orange) and CH<sub>4</sub> (green) at a)  $\lambda=1$ , b)  $\lambda=1.5$  and c)  $\lambda=2$  in the whole range of engine speeds (EVO: exhaust valve opening, IVO: intake valve opening, EVC: exhaust valve closure).

The manifold wave pressures influence the filling and exhaust processes of the cylinder [47]. In Figure A.4.4, the mass flow rates and accumulated mass transport exchange between the cylinder and the manifolds of COG at  $\lambda = 2$  and all the engine speeds are explained and graphed. The effects on the mass transport exchanges due to the valve overlap period graphed in Figure 4.2a are also explained. In addition, the mass exchange processes are graphed for all the fuels,  $\lambda$  values and engine speeds in Figure A.4.5, Figure A.4.6 and Figure A.4.7.

Furthermore, Figure 4.13 shows the fluid dynamics between the cylinder and the exhaust and intake manifolds for the simulation of  $H_2$  at  $\lambda = 1.5$  and 4000 rpm.

As can be noticed, the end of the exhaust process is carried out at high fluid velocity due to the pressure difference between the cylinder and the exhaust manifold and due to the upward movement of the piston. On the other hand, as this engine is naturally-aspirated, the fluid is introduced slowly at the beginning of the intake stroke, raising the velocity as the vacuum created by the piston with its downward movement increases. The swirls created within the cylinder by the intake valve promote the homogenization of the air-fuel mixture, which favors a more complete combustion.

Therefore, the engine design should take into account these effects when working with gaseous fuels to optimize the intake and exhaust processes to increase the mass of the air-fuel mixture inside the cylinder, reduce the residual mass fraction and avoid choking. This would increase the power output and the efficiency of the engine.

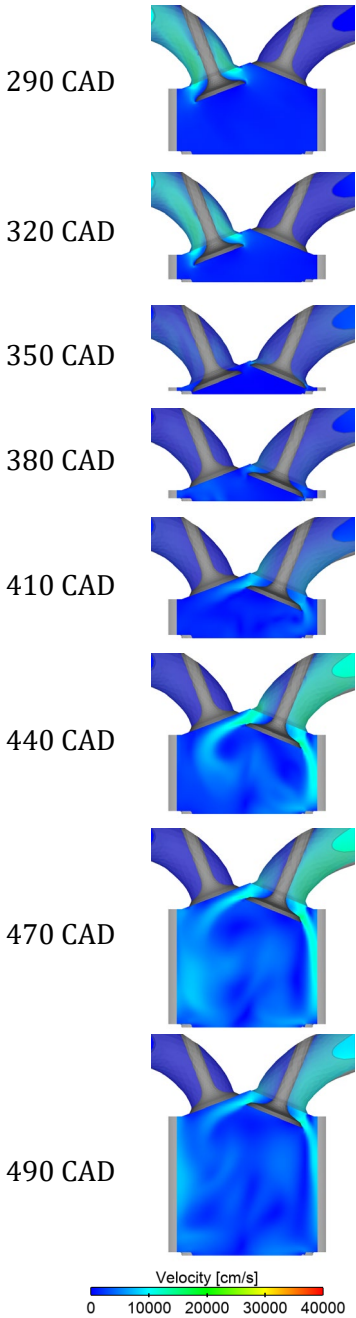


Figure 4.13. Fluid dynamics between the cylinder and the manifolds for  $H_2$  at  $\lambda=1.5$  and 4000 rpm.



#### 4.3.4. Sensitivity analysis of COG fuel low-content components

Regarding the role played by the fuel low-content components (CO and CO<sub>2</sub>) from COG, a sensitivity analysis on the composition has been carried out with the CFD model. The case studies considered are as follows, substituting the component by N<sub>2</sub> (in vol%):

- A: original COG (57% H<sub>2</sub>, 30% CH<sub>4</sub>, 6% CO, 2% CO<sub>2</sub>, 5% N<sub>2</sub>)
- B: CO<sub>2</sub> converted to N<sub>2</sub> (57% H<sub>2</sub>, 30% CH<sub>4</sub>, 6% CO, **0% CO<sub>2</sub>**, 7% N<sub>2</sub>)
- C: CO converted to N<sub>2</sub> (57% H<sub>2</sub>, 30% CH<sub>4</sub>, **0% CO**, 2% CO<sub>2</sub>, 11% N<sub>2</sub>)
- D: CO and CO<sub>2</sub> converted to N<sub>2</sub> (57% H<sub>2</sub>, 30% CH<sub>4</sub>, **0% CO, 0% CO<sub>2</sub>**, 13% N<sub>2</sub>)

Simulations were done at  $\lambda = 1.5$  and 2000 rpm. As the fuel density (g/L), the molar weight (g/mol) and the LHV (MJ/kg) are modified with the composition, the fuel injection has been adjusted in terms of injection velocity and pulse width to fit to the desired  $\lambda$  value.

The results are summarized in Table 4.3. As can be observed, the cases with CO (A and B) deliver the highest power, torque, BMEP and CHR values. A little decrease in the power (0.3%) is observed with the removal of CO<sub>2</sub> (B) due to a reduction in the density, and therefore in the total mass and fuel introduced into the cylinder. In addition, the removal of CO<sub>2</sub> decreases the emissions of CO<sub>2</sub> by 5.5%.

On the other hand, if the CO component is removed (case C), the power is reduced by 1.26% and the CHR decreases by 0.94% with respect to the original COG (A); however, the CO<sub>2</sub> emissions are reduced by 13.2%, which is a significant decrease because there is no CO combustion. Finally, if the CO and CO<sub>2</sub> components are substituted by N<sub>2</sub> (case D), a similar performance is obtained but the CO<sub>2</sub> emissions are reduced by 18.7% with respect to the original COG composition (A).

Table 4.3. Simulation results of the sensitivity analysis of COG fuel low-content components at four different case studies: A (original COG), B (without CO<sub>2</sub>), C (without CO) and D (without CO and CO<sub>2</sub>).

Case study	P (kW)	Torque (Nm)	BMEP (bar)	$\eta_t$ (%)	CHR (J)	Cylinder mass (mg)	CO <sub>2</sub> (%)
A	3.40	16.25	5.87	37.15	545.68	309.12	5.374
B	3.39	16.20	5.86	37.15	544.18	308.45	5.08
C	3.36	16.04	5.8	37.05	540.53	308.06	4.663
D	3.36	16.05	5.81	37.12	539.93	307.46	4.368

In conclusion, the role played by fuel low-content components from COG waste stream in engine performance is very low compared to the original composition, though a significant effect on CO<sub>2</sub> emissions can be observed. This should be taken into account if further restrictions on CO<sub>2</sub> emissions in engines are required.

#### 4.3.5. Spark advance sensitivity analysis

In addition to the previous comparison carried out for H<sub>2</sub>, CH<sub>4</sub> and COG with optimum spark advance, a brief analysis of the impact of the spark advance with model simulations will be carried out to support the aforementioned explanations. Simulations for COG at  $\lambda = 1.5$  and 3000 rpm varying the spark advance between 660 CAD to 730 CAD have been done.

Figure 4.14 shows the pressure and temperature evolution inside the cylinder for the different spark timings. As can be observed, as the spark is ignited earlier, the maximum values of pressure and temperature increase and are advanced with respect to TDC. However, in the case of spark timing at 660 and 670 CAD, the combustion finishes before TDC, but the pressure still increases further with a different slope due to the compression of the piston up to TDC. As the pressure after combustion inside the cylinder is very high, this increases the required work that the piston must exert to continue compression, decreasing the apparent heat release and the power output. On the other hand, the temperature reaches high values due to combustion and it still increases a little with the piston compression until TDC, decreasing afterward as the piston goes down.

As the spark is delayed, the pressure and temperature combustion peaks are closer or even after TDC, which avoids the waste of useful work on piston compression. Furthermore, the slopes of pressure and temperature tend to decrease, producing lower rates of chemical heat release. Besides, the total wall heat transfer is reduced because the high temperatures are maintained for a shorter time.

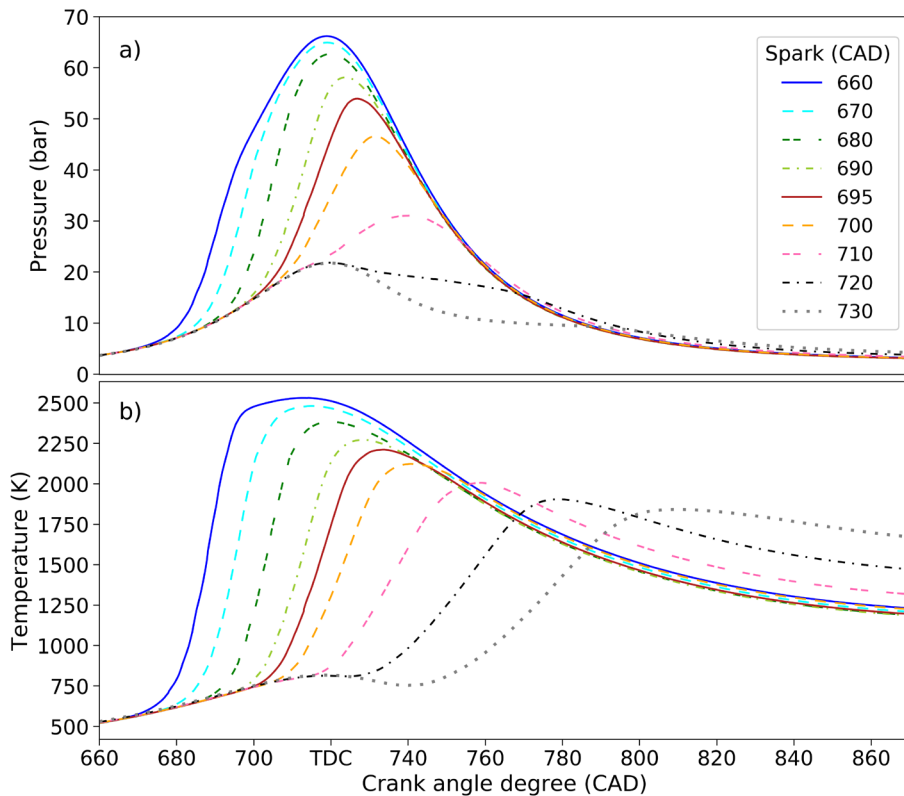


Figure 4.14. In-cylinder pressure (a) and temperature (b) for COG at 3000 rpm and  $\lambda=1.5$  at different spark ignition timings.

In the case of spark timing at 710 CAD, the combustion pressure peak is reached 20 CAD after TDC, when the piston has already started to move down, increasing the available cylinder volume. Thus, the peaks of pressure and temperature are reduced compared to higher SA values. With spark timings of 720 and 730 CAD, combustion takes place because the peak temperatures are greater than the temperatures corresponding only to compression (motoring conditions), which are around 820 K. However, the very high spark delays cause that the peak pressures from

combustion are lower than the pressure inside the cylinder at TDC due to gas compression (around 22 bar) because the available volume has increased.

In terms of performance, the spark advance has a high influence on the output variables, such as power and efficiency. As explained in section 1.3.2, the work transfer from the gas to the piston is the result of the integration around the pressure – volume curve ( $p - V$ ), known as indicator diagram [37]. In Figure 4.15, the indicator diagrams of the simulations of COG at 3000 rpm and  $\lambda = 1.5$  varying the spark timings are graphed. When the compression pressure, from point (1) to point (2), is lower than the expansion pressure, from point (3) to point (4), positive work is transferred from the gas to the piston due to combustion and visualized as the areas enclosed in the  $p - V$  diagram. The larger the area, the greater the work transferred to the piston and higher power output. However, for spark timings at 660 and 670 CAD, a small area is observed in the zoom detail where the compression pressure is higher than the expansion pressure at volumes lower than 60 and 50 cm<sup>3</sup>. This means that work is transferred from the piston to the gas because the combustion peak pressure is reached before TDC (Figure 4.14), and the piston has to compress the combustion products at higher pressure. Thus, a loss of work is produced for compression, reducing the power output. On the other hand, with high delayed spark timings (later than 720 CAD), the combustion peaks of pressure are reduced, even below TDC, decreasing the area and the gross work obtained.

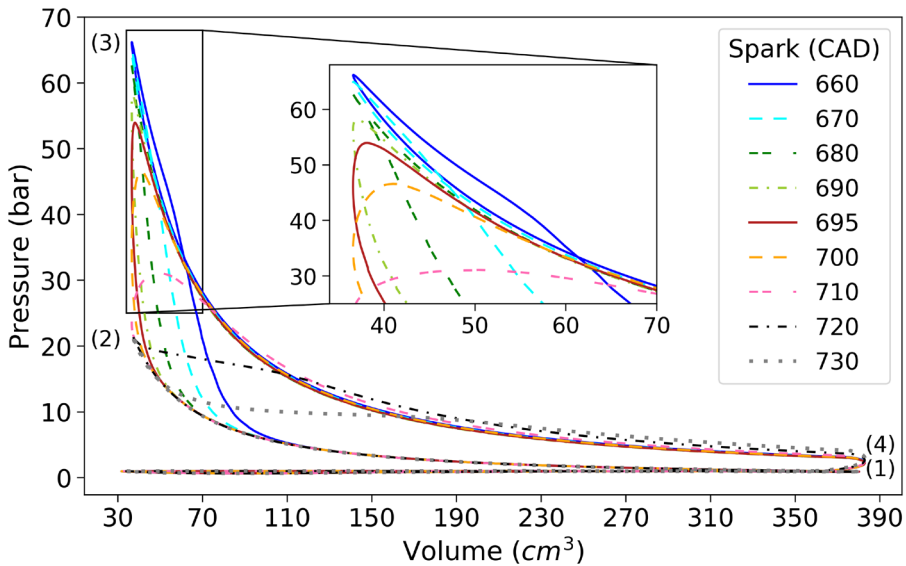


Figure 4.15. Indicator diagram ( $p - V$ ) at different spark timings of COG at  $\lambda=1.5$  and 3000 rpm.

Figure 4.16 supports these arguments plotting the influence of spark timing in brake power (kW), brake specific fuel consumption (BSFC) (g/kWh) and emissions of  $\text{CO}_2$  (%) and including the experimental values at 695 CAD. Very advanced or delayed spark timings produce a decrease in the brake power and that is the reason why experiments were carried out at optimal spark advance, providing the highest performance values with spark at 695 CAD. On the other hand, this operating condition delivers the maximum thermal efficiency (35.6%) and minimum BSFC values (254 g/kWh). With earlier spark timings, though the fuel quantity is the same, higher wall heat transfer and less useful work are obtained, decreasing the power and the efficiency, which translates into an increase in BSFC. However, if delayed spark timings are employed, the BSFC rises as the work obtained decreases due to a reduction in the area of  $p - V$  diagram. Regarding emissions, a constant concentration of  $\text{CO}_2$  emissions in %vol is observed for all spark timings. This can be explained because the combustion has been completed similarly, independently of the pressure and temperature achieved, but with different output work.

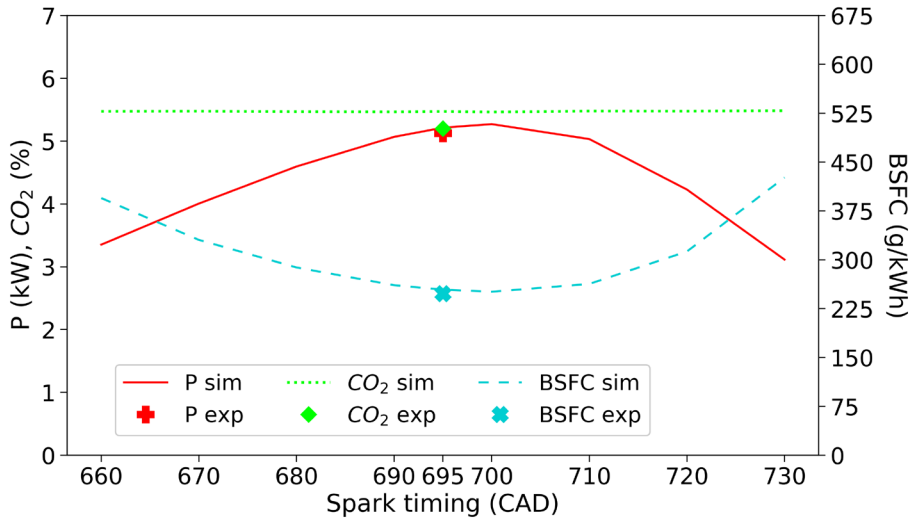


Figure 4.16. Simulated power (solid line), CO<sub>2</sub> emissions (dotted line) and BSFC (dashed line) output variables vs spark timing of COG at 3000 rpm and  $\lambda=1.5$ . Experimental values of P (+), CO<sub>2</sub> (♦) and BSFC (\* ) at spark timing of 695 CAD are included.

In addition, Figure 4.16 shows the good agreement between simulation and experimental values at spark timing of 695 CAD, highlighting the importance of using CFD simulations as a predictive tool for ICE optimization. Furthermore, these simulations enable the prediction of the optimum spark advance to achieve maximum power and efficiency for the different fuels and operating conditions, reducing expenditures during engine experiments.

#### 4.4. Conclusions

In this chapter the assessment of the engine performance and combustion of low-carbon fuels, H<sub>2</sub>, CH<sub>4</sub> and COG, has been carried out through CFD software simulation in terms of pressure, temperature, heat release, emissions, flame growth speed and volumetric efficiency. A CFD model of a symmetrical single cylinder from a naturally-aspirated port-fuel injection Volkswagen Polo 1.4L spark ignition engine has been developed. Simulations of H<sub>2</sub>, CH<sub>4</sub> and COG at the experimental operating conditions detailed in **Chapter 3** were carried out with Ansys® Forte®. The engine speed was varied in the range 2000 – 5000 rpm range and with  $\lambda$  between 1 and 2 at full load (WOT) and optimal spark advance. In

addition, a spark advance sensitivity analysis has been done for COG. A good agreement between simulations and experiments was achieved, with a weighted standard deviation lower than 12% for power and BMEP variables and 16.3% for thermal efficiency.

Leaner mixtures reduce the pressure and temperature inside the cylinder, as well as the chemical heat release and wall heat transfer, decreasing also NO emissions. •OH radical and NO compound are mainly generated in the hot core of the flame, reducing the concentration as moving away from the spark location.

Spark timing plays a key role, increasing the maximum value of pressure and temperature inside the cylinder and the chemical heat release rate operating at higher spark advances. However, higher wall heat transfer reduces the brake power.

Comparing the fuels at intermediate air-fuel ratios ( $\lambda = 1.5$ ), COG delivers the greatest power output due to a higher flame growth speed than  $\text{CH}_4$  and higher volumetric LHV than  $\text{H}_2$ . Therefore, the intermediate spark advance reduces the maximum temperature and pressure within the cylinder, decreasing the wall heat transfer and the NO emissions. For instance, COG releases up to 40.1% and 14.3% of WHT less than  $\text{CH}_4$  and  $\text{H}_2$  at 5000 rpm, increasing the apparent heat release by 16.5% and 5.1%, respectively. In addition, the high volumetric  $\text{H}_2$  percentage in the COG composition reduces the  $\text{CO}_2$  emissions compared to  $\text{CH}_4$ .

$\text{H}_2$  gaseous fuel, with the highest flame growth speed, reduces the combustion duration but increases the OH generation rate and the total NO emissions. On the other hand,  $\text{CH}_4$ , due to the lowest flame growth speed, requires very high spark advance values, increasing the maximum pressure and temperature inside the cylinder and maintaining the high values for a longer period of time. Thus, the wall heat transfer and the NO emissions increase with  $\text{CH}_4$  compared to the other gaseous fuels.

At richer and leaner mixtures ( $\lambda = 1$  and  $\lambda = 2$ ), similar performances are obtained with COG compared to  $\text{CH}_4$  and  $\text{H}_2$ , combining advantages of both pure fuels and widening the air-fuel operation range without abnormal combustion. Therefore, COG offers a very good fuel alternative to  $\text{H}_2$  and  $\text{CH}_4$  in terms of performance and emissions. Furthermore, COG comes from an industrial waste stream, thus, offering a very interesting

alternative for fuel recovery for stationary applications after optimization of the operating conditions.

In this sense, CFD has been identified as a very useful simulation tool in this thesis to acquire a more comprehensive understanding of the fluid dynamics and the combustion phenomena of different fuels and at a wide range of operating conditions. Furthermore, diverse sensitivity analyses have been carried out, evaluating the influence of important variables to achieve the best performance of low carbon fuels in internal combustion engines.

### Nomenclature

AHRR	Apparent heat release rate (J/CAD)
BMEP	Brake mean effective pressure (bar)
BSEC	Brake specific energy consumption (MJ/kWh)
BSFC	Brake specific fuel consumption (g/kWh)
CAD	Crank angle degree
CFD	Computational fluid dynamics
CHR	Chemical heat release (J)
COG	Coke oven gas
CR	Compression ratio
dABDC	Degrees after bottom dead center
dATDC	Degrees after top dead center
dBBDc	Degrees before bottom dead center
dBTDc	Degrees before top dead center
DI	Direct injection
EOI	End of injection
EVC	Exhaust valve closure
EVO	Exhaust valve opening
HCCI	Homogeneous charge compression ignition
ICE	Internal combustion engine
IVC	Intake valve closure
IVO	Intake valve opening
LHV	Lower heating value
MBT	Maximum brake torque



NG	Natural gas
PFI	Port-fuel injection
PW	Pulse width
RANS	Reynolds-Averaged-Navier-Stokes
RNG	Re-Normalization Group
SA	Spak advance
SI	Spark ignition
$S_L$	Laminar flame speed
SOI	Start of injection
TDC	Top dead center
WHT	Wall heat transfer (J)
WOT	Wide open throttle
$\lambda$	Air-fuel ratio
$\dot{m}$	Mass flow rate (g/s)
$\eta_v$	Volumetric efficiency
$\eta_m$	Mechanical efficiency
$\eta_t$	Thermal efficiency
$\rho$	Fuel density
$\sigma_w$	Weighted standard deviation
$v$	Injection velocity (m/s)
$\Delta\theta_d$	Flame-development combustion stage (CAD)
$\Delta\theta_b$	Rapid-burning combustion stage (CAD)
$\Delta\theta_o$	Overall burning (CAD)

## References

- [1] Gerke U. Numerical analysis of mixture formation and combustion in a hydrogen direct-injection internal combustion engine. PhD Thesis. ETH Zürich, 2007.
- [2] Knop V, Benkenida A, Jay S, Colin O. Modelling of combustion and nitrogen oxide formation in hydrogen-fuelled internal combustion engines within a 3D CFD code. *Int J Hydrogen Energy* 2008;33:5083–97. doi:10.1016/j.ijhydene.2008.06.027.
- [3] Messner D, Wimmer A, Gerke U, Gerbig F. Application and validation of the 3D CFD method for a hydrogen fueled IC engine with internal mixture formation. *SAE Tech Pap* 2006;2006. doi:10.4271/2006-01-0448.
- [4] Yang Z, Zhang F, Wang L, Wang K, Zhang D. Effects of injection mode on the mixture formation and combustion performance of the hydrogen internal combustion engine. *Energy* 2018;147:715–28. doi:10.1016/j.energy.2018.01.068.
- [5] Diéguez PM, Urroz JC, Sáinz D, Machin J, Arana M, Gandía LM. Characterization of combustion anomalies in a hydrogen-fueled 1.4 L commercial spark-ignition engine by means of in-cylinder pressure, block-engine vibration, and acoustic measurements. *Energy Convers Manag* 2018;172:67–80. doi:10.1016/j.enconman.2018.06.115.
- [6] Kosmadakis GM, Rakopoulos CD, Demuynck J, De Paepe M, Verhelst S. CFD modeling and experimental study of combustion and nitric oxide emissions in hydrogen-fueled spark-ignition engine operating in a very wide range of EGR rates. *Int J Hydrogen Energy* 2012;37:10917–34. doi:10.1016/j.ijhydene.2012.04.067.
- [7] Duan J, Liu F, Yang Z, Sun B, Chen W, Wang L. Study on the NO<sub>x</sub> emissions mechanism of an HICE under high load. *Int J Hydrogen Energy* 2017;42:22027–35. doi:10.1016/j.ijhydene.2017.07.048.
- [8] Liu X, Liu F, Zhou L, Sun B, Schock HJ. Backfire prediction in a manifold injection hydrogen internal combustion engine. *Int J Hydrogen Energy* 2008;33:3847–55. doi:10.1016/j.ijhydene.2008.04.051.
- [9] Duan J, Liu F, Sun B. Backfire control and power enhancement of a hydrogen internal combustion engine. *Int J Hydrogen Energy* 2014;39:4581–9. doi:10.1016/j.ijhydene.2013.12.175.

- 
- [10] Subramanian KA, Salvi BL. A Numerical Simulation of Analysis of Backfiring Phenomena in a Hydrogen-Fueled Spark Ignition Engine. *J Eng Gas Turbines Power* 2016;138:1–10. doi:10.1115/1.4033182.
- [11] Chintala V, Subramanian KA. A CFD (computational fluid dynamics) study for optimization of gas injector orientation for performance improvement of a dual-fuel diesel engine. *Energy* 2013;57:709–21. doi:10.1016/j.energy.2013.06.009.
- [12] Zhu H, Duan J. Research on emission characteristics of hydrogen fuel internal combustion engine based on more detailed mechanism. *Int J Hydrogen Energy* 2018;1–7. doi:10.1016/j.ijhydene.2018.08.044.
- [13] Duan J, Wu P, Zhu H, Qin G, Wei W. Simplification and applicability studies of a hydrogen-air detailed reaction mechanism. *Int J Hydrogen Energy* 2019;44:5538–42. doi:10.1016/j.ijhydene.2018.09.173.
- [14] Shu J, Fu J, Zhang Y, Xie M, Liu J, Liu J, et al. Influences of natural gas energy fraction on combustion and emission characteristics of a diesel pilot ignition natural gas engine based on a reduced chemical kinetic model. *Fuel* 2020;261:116432. doi:10.1016/j.fuel.2019.116432.
- [15] De Robbio R, Cameretti MC, Tuccillo R. Ignition and combustion modelling in a dual fuel diesel engine. *Propuls Power Res* 2020;9:116–31. doi:10.1016/j.jprr.2020.02.001.
- [16] Dai X, Singh S, Krishnan SR, Srinivasan KK. Numerical study of combustion characteristics and emissions of a diesel-methane dual-fuel engine for a wide range of injection timings. *Int J Engine Res* 2020;21:781–93. doi:10.1177/1468087418783637.
- [17] Yousefzadeh A, Jahanian O. Using detailed chemical kinetics 3D-CFD model to investigate combustion phase of a CNG-HCCI engine according to control strategy requirements. *Energy Convers Manag* 2017;133:524–34. doi:10.1016/j.enconman.2016.10.072.
- [18] Poorghasemi K, Saray RK, Bahlouli K, Zehni A. 3D CFD simulation of a natural gas fueled HCCI engine with employing a reduced mechanism. *Fuel* 2016;182:816–30. doi:10.1016/j.fuel.2016.06.005.
- [19] Baratta M, Misul D, Xu J. Development and application of a method for characterizing mixture formation in a port-injection natural gas

- engine. *Energy Convers Manag* 2021;227:113595. doi:10.1016/j.enconman.2020.113595.
- [20] Zhang S, Li Y, Wang S, Zeng H, Liu J, Duan X, et al. Experimental and numerical study the effect of EGR strategies on in-cylinder flow, combustion and emissions characteristics in a heavy-duty higher CR lean-burn NGSi engine coupled with detail combustion mechanism. *Fuel* 2020;276:118082. doi:10.1016/j.fuel.2020.118082.
- [21] Pan K, Wallace J. Computational studies of fuel injection strategies on natural gas combustion characteristics in direct-injection engines. *Fuel* 2021;288:119823. doi:10.1016/j.fuel.2020.119823.
- [22] Kosmadakis GM, Rakopoulos DC, Rakopoulos CD. Assessing the cyclic-variability of spark-ignition engine running on methane-hydrogen blends with high hydrogen contents of up to 50%. *Int J Hydrogen Energy* 2021. doi:10.1016/j.ijhydene.2021.02.158.
- [23] Zaker K, Askari MH, Jazayeri A, Ebrahimi R, Zaker B, Ashjaee M. Open cycle CFD investigation of SI engine fueled with hydrogen/methane blends using detailed kinetic mechanism. *Int J Hydrogen Energy* 2015;40:14006–19. doi:10.1016/j.ijhydene.2015.08.040.
- [24] Gharehghani A, Hosseini R, Mirsalim M, Yusaf TF. A computational study of operating range extension in a natural gas SI engine with the use of hydrogen. *Int J Hydrogen Energy* 2015;40:5966–75. doi:10.1016/j.ijhydene.2015.03.015.
- [25] Zaichenko VM, Kiverin AD, Smygalina AE, Tsyplakov AI. Combustion of Lean Hydrogen-Based Mixtures in a Spark Ignition Engine. *Therm Eng* 2018;65:1009–18. doi:10.1134/S0040601518130141.
- [26] Laget O, Richard S, Serrano D, Soleri D. Combining experimental and numerical investigations to explore the potential of downsized engines operating with methane/hydrogen blends. *Int J Hydrogen Energy* 2012;37:11514–30. doi:10.1016/j.ijhydene.2012.03.153.
- [27] He H, Yao D, Wu F. A reduced and optimized kinetic mechanism for coke oven gas as a clean alternative vehicle fuel. *J Zhejiang Univ A* 2017;18:511–30. doi:10.1631/jzus.A1600636.
- [28] Stylianidis N, Azimov U, Maheri A, Tomita E, Kawahara N. Chemical kinetics and CFD analysis of supercharged micro-pilot ignited dual-fuel engine combustion of syngas. *Fuel* 2017;203:591–606.

- doi:10.1016/j.fuel.2017.04.125.
- [29] Sopena C, Diéguez PM, Sáinz D, Urroz JC, Guelbenzu E, Gandía LM. Conversion of a commercial spark ignition engine to run on hydrogen: Performance comparison using hydrogen and gasoline. *Int J Hydrogen Energy* 2010;35:1420–9. doi:10.1016/j.ijhydene.2009.11.090.
  - [30] Ansys®. Accelerate your engine combustion CFD with Ansys Forte 2016.
  - [31] Ansys®. Academic Research Forte, Release 2021 R1, Help System, Forte Theory Manual, Ansys Inc. 2021.
  - [32] Smith GP, Golden DM, Frenklach M, Moriarty NW, Eiteneer B, Goldenberg M, et al. Gri-Mech 3.0 Mechanism n.d. <http://combustion.berkeley.edu/gri-mech/version30/text30.html> (accessed June 2, 2021).
  - [33] Han Z, Reitz RD. Turbulence Modeling of Internal Combustion Engines Using RNG  $\kappa$ - $\epsilon$  Models. *Combust Sci Technol* 1995;106:267–95. doi:10.1080/00102209508907782.
  - [34] Ansys®. Academic Research Forte, Release 2021 R1, Help System, Forte User's Guide, Ansys Inc. 2021.
  - [35] Sierens R. VS. Experimental study of a hydrogen-fueled engine. *J Eng Gas Turbines Power* 2001;123:211–6. doi:10.1115/1.1339989.
  - [36] Kamil M, Rahman MM. Performance prediction of spark-ignition engine running on gasoline-hydrogen and methane-hydrogen blends. *Appl Energy* 2015;158:556–67. doi:10.1016/j.apenergy.2015.08.041.
  - [37] Heywood JB. Internal combustion engine fundamentals. New York: McGraw-Hill Education; 2018.
  - [38] Sáinz Casas D. Adaptación de un motor de combustión interna alternativo de gasolina para su funcionamiento con hidrógeno como combustible. Aplicaciones energética y de automoción. (PhD Thesis). Universidad Pública de Navarra, 2014.
  - [39] Ma F, Wang Y, Wang J, Ding S, Wang Y, Zhao S. Effects of combustion phasing, combustion duration, and their cyclic variations on spark-ignition (SI) engine efficiency. *Energy and Fuels* 2008;22:3022–8. doi:10.1021/ef8003027.

- [40] Ortiz-Imedio R, Ortiz A, Urroz JC, Diéguez PM, Gorri D, Gandía LM, et al. Comparative performance of coke oven gas, hydrogen and methane in a spark ignition engine. *Int J Hydrogen Energy* 2021;46:17572–86. doi:10.1016/j.ijhydene.2019.12.165.
- [41] Wang J, Huang Z, Tang C, Miao H, Wang X. Numerical study of the effect of hydrogen addition on methane-air mixtures combustion. *Int J Hydrogen Energy* 2009;34:1084–96. doi:10.1016/j.ijhydene.2008.11.010.
- [42] Zhu H, Zhang Y, Liu F, Wei W. Effect of excess hydrogen on hydrogen fueled internal combustion engine under full load. *Int J Hydrogen Energy* 2020;45:20419–25. doi:10.1016/j.ijhydene.2019.12.022.
- [43] Cruccolini V, Discepoli G, Cimarello A, Battistoni M, Mariani F, Grimaldi CN, et al. Lean combustion analysis using a corona discharge igniter in an optical engine fueled with methane and a hydrogen-methane blend. *Fuel* 2020;259:116290. doi:10.1016/j.fuel.2019.116290.
- [44] Hamada KI, Rahman MM, Ramasamy D, Noor MM, Kadirgama K. Numerical investigation of in-cylinder flow characteristics of hydrogen-fuelled internal combustion engine. *J Mech Eng Sci* 2016;10:1792–802. doi:10.15282/jmes.10.1.2016.4.0172.
- [45] Pourkhesalian AM, Shamekhi AH, Salimi F. Alternative fuel and gasoline in an SI engine: A comparative study of performance and emissions characteristics. *Fuel* 2010;89:1056–63. doi:10.1016/j.fuel.2009.11.025.
- [46] Rahman MM, K. Mohamme M, A. Bakar R. Effects of Air-Fuel Ratio and Engine Speed on Performance of Hydrogen Fueled Port Injection Engine. *J Appl Sci* 2009;9:1128–34. doi:10.3923/jas.2009.1128.1134.
- [47] Duan X, Liu Y, Liu J, Lai MC, Jansons M, Guo G, et al. Experimental and numerical investigation of the effects of low-pressure, high-pressure and internal EGR configurations on the performance, combustion and emission characteristics in a hydrogen-enriched heavy-duty lean-burn natural gas SI engine. *Energy Convers Manag* 2019;195:1319–33. doi:10.1016/j.enconman.2019.05.059.

## Appendix

### Mesh size sensitivity analysis

Different “Global Mesh Size” values in Forte software have been studied (from 0.15 cm to 0.3 cm in steps of 0.05 cm) to analyze the influence of the mesh size in the results and computational time.

The analysis for the case of CH<sub>4</sub> at 4000 rpm and  $\lambda = 1.5$ , is shown in Table A.4.1, where 0.25 cm is the Global Mesh Size chosen in this work.

Table A.4.1. Mesh size sensitivity analysis for global mesh sizes from 0.15 cm to 0.3 cm.

Global Mesh Size (cm)	Fluid cells (200 CAD)	Fluid cells (EVO)	Computational simulation time (4 cycles)	CHR (J)	Max pressure (bar)	Fuel (mg)
0.15	692369	1184958	>3 days	667.6	77.56	13.53
0.2	313547	577491	2days, 11h, 34min	668.5	77.52	13.56
<b>0.25</b>	172392	314416	1day, 8h, 12min	669.1	77.79	13.57
0.3	105298	193788	21h, 16min	670.3	77.59	13.61

As can be observed, comparing at the same simulation time (200 crank angle degrees or at exhaust valve opening (EVO)), a small global mesh size (0.15 cm) raises the number of fluid cells to almost 700000 cells and 1.2M cells, respectively, and with a computational effort time of more than 3 days for the simulation of 4 consecutive cycles. The deviation in terms of chemical heat release (CHR, in J), maximum pressure (bar) and fuel quantity introduced in the cylinder (mg) is less than 0.3% compared to the 0.25 cm case.

Employing a value of 0.2 cm for the global mesh size creates nearly 315000 fluid cells at 200 CAD or 580000 at EVO, and decreases the computational time effort to almost 2.5 days. In this case, the deviation is 0.34% for the maximum pressure and less than 0.09% for the other two variables, compared to the 0.25 cm case. Finally, if a larger global mesh size is used (0.3 cm), the fluid cells (105000 at 200 CAD or 194000 at EVO) and the simulation time (21h) are reduced with a deviation lower than 0.3% with respect to the 0.25 cm case.

Therefore, the intermediate global mesh size of 0.25 cm was finally chosen with very good results and reasonable fluid cells number and computational time due to the large number of simulation cases studied.



### Model validation

Validation of the simulations has been carried out through a parity graph between the experiments and simulation results of BMEP and BSFC for the three gaseous fuels and working conditions (Figure A.4.1). A good agreement can be noticed, with nearly all the points falling in the region between the 15% deviation lines.

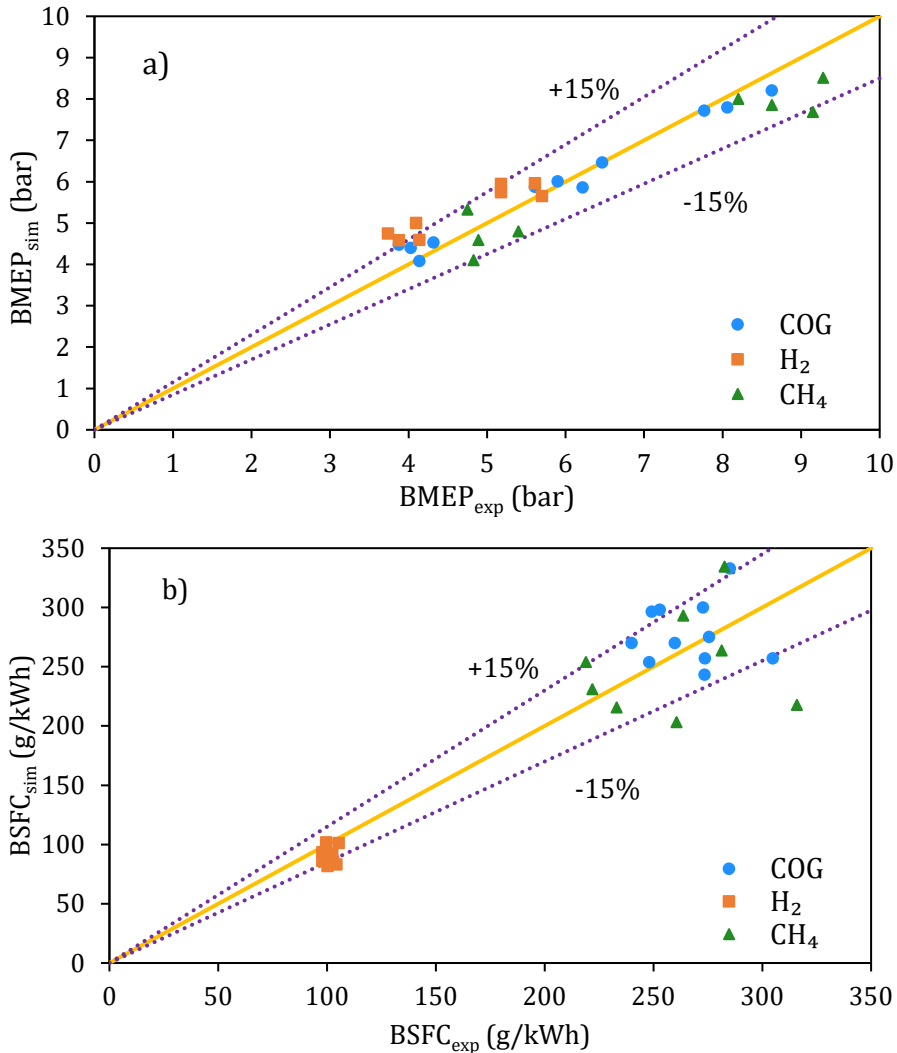


Figure A.4.1. Parity graph of experimental al simulated results of a) BMEP (bar) and b) BSFC (g/kWh) for COG (●), H<sub>2</sub> (■) and CH<sub>4</sub> (▲) at all operating conditions. Purple dotted lines represent deviation of 15%.

In addition, the CO<sub>2</sub> emissions (%vol) have been validated in Figure A.4.2 for COG and CH<sub>4</sub> in the entire range of study. Higher deviations in the case of CH<sub>4</sub> with leaner mixtures ( $\lambda = 1.5$ ) are observed due to a less stable combustion, increasing the difference between the experiments and the model prediction.

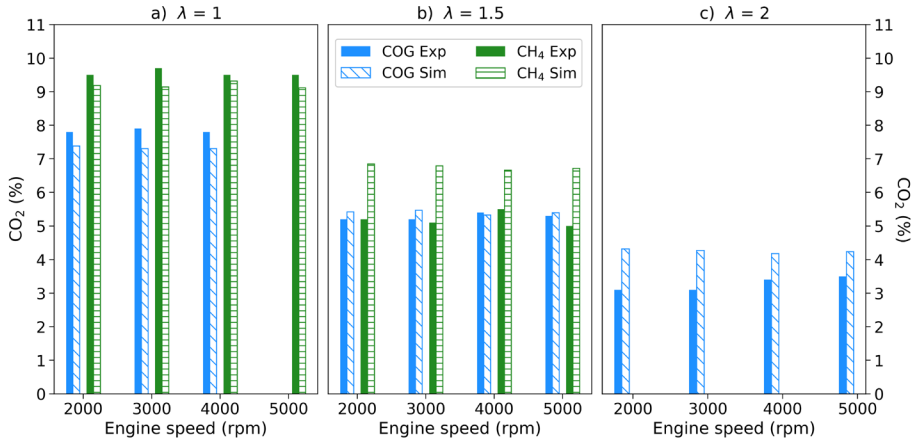


Figure A.4.2. Experimental and simulated CO<sub>2</sub> emissions (%vol) of COG and CH<sub>4</sub> versus engine speed (rpm) at a)  $\lambda=1$ , b)  $\lambda=1.5$  and c)  $\lambda=2$ .

Furthermore, the statistical parameter weighted standard deviation ( $\sigma_w$ ) defined in Equation (A.4.1) has been calculated for some of the variables, comparing the experimental and simulated values.

$$\sigma_w = \sqrt{\frac{\sum_{i=1}^S \left( \frac{exp - sim}{exp} \right)^2}{S - 1}} \quad (A.4.1)$$

Where  $S$  is the number of experiments and “exp” and “sim” are the experimental and simulated values of each variable, respectively. These  $\sigma_w$  calculated values have been collected in Table A.4.2, in which  $\eta_t$  is the thermal efficiency (%), BSFC is the brake specific fuel consumption (g/kWh) and BSEC is the brake specific energy consumption (MJ/kWh). A deviation lower than 15% for the performance variables is found, with the exception of the thermal efficiency ( $\eta_t$ ), increasing up to 16.3%. In the first case, an overestimation of the thermal efficiency is produced at low engine speeds because the model predicts a lower fuel consumption than in the experiments. On the contrary, an underestimation in  $\eta_t$  occurs at high engine speeds because the model assumes the engine consumes more fuel

than the required in the experiments and a lower performance is obtained at those engine speeds.

Table A.4.2. Weighted standard deviation ( $\sigma_w$ ) for some of the experimental variables.

Variable	BMEP (bar)	Power (kW)	$\eta_t$ (%)	BSFC (g/kWh)	BSEC (MJ/kWh)
$\sigma_w$	11.4 %	11.4 %	16.3 %	14.2 %	14.2 %

## Combustion stages

Table A.4.3. Combustion stages in terms of crank angles degrees: Flame-development ( $\Delta\theta_d$ ), Rapid-burning ( $\Delta\theta_b$ ) and Overall burning ( $\Delta\theta_o$ ) angles.

Gas	Speed	$\lambda$	$\Delta\theta_d$ 10-0% (CAD)	$\Delta\theta_b$ 90-10% (CAD)	$\Delta\theta_o$ 90-0% (CAD)
<b>H<sub>2</sub></b>	2000	1.5	7.13	12.7	19.8
	3000		9.19	12.7	21.8
	4000		9.71	10.9	20.6
	5000		9.26	9.9	19.2
	2000	2	10.04	16.8	26.8
	3000		11.37	18.4	29.8
	4000		10.43	18.5	28.9
	5000		10.85	18.2	29.0
<b>COG</b>	2000	1	9.73	11.8	21.6
	3000		10.2	14.7	24.9
	4000		10.73	17.1	27.9
	2000	1.5	12.64	20.1	32.7
	3000		13.73	23.1	36.8
	4000		13	21.8	34.8
	5000		12.79	21.8	34.6
	2000	2	17.29	23.8	41.1
	3000		19	25.0	44.0
	4000		18.69	23.0	41.7
	5000		17.81	22.7	40.5
<b>CH<sub>4</sub></b>	2000	1	13.29	25.5	38.8
	3000		15.07	28.7	43.7
	4000		14.22	30.4	44.6
	5000		14.13	30.6	44.7
	2000	1.5	18.76	22.0	40.7
	3000		23.75	20.8	44.5
	4000		21.61	18.0	39.6
	5000		21.11	17.9	39.0

### Flame brush thickness evolution

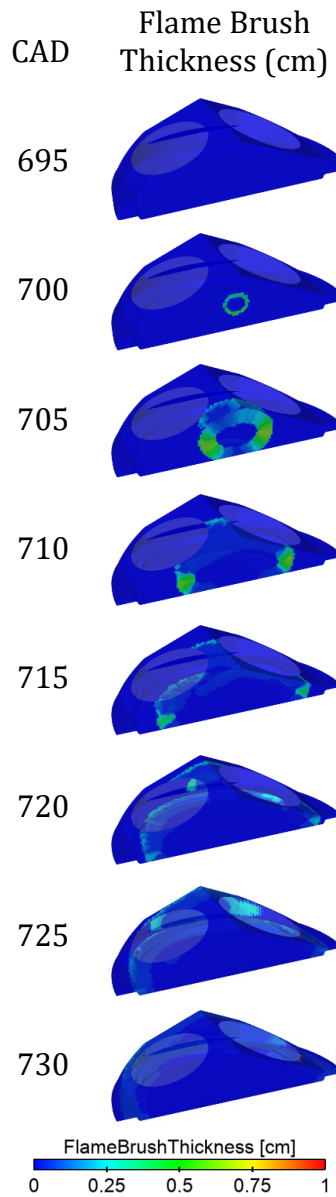


Figure A.4.3. Flame brush thickness (cm) evolution of COG at 4000 rpm and  $\lambda=1.5$ .  
(Screenshots used courtesy of ANSYS, Inc.)

## Fluid dynamics

In Figure A.4.4 the mass flow rates and accumulated mass transport exchange between the cylinder and the manifolds of COG at  $\lambda = 2$  and all the engine speeds are graphed. As can be observed in the mass flow rate to the exhaust manifold (Figure A.4.4a), as the engine speed rises, the cylinder mass is expelled at a higher rate. Furthermore, the wave frequency is reduced as the speed increases. However, in the case of 2000 rpm and 3000 rpm, negative mass flow rate values are produced at 50 CAD and 70 CAD after EVO, respectively. This implies a backflow from the exhaust to the cylinder, hindering the mass transport during a few crank angle degrees, as shown in Figure A.4.4b. Thus, a leap in the total mass of exhausted gas after exhaust valve closure (EVC) can be noted between 3000 rpm and 4000 rpm.

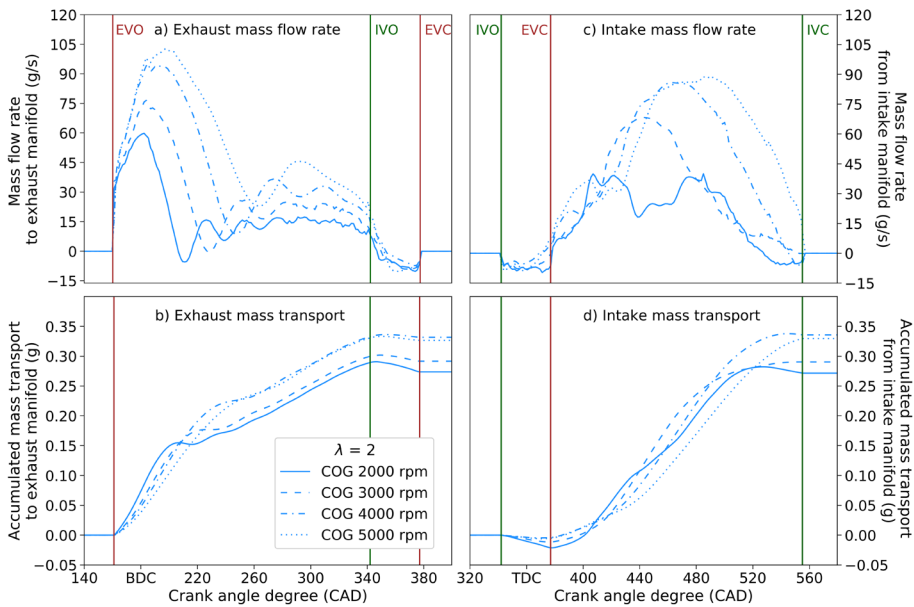


Figure A.4.4. Mass flow rate (a) and accumulated mass transport (b) from the cylinder to the exhaust manifold and mass flow rate (c) and accumulated mass transport (d) from the intake manifold to the cylinder for COG at  $\lambda=2$  in the whole speed range.

On the other hand, as there is a valve overlap period between intake valve opening (IVO) and EVC, as can be observed in Figure 4.2a, a mass flow rate from the exhaust manifold to the intake manifold is produced due to the pressure difference. This can be noticed in the negative values of the exhaust mass flow rate and a reduction of the total mass exhausted (Figure A.4.4). These phenomena affect the evacuation of mass from the cylinder, which reduces the input mass during the next intake stroke.

The mass flow rate from the intake manifold to the cylinder is graphed in Figure A.4.4c while the accumulated mass induced into the cylinder is plotted in Figure A.4.4d. During the valve overlap period, the mass flow rate from the intake manifold is negative, which means that the flow of air-fuel mixture circulates in the opposite direction. After EVC, the mass flow rates increase with a different waveform depending on the engine speed. In the case of 2000 rpm, a negative wave pressure is produced at half stroke, reducing the mass flow rate into the cylinder. This is reflected in the mass transport slope from the intake manifold at 2000 rpm (Figure A.4.4d). Furthermore, a negative mass flow rate is also generated with 2000 rpm at the end of the intake process.

In the case of 5000 rpm, the mass flow rate from the intake manifold is choked, reaching the same maximum value as the curve of 4000 rpm. This means that similar total mass is transported at 4000 rpm and 5000 rpm in both exhaust and intake strokes. This choking limits the power output generated (Figure 4.5).

These fluid dynamic phenomena occur independently of the gaseous fuel or the air-fuel ratio employed, as can be noticed in Figure A.4.5, Figure A.4.6 and Figure A.4.7.

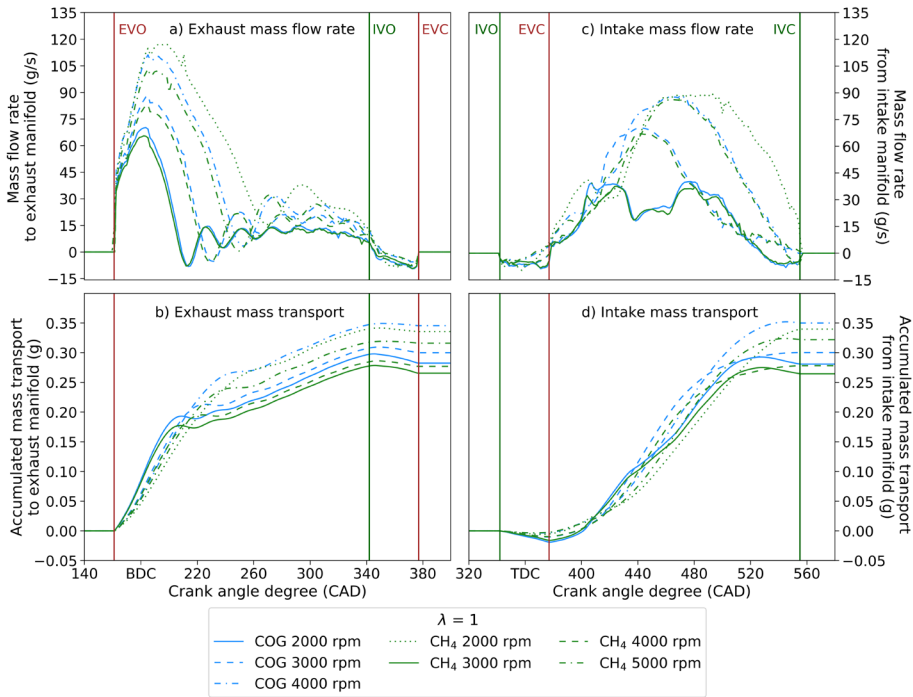


Figure A.4.5. Mass flow rate (a) and accumulated mass transport (b) from the cylinder to the exhaust manifold and mass flow rate (c) and accumulated mass transport (d) from the intake manifold to the cylinder for fuels at  $\lambda=1$  in the whole speed range.



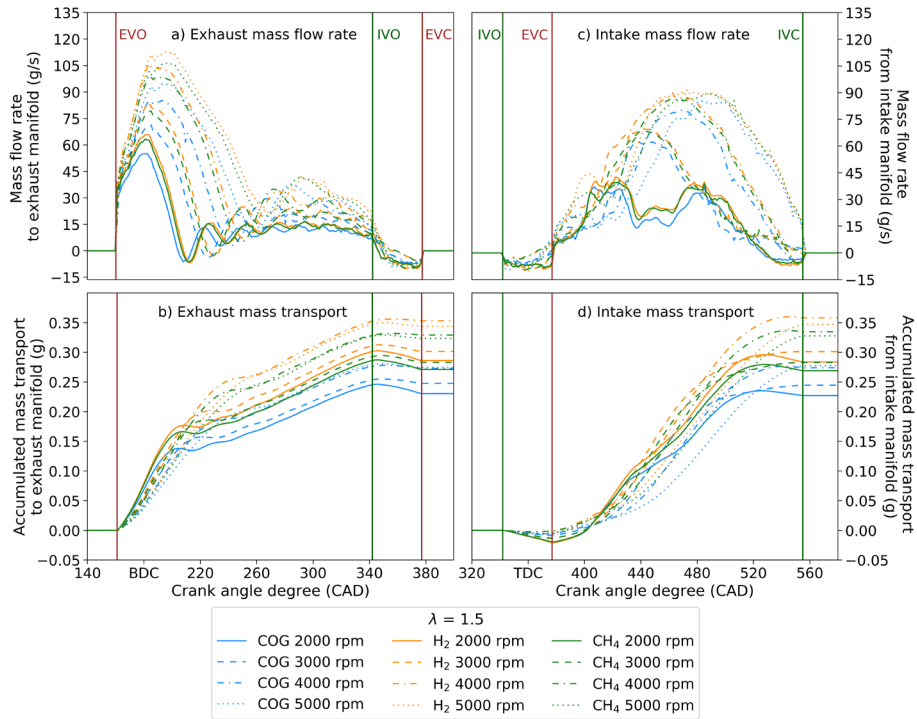


Figure A.4.6. Mass flow rate (a) and accumulated mass transport (b) from the cylinder to the exhaust manifold and mass flow rate (c) and accumulated mass transport (d) from the intake manifold to the cylinder for fuels at  $\lambda=1.5$  in the whole speed range.

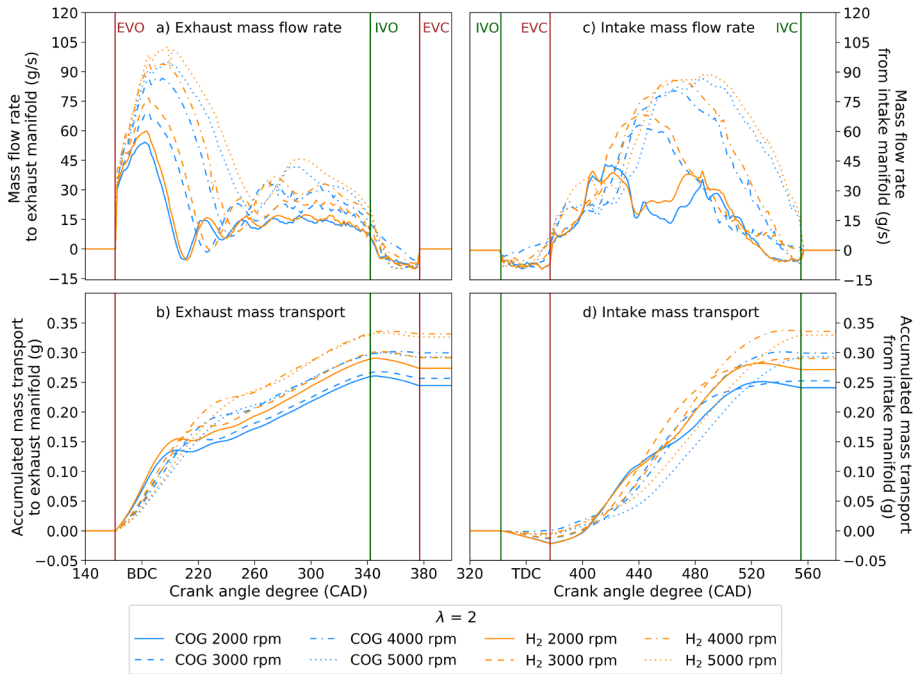


Figure A.4.7. Mass flow rate (a) and accumulated mass transport (b) from the cylinder to the exhaust manifold and mass flow rate (c) and accumulated mass transport (d) from the intake manifold to the cylinder for fuels at  $\lambda=2$  in the whole speed range.

As consequence of these mass transport exchanges between the cylinder and the manifolds, the residual mass fractions, corresponding to the mass remaining inside the cylinder between cycles, depend on the operating condition. Estimations of the residual mass fraction have been carried out as the ratio of the in-cylinder mass just after EVC and after IVC. The results are shown in Table A.4.4 and Figure A.4.8 for the cases of H<sub>2</sub>, CH<sub>4</sub> and COG at 2000 rpm and 4000 rpm and  $\lambda$  between 1 and 2.

As can be observed, the residual mass fraction is dependent on the air-fuel ratio, the engine speed and the fuel. As the engine speed raises at  $\lambda$  values lower than 2 or the fuel density increases (CH<sub>4</sub>>COG>H<sub>2</sub>), higher total mass enters into the cylinder and a good exhaust process is developed, reducing the residual mass; therefore, lower residual mass fraction is obtained. On the other hand, as the mixture becomes leaner (higher  $\lambda$ ), though also higher total mass is introduced into the cylinder, lower combustion temperature is obtained and a worse exhaust process is carried out, increasing the residual mass fraction inside the cylinder.

Table A.4.4. Simulated residual mass fractions inside the cylinder at 2000 rpm and 4000 rpm and  $\lambda$  between 1 and 2 for H<sub>2</sub>, CH<sub>4</sub> and COG gaseous fuels.

Gas	$\lambda$	Engine (rpm)	Residual mass fraction (%)
H <sub>2</sub>	1.5	2000	6.03
		4000	5.74
	2	2000	6.21
		4000	6.32
CH <sub>4</sub>	1	2000	4.98
		4000	4.81
	1.5	2000	5.65
		4000	5.59
COG	1	2000	5.19
		4000	4.90
	1.5	2000	5.77
		4000	5.50
	2	2000	6.10
		4000	6.26

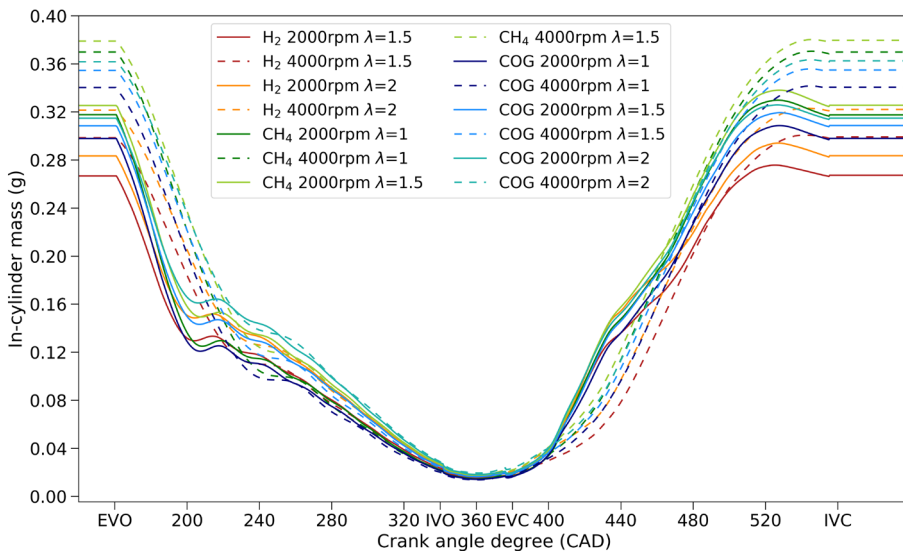


Figure A.4.8. In-cylinder mass evolution versus crank angle degree (CAD) for H<sub>2</sub>, CH<sub>4</sub> and COG gaseous fuels at 2000 rpm (solid lines) and 4000 rpm (dashed lines) and  $\lambda$  between 1 and 2.



# CHAPTER 5

---

CONCLUSIONS AND FUTURE WORK



## 4.5. Conclusions

This thesis has shed light on the requirements for the achievement of a futuristic European energy system by 2050 based on 100% renewable energy sources (RES) coupled to the hydrogen energy vector. In this way, the electrical grid can be balanced, fulfilling the hydrogen and electricity demands, including the maritime transport sector. Furthermore, this thesis has highlighted the pivotal role of low carbon fuels in a mature and easily adaptable technology, internal combustion engines (ICEs). In this way, the energy content of industrial waste streams like coke oven gas can be recovered, paving the way to a more sustainable energy system.

**Chapter 1** has shown the current global energetic system dependence on fossil fuels, leading to an unstable situation of greenhouse gas emissions. In addition, the uneven distribution of fossil fuels reserves is at the root of many international issues and difficulties for a constant energy supply. In contrast, RES coupled to hydrogen as energy vector could become a feasible solution, promoting a more distributed energy system. An insight into the capabilities and costs of hydrogen technologies and storage systems to balance the electrical grid and with a high number of applications is provided. In the transition to a futuristic clean energy system based on  $H_2$  infrastructure, internal combustion engines fueled with low carbon fuels constitute a key technology for pollutants reduction. Coke oven gas (COG), an industrial waste stream with high percentages of  $H_2$  and  $CH_4$ , is considered an interesting low carbon fuel with suitable physicochemical properties to harness its energy content in ICEs. Finally, computational fluid dynamics (CFD) offer a versatile tool to optimize the engine design and operating conditions through simulations, reducing the need for expensive experiments.

In **Chapter 2**, a European 100% RES energy system infrastructure by 2050 coupled with  $H_2$  as energy vector has been optimized to minimize total annual costs. Electricity demands for space and water heating and ships in the Atlantic area of Europe are included. The hydrogen demand is constituted by a 50% market penetration of fuel cell electric vehicles (FCEVs) in that year, and different penetration scenarios of ships powered by  $H_2$  in the Atlantic region are analyzed to observe its influence in the European energy system. Ireland has been found as the main energy

producer based on onshore wind turbines and electrolyzers. Scenarios with higher ship  $H_2$  demands require the reinforcement of salt caverns and the pipelines infrastructure, especially in the United Kingdom and the interconnection with France. The  $H_2$  energy vector has been identified to play a key role to balance the electrical grid, dampening the intermittent fluctuations from RES with  $H_2$  stored in salt caverns and vessels, while satisfying the energy demands. Furthermore,  $H_2$  allows the deployment of a more sustainable transport at a relatively low cost.

The experimental results obtained fueling low carbon fuels in a port-fuel naturally aspirated spark ignition engine are reported in **Chapter 3**. The performance and the emissions of COG have been assessed and compared with its main constituents, pure  $H_2$  and pure  $CH_4$ . COG combines the benefits of  $H_2$  and  $CH_4$ , with higher volumetric lower heating value than  $H_2$  and higher laminar flame speed than  $CH_4$ , increasing the power and efficiency performance at air-fuel ratios ( $\lambda$ ) higher than 1. Besides, a wider  $\lambda$  range can be used with COG with less abnormal combustion tendency than fueling  $H_2$  with rich air-fuel mixtures, and better combustion stability than  $CH_4$  with lean mixtures. Lower specific emissions of  $NO_x$  are achieved due to the lower  $H_2$  content with respect to pure  $H_2$  and lower spark advance than  $CH_4$ , reducing the combustion temperature. Besides, the specific emissions of hydrocarbons, CO and  $CO_2$  are reduced with COG compared to  $CH_4$  because of the lower carbon content and the better combustion. Therefore, COG appears as a very good fuel in ICEs, especially focused in stationary systems at the outlet of the coke plant.

A CFD simulation model of a symmetrical cylinder of the same engine has been developed in **Chapter 4**. The same operating conditions as in **Chapter 3** have been used in the simulation runs with the three fuels. A good agreement between experiments and simulations has been achieved with a weighted standard deviation lower than 12% for power and brake mean effective pressure variables and 16.3% for thermal efficiency. With lean air-fuel mixtures, lower pressure, temperature, chemical heat release, wall heat transfer and NO emissions have been obtained. Spark timing plays a key role, increasing peak pressures and temperatures for a longer time with high spark advance values, which raise the NO and the wall heat transfer values, and reduce the brake power. This is the case of  $CH_4$ , requiring high spark advances due to the low flame growth speed.  $H_2$



has lower combustion duration but increases the OH generation rate and the NO emissions. At  $\lambda = 1.5$ , COG delivers the highest power output due to higher flame growth speed than  $\text{CH}_4$  and higher volumetric lower heating value than  $\text{H}_2$ . In addition, the intermediate spark advance values of COG reduce NO emissions and the wall heat transfer, increasing the power generated. At lower and richer air-fuel mixtures, similar performances are obtained with COG compared to  $\text{H}_2$  and  $\text{CH}_4$ , widening the air-fuel ratio operation range, becoming an interesting alternative for fuel recovery for stationary applications after optimizing the operating conditions.

#### **4.6. Future work**

This thesis clears the way for two research lines in which a wide range of possibilities for improvement could be investigated.

Regarding the energy system model, further work will be necessary to adopt more realistic electrical and hydrogen demand curves throughout the year according to the different types of ships that travel within the region under study. This will enable a more accurate quantitative evaluation of hydrogen demand for maritime operations and its impact on the energy system in Europe by 2050. An alternative scenario based on isolated European countries could be studied, assessing the costs of an energy system without electricity or  $\text{H}_2$  exchange between them. In contrast, connections with other continents could be analyzed to quantify the hydrogen that could be exported/imported to/from other regions, further optimizing the energy production from RES and its storage during the year.

In the field of ICEs, many configurations and operating conditions can be studied to improve the performance and reduce emissions generated during combustion of low carbon fuels. Regarding fuel injection, direct injection of COG into the cylinder at high pressure during the compression stroke could be analyzed to observe its influence on the temperature, the heat transfer and the emissions that would be generated. This injection type avoids backfire into the intake manifold, increases the air-fuel mixture and reduces the limitation of the quantity of fuel that can be introduced, raising the engine performance. Variation of the valve timings

and the valve lifts could be also considered to study the effect on the efficiency and the emissions.

On the other hand, devices like turbochargers could be coupled to the engine to increase the air mass introduced, implying higher volumetric efficiency and higher power output. An interesting strategy to further reduce NO emissions would be the incorporation of an exhaust gas recirculation system, which reduces the combustion temperature but also influences the air-fuel ratio and the performance. Moreover, the employment of rich air-fuel mixtures would require the use of a three-way catalyst system, oxidizing hydrocarbon exhaust gases and reducing the NO emissions at the engine outlet.

Finally, prediction of the engine behavior with computational fluid dynamics simulations can be further improved by comparing different chemical kinetic mechanisms, selecting the mechanisms that are better suited for coke oven and hydrogen gases. The predicted heat transfer could be better adjusted to the experiments coupling the cylinder geometry to a cooling system that surrounds the cylinder, as in the case of real engines. Furthermore, better accurate simulations could be achieved extending the geometry included in the domain, with more cylinders operating at the same time and including the full geometry of the manifolds, improving the prediction of the fluid dynamics and the combustion performance of low carbon fuels.

# CAPÍTULO 5

---

CONCLUSIONES Y TRABAJO FUTURO



## 5.1. Conclusiones

Esta tesis analiza los requisitos para conseguir un sistema energético europeo basado en un 100% de fuentes de energía renovables (RES, por sus siglas en inglés) acopladas al hidrógeno como vector energético en el horizonte 2050. De este modo, se favorece equilibrar la red eléctrica, satisfaciendo las demandas de hidrógeno y electricidad, incluido el sector del transporte marítimo. Además, esta tesis ha puesto de relieve el papel fundamental de los combustibles bajos en carbono en una tecnología madura y fácilmente adaptable, los motores de combustión interna (ICEs, por sus siglas en inglés). De este modo, se puede recuperar el contenido energético de las corrientes residuales industriales, como el gas de coque, allanando el camino hacia un sistema energético más sostenible.

El **Capítulo 1** ha mostrado la actual dependencia del sistema energético mundial de los combustibles fósiles, que conduce a una situación insostenible de emisiones de gases de efecto invernadero. Además, la desigual distribución de las reservas de combustibles fósiles es la causa de muchos problemas internacionales y de las dificultades para un suministro energético constante. En cambio, las RES acopladas al hidrógeno como vector energético podrían convertirse en una solución viable, promoviendo un sistema energético más distribuido. Se ha proporcionado una visión de las capacidades y los costes de las tecnologías y los sistemas de almacenamiento de hidrógeno para equilibrar la red eléctrica y con un elevado número de aplicaciones. En la transición hacia un futuro sistema energético limpio basado en la infraestructura de  $H_2$ , los motores de combustión interna alimentados con combustibles bajos en carbono constituyen una tecnología clave para reducir la emisión de contaminantes. El gas de coque (COG, por sus siglas en inglés), una corriente residual industrial con alto porcentaje de  $H_2$  y  $CH_4$ , se considera un interesante combustible bajo en carbono con propiedades fisicoquímicas adecuadas para aprovechar su contenido energético en ICEs. Por último, la dinámica de fluidos computacional (CFD, por sus siglas en inglés) ofrece una herramienta versátil para optimizar el diseño del motor y las condiciones de funcionamiento mediante simulación; la capacidad predictiva reduce significativamente la necesidad de realizar costosos experimentos.

En el **Capítulo 2**, se ha optimizado y minimizado los costes totales anuales de una infraestructura del sistema energético europeo basado en un 100% de RES acoplado a  $H_2$  como vector energético en el horizonte 2050. Se han incluido las demandas de electricidad para la calefacción de espacios y agua y para los barcos en la zona atlántica de Europa. La demanda de hidrógeno está constituida por una penetración en el mercado del 50% de los vehículos eléctricos de pila de combustible (FCEVs, por sus siglas en inglés) en ese año, y se han analizado diferentes escenarios de penetración de barcos alimentados con  $H_2$  en la región atlántica para observar su influencia en el sistema energético europeo. Se ha descubierto que Irlanda es el principal productor de energía basado en turbinas eólicas terrestres y electrolizadores. Los escenarios con mayor demanda de  $H_2$  para barcos requieren el refuerzo de las cavernas de sal y de la infraestructura de tuberías, especialmente en el Reino Unido y la interconexión con Francia. Se ha determinado que el  $H_2$  como vector energético desempeña un papel clave para equilibrar la red eléctrica, amortiguando las fluctuaciones intermitentes de RES con el  $H_2$  almacenado en las cavernas de sal y en las vasijas, al tiempo que satisface la demanda de energía. Además, el  $H_2$  favorece el desarrollo de un transporte más sostenible a un coste relativamente bajo.

En el **Capítulo 3** se presentan los resultados experimentales obtenidos en un motor de encendido por chispa de aspiración natural alimentado con combustibles bajos en carbono. El rendimiento y las emisiones del COG se han evaluado y comparado con sus principales componentes, el  $H_2$  puro y el  $CH_4$  puro. El COG combina las ventajas del  $H_2$  y del  $CH_4$ , con un poder calorífico inferior volumétrico más alto que el  $H_2$  y una velocidad de llama laminar más alta que la del  $CH_4$ , lo que aumenta la potencia y el rendimiento con relaciones aire-combustible ( $\lambda$ ) superiores a 1. Además, con el COG se puede utilizar un rango de  $\lambda$  más amplio, con menor tendencia a la combustión anómala que el  $H_2$  con mezclas aire-combustible ricas, y mejor estabilidad de la combustión que la del  $CH_4$  con mezclas pobres. Se reducen las emisiones específicas de  $NO_x$  debido al menor contenido de  $H_2$  con respecto al  $H_2$  puro y al menor avance de la chispa que el  $CH_4$ , reduciendo la temperatura de combustión. Además, las emisiones específicas de hidrocarburos, CO y  $CO_2$  se reducen con el COG en comparación con el  $CH_4$  debido al menor contenido de carbono y a la mejor combustión. Por lo tanto, el COG aparece como un

combustible con muy buen rendimiento en los ICEs, especialmente enfocado en sistemas estacionarios a la salida de la planta de coque.

En el **Capítulo 4** se ha desarrollado un modelo de simulación CFD de un cilindro simétrico del mismo motor. Se han utilizado las mismas condiciones de funcionamiento que en el **Capítulo 3** para las simulaciones con los tres combustibles. Se ha obtenido buena concordancia entre los experimentos y las simulaciones, con una desviación estándar ponderada inferior al 12% para las variables de potencia y presión media efectiva y al 16.3% para el rendimiento térmico. Con mezclas pobres de aire-combustible se han obtenido menores presiones, temperaturas, liberación de calor químico, transferencia de calor a la pared y emisiones de NO. El tiempo de ignición de la chispa desempeña un papel fundamental, ya que aumenta la presión y temperatura máximas durante más tiempo con valores elevados de avance de chispa; ello da lugar al aumento de los valores de NO y de transferencia de calor a la pared, y reduce la potencia efectiva. Este es el caso del CH<sub>4</sub>, que requiere altos avances de chispa debido a la baja velocidad de crecimiento de la llama. El H<sub>2</sub> tiene una duración de combustión menor, pero aumenta la velocidad de generación de OH y las emisiones de NO. Con  $\lambda = 1.5$ , el COG proporciona la mayor potencia debido a la mayor velocidad de crecimiento de llama que cuando se alimenta con CH<sub>4</sub> y al mayor poder calorífico inferior volumétrico que el del H<sub>2</sub>. Además, los valores intermedios de avance de chispa del COG reducen las emisiones de NO y la transferencia de calor a la pared, aumentando la potencia generada. En mezclas aire-combustible más bajas y ricas, se obtienen rendimientos similares con el COG en comparación al H<sub>2</sub> y al CH<sub>4</sub>, ampliando el rango de operación de las relación aire-combustible. De esta manera se ofrece una alternativa interesante para la recuperación de la energía de una corriente residual en aplicaciones estacionarias tras optimizar las condiciones de operación.

## 5.2. Trabajo futuro

Esta tesis abre el camino a dos líneas de investigación en las que se podría investigar un amplio abanico de posibilidades de mejora.

En lo que respecta al modelo del sistema energético, será necesario seguir trabajando para utilizar curvas de demanda eléctrica y de hidrógeno más realistas a lo largo del año en función de los diferentes tipos de barcos que circulan por la región estudiada. Esto permitirá una evaluación cuantitativa más precisa de la demanda de hidrógeno para las operaciones marítimas y de su impacto en el sistema energético de Europa en el horizonte 2050. Podría estudiarse un escenario alternativo basado en países europeos aislados, evaluando los costes de un sistema energético sin intercambio de electricidad ni  $H_2$  entre ellos. En cambio, podrían analizarse las conexiones con otros continentes para cuantificar el hidrógeno que podría exportarse/importarse a/desde otras regiones, optimizando aún más la producción de energía a partir de RES y su almacenamiento durante el año.

En el ámbito de los ICEs, pueden estudiarse muchas configuraciones y condiciones de funcionamiento para mejorar el rendimiento y reducir las emisiones generadas durante la combustión de combustibles bajos en carbono. En cuanto a la inyección de combustible, se podría analizar la inyección directa de COG en el cilindro a alta presión durante la carrera de compresión para observar su influencia en la temperatura, la transferencia de calor y las emisiones que se generarían. Este tipo de inyección evita el retroceso de llama en el colector de admisión, aumenta la mezcla aire-combustible y reduce la limitación de la cantidad de combustible que se puede introducir, elevando el rendimiento del motor. También se podría considerar la variación de los tiempos de las válvulas y las elevaciones de las válvulas para estudiar su efecto sobre la eficiencia y las emisiones.

Por otro lado, se podrían acoplar al motor dispositivos como turbocompresores para aumentar la masa de aire introducida, lo que implicaría una mayor eficiencia volumétrica y mayor potencia. Una estrategia interesante para reducir aún más las emisiones de NO sería la incorporación de un sistema de recirculación de los gases de escape, que reduce la temperatura de combustión, pero también influye en la relación aire-combustible y en el rendimiento. Además, el empleo de mezclas aire-



combustible ricas requeriría el uso de un catalizador de tres vías, que oxida los gases de escape de hidrocarburos y reduce las emisiones de NO a la salida del motor.

Por último, la predicción del comportamiento del motor con simulación de dinámica de fluidos computacional puede mejorarse comparando diferentes mecanismos cinéticos químicos, seleccionando los mecanismos que mejor se adapten a los gases de coque y de hidrógeno. La transferencia de calor pronosticada podría ajustarse mejor a los experimentos acoplando la geometría del cilindro a un sistema de refrigeración que lo rodee, como en el caso de los motores reales. Además, se podrían conseguir simulaciones más precisas ampliando la geometría incluida en el dominio, con más cilindros funcionando al mismo tiempo e incluyendo la geometría completa de los colectores, mejorando la predicción de la dinámica de los fluidos y el rendimiento de la combustión de los combustibles bajos en carbono.



# APPENDIX I

---

SCIENTIFIC CONTRIBUTIONS



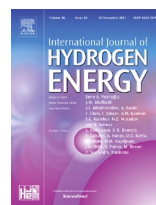
In this appendix, the scientific contributions in published articles and contributions to national and international conferences during the predoctoral period are listed.

- Articles published in international journals indexed in the Journal Citation Reports® (JCR)

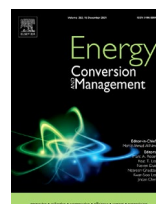
1. Ortiz-Imedio R, Caglayan D, Ortiz A, Heinrichs H, Robinius M, Stolten D, et al. Power-to-Ships: Future electricity and hydrogen demands for shipping on the Atlantic coast of Europe in 2050. *Energy* 2021;228:120660. doi:10.1016/j.energy.2021.120660. (JCR impact factor 2020: 7.147, Q1 position 22 of 114 in the Energy & Fuels Category) (Chapter 2 of this thesis)



2. Ortiz-Imedio R, Ortiz A, Urroz JC, Diéguez PM, Gorri D, Gandía LM, et al. Comparative performance of coke oven gas, hydrogen and methane in a spark ignition engine. *Int J Hydrogen Energy* 2021;46:17572–86. doi:10.1016/j.ijhydene.2019.12.165. (JCR impact factor 2020: 5.816, Q2 position 37 of 114 in the Energy & Fuels Category) (Chapter 3 of this thesis)



3. Ortiz-Imedio R, Ortiz A, Ortiz I. Comprehensive analysis of the combustion of low carbon fuels (hydrogen, methane and coke oven gas) in a spark ignition engine through CFD modeling. *Energy Conversion Management* 2022;251:114918. doi:10.1016/j.enconman.2021.114918. (JCR impact factor 2020: 9.709, Q1 position 10 of 114 in the Energy & Fuels Category) (Chapter 4 of this thesis)



4. Moral G, Ortiz-Imedio R, Ortiz A, Gorri D, Ortiz I. Coke Oven Gas as a sustainable source of hydrogen. State-of-the-art and prospects. Industrial & Engineering Chemical Research (Submitted in November 2021, Under review) (JCR impact factor 2020: 3.764, Q2 position 50 of 143 in the Chemical Engineering Category)



- Publication in conference proceedings

Ortiz R, Ortiz A, Ortiz I. POWER TO GAS: Integration of wind renewable energy for Hydrogen generation as a future energetic vector in the Atlantic area. European Hydrogen Energy Conference (EHEC) 2018, ISBN: 978-84-09-01620-4.

Ortiz-Imedio R, Ortiz A, Urroz JC, Diéguez PM, Gorri D, Gandía LM, Ortiz I. Specific CO<sub>2</sub> emissions of Coke Oven Gas applied in internal combustion engines. 3<sup>rd</sup> International Congress of Chemical Engineering (ANQUE - ICCE 3), ISBN: 978-84-09-12430-5.

Ortiz-Imedio R, Ortiz A, Urroz JC, Diéguez PM, Gorri D, Gandía LM, Ortiz I. Performance and specific NO<sub>x</sub> emissions of a spark ignition engine fuelled with Coke Oven Gas. Hydrogen Power Theoretical & Engineering Solutions International Symposium (Hypothesis) XVI, ISBN: 979-12-200-9642-3.

- Contributions to scientific meetings and conferences

Ortiz R, Ortiz A, Ortiz I. POWER TO GAS: Integration of wind renewable energy for Hydrogen generation as a future energetic vector in the Atlantic area. European Hydrogen Energy Conference (EHEC), March 14 – 16, 2018, Málaga (Spain). Poster presentation.



Ortiz R, Ortiz A, Urroz JC, Diéguez PM, Gorri D, Gandía LM, Ortiz I. Valorization of Coke Oven Gas waste stream applied in a Spark Ignition Engine. World Hydrogen Technologies Convention (WHTC), June 2 – 7, 2019, Tokyo (Japan). Poster presentation.



Ortiz-Imedio R, Ortiz A, Urroz JC, Diéguez PM, Gorri D, Gandía LM, Ortiz I. Specific CO<sub>2</sub> emissions of Coke Oven Gas applied in internal combustion engines. 3<sup>rd</sup> International Congress of Chemical Engineering (ANQUE - ICCE 3), June 19 – 21, 2019, Santander (Spain). Poster presentation.



Ortiz-Imedio R, Ortiz A, Urroz JC, Diéguez PM, Gorri D, Gandía LM, Ortiz I. Performance and specific NO<sub>x</sub> emissions of a spark ignition engine fuelled with Coke Oven Gas. Online Hydrogen Power Theoretical & Engineering Solutions International Symposium (Hypothesis) XVI, November 8 – 10, 2021. Oral presentation.

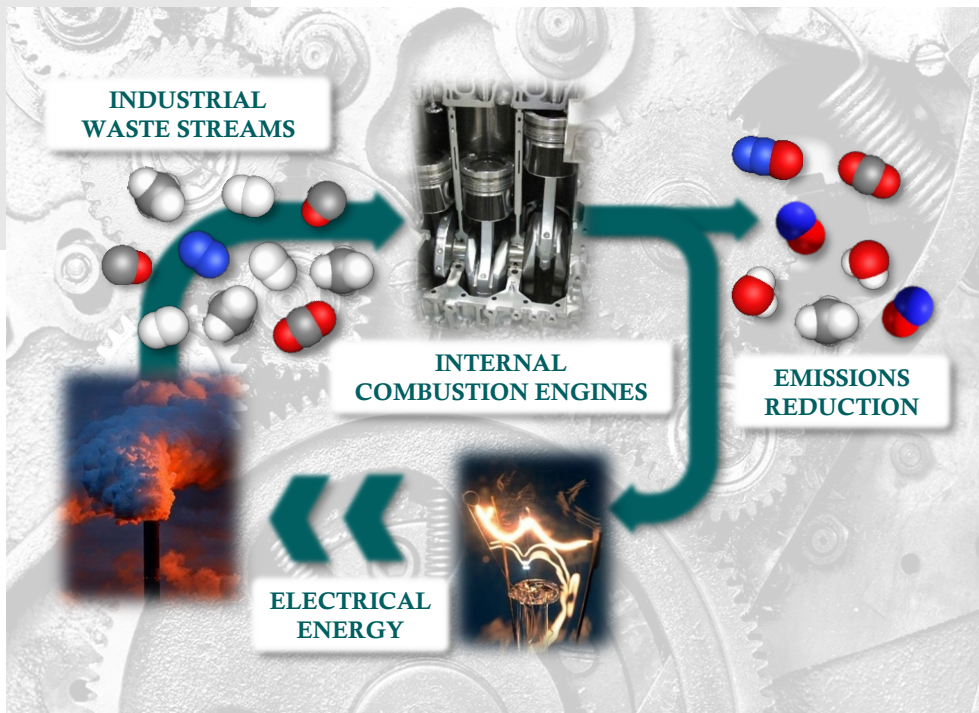


Ortiz-Imedio R, Maestre VM, Ortiz A, Gorri D, Ortiz I. Coke oven gas as potential fuel for stationary SI engines. 23<sup>th</sup> World Hydrogen Energy Conference (WHEC) 2022, June 26-30, 2022, Istanbul (Turkey). Submitted









Los combustibles bajos en carbono son clave para la transición hacia un sistema energético sostenible con menos emisiones contaminantes y menos dependiente de los combustibles fósiles. El hidrógeno como vector energético permite una amplia implementación de las fuentes de energía renovables, con una generación de energía limpia más distribuida en las diferentes regiones del mundo. Además, el hidrógeno puede utilizarse en muchos sectores, como el marítimo, con una importante contribución al transporte de mercancías y pasajeros. Asimismo, hay corrientes residuales industriales con un elevado porcentaje de hidrógeno y alto contenido energético, permitiendo su recuperación con motores de combustión interna, una tecnología empleada mundialmente. La primera parte de esta tesis se enfoca en el análisis de un sistema energético europeo en 2050 basado en hidrógeno orientado a barcos, mientras que en la segunda parte se realiza el estudio del gas de coque en un motor, tanto experimentalmente como en un modelo CFD.

Low carbon fuels are key to the transition to a sustainable energy system with lower pollutant emissions and less dependence on fossil fuels. Hydrogen as an energy vector allows a wide implementation of renewable energy sources, with a more distributed clean energy generation across the world. In addition, hydrogen can be used in many sectors, such as the maritime sector, with an important contribution to freight and passengers transport. Likewise, there are industrial waste streams with a high percentage of hydrogen and high energy content, allowing its recovery with internal combustion engines, a worldwide deployed technology. The first part of this thesis focuses on the analysis of a European energy system in 2050 based on hydrogen oriented to ships, while in the second part the study of coke oven gas in an engine is carried out, both experimentally and in a CFD model.